

Sister Rod Destructive Examinations (FY22)

Appendix F: Cyclic Integrated Reversible- Bending Fatigue Tests

Spent Fuel and Waste Disposition

*Prepared for
US Department of Energy
Spent Fuel and Waste Science
and Technology*

Oak Ridge National Laboratory

*Paul Cantonwine,
Rose Montgomery,
Jy-An Wang, Hong Wang,
Bruce Bevard, Darren Skitt,
Yadukrishnan Sasikumar,
Oscar Martinez*

January 13, 2023

M2SF-23OR010201024 ORNL/TM-2022/2733

This report was prepared as an account of work sponsored by an agency of the United States Government. Neither the United States Government nor any agency thereof, nor any of their employees, makes any warranty, express or implied, or assumes any legal liability or responsibility for the accuracy, completeness, or usefulness of any information, apparatus, product, or process disclosed, or represents that its use would not infringe privately owned rights. Reference herein to any specific commercial product, process, or service by trade name, trademark, manufacturer, or otherwise, does not necessarily constitute or imply its endorsement, recommendation, or favoring by the United States Government or any agency thereof. The views and opinions of authors expressed herein do not necessarily state or reflect those of the United States Government or any agency thereof.

SUMMARY

This report documents work performed under the Spent Fuel and Waste Disposition's Spent Fuel and Waste Science and Technology program for the US Department of Energy (DOE) Office of Nuclear Energy (NE). This work was performed to fulfill Level 2 Milestone M2SF-23OR010201024, "FY22 Report on ORNL Sibling Rod Testing Results," within work package SF-23OR01020102 and is an update to the work reported in M2SF-22OR010201047, M2SF-21OR010201032, M2SF-19OR0010201026, and M2SF-19OR010201028.

As a part of DOE NE High Burnup Spent Fuel Data Project, Oak Ridge National Laboratory (ORNL) is performing destructive examinations (DEs) of high burnup (HBU) (>45 GWd/MTU) spent nuclear fuel (SNF) rods from the North Anna Nuclear Power Station operated by Dominion Energy. The SNF rods, called *sister rods* or *sibling rods*, are all HBU and include four different kinds of fuel rod cladding: standard Zircaloy-4 (Zirc-4), low-tin (LT) Zirc-4, ZIRLO, and M5. The DEs are being conducted to obtain a baseline of the HBU rods' condition before dry storage and are focused on understanding overall SNF rod strength and durability. Composite fuel and defueled cladding will be tested to derive material properties. Although the data generated can be used for multiple purposes, one primary goal for obtaining the post-irradiation examination data and the associated measured mechanical properties is to support SNF dry storage licensing and relicensing activities by (1) addressing identified knowledge gaps and (2) enhancing the technical basis for post-storage transportation, handling, and subsequent disposition.

This appendix documents the status of the ORNL Phase 1 DE activities related to tests of the sister rods using the Cyclic Integrated Reversible-Bending Fatigue Tester (CIRFT) in Phase 1 of the sister rod test program.

Table FS-1 provides the status of the CIRFT tests.

Table FS-1. DE.05 Status.

| Planned DE | | P.I. | Status | Comments |
|------------|---|------------|-------------|---|
| DE.05 | Perform CIRFT tests to determine static, dynamic, and cumulative effects and fatigue lifetime | Cantonwine | In progress | <p>Thirty-one tests using the CIRFT were completed on 25 specimens. The results are consistent with those for other rods of the same type that were tested in the past, but they fall on the lower side of the database, especially the rods with Zirc-4 and LT Zirc-4 cladding. One dynamic test was removed from the fatigue database because closer examination of the data showed that it was failed during the preceding static test. The heat treatments applied to selected rods resulted in a shorter fatigue lifetime, which is suspected to be related to their observed reduced flexural rigidity.</p> <p>The flexural rigidity measured for the baseline sister rods is consistent with (although on the lower side of) previously tested 17×17 specimens for M5-, ZIRLO-, and LT Zirc-4 clad specimens. Because of the large uncertainties in the tests at low</p> |

| Planned DE | | P.I. | Status | Comments |
|------------|---|------------|-------------|--|
| | | | | <p>applied moment and because all the samples at high applied moment were tested statically prior to dynamic testing, only the samples tested at applied moments between 8 and 14 N-m are used in calculating the average dynamic flexural rigidity, which is 27 N-m².</p> <p>A test on a specimen with a grid-to-rod-fretting mark in the maximum strain location did not result in a reduced fatigue lifetime.</p> <p>One remaining test will be completed on a specimen that has multiple pellet-pellet gaps to determine whether the gaps have an impact on the fatigue lifetime.</p> <p>The cumulative effects test fixture is being redesigned.</p> |
| | Comparison of fueled segment CIRFT performance with cladding-only data and O-Donnell Langer historical data | Cantonwine | In progress | <p>CIRFT results were compared with open literature fatigue data on zirconium alloys (specifically Zircaloy-2 and Zirc-4) that used other unfueled material geometries. To determine if the open literature data are representative of empty cladding and/or fueled rod geometry, a verification study is being performed using CIRFT and unirradiated and irradiated cladding specimens. To date, 5 CIRFT tests have been performed on unirradiated Zirc-4 tubes for comparison with fuel rod segment and open literature data for alloy tubes and coupons. It was found that the fatigue of the high burnup fuel rods is degraded compared to the cladding-only tube and other specimens described in open literature on zirconium alloys. It is also noted that testing to date is under zero-mean strain conditions, which is likely non-conservative relative to the expected condition of the fuel rod, which includes axial strain from rod internal pressure and bending under gravity. A proposed modified fatigue design limit is compared with the data in hand. Additional testing to quantify the impact of a non-zero mean strain is planned for FY23.</p> |

| Planned DE | | P.I. | Status | Comments |
|------------|---|-----------|-------------|---|
| | Post-test imaging and dogbone characterization | Skitt | Complete | All completed test pairs have been characterized. |
| | Post-test SEM characterization of fracture surface | Sasikumar | In Progress | A sample preparation procedure was developed, and the fracture surfaces of two failed fuel rods and two failed Zirc-4 tubes have been characterized. Features consistent with fatigue were observed, and the indications are that fatigue failure initiated on the ID in both the fuel segments and the cladding-only tube samples. It is most likely that the stress concentrations at pellet discontinuities are the source of the ID cracks that initiated fatigue failure in the fuel segments, but ID surface damage was created during testing of unirradiated cladding tubes that caused the initiation of fatigue failures. Initiation on the ID of the cladding tubes was unexpected because the maximum strain is on the OD. Future SEM characterization is planned to explore whether hydride formation is a factor in fatigue initiation. |
| | Finite element modeling of selected performance characteristics | Martinez | In progress | Modeling of the cumulative impact test to determine the appropriate fixture configuration is complete and indicates that applying an impact to a specimen mounted in a dogbone will yield an impact load that is higher than desired. In the coming year, an alternative testing approach will be developed to analyze the effect of cumulative impact loads on fatigue. |

This page intentionally blank

ACKNOWLEDGMENTS

Many thanks to our US Department of Energy Office of Nuclear Energy sponsor Ned Larson, along with the Spent Fuel and Waste Science and Technology storage and transportation program leadership for their continued support. The sister rod project would not have been possible without the vision and support of the Electric Power Research Institute, Westinghouse, Framatome, and Dominion Energy.

This work would not have been possible without the support and expertise provided by the leadership and staff members of Oak Ridge National Laboratory's Irradiated Fuel Examination Laboratory. Special thanks go to Scott Thurman, who built the dogbones in-cell, tracked the specimens and the tests, and helped perform the testing, and to Bryan Woody for his assistance with in-cell testing activities. Ricardo Muse supported the fabrication jobs associated with the Cyclic Integrated Reversible-Bending Fatigue Tester tests, and we appreciate his continued support. Many thanks to Tracie Lowe for her work on the scanning electron microscope imaging included in this report.

This page intentionally blank

CONTENTS

| | |
|---|------|
| SUMMARY | iii |
| ACKNOWLEDGMENTS | vii |
| CONTENTS..... | ix |
| LIST OF FIGURES | xi |
| LIST OF TABLES..... | xv |
| REVISION HISTORY..... | xvii |
| ACRONYMS..... | xix |
| F-1. Introduction | 1 |
| F-2. CIRFT Description | 1 |
| F-3. Data Acquisition, Data Processing, Basic Information, and Extended Information | 4 |
| F-3.1 Basic Calculated Information..... | 7 |
| F-3.2 Extended Calculated Information within the Context of CIRFT | 7 |
| F-3.2.1 Pellet Bonding Stiffening..... | 8 |
| F-3.2.2 Discontinuous Cladding Support | 8 |
| F-3.2.3 Cladding Hydride Reorientation Effects..... | 9 |
| F-3.2.4 Cladding Irradiation Defect Annealing..... | 9 |
| F-3.2.5 Normal Condition Impacts..... | 9 |
| F-4. Comparison Data Available from Previous ORNL Tests of Irradiated Rod Segments..... | 11 |
| F-5. Comparison Data from Cladding Tests | 13 |
| F-5.1 Unirradiated Zirc-4 Cladding Tests | 13 |
| F-5.1.1 Calibration Sample (Zr4-W-2)..... | 14 |
| F-5.1.2 High Cycle Fatigue Response..... | 17 |
| F-6. Description of the Sister Rods Tested | 19 |
| F-7. Selection of CIRFT Test Conditions | 27 |
| F-8. CIRFT Test Results for the Sister Rods Tested..... | 29 |
| F-8.1 Static Tests | 29 |
| F-8.2 Dynamic Tests..... | 31 |
| F-8.2.1 Comparisons on the Basis of Stress Amplitude | 31 |
| F-8.2.2 Comparisons on the Basis of Strain Amplitude | 31 |
| F-8.2.3 CIRFT-measured Flexural Rigidity of HBU Fuel Rods | 32 |
| F-8.3 Comparisons of Paired Specimens..... | 42 |
| F-8.4 Optical Imaging of the Fractured Specimens..... | 44 |
| F-8.5 Scanning Electron Microscope (SEM) Characterization of Selected CIRFT Fractures..... | 70 |
| F-8.5.1 Sample preparation | 70 |
| F-8.5.2 Characterization of Fracture in ZIRLO- 17×17 | 71 |
| F-8.5.3 Characterization of Fracture in LT Zirc-4 Fuel Rods | 75 |
| F-8.5.4 Fractography of unirradiated Zirc-4 CIRFT specimens..... | 79 |
| F-8.5.4.1 Zr4-W-4..... | 79 |

| | |
|---|-----|
| F-8.5.4.2 Zr4-W-3 | 84 |
| F-8.5.5 Future work | 89 |
| F-9. CIRFT Cumulative Effects Fixture Development | 90 |
| F-9.1 Finite Element Modeling of the Cumulative Impactor | 91 |
| F-9.1.1 Finite Element Modeling Software | 91 |
| F-9.1.2 Finite Element Model..... | 92 |
| F-9.1.3 Material Models | 93 |
| F-9.1.4 Initial Conditions, Boundary Conditions and Load Cases | 94 |
| F-9.1.5 Load Cases | 94 |
| F-9.2 Results, Discussion, and Conclusions from the Cumulative Effects Fixture Modeling | 95 |
| F-9.3 Verification of FEA Results Using the Cumulative Effects Fixture | 98 |
| F-9.4 Summary, Cumulative Effects Fixture Development | 99 |
| REFERENCES | 100 |

LIST OF FIGURES

| | |
|--|----|
| Figure F-1 Two views of the ORNL CIRFT: (a) a surrogate rod specimen undergoing out-of-cell testing with three linear variable differential transducers (LVDTs) for curvature measurements, and (b) an SNF rod being tested in the hot cell..... | 2 |
| Figure F-2. Schematic drawings of U-frame setup for reversal bending when rigid arms are (a) closing, (b) neutral, and (c) opening..... | 3 |
| Figure F-3. Image showing the grip design of CIRFT with one end-block removed..... | 4 |
| Figure F-4. The LVDT measurements for the curvature calculation..... | 5 |
| Figure F-5. An example of a single cycle from two low cycle (0.05 Hz) tests used for equipment performance confirmation showing (a) the instantaneous applied bending moment, (b) the calculated curvature, and (c) the moment-curvature hysteresis loop. The example is also representative of the type of data collected in the fatigue performance portion of the test session. | 6 |
| Figure F-6. Cladding and pellet stack (a) in the neutral position and (b) in bending. [F-5] | 8 |
| Figure F-7. Results for the Strain Gauge Sample, Zr4-W-2 | 15 |
| Figure F-8. CIRFT results of unirradiated Zirc-4 tubes compared to previously reported data on both unirradiated and irradiated Zircaloy-2 [F-9] and unirradiated Zirc-4 [F-10],[F-11]. | 18 |
| Figure F-9. The static test data for 30AD05-0697-0850 represent the typical result..... | 29 |
| Figure F-10. Results of CIRFT tests plotted with reference data, applied moment vs. cycles to failure..... | 35 |
| Figure F-11. Results of CIRFT tests completed to date, strain amplitude vs. cycles to failure..... | 36 |
| Figure F-12. Stress amplitude of the composite rod based on Eq. (F-7), as a function of cycles to failure for the sister rods. The stresses representing the conditions observed in the MMTT test are calculated based on measured strains: 1 MPa for the lower strain of 0.001% (or 10 μ strain) [F-25], which is the minimum strain of the highest 4000 cycles observed, and 4.2 MPa for the upper strain of 0.0042% (or 42 μ strain), which is the maximum strain observed during TTCI testing [F-16]..... | 37 |
| Figure F-13. Cladding stress amplitude as a function of cycles to failure for the sister rods. The stresses representing the conditions observed in the MMTT test are calculated based on measured strains: 1 MPa for the lower strain of 0.001% (or 10 μ strain) [F-25], which is the minimum strain of the highest 4000 cycles observed, and 4.2 MPa for the upper strain of 0.0042% (or 42 μ strain), which is the maximum strain observed during TTCI testing [F-16]..... | 38 |
| Figure F-14. Strain amplitude as a function of cycles to failure for the sister rods compared to the fatigue data on cladding alloys from Figure F-7 and the proposed ORNL fatigue limit for fuel rods. [F-24] The strains representing the conditions observed in the MMTT test are based on measured strains: the lower strain is 0.001% (or 10 μ strain) [F-25], which is the minimum strain of the highest 4000 cycles observed, and the upper strain is 0.0042% (or 42 μ strain), which is the maximum strain observed during TTCI testing [F-16]. | 39 |
| Figure F-15. CIRFT-measured flexural rigidity of the sister rod segments tested as a function of estimated segment burnup plotted with previous CIRFT data. | 40 |
| Figure F-16. Trend of CIRFT-measured dynamic flexural rigidity with applied bending moment. | 41 |

| | |
|--|----|
| Figure F-17. 6U3K09-3353-3506 post-fatigue test condition..... | 46 |
| Figure F-18. 6U3K09-2310-2463 post-fatigue test condition..... | 47 |
| Figure F-19. 6U3K09-3200-3353 post-fatigue test condition..... | 48 |
| Figure F-20. 6U3K09-2635-2788 post-fatigue test condition..... | 49 |
| Figure F-21. 6U3K09-2463-2616 post-fatigue test condition..... | 50 |
| Figure F-22. 3F9N05-2710-2863 post-fatigue test condition. | 51 |
| Figure F-23. 3F9N05-2329-2482 post-fatigue test condition. | 52 |
| Figure F-24. 3F9N05-0719-0872 post-fatigue test condition. | 53 |
| Figure F-25. 3D8E14-2963-3116 post-fatigue test condition. | 54 |
| Figure F-26. 30AD05-2630-2783 post-fatigue test condition..... | 55 |
| Figure F-27. 30AE14-0672-0825 post-fatigue test condition. | 56 |
| Figure F-28. F35P17-1855-2008 post-fatigue test condition..... | 57 |
| Figure F-29. F35P17-3159-3312 post-fatigue test condition. | 58 |
| Figure F-30. 3A1F05-2025-2178 post-fatigue test condition. | 59 |
| Figure F-31. 3A1F05-1853-2006 post-fatigue test condition. | 60 |
| Figure F-32. 30AD05-0697-0850 post-fatigue test condition (broken ends only). | 61 |
| Figure F-33. 30AD05-2050-2203 post-fatigue test condition (broken ends only). | 62 |
| Figure F-34. 30AE14-2850-3003 post-fatigue test condition (broken ends only). | 63 |
| Figure F-35. 30AE14-3156-3309 post-fatigue test condition (broken ends only). | 64 |
| Figure F-36. 3A1F05-3214-3367 post-fatigue test condition. | 65 |
| Figure F-37. 3D8E14-719-872 post-fatigue test condition. | 66 |
| Figure F-38. 3D8E14-2412-2565 post-fatigue test condition. | 67 |
| Figure F-39. 3A1F05-3367-3520 post-fatigue test condition. | 68 |
| Figure F-40. 3D8E14-1178-1331 post-fatigue test condition. | 69 |
| Figure F-41. 23× montage of the surface of the fatigue failure in sample 3D8E14-2963-3116. The areas identified in the various quadrants were investigated at higher magnification (see Figures F-42 to F-45)..... | 72 |
| Figure F-42. 330× and 1,000× images of quadrant 1 in sample 3D8E14-2963-3116..... | 73 |
| Figure F-43. 100× and 1,000× images of quadrant 3 in sample 3D8E14-2963-3116, approximately 180° from region in quadrant 1, that is suspected to have failed after fatigue test ended. | 73 |
| Figure F-44. 120× and 500× images of quadrant 2 in sample 3D8E14-2963-3116, showing signs of fatigue striations typical of fatigue crack propagation, indicating propagation in the circumferential direction. | 74 |
| Figure F-45. 120× and 350× images of quadrant 4 in sample 3D8E14-2963-3116 showing signs of fatigue striations typical of fatigue crack propagation. The flatness of the feature on the cladding ID may be associated with fatigue initiation. There are also circumferential cracks near the cladding OD that may be associated with hydrides. | 74 |

| | |
|--|----|
| Figure F-46. 100X montage of the surface of the fatigue failure in dogbone sample DE50017. The areas identified in the various quadrants were investigated at higher magnification. | 76 |
| Figure F-47. Ductile regions and wear marks of Q1 in sample 3A1F05-2025-2178..... | 77 |
| Figure F-48. Fuel-side brittle regions of Q1 (approaching Q2) in sample 3A1F05-2025-2178. | 77 |
| Figure F-49. Cleavage-like regions, apparent fatigue striations, and flat wear marks on the fuel side of Q2 in sample 3A1F05-2025-2178. | 78 |
| Figure F-50. Ductile fracture regions amidst striations and brittle cracks on Q3 in sample 3A1F05-2025-2178. | 78 |
| Figure F-51. Flat cleavage-like regions on the fuel side leading to cracks and ductile failure seen on Q4 in sample 3A1F05-2025-2178. | 79 |
| Figure F-52. 100× montage of the surface of the fatigue failure in dogbone sample Zirc-4-W-4. Arrow marks show regions of high bending strain in the sample. | 80 |
| Figure F-53. Top (fracture) view and side view of the fatigue failure region in Q2 and Q3 of sample Zirc-4-W-4..... | 81 |
| Figure F-54. Fatigue crack initiation region in Q4 of sample Zirc-4-W-4: (A) location of the region in a low-magnification image of the sample; (B) OD side of the fatigue failure initiation site; (C) ID side of the fatigue crack initiation site; and (D) detail view of C..... | 81 |
| Figure F-55. Tilted image of Figure F-53 revealing the ID side of the fatigue failure initiation site on sample Zirc-4-W-4: (A) location of the region in a low magnification image of the sample; (B) ID side of the fatigue failure initiation site; and (C) detail view of the fatigue failure initiation fracture surface. | 82 |
| Figure F-56. Brittle fracture regions and potential wear marks of sample Zirc-4-W-4: (A) location of the region in a low magnification image of the sample; (B) Brittle or cleavage-like regions on Q1; and (C) potential wear marks observed between the brittle regions in Q1. | 83 |
| Figure F-57. 100X montage of the fatigue failure surface in dogbone sample Zirc-4-W-3. | 85 |
| Figure F-58. The top (fracture) view and side view of the fatigue failure region in Q2 and Q3 of sample Zirc-4-W-3. | 86 |
| Figure F-59. Fatigue crack initiation region in Q4 of sample Zirc-4-W-3: (A) The location of the region in a low magnification image of the sample; (B) ID side of the fatigue crack initiation site; and (C) detail view of B | 87 |
| Figure F-60. Optical microscope image of sample Zirc-4-W-3 showing the fatigue failure initiation site; the peripheral region containing the LVDT marks is not visible..... | 87 |
| Figure F-61. Tilted SEM image of Figure F-59 revealing the ID side of the fatigue failure initiation site of sample Zirc-4-W-3: (A) location of the region in a low magnification image of the sample; (B) OD side of the fatigue failure initiation site; (C) ID side of the fatigue initiation site; and (D) inside of the ID side of sample Zirc-4-W-3 at the fatigue initiation site. | 88 |
| Figure F-62. Some striations visible amidst brittle or cleavage fracture like regions and wear marks of sample Zirc-4-W-3: (A) location of the region in a wide field view of the sample; (B) wear marks observed on the ID with striations on the OD and brittle fracture regions in the middle of Q1; and (C) detail view of the flat wear-like features between striations. | 88 |

| | |
|---|----|
| Figure F-63. Fatigue failure in sample 6U3K09-2310-2463 showing the second crack observed in the sample..... | 89 |
| Figure F-64. Images of the circumferential cut-2 from sample 6U3K09-2310-2463 wrapped around a 3D cylinder to show a realistic image..... | 89 |
| Figure F-65 Cumulative shock fixture developed to apply a normal transport condition shock before fatigue testing. | 90 |
| Figure F-66. The cumulative impactor CAD model (left) and finite element model (right) include a rod segment with discrete pellets, guide blocks, and a weight with impact geometry. | 92 |
| Figure F-67. 304 stainless steel (left) and Zirc-4 (right) true stress–strain curves used compared with corresponding engineering stress–strain curves. | 94 |
| Figure F-68. Impactor end configuration (a) results for load cases 1–4. | 95 |
| Figure F-69. Impactor end configuration (a) results for load cases 5–9. | 96 |
| Figure F-70. Plastic strain occurred on the dimples for impactor end configuration (a). | 97 |
| Figure F-71. CIRFT dogbone. | 97 |
| Figure F-72. Physical test configurations with the cumulative effects fixture..... | 98 |
| Figure F-73. Impactors used in the physical tests. | 98 |

LIST OF TABLES

| | |
|---|-----|
| Table FS-1. DE.05 Status..... | iii |
| Table F-1. Reference Dynamic Dataset [F-4]..... | 11 |
| Table F-2. Test Conditions for Strain-gauged Test Sample..... | 13 |
| Table F-3. Test Conditions for Fatigue Tests on Cladding-only Zirc-4 Tubes (no strain gauges) | 14 |
| Table F-4. The Dynamic Correction Factor as a Function of the Strain Gauge Strain Amplitude for Testing at 0.05 and 5 Hz..... | 15 |
| Table F-5. Curvature, Strain Amplitude, Applied Moment, and Cycles to Failure for the Unirradiated Zirc-4 Cladding Tubes..... | 17 |
| Table F-6. Maximum Average Stress, Maximum Stress, Dynamic Flexural Rigidity, and Rigidity Standard Deviation for the Unirradiated Zirc-4 Cladding Tubes | 18 |
| Table F-7. Sister Rod Segments Selected for CIRFT. | 20 |
| Table F-8. CIRFT Specimen and Test Pairing..... | 28 |
| Table F-9. Static Test Results. | 30 |
| Table F-10. Sister Rod CIRFT Test Results to Date..... | 34 |
| Table F-11. Results Arranged by Paired Specimens (Baseline Rods vs. Heat-treated Rods) for Static/Dynamic and Dynamic CIRFT..... | 43 |
| Table F-12. Summary of Visual Observations of CIRFT-fractured Dogbones. | 45 |
| Table F-13. CIRFT Specimens Identified for Potential SEM Characterization. | 70 |
| Table F-14. Cumulative Impactor Model Minimum Material Properties..... | 93 |
| Table F-15. Cumulative Tester FEA Load Case Summary. | 94 |
| Table F-16. Summary of Fuel Rod Maximum g-load during Impact with End Configuration (a)..... | 96 |

This page is intentionally left blank.

REVISION HISTORY

| Date | Changes |
|------------|--|
| 3/29/2019 | Initial release |
| 9/27/2019 | Revised to include additional data and incorporate comments from the previously released report. |
| 10/29/2020 | The CIRFT detailed report was moved to Appendix F and was updated to include the most recent information. |
| 11/30/2020 | Comments received on the draft were incorporated, and the document numbering was revised to reflect its M2 status. |
| 10/29/21 | Section F-7.6 was added. The results of the uncertainty estimates (Appendix G) were integrated into the data table and plots, and related discussions were modified. One low data point was investigated and removed from the CIRFT dataset, and the supporting information was added to the report (Section F-7.1). Minor clarifications have been made throughout. |
| 3/31/22 | Minor formatting changes and clarifications have been made in response to comments received on the 10/29/21 report (Section F-2 paragraph 4, Section F-3 paragraph 1, Figure F-5 caption, addition of reference F-19). The document ID number was revised to reflect its M2 status and the issue date was changed. |
| 10/28/22 | Sections F-5 and F-8.5 were added. The Summary section and Table FS-1 was updated. Two references were added. Section F-8.2 was revised and incorporates a new section, F-8.2.2, to reflect our most up-to-date understanding of the data, and Figure F-14 was added. |
| 1/13/2023 | Comments received from the team were incorporated throughout and the document ID number was revised to reflect its M2 status and the issue date was changed. |

This page is intentionally left blank.

ACRONYMS

| | |
|-------|---|
| ASME | American Society of Mechanical Engineers |
| BPVC | Boiler and Pressure Vessel Code |
| BWR | boiling water reactor |
| CIRFT | cyclic integrated reversible-bending fatigue tester |
| DE | destructive examination |
| DOE | US Department of Energy |
| FEA | finite element analysis |
| FHT | full-length fuel rod heat treatment |
| GTRF | grid-to-rod fretting |
| HBU | high burnup |
| ID | inner diameter |
| LSTC | Livermore Software Technology Corporation |
| LT | low tin |
| NDE | nondestructive examination |
| NE | Office of Nuclear Energy |
| NRC | US Nuclear Regulatory Commission |
| OD | outer diameter |
| ORNL | Oak Ridge National Laboratory |
| PWR | pressurized water reactor |
| SEM | scanning electron microscope |
| SNF | spent nuclear fuel |

This page is intentionally left blank.

F-1. Introduction

Spent nuclear fuel (SNF) assemblies must be shipped to other sites for processing and disposal. During shipment, the fuel is typically oriented horizontally, and the fuel rods are subject to periodic alternating loads related to the movement of the vehicle that results in alternating bending of the SNF fuel rods. The number of bending cycles is related to the length of the shipping route, with longer routes producing more cycles. Because it is well-known that cyclic loads can produce failures, even when the stress and strain imposed are below the material's yield point, investigation of the SNF's fatigue behavior is prudent.

This report discusses the results of fatigue testing conducted at Oak Ridge National Laboratory (ORNL) using the Cyclic Integrated Reversible-Bending Fatigue Tester (CIRFT) created by the US Department of Energy (DOE) Office of Nuclear Energy (NE) for the High Burnup Spent Fuel Data Project and its sister rods [F-1, F-2, F-3]. The results of the tests are compared with results obtained over the last decade using the same CIRFT for the US Nuclear Regulatory Commission (NRC).

F-2. CIRFT Description

The CIRFT, shown in Figure F-1, is hardware developed by ORNL [F-4, F-5] to test the fatigue lifetime of SNF in postulated normal transportation vibration conditions. The machine oscillates 6-inch segments of high burnup (HBU) SNF until fatigue failure occurs. The CIRFT uses a U-frame with two rigid arms that convert the motor's linear motion into a bending moment exerted on the rod segment. The two U-frame arms are driven by two electromagnetic-force-based motors. The motors (Bose model LM2) have a maximum load capacity of $\pm 3,000$ N and a maximum stroke of ± 25.6 mm.

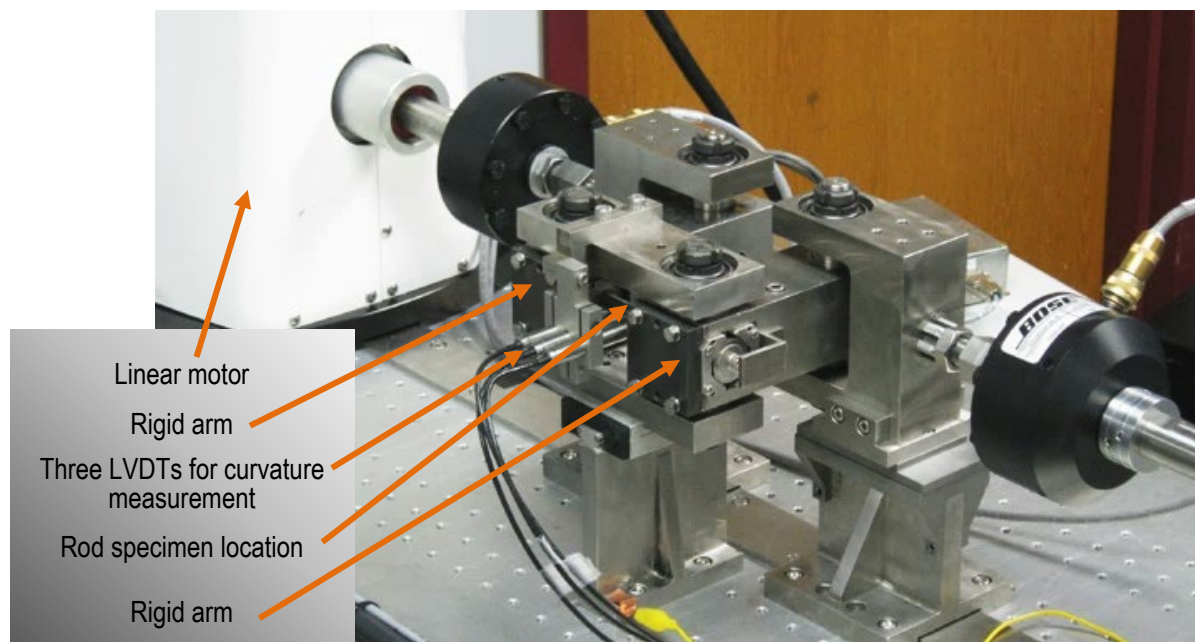
Each tested SNF segment is fitted with special end grips, or *dogbones*, which are epoxied onto both ends of the segment. When prepared this way, the SNF segment is referred to as a *dogbone*. The epoxy provides a compliant layer that is important for ensuring pure bending. The epoxy layer thickness depends on the as-built diameter of dogbone recesses and segment outer diameter. This layer is important for ensuring pure bending. When the dogbone is engaged with the U-frame, bending is imposed by the motor through the U-frame, as illustrated in Figure F-2, with a cycle that progresses as follows: the dogbone (1) begins in the neutral position (i.e., no bending), (2) is flexed laterally away from the front face of the machine, (3) is returned to the neutral position, (4) is flexed laterally toward the front face of the machine, and (5) is returned to the neutral position. The CIRFT can flex the rod specimen at 5–10 Hz during the dynamic test, with the sister rod tests performed at 5 Hz.

To ensure the desired motion, the CIRFT is specifically configured to test SNF rod segments that have diameters ranging from 9.70 to 11.74 mm, with a fixed segment length of 152.40 mm (6 in.). The test's gauge section is the 50.80 mm (2 in.) SNF rod length between the dogbones, where the maximum bending deflection occurs.

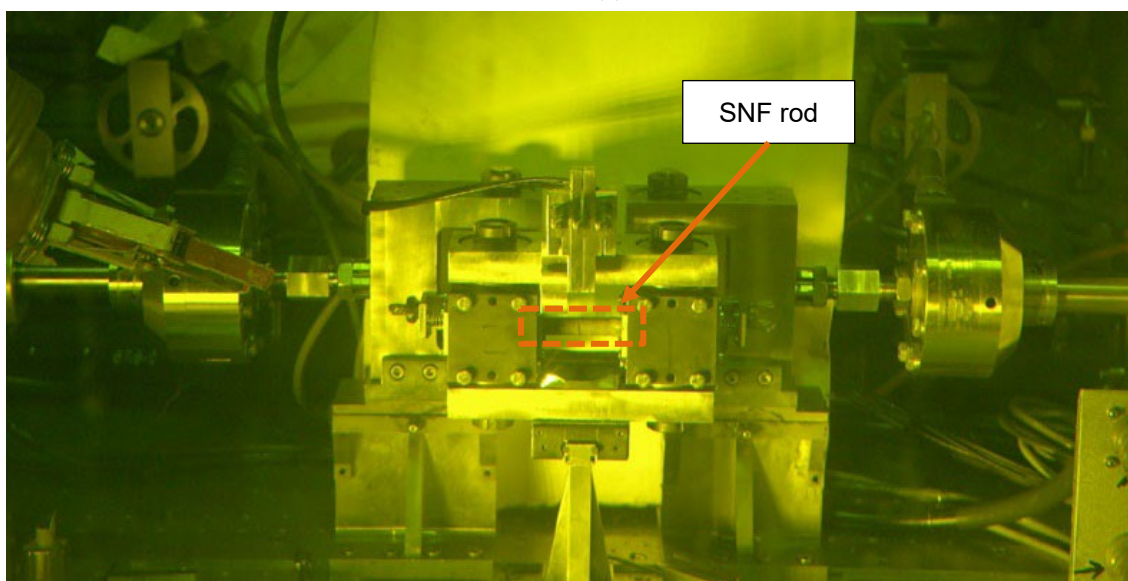
To date, two types of tests have been performed: a *static* test and a *dynamic* test. A third test, the *cumulative effects* test, is still in the equipment development stage. The dynamic test is the standard fatigue test performed on the CIRFT. Dynamic testing is performed in a series of sessions, where a session consists of two displacement-controlled cyclic tests performed at 0.05 Hz for a low number of cycles at loads less than the 5 Hz fatigue test (to confirm equipment performance) and a load-controlled cyclic test at 5 Hz (to test fatigue performance). The number of sessions in a complete dynamic test is dependent on the cycles to failure and varies from 1 session (for low-cycle fatigue conditions) to as many as 7 sessions (for high-cycle fatigue conditions) [F-19]. During the dynamic test, the SNF segment is flexed at a fixed frequency and motor stroke length. For the static test, the segment is flexed slowly to the maximum stroke of the machine and the deflection of the SNF specimen is measured. The static test does not typically result in fracture of the specimen because the largest possible machine stroke usually cannot impose enough deflection on the SNF specimen to exceed the cladding tensile strength and cause a non-fatigue fracture. Although the static

January 13, 2023

test can be followed by a dynamic test, the flexure imposed during the static test is much higher than that imposed during the dynamic test, and the large deflection may reduce the flexural rigidity and fatigue lifetime, even without fracture of the SNF segment, as discussed in later sections of this appendix. The cumulative test will impose impacts on the SNF segment before a dynamic test is performed; the cumulative test is meant to determine whether periodic impacts of the rod with other rods or the packaging during transport are detrimental to the fatigue lifetime.

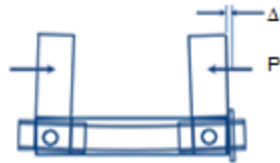


(a)

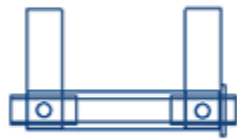


(b)

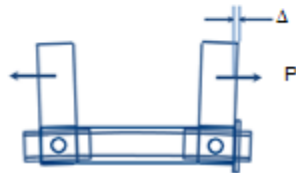
Figure F-1 Two views of the ORNL CIRFT: (a) a surrogate rod specimen undergoing out-of-cell testing with three linear variable differential transducers (LVDTs) for curvature measurements, and (b) an SNF rod being tested in the hot cell.



(a) Rigid arms are closing. The curvature is concave outward and designated with a negative sign.



(b) Rigid arms are in neutral position.



(c) Rigid arms are opening. The curvature concave inward and designated with a positive sign.

Figure F-2. Schematic drawings of U-frame setup for reversal bending when rigid arms are (a) closing, (b) neutral, and (c) opening.

F-3. Data Acquisition, Data Processing, Basic Information, and Extended Information

This section summarizes the full discussion provided by Wang and Wang [F-4, F-5, F-21]. The key data acquired during the CIRFT test include the number of cycles to failure and the bending moment imposed. The bending moment is calculated based on the motor stroke length applied (set by the user) and the deflection of the SNF rod segment, which is measured using three LVDTs, as shown in Figure F-3. A view of one end of a test specimen is shown in Figure F-3 with the end-block removed, allowing a view of the LVDTs. Online monitoring of the calculated flexural rigidity is used to shut down the machine at the onset of failure.

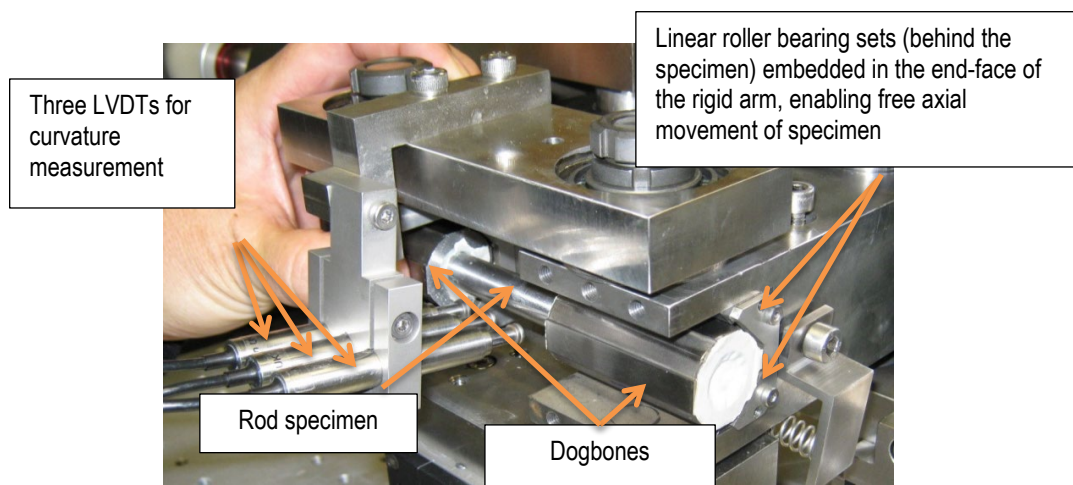


Figure F-3. Image showing the grip design of CIRFT with one end-block removed.

The distances built into the CIRFT machine and the length of the segment dogbone are important because they are used to calculate all load, moment, and curvature values. Important fixed physical distances include the length of the U-frame arms (101.60 mm) and the location and contact geometry of the LVDTs. Also, the motor's recorded stroke length during the test is directly applied in the data reduction, and the SNF rod outer diameter (OD) is used to calculate strain and stress.

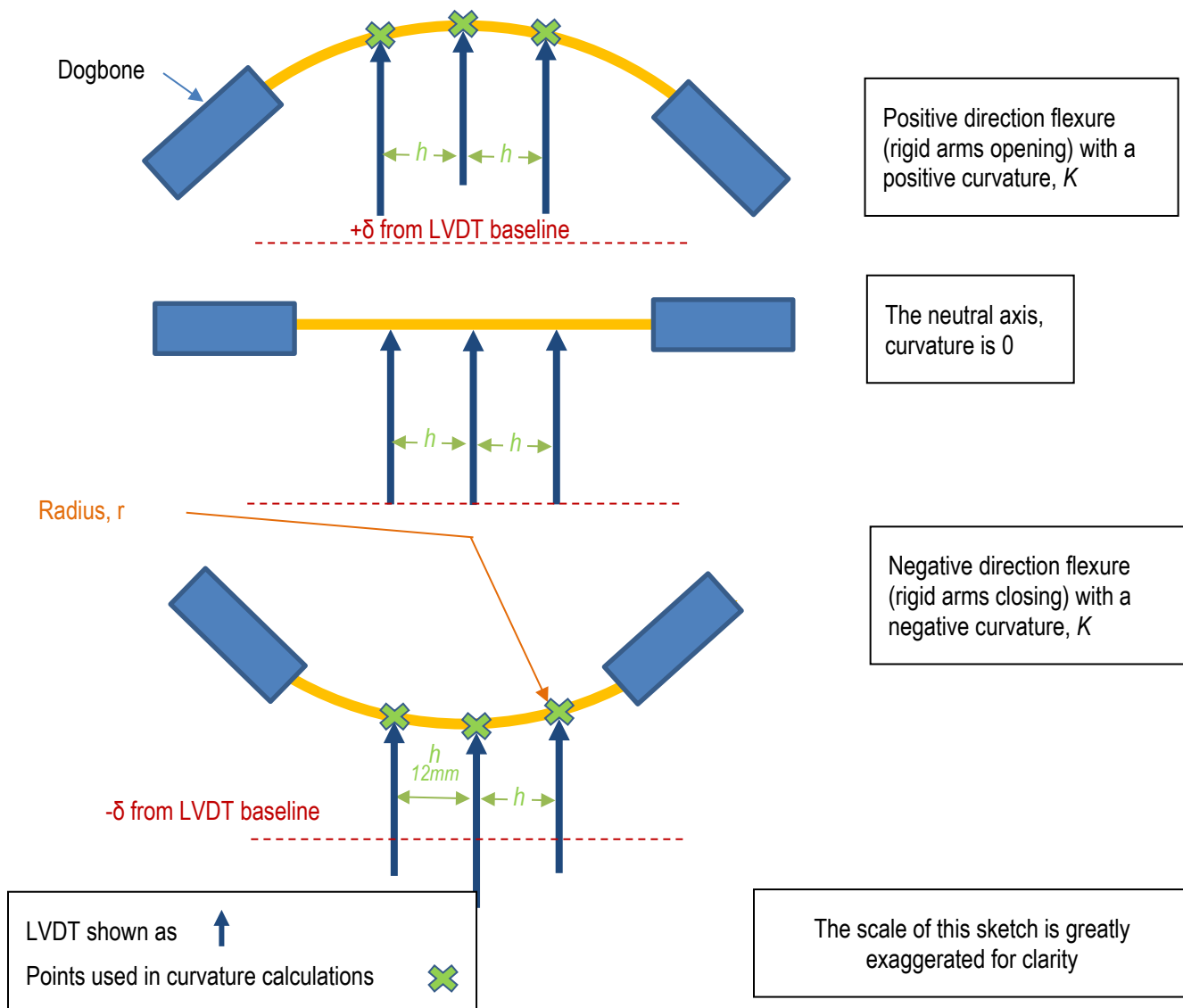


Figure F-4. The LVDT measurements for the curvature calculation.

The rod curvature, K , is calculated as the inverse of the radius, assuming the SNF segment forms a short circular arc. As illustrated in Figure F-4, the known spacing between the LVDTs (h , 12 mm) is used with the measured LVDT deflection to determine the instantaneous curvature of the dogbone gauge section during the test. The raw data are denoised and further adjusted based on the type of LVDT used in the test and any bias observed in the LVDT measurements. An example of the processed data is provided in Figure F-5.

January 13, 2023

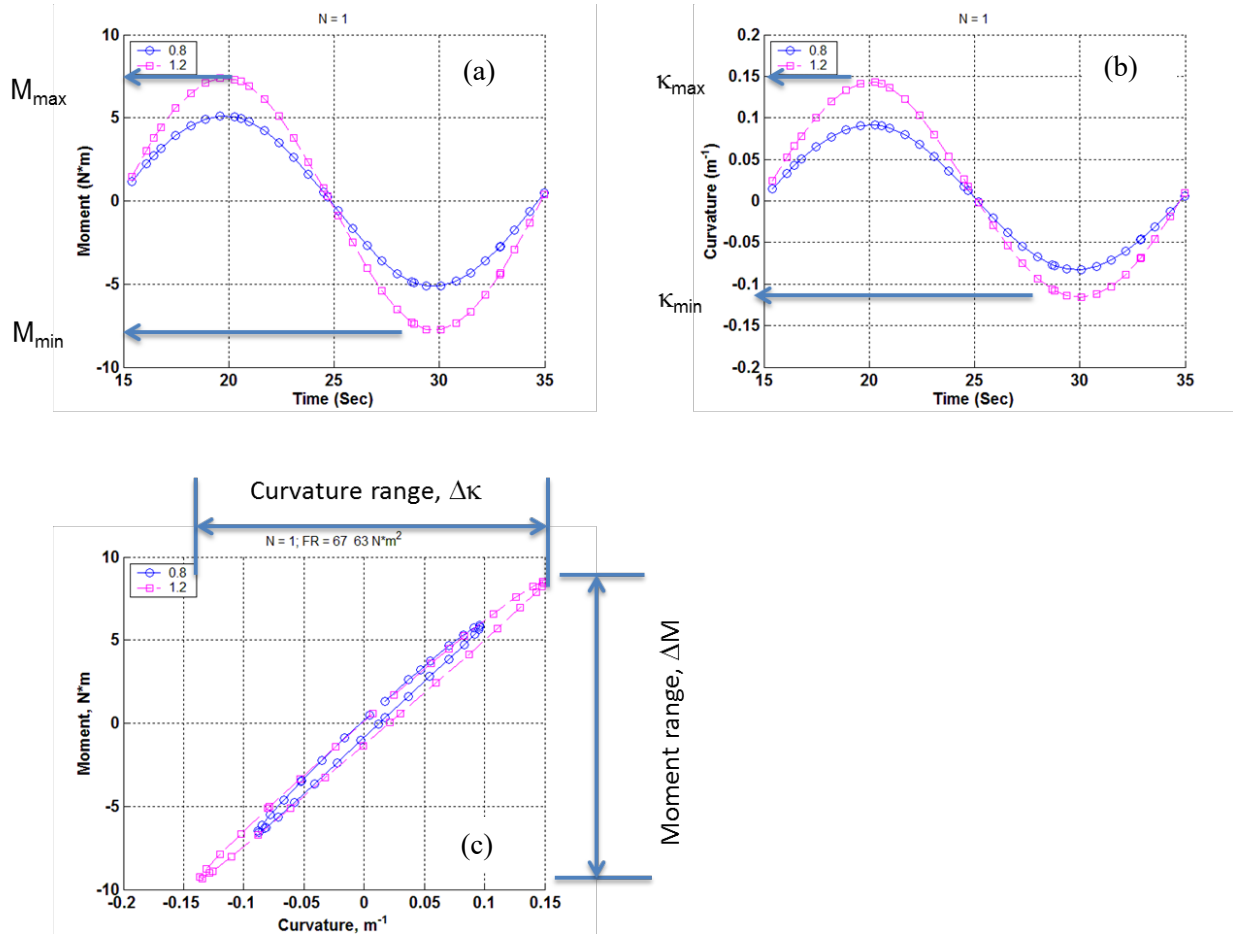


Figure F-5. An example of a single cycle from two low cycle (0.05 Hz) tests used for equipment performance confirmation showing (a) the instantaneous applied bending moment, (b) the calculated curvature, and (c) the moment-curvature hysteresis loop. The example is also representative of the type of data collected in the fatigue performance portion of the test session.

The radius, r , is calculated by determining the physical coordinates described by the measured LVDT deflections d_1 , d_2 , and d_3 and by scribing them with a circle:

$$\sqrt{(x_0 - d_2)^2 + y_0^2}, \quad (\text{F-1})$$

where:

$$x_0 = \frac{-2m_a m_b h - m_a(d_2 + d_3) + m_b(d_1 + d_2)}{2(m_b - m_a)}, \quad (\text{F-2})$$

and

$$y_0 = -\frac{1}{m_a} \left(x_0 - \frac{d_1 + d_2}{2} \right) - \frac{h}{2}, \quad (\text{F-3})$$

where

$$m_a = \frac{h}{d_2 - d_1} \text{ and } m_b = \frac{h}{d_3 - d_2}, \quad (\text{F-4})$$

and h is the sensor distance fixed at 12 mm.

Corrections are made to the LVDT data (d_1 , d_2 , d_3 , and h) as described in the work by Wang and Wang [F-7].

F-3.1 Basic Calculated Information

To provide a basis for comparing the performance of different fuel rod designs, it is necessary to calculate additional parameters such as the stress and strain, and they are typically discussed in terms of their maximum amplitude for CIRFT. It is also useful to survey the flexural rigidity, which tends to decrease as the test progresses. Typically, the flexural rigidity at the beginning of the test is discussed as a comparison point among rod types. The strain and stress parameters are calculated based on standard formulae for a circular beam in bending.

The maximum gauge strain, which occurs at the maximum deflections in the cycle and at the outermost radius of the rod, is calculated as the curvature multiplied by the radius of the rod, which is the maximum distance from the neutral axis, y_{max} :

$$\varepsilon = \kappa \times y_{max}. \quad (\text{F-5})$$

The average moment applied to the rod is

$$M = F \times L, \quad (\text{F-6})$$

where F is the averaged value of the load applied at the timespan of interest (typically 0.001 s in the dynamic test) by the CIRFT motors, and L is the fixed U-frame loading arm length (101.60 mm).

The maximum rod stress is calculated as

$$\sigma = M \times y_{max} / I, \quad (\text{F-7})$$

where I is the area moment of inertia of the composite SNF rod calculated based on the geometry of cladding and solid pellet section.

The flexural rigidity, EI , provides a means to generate the stress-strain relationship associated with M- κ . The average calculated bending moment (ΔM) and average measured curvature ($\Delta \kappa$) are used to characterize the average flexural rigidity over the timespan of interest:

$$EI = \Delta M / \Delta \kappa. \quad (\text{F-8})$$

F-3.2 Extended Calculated Information within the Context of CIRFT

In addition to the basic information discussed in Section F-3.1, other parameters of interest are developed to study the effect of particular rod characteristics on the fatigue.

SNF fuel rods are heterogeneous. Although the geometry of the irradiated rod can be estimated, it varies based on rod type, manufacture, and operation. The irradiated rod contains cracked pellets (some with HBU rims), an inner cladding oxide layer, potentially a layer of pellet bonded with the cladding ID, cladding with radiation-induced flaws, and an outer cladding oxide layer that is potentially discontinuous due to spalling. Axially, the fuel column is not continuous; it is composed of numerous short pellets. Although there could be some bonding between pellet ends as a result of an in-reactor diffusion bonding or galling process, the contacting surface areas are small as a result of the pellet chamfers and dishes, and the pellet-pellet bonding

January 13, 2023

is not expected to be strong. Given these conditions, an SNF rod is far from an ideal homogeneous material, and the idealized treatment described in previous sections is not completely accurate.

To improve understanding of the rod's performance, some of these heterogeneous effects on fatigue lifetime were explored by mining the CIRFT data, including: (1) pellet-pellet and pellet-cladding bonding rod stiffening, (2) discontinuities in cladding support conditions at pellet-pellet interfaces, (3) cladding hydride reorientation, and (4) effects of the heat treatment applied to three of the SNF rods tested, as described in the following subsections.

F-3.2.1 Pellet Bonding Stiffening

Although the CIRFT data do not allow for separate effects testing, the measured flexural rigidity data can be trended to look for sudden shifts that could indicate pellet-pellet and pellet-cladding debonding. Results from previous testing [F-4, F-5] indicate that pellet-pellet bonding is relatively weak and likely becomes debonded after only a few CIRFT cycles. However, the pellet-cladding bond is expected to be stronger than the pellet-pellet bond. For cases in which the rod was operated in-reactor at high temperature and power, a chemical bond may be developed between the pellet OD and the cladding inner diameter (ID). Wang and Wang proposed a dual flexural rigidity (i.e., before and after the bond is disrupted) with a bonding efficiency that can be applied in rod mechanical performance modeling.

F-3.2.2 Discontinuous Cladding Support

Although the LVDTs used on the CIRFT device only measure the gross rod deflection within the gauge section, several pellet lengths with several pellet-pellet interfaces are included in the gauge section, and any effects related to the pellet-pellet interfaces are embedded in the CIRFT data. As observed in previous test results, fractures are typically located at the pellet-pellet interfaces, which is consistent with the reduced mechanical cross section and potential interaction between the pellet end and cladding at those locations during bending. This is described by Wang and Wang as a fuel pellet “pinning” effect, as illustrated in Figure F-6.

Wang and Wang investigated the effects on the cladding using finite element analysis (FEA) and found that the localized strain in the cladding at the pellet-pellet-cladding interface region is three to four times higher than that in regions supported by the body of the fuel pellet. This is caused by (1) the interaction of the pellet end with the cladding, and (2) the localized axial tension that is applied as the gap is opened.

Wang and Wang further explored the shift in the neutral axis that occurs during pinning. The neutral axis shifts constantly with each cycle, but the maximum strain still occurs at the outer radius of the cladding.

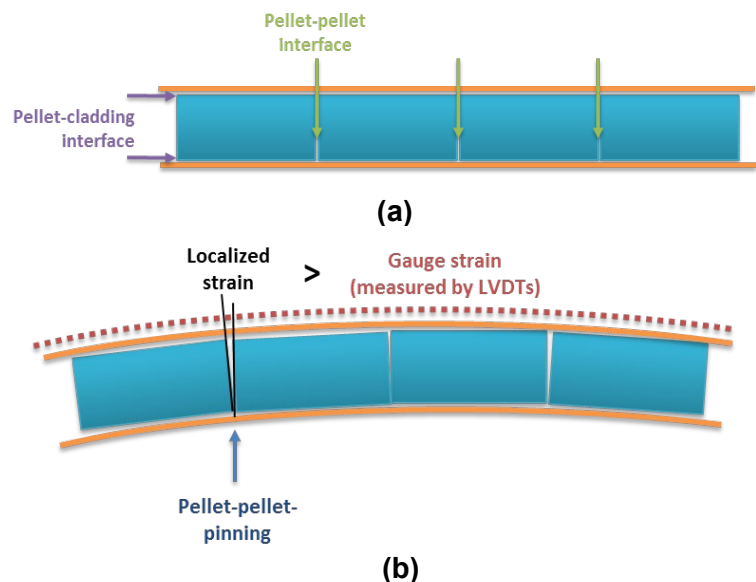


Figure F-6. Cladding and pellet stack (a) in the neutral position and (b) in bending. [F-5]

F-3.2.3 Cladding Hydride Reorientation Effects

Hydrogen taken up by the fuel rod cladding in-reactor can be detrimental to performance when the hydrogen concentration exceeds the alloy's solubility and zirconium hydride platelets are precipitated within the cladding. Wang and Wang completed four CIRFT tests with cladding hydrides that had been purposely reoriented from circumferential to radial; however, a large difference in performance was not observed in fatigue lifetime, and no definitive conclusions could be made.

The sister rod tests provide additional insight with comparisons between heat-treated rods and baseline rods. However, not all sister rod heat treatments resulted in reoriented hydrides, because they were treated at more realistic temperature and cladding stress conditions. A description of the heat treatments and the degree of reorientation are provided in Appendices A and B.

F-3.2.4 Cladding Irradiation Defect Annealing

During reactor operation, the cladding is hardened and embrittled through the accumulation of irradiation defects. The baseline sister rods were tested in the as-received condition, and three rods were heat-treated to subject them to the potential for irradiation defect annealing.

F-3.2.5 Normal Condition Impacts

Impacts to the fuel rod are expected to reduce fatigue lifetime because (1) they are expected to disrupt pellet-pellet bonds and pellet-cladding bonds at the impact site, thus leading to a reduced flexural rigidity, (2) the rod's flexural rigidity determines the total deflection of the rod in bending, and (3) a low flexural rigidity results in larger deflections and a corresponding higher stress and strain for a given applied acceleration. Thus, it is postulated that normal condition impacts could reduce the fatigue lifetime of the SNF rods.

Previous testing by Wang and Wang included non-normal impacts from a drop height of 12 in. with indeterminant results that were on the low side of the existing dataset. Future testing is expected to explore this effect with a more controlled impact method.

This page is intentionally blank

F-4. Comparison Data Available from Previous ORNL Tests of Irradiated Rod Segments

The NRC funded the development of the CIRFT and performed testing on HBU SNF with Zirc-4 and M5 cladding from pressurized water reactors (PWRs) and Zircaloy-2 (Zirc-2) from boiling water reactors (BWRs). Fifty-three cyclic fatigue tests in a range of load amplitudes were performed on PWR rod segments, and 17 tests were performed on BWR rod segments. The burnup of the tested rod segments ranged between 45 and 67 GWd/MTU. The oxide layer thickness on the waterside surface of each segment was not specifically measured but was estimated to be between 20 to 110 μm , with a corresponding estimated hydrogen concentration of 110–800 wppm. Wang and Wang completed four CIRFT tests in which the cladding hydrides were reoriented by pressurizing the segment and applying a thermal transient to determine whether the radial hydrides reduced the fatigue lifetime. The basic data from these tests are directly comparable with the sister rod test results as summarized in Table F-1 [F-4].

Table F-1. Reference Dynamic Dataset [F-4].

| Rod type | Cladding material | Parent rod-average burnup (GWd/MTU) | Test ID | Cycles to failure | Average moment (N-m) | Maximum cladding stress ^d (MPa) | Maximum average stress ^e (MPa) | Maximum average strain (%) | Flexural rigidity (N-m ²) |
|----------|-------------------|-------------------------------------|--------------------|----------------------|----------------------|--|---|----------------------------|---------------------------------------|
| 15×15 | Zirc-4 | 67 | Demo1 | 4.0E+03 | 28.5 | 456 | 233 | 0.51 | 30.2 |
| 15×15 | Zirc-4 | 67 | Dcal ^c | 9.6E+03 | 28.6 | 366 | 234 | 0.41 | 37.9 |
| 15×15 | Zirc-4 | 67 | DL2H | 1.8E+03 | 34.1 | 362 | 279 | 0.40 | 45.6 |
| 15×15 | Zirc-4 | 67 | S1 ^c | 4.6E+03 | 28.5 | 327 | 233 | 0.36 | 42.3 |
| 15×15 | Zirc-4 | 67 | S2 ^c | 7.2E+03 | 28.3 | 318 | 231 | 0.35 | 43.3 |
| 15×15 | Zirc-4 | 67 | DH3 | 7.1E+03 | 33.7 | 282 | 276 | 0.31 | 57.9 |
| 15×15 | Zirc-4 | 67 | R1 | 5.5E+03 | 29.0 | 227 | 237 | 0.25 | 61.9 |
| 15×15 | Zirc-4 | 67 | S3 ^c | 2.5E+04 | 24.1 | 214 | 197 | 0.24 | 54.8 |
| 15×15 | Zirc-4 | 67 | DH2 | 6.5E+04 | 18.9 | 170 | 155 | 0.19 | 53.9 |
| 15×15 | Zirc-4 | 67 | DL1 | 1.1E+05 | 14.1 | 104 | 115 | 0.12 | 65.6 |
| 15×15 | Zirc-4 | 67 | DH1 | 2.5E+05 | 11.6 | 99 | 95 | 0.11 | 56.7 |
| 15×15 | Zirc-4 | 67 | S5 | 1.8E+05 | 11.6 | 84 | 95 | 0.09 | 66.4 |
| 15×15 | Zirc-4 | 67 | R3 | 1.3E+05 | 12.6 | 73 | 103 | 0.08 | 82.6 |
| 15×15 | Zirc-4 | 67 | R2 | 3.9E+05 | 10.0 | 70 | 82 | 0.08 | 69.3 |
| 15×15 | Zirc-4 | 67 | DL3 | 1.0E+06 | 9.2 | 60 | 75 | 0.07 | 73.4 |
| 15×15 | Zirc-4 | 67 | DM2 | 2.3E+06 | 8.2 | 56 | 67 | 0.06 | 71.9 |
| 15×15 | Zirc-4 | 67 | R4 | 2.7E+05 | 7.8 | 54 | 64 | 0.06 | 70.0 |
| 15×15 | Zirc-4 | 67 | HR1 ^a | 4.2E+04 | 15.2 | 207 | 124 | 0.28 | 29.3 |
| 15×15 | Zirc-4 | 67 | HR2 ^{a,c} | 9.5E+03 | 14.7 | 191 | 120 | 0.26 | 31.6 |
| 15×15 | Zirc-4 | 67 | HR4 ^a | 5.5E+04 | 14.8 | 158 | 121 | 0.21 | 37.5 |
| 15×15 | Zirc-4 | 67 | HR3 ^a | 2.4E+05 | 9.0 | 107 | 74 | 0.14 | 33.6 |
| 15×15 | Zirc-4 | 67 | DM3 | 1.3E+07 ^b | 7.7 | 51 | 63 | 0.06 | 73.8 |
| 15×15 | Zirc-4 | 67 | DM1 | 1.1E+07 ^b | 6.7 | 44 | 55 | 0.05 | 75.6 |
| 15×15 | Zirc-4 | 67 | R5 | 2.2E+07 ^b | 6.6 | 42 | 54 | 0.05 | 76.3 |
| 15×15 | Zirc-4 | 67 | DL2 | 6.4E+06 ^b | 4.2 | 22 | 34 | 0.03 | 91.5 |
| 17×17 | M5 | 45 | TH5 | 2.8E+04 | 11.2 | 312 | 129 | 0.32 | 16.6 |
| 17×17 | M5 | 45 | TH6 | 1.3E+04 | 13.4 | 308 | 154 | 0.32 | 20.1 |
| 17×17 | M5 | 45 | MOX17 | 1.2E+04 | 11.1 | 266 | 128 | 0.28 | 19.3 |

^a The specimens were pressurized and subjected to a thermal transient to induce cladding hydride reorientation prior to conducting the unpressurized CIRFT test.

^b The test was discontinued without specimen fracture.

^c Samples were tested statically prior to dynamic testing.

^d Stress calculated using the modified equivalent stress approach [F-4] to represent the cladding surface stress

^e Stress calculated using the equivalent stress approach per Eq. (F-7) where fuel rod OD for 15×15, 17×17, and 9×9 fuel rods are 10.76, 9.6 and 11.43 mm, respectively [F-23], meaning $I_{15\times15} = 6.58\text{E-}10 \text{ m}^4$, $I_{17\times17} = 4.2\text{E-}10 \text{ m}^4$, and $I_{9\times9} = 8.34\text{E-}10 \text{ m}^4$.

Table F-1. Reference Dynamic Dataset [F-4] (continued).

| Rod type | Cladding material | Parent rod-average burnup (GWd/MTU) | Test ID | Cycles to failure | Average moment (N-m) | Maximum cladding stress (MPa) | Maximum average stress ^e (MPa) | Maximum average strain (%) | Flexural rigidity (N-m ²) |
|----------|-------------------|-------------------------------------|------------------|----------------------|----------------------|-------------------------------|---|----------------------------|---------------------------------------|
| 17×17 | M5 | 45 | TH3 | 1.5E+04 | 10.6 | 264 | 122 | 0.27 | 18.5 |
| 17×17 | M5 | 45 | TH2 | 5.7E+04 | 11.0 | 255 | 127 | 0.14 | 20.1 |
| 17×17 | M5 | 45 | MOX14 | 8.7E+04 | 6.2 | 254 | 71 | 0.26 | 11.3 |
| 17×17 | M5 | 45 | MOX7 | 1.6E+04 | 13.9 | 239 | 160 | 0.25 | 26.9 |
| 17×17 | M5 | 52 | NA7 | 1.3E+04 | 13.5 | 232 | 155 | 0.30 | 27.1 |
| 17×17 | M5 | 45 | MOX8 | 1.3E+04 | 11.0 | 206 | 127 | 0.21 | 24.9 |
| 17×17 | M5 | 45 | TH1 | 5.7E+04 | 8.8 | 204 | 101 | 0.21 | 19.9 |
| 17×17 | M5 | 52 | NA1 | 1.6E+04 | 11.0 | 194 | 127 | 0.25 | 26.2 |
| 17×17 | M5 | 45 | MOX13 | 2.7E+04 | 8.7 | 171 | 100 | 0.18 | 23.6 |
| 17×17 | M5 | 45 | MOX15 | 2.0E+04 | 8.5 | 167 | 98 | 0.17 | 23.5 |
| 17×17 | M5 | 45 | MOX2 | 3.7E+04 | 8.5 | 161 | 98 | 0.17 | 24.3 |
| 17×17 | M5 | 45 | MOX12 | 4.2E+04 | 8.7 | 158 | 100 | 0.16 | 25.6 |
| 17×17 | M5 | 45 | TH4 | 2.5E+06 | 6.3 | 151 | 73 | 0.16 | 19.2 |
| 17×17 | M5 | 52 | NA2 | 2.2E+04 | 8.8 | 149 | 101 | 0.19 | 27.4 |
| 17×17 | M5 | 45 | MOX10 | 3.9E+04 | 8.7 | 144 | 100 | 0.15 | 28.2 |
| 17×17 | M5 | 45 | MOX11 | 4.2E+04 | 8.7 | 142 | 100 | 0.15 | 28.1 |
| 17×17 | M5 | 45 | MOX9 | 9.0E+04 | 6.3 | 121 | 73 | 0.13 | 24.0 |
| 17×17 | M5 | 52 | NA4 | 6.1E+04 | 6.3 | 84 | 73 | 0.11 | 35.0 |
| 17×17 | M5 | 45 | MOX16 | 3.7E+03 | 13.2 | 374 | 152 | 0.39 | 16.3 |
| 17×17 | M5 | 45 | MOX5 | 4.5E+05 | 4.8 | 68 | 55 | 0.07 | 32.6 |
| 17×17 | M5 | 45 | MOX6 | 5.4E+05 | 3.8 | 64 | 44 | 0.07 | 27.6 |
| 17×17 | M5 | 45 | MOX4 | 2.2E+06 | 3.9 | 50 | 45 | 0.05 | 36.1 |
| 17×17 | M5 | 52 | NA6 | 4.3E+05 | 4.0 | 46 | 46 | 0.06 | 40.3 |
| 17×17 | M5 | 45 | TH2 | 3.8E+06 ^b | 6.2 | 134 | 71 | 0.14 | 21.6 |
| 17×17 | M5 | 52 | NA5 | 5.1E+06 ^b | 4.0 | 54 | 46 | 0.07 | 34.0 |
| 9×9 | Zirc-2 | 57 | LM1 ^c | 9.4E+03 | 23.4 | 386 | 160 | 0.42 | 31.7 |
| 9×9 | Zirc-2 | 57 | LM17 | 1.3E+04 | 28.1 | 365 | 192 | 0.40 | 40.1 |
| 9×9 | Zirc-2 | 57 | LM16 | 1.4E+04 | 28.6 | 280 | 195 | 0.31 | 53.3 |
| 9×9 | Zirc-2 | 57 | LM13 | 2.1E+04 | 21.4 | 228 | 146 | 0.25 | 49.0 |
| 9×9 | Zirc-2 | 57 | LM10 | 5.2E+04 | 18.9 | 210 | 129 | 0.23 | 47.0 |
| 9×9 | Zirc-2 | 57 | LM7 | 1.2E+05 | 13.9 | 149 | 95 | 0.16 | 48.9 |
| 9×9 | Zirc-2 | 57 | LM2 | 1.7E+05 | 11.5 | 114 | 78 | 0.12 | 52.6 |
| 9×9 | Zirc-2 | 57 | LM3 | 4.9E+05 | 9.0 | 104 | 61 | 0.11 | 45.3 |
| 9×9 | Zirc-2 | 57 | LM15 | 4.4E+05 | 9.0 | 96 | 61 | 0.11 | 48.6 |
| 9×9 | Zirc-2 | 57 | LM9 | 7.3E+05 | 9.1 | 92 | 62 | 0.10 | 51.2 |
| 9×9 | Zirc-2 | 57 | LM14 | 3.9E+05 | 9.0 | 85 | 61 | 0.09 | 55.9 |
| 9×9 | Zirc-2 | 57 | LM5 | 2.5E+05 | 7.6 | 71 | 52 | 0.08 | 56.1 |
| 9×9 | Zirc-2 | 57 | LM11 | 3.6E+05 | 7.7 | 69 | 53 | 0.08 | 57.6 |
| 9×9 | Zirc-2 | 57 | LM6 | 1.8E+06 | 6.5 | 66 | 44 | 0.07 | 51.5 |
| 9×9 | Zirc-2 | 57 | LM8 | 4.7E+06 | 6.6 | 55 | 45 | 0.06 | 62.9 |
| 9×9 | Zirc-2 | 57 | LM12 | 7.6E+06 ^b | 6.1 | 88 | 42 | 0.10 | 36.3 |
| 9×9 | Zirc-2 | 57 | LM17 | 3.4E+06 ^b | 7.5 | 87 | 51 | 0.10 | 44.7 |

^a The specimens were pressurized and subjected to a thermal transient to induce cladding hydride reorientation prior to conducting the unpressurized CIRFT test.

^b The test was discontinued without specimen fracture.

^c Samples were tested statically prior to dynamic testing.

^d Stress calculated using the modified equivalent stress approach [F-4] to represent the cladding surface stress

^e Stress calculated using the equivalent stress approach per Eq. (F-7) where fuel rod OD for 15×15, 17×17 and 9×9 fuel rods are 10.76, 9.6, and 11.43 mm, respectively [F-23], meaning $I_{15 \times 15} = 6.58\text{E-}10 \text{ m}^4$, $I_{17 \times 17} = 4.2\text{E-}10 \text{ m}^4$, and $I_{9 \times 9} = 8.34\text{E-}10 \text{ m}^4$.

F-5. Comparison Data from Cladding Tests

Tests of Zirc-4 cladding tubes are being performed to provide data for comparison with the fuel rod segment tests. The cladding tests can also be used to verify whether previously reported fatigue data [F-9] on zirconium alloys (specifically Zircaloy-2 and Zirc-4) are representative of the tube geometry. A comparison of cladding tube fatigue with fuel rod fatigue offers a direct indication of the effect of the pellet on fatigue performance. The discontinuities in the pellet cause stress concentrations on the cladding (Section F-3.2.2), so it is expected that the inclusion of the pellet will have a detrimental effect on the fatigue life of the fuel rod compared to cladding-only performance.

This report discusses the results of tests using unirradiated cladding; irradiated cladding tests will be completed in FY23.

F-5.1 Unirradiated Zirc-4 Cladding Tests

The material used was a 17×17 PWR cladding tube made of standard Zirc-4 from two different lots of material: (1) provided by Framatome and received by ORNL in 2015 and (2) provided by Westinghouse (lot W58H7L8F). Samples from the first lot are labelled *Zr4 2015 Rod 1*, and so on, and samples from the second lot are labelled *Zr4-W-1*, and so on. The dimensions of the cladding tubes are consistent with standard 17×17 PWR fuel rods (OD = 9.5 mm, ID = 8.3 mm).

The tubes were mounted into the endcaps using the normal process, ensuring that the epoxy was only applied to the OD surfaces being bonded with the dogbone. A strain gauge was attached to one sample (Zr4-W-2) to develop LVDT dynamic correction factors for cladding tubes; these correction factors are applied to the subsequent fatigue tests and compared to the previously developed LVDT dynamic correction factors for fuel rods [F-7].

Testing was performed on the out-of-cell CIRFT system rather than the system in the hot-cell that was used to test irradiated fuel rods. The data processing was consistent with the processing used by Wang and Wang [F-21]. The test conditions for the strain-gauged specimen, Zr4-W-2 were used to determine the dynamic corrections factor and were chosen to cover the full range of strain amplitudes in both the fuel rod segment and cladding-only testing (ranging from ~0.05 to ~0.5%, see Table F-2). The test conditions used to measure fatigue performance are defined to establish a characteristic fatigue limit, thus, the focus of this study was on high-cycle fatigue performance, as listed in Table F-3. Testing on all samples was performed under displacement-controlled (or strain-controlled) conditions rather than load-control (or stress-controlled) conditions to be consistent with test conditions of O'Donnell-Langer [F-9] rather than to be consistent with how the fuel rods were tested. The mean strain for all tests was 0.

Table F-2. Test Conditions for Strain-gauged Test Sample (Zr4-W-2)

| Target Strain Amplitude (%) | Frequency | Cycles |
|-----------------------------|-----------|--------|
| 0.06 | 0.05 | 3 |
| 0.06 | 5.00 | 200 |
| 0.18 | 0.05 | 3 |
| 0.18 | 5.00 | 200 |
| 0.37 | 0.05 | 3 |
| 0.37 | 5.00 | 200 |
| 0.47 | 0.05 | 3 |
| 0.47 | 5.00 | 200 |

Table F-3. Test Conditions for Fatigue Tests on Cladding-only Zirc-4 Tubes (no strain gauges)

| Specimen ID | Displacement Control Condition (mm) | Target Strain Amplitude (%) | Test Frequency (Hz) |
|----------------|-------------------------------------|-----------------------------|---------------------|
| Zr4-W-1 | 4.5 | 0.55 | 5 |
| Zr4 2015 Rod 2 | 1.5 | 0.20 | 5 |
| Zr4 2015 Rod 2 | 4.5 | 0.55 | 5 |
| Zr4 2015 Rod 3 | 3.0 | 0.37 | 5 |
| Zr4-W-3 | 3.8 | 0.47 | 5 |
| Zr4-W-4 | 3.3 | 0.40 | 5 |

During these tests, it was observed that the LVDTs produced wear marks on the OD surface of sample Zr4-W-1. To investigate potential effects related to the wear, Sample Zr4 2015 Rod 2 was tested under two conditions: (1) 2×10^6 cycles at $\sim 0.2\%$ strain amplitude with LVDTs in place, and (2) after 2×10^6 cycles, it was tested at 0.55% strain amplitude without the LVDTs to directly measure strain and to determine if the LVDTs had any impact on failure.

Future testing will be performed at strain amplitudes between 0.4% and 0.35% and the test of Zr4 2015 Rod 3 will continue until failure occurs or 1×10^7 cycles is reached without failure. Typically, if failure has not occurred by 1×10^7 cycles, fatigue failure is not expected at the test conditions.

F-5.1.1 Calibration Sample (Zr4-W-2)

Because of the larger amount of data generated with performing the fatigue tests 5 Hz for 200 cycles, only a subset of data was collected. Specifically, 10 samples of data were taken (2.5 cycles in length) rather than collecting the entire dataset. Of these 10 samples, the first three were not included in the averages that characterized the test because of startup variations. The reported data includes the average calculated curvature, strain amplitude, applied moment and stress at the peaks/valleys of the fatigue cycles.

The test results for the calibration sample are provided in Figure F-7. The LVDT strain amplitude includes the normal correction for Δh as described in [F-7], but doesn't include the dynamic correction factor, which is the ratio of the strain-gauge strain amplitude and the LVDT strain amplitude (after correction for Δh). This ratio is provided in Table F-4, and the average is plotted in Figure F-7 for testing at both 0.05 Hz and 5 Hz . The correction factor increases with strain amplitude: from 0.83 below 0.2% to 0.87 and 0.91 at 0.37% and 0.47% , respectively. When performing fatigue tests without a strain gauge, the dynamic correction factor is applied after the normal correction for Δh . As a comparison, the correction factor used for evaluating the sister rod test data was 0.82 , which compares well to the cladding-only data given most of the sister rod tests were also performed at strain amplitudes less than 0.2% .

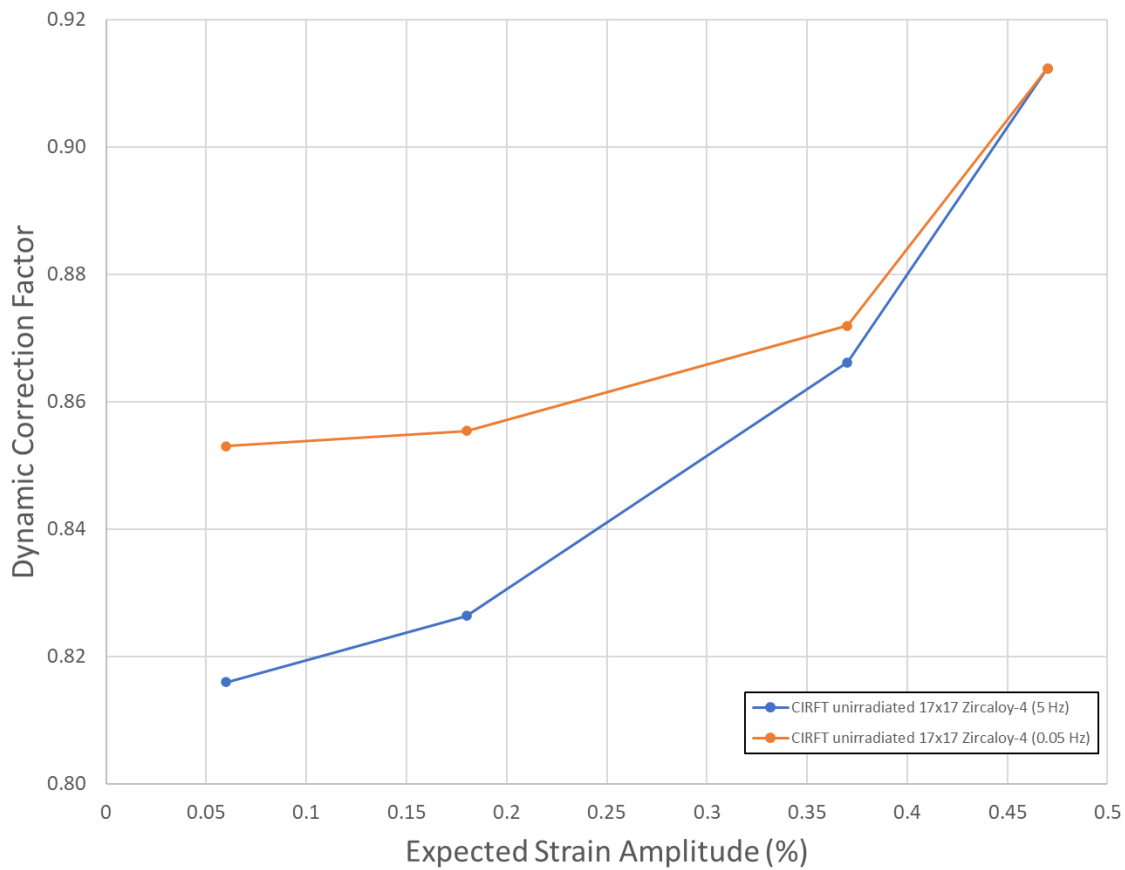


Figure F-7. Results for the Strain Gauge Sample, Zr4-W-2

Table F-4. The Dynamic Correction Factor as a Function of the Strain Gauge Strain Amplitude for Testing at 0.05 and 5 Hz.

| Test ID | Test Conditions (strain amplitude- %/frequency-Hz) | LVDT Strain Amplitude (%) | Strain Gauge Strain Amplitude (%) | Dynamic Correction Factor | Corrected LVDT Curvature (1/m) | Applied Moment (N-M) | Dynamic flexural rigidity (N-m ²) |
|-----------------|--|------------------------------------|---|---------------------------------|---|----------------------------|--|
| Zr4-W-2-05-05-1 | 0.06/0.05 | 0.075 | 0.062 | 0.83 | 0.13 | 2.43 | 18.58 |
| Zr4-W-2-05-05-2 | 0.06/0.05 | 0.070 | 0.062 | 0.89 | 0.13 | 2.53 | 19.34 |
| Zr4-W-2-05-05-3 | 0.06/0.05 | 0.074 | 0.062 | 0.84 | 0.13 | 2.52 | 19.21 |
| | Mean | 0.073 | 0.062 | 0.85 | 0.13 | 2.49 | 19.05 |
| | St.Dev | 0.0026 | 0.0001 | 0.0304 | 0.0047 | 0.0559 | 0.4106 |
| Zr4-W-2-05-5-1 | 0.06/5 | 0.078 | 0.064 | 0.82 | 0.13 | 2.35 | 17.45 |
| Zr4-W-2-05-5-2 | 0.06/5 | 0.082 | 0.064 | 0.78 | 0.14 | 2.36 | 17.43 |
| Zr4-W-2-05-5-3 | 0.06/5 | 0.076 | 0.064 | 0.84 | 0.13 | 2.34 | 17.41 |
| | Mean | 0.079 | 0.064 | 0.82 | 0.14 | 2.35 | 17.43 |
| | St.Dev | 0.0033 | 0.0002 | 0.0323 | 0.0057 | 0.0069 | 0.0207 |

Table F-4. The Dynamic Correction Factor as a Function of the Strain Gauge Strain Amplitude for Testing at 0.05 and 5 Hz (continued)

| Test ID | Test Conditions (strain amplitude- %/frequency-Hz) | LVDT Strain Amplitude (%) | Strain Gauge Strain Amplitude (%) | Dynamic Correction Factor | Corrected LVDT Curvature (1/m) | Applied Moment (N-M) | Dynamic flexural rigidity (N- m ²) |
|-----------------|--|------------------------------------|---|---------------------------------|---|----------------------------|---|
| Zr4-W-2-15-05-1 | 0.18/0.05 | 0.219 | 0.185 | 0.85 | 0.39 | 6.59 | 16.90 |
| Zr4-W-2-15-05-2 | 0.18/0.05 | 0.221 | 0.185 | 0.84 | 0.40 | 6.65 | 17.07 |
| Zr4-W-2-15-05-3 | 0.18/0.05 | 0.210 | 0.186 | 0.88 | 0.38 | 6.62 | 16.92 |
| | Mean | 0.217 | 0.185 | 0.86 | 0.39 | 6.62 | 16.96 |
| | St.Dev | 0.0056 | 0.0004 | 0.0245 | 0.0101 | 0.0286 | 0.0909 |
| Zr4-W-2-15-5-1 | 0.18/5 | 0.228 | 0.185 | 0.81 | 0.40 | 5.27 | 13.53 |
| Zr4-W-2-15-5-2 | 0.18/5 | 0.231 | 0.185 | 0.80 | 0.40 | 5.34 | 13.72 |
| Zr4-W-2-15-5-3 | 0.18/5 | 0.215 | 0.186 | 0.86 | 0.37 | 5.38 | 13.78 |
| | Mean | 0.224 | 0.185 | 0.83 | 0.39 | 5.33 | 13.68 |
| | St.Dev | 0.0084 | 0.0004 | 0.0336 | 0.0147 | 0.0593 | 0.1282 |
| Zr4-W-2-30-05-1 | 0.37/0.05 | 0.432 | 0.372 | 0.86 | 0.79 | 12.75 | 16.27 |
| Zr4-W-2-30-05-2 | 0.37/0.05 | 0.426 | 0.375 | 0.88 | 0.78 | 12.72 | 16.14 |
| Zr4-W-2-30-05-3 | 0.37/0.05 | 0.428 | 0.375 | 0.87 | 0.79 | 12.74 | 16.16 |
| | Mean | 0.429 | 0.374 | 0.87 | 0.79 | 12.74 | 16.19 |
| | St.Dev | 0.0029 | 0.0012 | 0.0086 | 0.0053 | 0.0143 | 0.0676 |
| Zr4-W-2-30-5-1 | 0.37/5 | 0.433 | 0.375 | 0.86 | 0.79 | 11.11 | 14.10 |
| Zr4-W-2-30-5-2 | 0.37/5 | 0.433 | 0.376 | 0.87 | 0.79 | 11.20 | 14.17 |
| Zr4-W-2-30-5-3 | 0.37/5 | 0.434 | 0.376 | 0.87 | 0.79 | 11.10 | 14.04 |
| | Mean | 0.433 | 0.375 | 0.87 | 0.79 | 11.14 | 14.10 |
| | St.Dev | 0.0008 | 0.0007 | 0.0016 | 0.0015 | 0.0516 | 0.0666 |
| Zr4-W-2-38-05-1 | 0.47/0.05 | 0.519 | 0.476 | 0.92 | 1.00 | 16.14 | 16.11 |
| Zr4-W-2-38-05-2 | 0.47/0.05 | 0.524 | 0.477 | 0.91 | 1.01 | 16.03 | 15.98 |
| Zr4-W-2-38-05-3 | 0.47/0.05 | 0.527 | 0.479 | 0.91 | 1.01 | 16.07 | 15.95 |
| | Mean | 0.523 | 0.477 | 0.91 | 1.00 | 16.08 | 16.01 |
| | St.Dev | 0.0040 | 0.0014 | 0.0050 | 0.0076 | 0.0585 | 0.0843 |
| Zr4-W-2-38-5-1 | 0.47/5 | 0.524 | 0.479 | 0.92 | 1.01 | 14.32 | 14.20 |
| Zr4-W-2-38-5-2 | 0.47/5 | 0.523 | 0.480 | 0.92 | 1.01 | 14.17 | 14.04 |
| Zr4-W-2-38-5-3 | 0.47/5 | 0.530 | 0.481 | 0.91 | 1.02 | 14.11 | 13.94 |
| | Mean | 0.526 | 0.480 | 0.91 | 1.01 | 14.20 | 14.06 |
| | St.Dev | 0.0036 | 0.0008 | 0.0050 | 0.0070 | 0.1068 | 0.1265 |

F-5.1.2 High Cycle Fatigue Response

Like the testing performed at 5 Hz on the calibration sample, the fatigue data reported for the cladding-only samples are averages of a subset of the data. Because the number of cycles varied during the test, the total number of datasets included in the average also varied. The reported data provided in Table F-5 and Table F-6 includes the average calculated curvature, strain amplitude, applied moment, dynamic flexural rigidity, and stress at the peaks/valleys of a fatigue cycle with the number of cycles to failure. Two stress values are reported in Table F-6. The first is the average stress based on beam theory assuming a homogeneous rod with the flexural rigidity of the tube; this value is reported to be compared directly to the fuel rod data in Section F-8. The second is the cladding stress, which is calculated as the product of the Young's modulus and strain amplitude. The strain amplitude is plotted in Figure F-8 as a function of fatigue cycles, and the results are compared to data on unirradiated and irradiated Zircaloy-2 from O'Donnell-Langer [F-9] and open literature data on Zirc-4 [F-10],[F-11]. The cladding-only data indicate fatigue performance similar to other Zirc-4 data and are consistent with a higher fatigue limit than represented by the best estimate correlation of O'Donnell-Langer for Zircaloy-2. The results support the conclusion that the tube geometry does not alter the expected fatigue behavior based on O'Donnell-Langer (and other open literature) data on zirconium alloys and the conclusion that the O'Donnell-Langer design curve is applicable for Zirc-4 in a tube geometry.

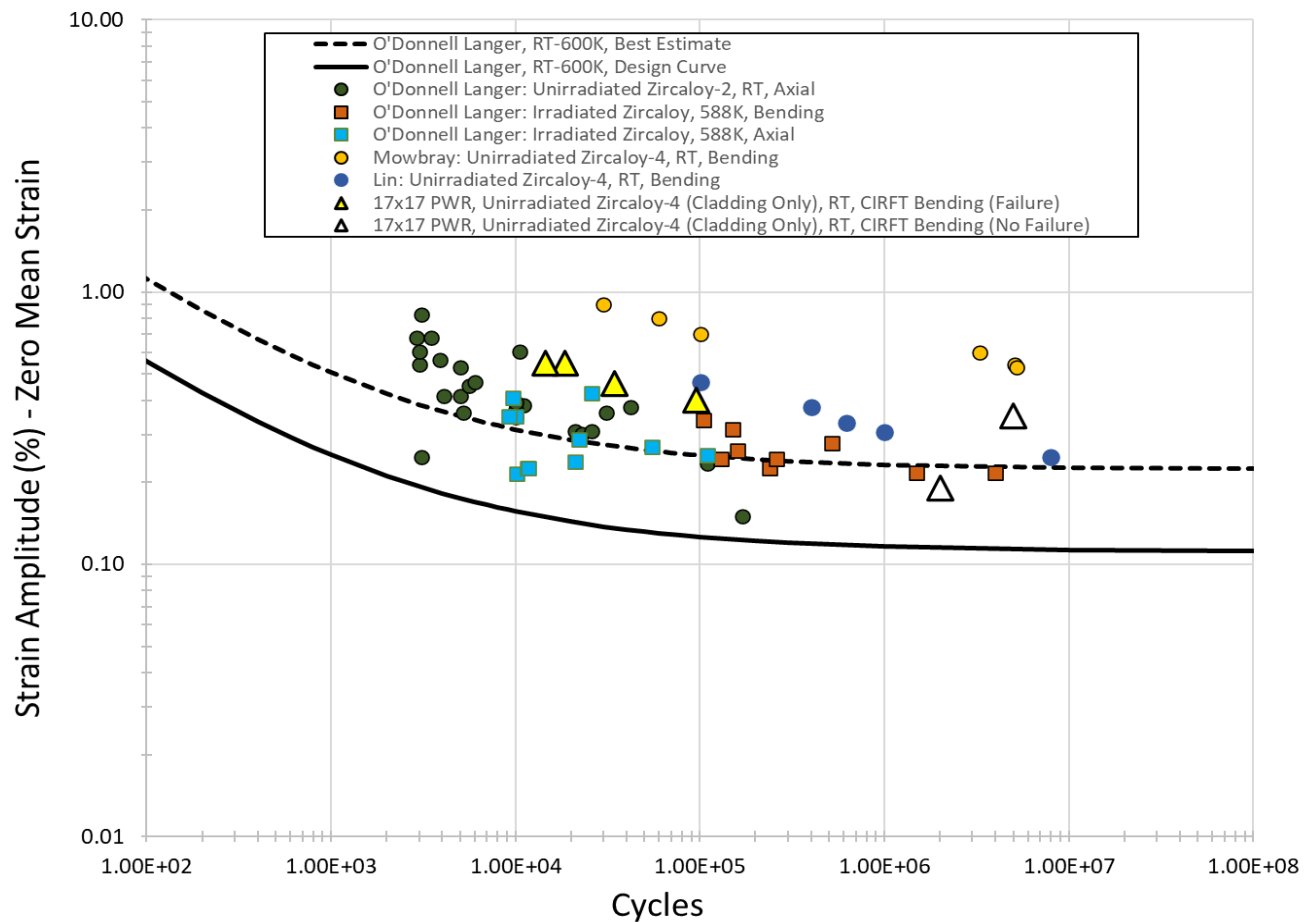
Table F-5. Curvature, Strain Amplitude, Applied Moment, and Cycles to Failure for the Unirradiated Zirc-4 Cladding Tubes

| Specimen Material | Specimen ID | Target Displacement and Strain Amplitude (1/m) | LVDT Curvature (1/m) | St. Dev. LVDT Curvature (1/m) | LVDT Strain Amplitude (%) | St. Dev LVDT Strain Amplitude (%) | Applied Moment Amplitude (N-m) | St. Dev. Applied Moment Amplitude (N-m) | Fatigue Cycles (N) | Failed (Yes/No) |
|-------------------|----------------|--|----------------------|-------------------------------|---------------------------|-----------------------------------|--------------------------------|---|--------------------|-----------------|
| Zirc-4 | Zr4-W-1 | 4.5/0.55 | 1.12 | 0.17 | 0.53 | 0.08 | 14.25 | 0.66 | 14,500 | Yes |
| Zirc-4 | Zr4 2015 Rod 2 | 1.5/0.20 | 0.43 | 0.01 | 0.21 | 0.003 | 5.61 | 0.09 | 2,000,000 | No |
| Zirc-4 | Zr4 2015 Rod 2 | 4.5/0.55 | N/A | N/A | N/A | N/A | 15.65 | 0.13 | 18,500 | Yes |
| Zirc-4 | Zr4 2015 Rod 3 | 3.0/0.35 | 0.83 | 0.02 | 0.39 | 0.01 | 11.14 | 0.08 | 5,000,000 | No |
| Zirc-4 | Zr4-W-3 | 3.8/0.46 | 0.97 | 0.02 | 0.46 | 0.01 | 12.89 | 0.23 | 34,300 | Yes |
| Zirc-4 | Zr4-W-4 | 3.3/0.40 | 0.85 | 0.03 | 0.40 | 0.01 | 10.98 | 0.16 | 95,000 | Yes |

Note – the dynamic correction factor Zr4 2015 Rod 2 (0.21% strain amplitude) was 0.82; the dynamic corrections factor for all other tests was 0.87.

Table F-6. Maximum Average Stress, Maximum Stress, Dynamic Flexural Rigidity, and Rigidity Standard Deviation for the Unirradiated Zirc-4 Cladding Tubes

| Cladding Material | Specimen ID | Maximum Average Stress (Mpa) | Maximum Cladding Stress (MPa) | Dynamic Flexural Rigidity Stress (N-m ²) | St. Dev. Dynamic Flexural Rigidity (N-m ²) |
|-------------------|----------------|------------------------------|-------------------------------|--|--|
| Zirc-4 | Zr4-W-1 | 423 | 485 | 12.9 | 0.8 |
| Zirc-4 | Zr4 2015 Rod 2 | 167 | 189 | 13.3 | 0.1 |
| Zirc-4 | Zr4 2015 Rod 2 | 464 | N/A | N/A | N/A |
| Zirc-4 | Zr4 2015 Rod 3 | 331 | 361 | 13.4 | 0.4 |
| Zirc-4 | Zr4-W-3 | 382 | 421 | 13.3 | 0.1 |
| Zirc-4 | Zr4-W-4 | 326 | 368 | 13.0 | 0.7 |

**Figure F-8. CIRFT results of unirradiated Zirc-4 tubes compared to previously reported data on both unirradiated and irradiated Zircaloy-2 [F-9] and unirradiated Zirc-4 [F-10],[F-11].**

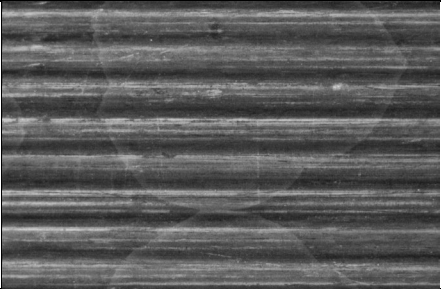
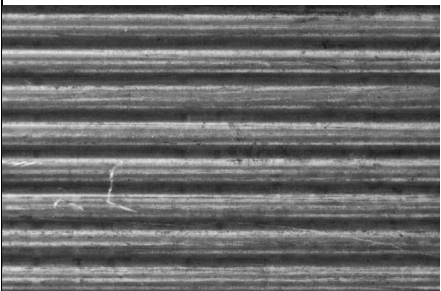
F-6. Description of the Sister Rods Tested

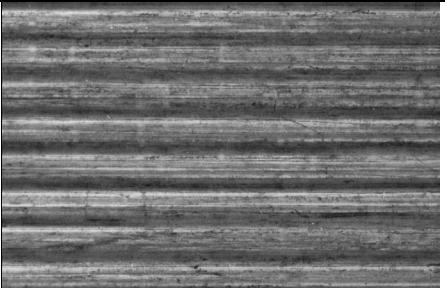
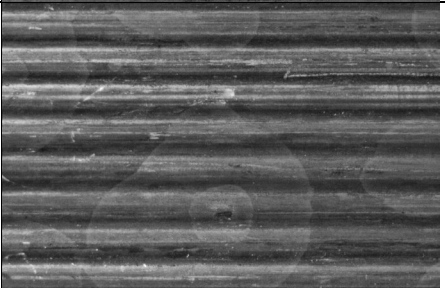
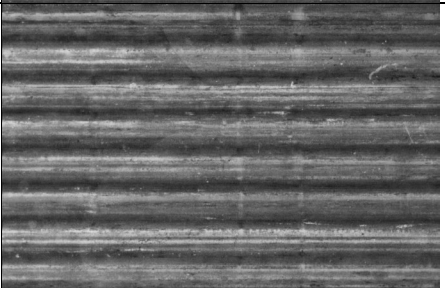


Additional descriptions of the rods used in these tests are provided in the sister rod test plan [F-3] and the nondestructive test results [F-6]. All rods were operated by Dominion Energy at the North Anna Power Station to high rod average burnup (>45 GWd/MTU). Table F-7 summarizes the parent assembly operation and lattice location for the rods test using CIRFT.

In Phase 1 of the sister rod test program [F-1, F-2], seven of ORNL's 15 sister rods were selected for paired testing: one baseline fuel rod and one heat-treated fuel rod of each cladding type (M5, ZIRLO, and Zirc-4/LT-Zirc-4), plus an extra ZIRLO-clad rod for additional datapoints, because no ZIRLO-clad rods were tested in previous campaigns. Baseline rods are tested in the condition in which they were received at ORNL, and full-length heat-treatment (FHT) rods are subjected to a thermal transient before testing, as described in Appendix A, to simulate dry storage conditions. Three full-length fuel rods have been heat-treated to date—one Zirc-4-clad (F35P17), one ZIRLO-clad (3F9N05), and one M5-clad (30AE14)—and the results from the heat-treated rods were compared with the results from the baseline rods to determine whether the fatigue lifetime is affected by dry storage thermal transients.

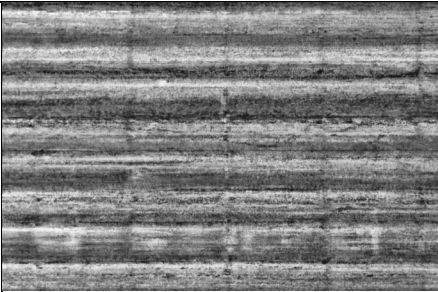
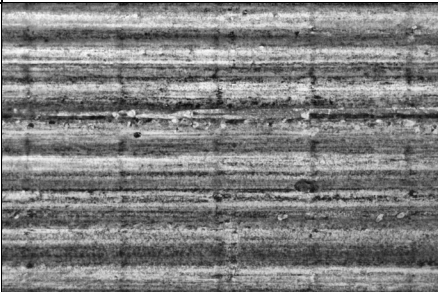
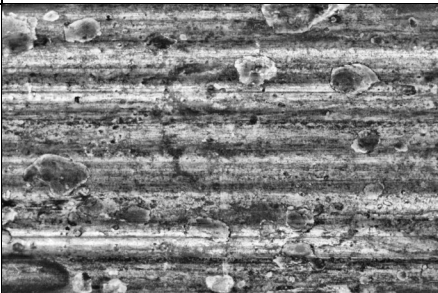
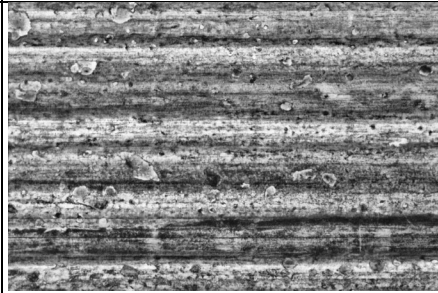
The CIRFT uses specimens that are 152.4 mm (6 in.) long that were taken from various elevations along the SNF rods. Because rod burnup varies as a function of elevation, the rod average burnup is used in conjunction with the gamma scans of the rod [F-6] to estimate the average burnup of the CIRFT segment, as listed in Table F-7. Full-circumference flattened images—as defined in nondestructive examination (NDE) report [F-6]—of the pretest waterside surface condition of the CIRFT segments are also provided in Table F-7.

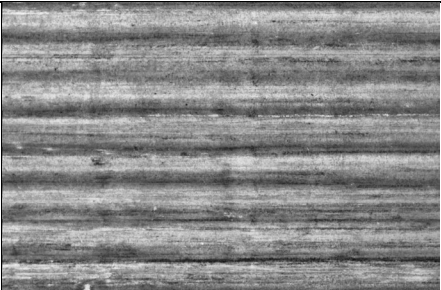
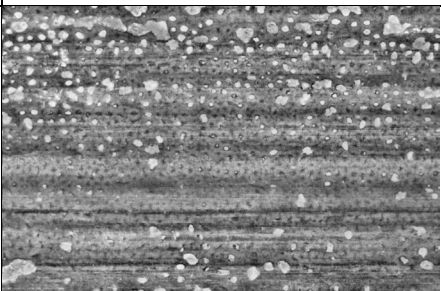
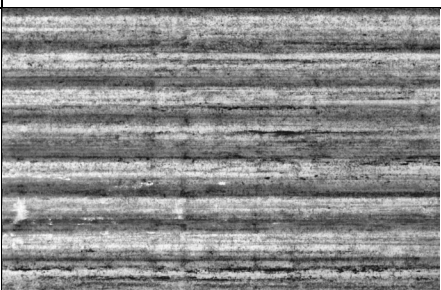
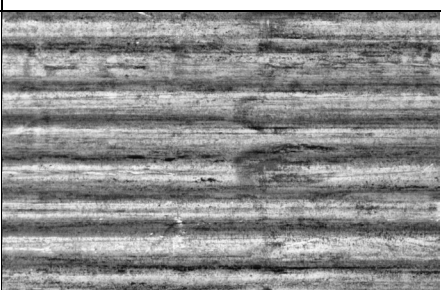
Table F-7. Sister Rod Segments Selected for CIRFT.

| Clad material | Donor assembly | Sister rod lattice location | Assembly average burnup (GWd/MTU) | Rod average burnup (GWd/MTU) | Heat treatment applied to the rod | Measured rod internal pressure (MPa) | Measured rod void volume (cc) | Specimen lower elevation (mm) | Specimen upper elevation (mm) | Average specimen burnup (GWd/MTU) | Rod 360° appearance near the CIRFT gauge section pretest |
|---|----------------|-----------------------------|-----------------------------------|------------------------------|-----------------------------------|--------------------------------------|-------------------------------|-------------------------------|-------------------------------|-----------------------------------|---|
| The M5-clad rods exhibited very light waterside oxide that is visible as irregular, somewhat circular patches, with some areas including an interior patch that appears to have peeling oxide. Grid-to-rod-fretting (GTRF) marks are visible in some grid elevations, along with rod removal scratches. | | | | | | | | | | | |
| M5 | 30A | D05 | 52.0 | 54 | No | 3.46 | 10.63 | 697 | 850 | 58 |  |
| | 30A | D05 | 52.0 | 54 | No | 3.46 | 10.63 | 2,050 | 2,203 | 59 | |
| | 30A | D05 | 52.0 | 54 | No | 3.46 | 10.63 | 2,630 | 2,783 | 59 | |
| | 30A | D05 | 52.0 | 54 | No | 3.46 | 10.63 | 3,732 | 3,886 | 24 |  |
| | | | | | | | | | | | Pellet-pellet gaps throughout |

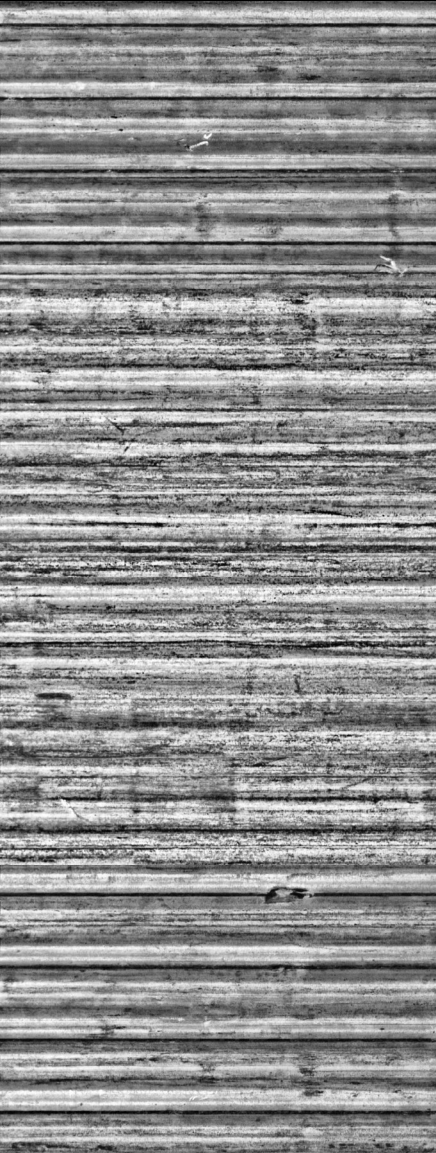
| Clad material | Donor assembly | Sister rod lattice location | Assembly average burnup (GWd/MTU) | Rod average burnup (GWd/MTU) | Heat treatment applied to the rod | Measured rod internal pressure (MPa) | Measured rod void volume (cc) | Specimen lower elevation (mm) | Specimen upper elevation (mm) | Average specimen burnup (GWd/MTU) | Rod 360° appearance near the CIRFT gauge section pretest |
|---------------|----------------|-----------------------------|-----------------------------------|------------------------------|-----------------------------------|--------------------------------------|-------------------------------|-------------------------------|-------------------------------|-----------------------------------|---|
| M5 | 30A | D05 | 52 | 54 | No | 3.46 | 10.63 | 3,452 | 3,605 | 38 |  |
| | 30A | E14 | 52 | 54 | Yes | 3.22 | 10.99 | 672 | 825 | 56 |  |
| | 30A | E14 | 52 | 54 | Yes | 3.22 | 10.99 | 2,850 | 3,003 | 60 |  |
| | 30A | E14 | 52 | 54 | Yes | 3.22 | 10.99 | 3,156 | 3,309 | 56 |  |
| | 30A | E14 | 52 | 54 | Yes | 3.22 | 10.99 | 3,003 | 3,156 | 58 |  |

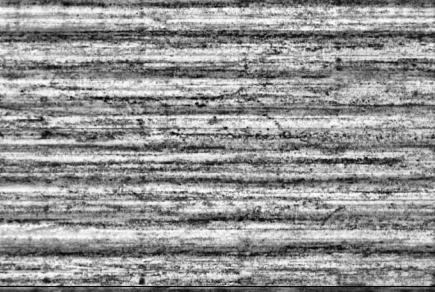
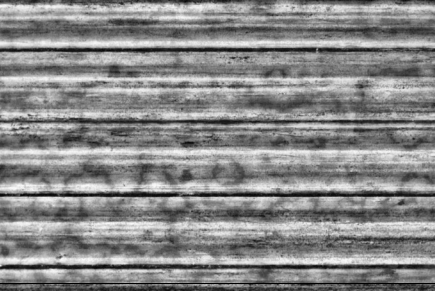
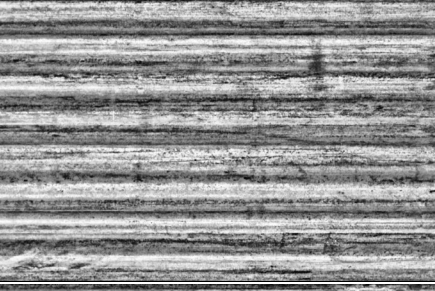
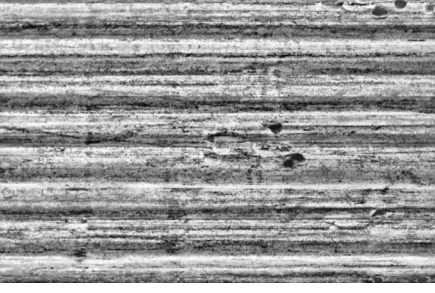
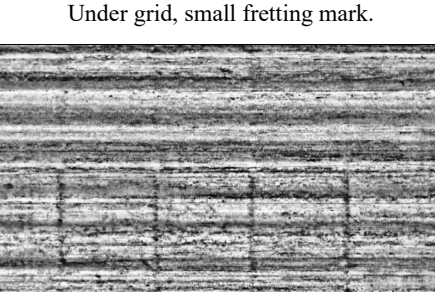
January 13, 2023

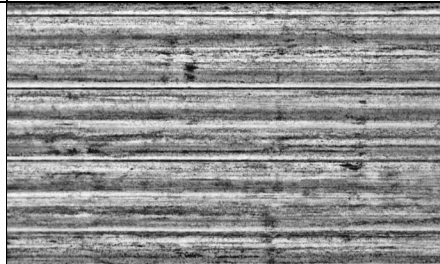
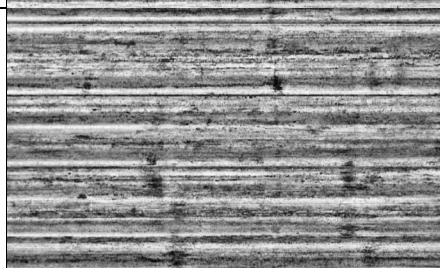
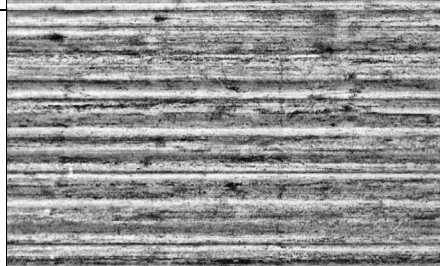
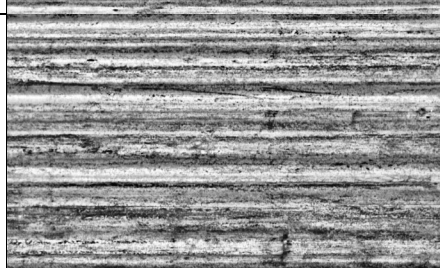
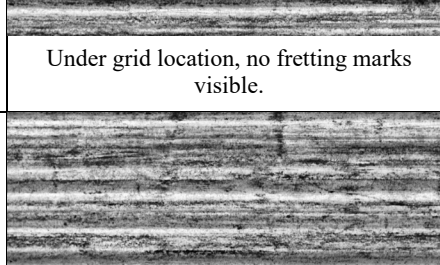
| Clad material | Donor assembly | Sister rod lattice location | Assembly average burnup (GWd/MTU) | Rod average burnup (GWd/MTU) | Heat treatment applied to the rod | Measured rod internal pressure (MPa) | Measured rod void volume (cc) | Specimen lower elevation (mm) | Specimen upper elevation (mm) | Average specimen burnup (GWd/MTU) | Rod 360° appearance near the CIRFT gauge section pretest |
|---|----------------|-----------------------------|-----------------------------------|------------------------------|-----------------------------------|--------------------------------------|-------------------------------|-------------------------------|-------------------------------|-----------------------------------|--|
| Assemblies 3A1 and F35 (Zirc-4 / LT Zirc-4 cladding types) appeared to have the greatest amount of oxide buildup/spalling among the sister rods. No visible signs of through-wall damage or large areas of clad degradation were found, but some areas of significant oxidation have a flake-like appearance, and spalling is evident at some elevations. Some shallow GTRF marks are visible, and some features that appear to be GTRF marks oxidized in later cycles are visible. | | | | | | | | | | | |
| LT Zirc-4 | 3A1 | F05 | 50 | 51 | No | 3.73 | 12.94 | 1,853 | 2,006 | 56 |  |
| | 3A1 | F05 | 50 | 51 | No | 3.73 | 12.94 | 2,025 | 2,178 | 56 |  |
| | 3A1 | F05 | 50 | 51 | No | 3.73 | 12.94 | 3,214 | 3,367 | 48 |  Under grid location, no fretting marks visible. |
| | 3A1 | F05 | 50 | 51 | No | 3.73 | 12.94 | 3,367 | 3,520 | 44 |  |

| Clad material | Donor assembly | Sister rod lattice location | Assembly average burnup (GWd/MTU) | Rod average burnup (GWd/MTU) | Heat treatment applied to the rod | Measured rod internal pressure (MPa) | Measured rod void volume (cc) | Specimen lower elevation (mm) | Specimen upper elevation (mm) | Average specimen burnup (GWd/MTU) | Rod 360° appearance near the CIRFT gauge section pretest |
|--|----------------|-----------------------------|-----------------------------------|------------------------------|-----------------------------------|--------------------------------------|-------------------------------|-------------------------------|-------------------------------|-----------------------------------|---|
| Assemblies 3A1 and F35 (Zirc-4 / LT Zirc-4 cladding types) appeared to have the greatest amount of oxide buildup/spalling among the sister rods. No visible signs of through-wall damage or large areas of clad degradation were found, but some areas of significant oxidation have a flake-like appearance and spalling is evident at some elevations. Some shallow GTRF marks are visible, and some features that appear to be GTRF marks that have oxidized in later cycles are visible. | | | | | | | | | | | |
| Zirc-4 | F35 | P17 | 58 | 60 | Yes | 4.68 | 13.32 | 2,027 | 2,180 | 52 |  |
| | F35 | P17 | 58 | 60 | Yes | 4.68 | 13.32 | 1,855 | 2,008 | 53 |  |
| | F35 | P17 | 58 | 60 | Yes | 4.68 | 13.32 | 3,159 | 3,312 | 47 |  |
| | F35 | P17 | 58 | 60 | Yes | 4.68 | 13.32 | 3,312 | 3,465 | 43 |  |

January 13, 2023

| Clad material | Donor assembly | Sister rod lattice location | Assembly average burnup (GWd/MTU) | Rod average burnup (GWd/MTU) | Heat treatment applied to the rod | Measured rod internal pressure (MPa) | Measured rod void volume (cc) | Specimen lower elevation (mm) | Specimen upper elevation (mm) | Average specimen burnup (GWd/MTU) | Rod 360° appearance near the CIRFT gauge section pretest |
|---|----------------|-----------------------------|-----------------------------------|------------------------------|-----------------------------------|--------------------------------------|-------------------------------|-------------------------------|-------------------------------|-----------------------------------|--|
| The ZIRLO-clad rods have a moderate-to-heavy oxide layer, with some oxide peeling observed. GTRF marks are present on most rods and range in severity from shallow to deep. No visible signs of through-wall cladding damage were observed. Darker regions are present at grid elevations, indicating either CRUD or possibly a thinner oxidation layer (attributed to better heat transfer in those areas resulting from flow turbulence). | | | | | | | | | | | |
| ZIRLO | 3D8 | E14 | 55 | 59 | No | 4.18 | 11.73 | 719 | 872 | 64 |  |
| | 3D8 | E14 | 55 | 59 | No | 4.18 | 11.73 | 2,412 | 2,565 | 64 | |
| | 3D8 | E14 | 55 | 59 | No | 4.18 | 11.73 | 2,963 | 3,116 | 62 | |
| | 3D8 | E14 | 55 | 59 | No | 4.18 | 11.73 | 1,178 | 1,331 | 63 | |
| | | | | | | | | | | | Under grid location, GTRF mark aligned at maximum strain location |

| Clad material | Donor assembly | Sister rod lattice location | Assembly average burnup (GWd/MTU) | Rod average burnup (GWd/MTU) | Heat treatment applied to the rod | Measured rod internal pressure (MPa) | Measured rod void volume (cc) | Specimen lower elevation (mm) | Specimen upper elevation (mm) | Average specimen burnup (GWd/MTU) | Rod 360° appearance near the CIRFT gauge section pretest |
|---------------|----------------|-----------------------------|-----------------------------------|------------------------------|-----------------------------------|--------------------------------------|-------------------------------|-------------------------------|-------------------------------|-----------------------------------|---|
| ZIRLO | 3D8 | E14 | 55 | 59 | No | 4.18 | 11.73 | 3,225 | 3,378 | 56 |  |
| | 3F9 | N05 | 52 | 54 | Yes | 3.98 | 12.74 | 719 | 872 | 59 |  |
| | 3F9 | N05 | 52 | 54 | Yes | 3.98 | 12.74 | 2,329 | 2,482 | 59 |  |
| | 3F9 | N05 | 52 | 54 | Yes | 3.98 | 12.74 | 2,710 | 2,863 | 57 |  |
| | 3F9 | N05 | 52 | 54 | Yes | 3.98 | 12.74 | 3,440 | 3,593 | 45 |  |

| Clad material | Donor assembly | Sister rod lattice location | Assembly average burnup (GWd/MTU) | Rod average burnup (GWd/MTU) | Heat treatment applied to the rod | Measured rod internal pressure (MPa) | Measured rod void volume (cc) | Specimen lower elevation (mm) | Specimen upper elevation (mm) | Average specimen burnup (GWd/MTU) | Rod 360° appearance near the CIRFT gauge section pretest |
|---------------|----------------|-----------------------------|-----------------------------------|------------------------------|-----------------------------------|--------------------------------------|-------------------------------|-------------------------------|-------------------------------|-----------------------------------|--|
| ZIRLO | 6U3 | K09 | 53 | 55 | no | 3.64 | 11.78 | 2,310 | 2,463 | 59 |  |
| | 6U3 | K09 | 53 | 55 | no | 3.64 | 11.78 | 2,463 | 2,616 | 59 |  |
| | 6U3 | K09 | 53 | 55 | no | 3.64 | 11.78 | 2,635 | 2,788 | 58 |  |
| | 6U3 | K09 | 53 | 55 | no | 3.64 | 11.78 | 3,200 | 3,353 | 50 |  <p>Under grid location, no fretting marks visible.</p> |
| | 6U3 | K09 | 53 | 55 | no | 3.64 | 11.78 | 3,353 | 3,506 | 46 |  |

F-7. Selection of CIRFT Test Conditions

In specifying the loading conditions for the CIRFT tests, the previous data for M5 and Zirc-4 clad fuel rods were surveyed [F-4,F-5] and several objectives were identified for the sister rod tests:

- Demonstrate that M5 and Zirc-4 clad sister rod fatigue performance is consistent with the data given in the established database for those cladding alloys
- Demonstrate whether FHT changes the fatigue lifetime of the cladding/rod when compared with non-FHT segments
- Demonstrate whether GTRF marks result in a reduced fatigue lifetime when they are aligned with the point of peak cladding deflection during the test
- Establish a range of tests for rods that have ZIRLO cladding consistent with the data given in the established database for other cladding alloys and demonstrate whether the ZIRLO-clad rods are consistent with other rods

The sister rods are tested statically and dynamically as paired samples with similar burnup and oxide thicknesses.

- a. **Baseline rod specimens:** one specimen tested statically followed by a dynamic test at a relatively high load (~175 N-m), one specimen tested dynamically at a moderate load (~10–12 N-m), and one specimen tested dynamically at a low load (~5–6 N-m)
- b. **Heat-treated rod specimens:** one specimen tested statically followed by a dynamic test at the same load used for the baseline specimen, one specimen tested dynamically at the same moderate load used for the baseline specimen, and one specimen tested dynamically at the same low load used for the baseline specimen

Table F-8 lists the selected test type, test load, and paired specimens.

Table F-8. CIRFT Specimen and Test Pairing

| Baseline specimens | | | | | Heat-treated specimens | | | | | Test Type | Nominal test moment applied (N-m) | Notes |
|--------------------|------|---------------|---|----|------------------------|------|---------------|---|----|----------------------------|-----------------------------------|--|
| Specimen ID | | Cladding type | Estimated specimen average burnup (GWd/MTU) | | Specimen ID | | Cladding type | Estimated specimen average burnup (GWd/MTU) | | | | |
| 30AD05 | 0697 | 0850 | M5 | 58 | 30AE14 | 0672 | 0825 | M5 | 56 | Static followed by Dynamic | 17.8 | --- |
| 30AD05 | 2050 | 2203 | | 59 | 30AE14 | 3156 | 3309 | | 56 | Dynamic | 6.1 | --- |
| 30AD05 | 2630 | 2783 | | 59 | 30AE14 | 2850 | 3003 | | 60 | Dynamic | 12.2 | --- |
| 30AD05 | 3732 | 3886 | | 24 | | | | | | Dynamic | -- | pellet-pellet gaps – not yet tested |
| 30AD05 | 3452 | 3605 | M5 | 38 | 30AE14 | 3003 | 3156 | M5 | 58 | Cumulative | -- | Future test |
| 3A1F05 | 1853 | 2006 | LT Zirc-4 | 56 | F35P17 | 1855 | 2008 | Zirc-4 | 53 | Static followed by Dynamic | 17.8 | --- |
| 3A1F05 | 3367 | 3520 | | 44 | F35P17 | 2027 | 2180 | | 52 | Dynamic | 5.1 | Replacement; originally allocated as a cumulative test specimen |
| 3A1F05 | 2025 | 2178 | | 56 | | | | | | Dynamic | 10.2 | Originally allocated for 5.1 N-m, but mistakenly tested at 10.2 N-m |
| 3A1F05 | 3214 | 3367 | | 48 | F35P17 | 3159 | 3312 | | 47 | Dynamic | 10.2 | |
| | | | | | F35P17 | 3312 | 3465 | Zirc-4 | 43 | Cumulative | -- | Future test |
| 3D8E14 | 0719 | 0872 | ZIRLO | 64 | 3F9N05 | 719 | 872 | ZIRLO | 59 | Static followed by Dynamic | 17.8 | --- |
| 3D8E14 | 2412 | 2565 | | 64 | 3F9N05 | 2329 | 2482 | | 59 | Dynamic | 6.1 | --- |
| 3D8E14 | 2963 | 3116 | | 62 | 3F9N05 | 2710 | 2863 | | 57 | Dynamic | 10.2 | --- |
| 3D8E14 | 1178 | 1331 | | 63 | | | | | | Dynamic | 6.1 | --- |
| 6U3K09 | 2310 | 2463 | | 59 | | | | | | Dynamic | 14.3 | Additional higher load data point |
| 6U3K09 | 2463 | 2616 | | 59 | | | | | | Dynamic | 10.2 | Provides a good comparison with 3F9N05-2710-2863 based on segment burnup |
| 6U3K09 | 2635 | 2788 | | 58 | | | | | | Dynamic | 7.6 | Provides a good comparison with 3F9N05-2329-2482 based on segment burnup |
| 6U3K09 | 3200 | 3353 | | 50 | | | | | | Dynamic | 10.2 | Provides a comparison with 3F9N05-2710-2863 based on segment burnup |
| 6U3K09 | 3353 | 3506 | | 46 | | | | | | Dynamic | 13.3 | Additional higher load data point |
| 3D8E14 | 3225 | 3378 | ZIRLO | 56 | 3F9N05 | 3440 | 3593 | ZIRLO | 45 | Cumulative | -- | Future test |

F-8. CIRFT Test Results for the Sister Rods Tested

F-8.1 Static Tests

The static test is performed to measure the range of flexure of representative specimens for each sister rod cladding type: M5, ZIRLO, and Zirc-4 or LT Zirc-4. Six specimens—one of each cladding type and heat treatment—were tested in static mode to measure the flexural rigidity before testing the fatigue response in dynamic mode. An example of the data typically acquired is shown in Figure F-9; all were flexed beyond the knee in the curve, which is labeled as point B in Figure F-9 (a). The static flexural rigidity is calculated on the linear portion of the curve from approximately points A to B; this is consistent with the definition of EI2 in Reference [F-22].

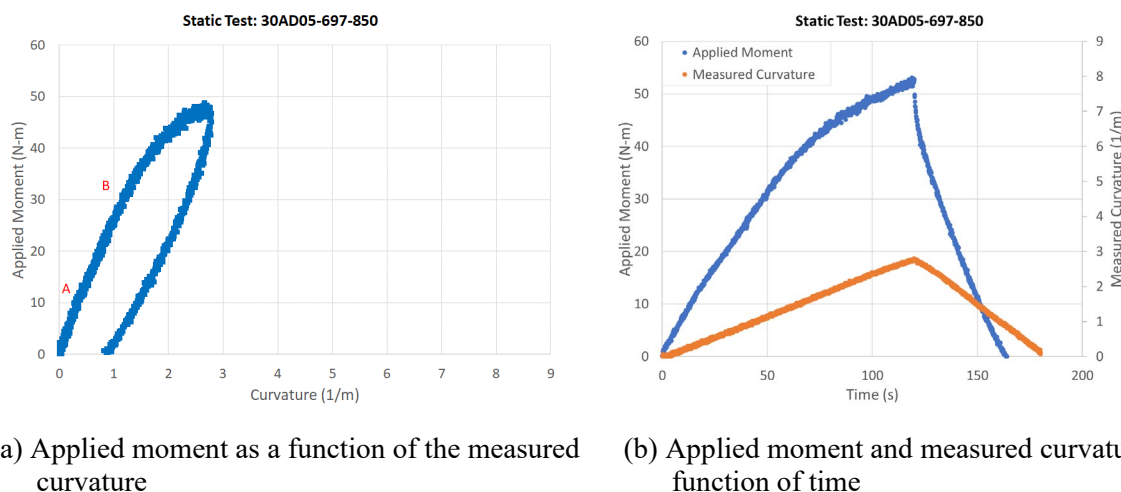


Figure F-9. The static test data for 30AD05-697-850 represent the typical result

A deep investigation of the static test data revealed that specimen F35P17-1855-2008 failed during the static test. Rod F35P17 is a Zirc-4 clad rod that was heat treated prior to CIRFT testing. During the static test, there was an observed drop in the applied moment that correlated with an increase in the measured curvature. In addition, in subsequent dynamic fatigue testing the measured applied moment was lower than expected based on the measured flexural rigidity before failure. There are indications of oxide spalling on the specimen tested (see Figure F-28), which may have contributed to the failure of the rod. Based on these observations, the only data from the static test considered valid for this specimen is the pre-failure static flexural rigidity, which is reported in Table F-9; subsequent dynamic test data are not valid and are not included in the reported CIRFT dataset.

During the static tests of 30AE14-0672-0825 and 3D8E14-0719-0872, the LVDTs were not responding as expected, appearing to be stuck at times, and they did not provide consistent curvature or rigidity information. Therefore, data from these static tests are not reported in Table F-4.

The results of the remaining valid static tests are provided in Table F-9 with a comparison of the flexural rigidity results from the dynamic tests (Section F-8.2). Generally, the dynamically measured A-B rigidity of the statically-tested specimens should be lower than the statically measured rigidity because the rod is usually flexed past the yield point during the static test. This was observed in the 3 samples that had valid rigidity measurements in both the static and dynamic tests (30AD05-0697-0850, 3A1F05-1853-2006 and 3F9N05-0719-0872), though in two cases the difference is within the measurement uncertainty.

Table F-9. Static Test Results.

| Cladding material | Heat-treated? | Estimated specimen-average burnup (GWd/MTU) | Specimen ID | Maximum Applied Moment (N-m) | Applied moment from A to B (N-m) | Flexural rigidity in A to B region (N-m ²) | Dynamically applied moment (N-m) ^a | Dynamically measured flexural rigidity (after static flexure) (N-m ²) ^a |
|-------------------|---------------|---|------------------|--|----------------------------------|--|---|--|
| M5 | No | 58 | 30AD05-0697-0850 | 47.4 | 11.1-30.9 | 23.7 ± 7.8 | 15.8 | 15.6 ± 1.2 |
| M5 | Yes | 56 | 30AE14-0672-0825 | Not reported due to data acquisition issue | | | 15.55 | 20.5 ± 4.2 |
| LT Zirc-4 | No | 56 | 3A1F05-1853-2006 | 49.8 | 16.0 – 35.4 | 20.3 ± 6.5 | 15.92 | 19.3 ± 3.9 |
| Zirc-4 | Yes | 66 | F35P17-1855-2008 | Not reported due to data acquisition issue | 8.8 – 24.8 | 20.6 ± 7.2 | N/A ^c | N/A ^c |
| ZIRLO | No | 64 | 3D8E14-0719-0872 | Not reported due to data acquisition issue | | | 15.3 | 18.4 ^b |
| ZIRLO | Yes | 59 | 3F9N05-0719-0872 | 46.6 | 17.2 to 31.9 | 21.9 ± 9.2 | 15.53 | 18.0 ± 3.6 |

^a Data are discussed in Section F-8.2.

^b Because of invalid curvature measurement, the flexural rigidity is estimated as the average of other four measurements.

^c Specimen failed in static test.

F-8.2 Dynamic Tests

All Phase 1 CIRFT dynamic tests were completed except for one sample with pellet-to-pellet gaps. Six specimens were cycled in static mode before being tested dynamically using a process referred to as *static/dynamic testing*. The results from the static/dynamic tests are not strictly comparable with the other tests because some changes in the rod condition may have occurred during the static test. The CIRFT fatigue data (applied moment, cycles to failure, maximum strain amplitude, maximum stress amplitude as discussed in Section F-3.1), maximum cladding stress amplitude (based on the modified equivalent stress approach in [F-4]), and dynamic flexural rigidity are provided in Table F-10.

Figure F-10 plots the applied bending moment, with the number of cycles to failure measured for completed tests with the available previous data [F-4, F-5]. The stress and strain amplitudes can be plotted as functions of the number of cycles to failure to map the fatigue limits of the composite rods. Figure F-11 plots the strain amplitude as a function of the number of cycles to failure for tests where an extended analysis of the test data is available.

While most of the data are consistent with previous data from other 17×17 rods, two specimens failed earlier than expected: 3A1F05-3214-3367 (LT Zirc-4 clad) and F35P17-3159-3312 (Zirc-4 clad). At the tested rod elevations, both specimens have estimated oxide thicknesses of $\sim 140 \mu\text{m}$. Other specimens were tested from nearby elevations on both rods, but only one was tested at a similar load: 3A1F05-2025-2178 failed at 48,200 cycles but only had a local oxide thickness of $\sim 80 \mu\text{m}$. Other sister rod segments tested have oxide thicknesses less than $70 \mu\text{m}$ (M5 and ZIRLO clad segments). For the Zirc-4 clad rod, the difference in the performance could also be a result of the main geometric difference of the rods—the pellet length—and if so, then further data analysis focused on pellet length could clarify the effect.

F-8.2.1 Comparisons Based on Stress Amplitude ****Section Header Added****

In previous revisions of this Appendix, the fatigue data was plotted as a function of stress amplitude and compared to the O'Donnell-Langer design curve on the basis of stress, in addition to comparisons with the measured stress amplitudes and cycles measured during transportation tests (see Figure F-12 and Figure F-13). In Figure F-12, the stress amplitude is calculated based on the composite rod maximum stress per Eq. (F-7), and in Figure F-13, the stress amplitude is calculated as the maximum cladding stress. The purpose of these plots was to show that the expected stress amplitude is well below the design limit. It was previously noted that the sister rod data were on the lower side of the other lifetime estimates [F-9, F-10, F-11], and that some data are below the O'Donnell-Langer fatigue curve [F-9].

F-8.2.2 Comparisons Based on Strain Amplitude

A review of the O'Donnell-Langer fatigue design limit development process [F-9] illuminates that while the design limit includes the effect of non-zero mean stress the data were generated at zero-mean stress. This prompted a second look at the sister rod fatigue evaluation and its approach, as discussed in Cantonwine et al. [F-24] and in this Section.

First, Cantonwine et al. [F-24] addresses the benefit of plotting the fatigue data in terms of strain amplitude, as opposed to stress amplitude. Strain amplitude is concluded to be more appropriate because it is independent of the composite nature of the fuel rod while stress can be calculated two different ways: (1) using the modified equivalent stress approach defined by Wang and Wang [F-4] to represent the cladding surface stress, and (2) using the equivalent stress approach per Eq. (F-7). Further, strain is directly measured in the shipping tests that provide representative data for the expected applied fatigue cycles, which means it can be compared directly to the strain amplitude fatigue data.

Cantonwine et al. [F-24] also considered whether to calculate fatigue damage as the sum of the ratio of applied cycles to cycles-to-failure or to compare a conservative representation of the applied cycles to the

fatigue limit (the fatigue limit is strain amplitude below which fatigue damage does not occur – typically taken at 10^7 cycles). It was concluded that it is inappropriate to calculate fatigue damage when the applied cycles are less than the fatigue limit, because the fatigue curve must be extrapolated well beyond where there is fatigue data. Thus, the approach in [F-24] is to define a conservative fatigue limit based on the fatigue data reported herein and show that a conservative strain amplitude representing the fatigue cycles experienced in transportation [F-16] is below that limit.

The high burnup fuel rod fatigue data are plotted in Figure F-14 and compared to the fatigue performance of cladding-only tubes as reported in Section F-5 and open literature data on cladding alloys [F-9]. In Figure F-14, it can be clearly observed that the fatigue performance of high burnup fuel rods is degraded compared to fatigue of cladding-only test specimens and test coupons (see Section F-5 and O'Donnell-Langer [F-9]). The fatigue limit decreased from $\sim 0.20\%$ for the cladding alloys to $\sim 0.06\%$ for the high burnup fuel rods and is significantly lower than the O'Donnell-Langer design curve for zero-mean strain conditions. As pointed out in Section F-3.2.2, discontinuities within the pellets and pellet-pellet interfaces are sources of stress/strain concentration, and it is concluded that these discontinuities in cladding support applied by the pellet are the cause of the observed degradation in fatigue performance. The magnitude of the stress/strain concentration can be estimated as the ratio of the fatigue limit for cladding alloys to that of the high burnup fuel rods ($0.20\%/0.06\% = 3.3$). To account for this degradation, a modification to the O'Donnell-Langer correlation was developed and is compared to the CIRFT data in Figure F-14. The proposed design limit (ORNL fatigue limit) was defined using the same approach applied to cladding-only data by O'Donnell-Langer (i.e., decrease the strain amplitude by a factor of 2). The area below the proposed ORNL design limit is the region where fatigue damage does not to accumulate and is compared to the range of most limiting conditions observed in the MMTT shipping test [F-16], [F-25] (see Figure F-14).

However, even the proposed ORNL fatigue design limit for fuel rods is potentially non-conservative because there will be a non-zero mean strain as a result of the rod-internal pressure and nominal rod bending during transportation resulting from gravity. The mean strain in spent nuclear fuel rods transported in a horizontal orientation ranges from 0.03 to 0.10% depending on assumed burnup and temperature conditions [F-24]. This range is significant compared to the fatigue limit of high burnup fuel rods, which is $\sim 0.06\%$ on a best estimate basis and 0.03% on a design basis. Thus, additional fatigue testing of high burnup fuel segments is planned to determine the potential magnitude of the degradation in performance because of this non-zero mean strain effect.

F-8.2.3 CIRFT-measured Flexural Rigidity of HBU Fuel Rods **Section Header Added**

Flexural rigidity is also measured during the dynamic test at the specific test conditions. The flexural rigidity of the specimen can change over the duration of the CIRFT test; a rod subjected to many bending cycles is expected to have a lower flexural rigidity than an uncycled rod, especially at large applied moments, and the rigidity reported herein is evaluated using data from the beginning of the test. The results of the dynamic flexural rigidity measurements are provided in Table F-10. For one of the static tests (3D8E14-0719-0872), the data required to calculate the curvature, strain, and flexural rigidity were unavailable, so the data are estimated as the average of the other static tests. The flexural rigidity measured for the sister rod specimens is plotted as a function of the estimated specimen burnup in Figure F-15, along with the measured flexural rigidity of other 17×17 rods tested at ORNL using CIRFT [F-7,F-8]; there is no observed trend with burnup. The flexural rigidity (including the measurement uncertainties from Appendix G) was also evaluated as a function of the applied bending moment (Figure F-15), and the decreasing trend is consistent with previous data. Because of the large uncertainties in the tests at low applied moment and because all the samples at high applied moment were tested statically prior to dynamic testing, only the samples tested at applied moments between 8 and 14 N-m are used in calculating the average dynamic flexural rigidity, which is 27 N-m^2 .

As discussed in Section F-8.1, the static specimens are tested in dynamic mode after the static test, but the dynamic results for these specimens are not strictly comparable with the dynamic-only test results. The results of the dynamic tests of these specimens are provided for information in Table F-10.

Table F-10. Sister Rod CIRFT Test Results to Date.

| Rod type | Cladding material | Estimated specimen-average burnup (GWd/MTU) | Specimen ID | Curvature (1/m) | Cycles to failure | Applied moment (N-m) (± 0.9 N-m) | Maximum Average Stress ^f (MPa) (± 10.7 MPa) | Maximum Cladding Stress ^g (MPa) | Maximum Strain (%) | Dynamic flexural rigidity (N-m ²) |
|----------|-------------------|---|---------------------------------|------------------------------|-------------------|---------------------------------------|---|--|--------------------|---|
| 17×17 | M5 | 58 | 30AD05-0697-0850 ^a | 1.0 \pm 0.18 | 3,368 | 15.8 | 186.0 | 437 | 0.47 \pm 0.09 | 15.6 \pm 1.2 |
| 17×17 | M5 | 59 | 30AD05-2050-2203 | 0.18 \pm 0.10 | 133,000 | 5.1 | 61.9 | 76 | 0.08 \pm 0.04 | 28.7 \pm 25.8 |
| 17×17 | M5 | 59 | 30AD05-2630-2783 | 0.38 \pm 0.11 | 22,300 | 10.7 | 129.6 | 164 | 0.18 \pm 0.05 | 28.0 \pm 8.4 |
| 17×17 | M5 | 56 | 30AE14-0672-0825 ^{a,c} | 0.76 \pm 0.15 | 1,630 | 15.6 | 187.0 | 328 | 0.36 \pm 0.07 | 20.5 \pm 4.2 |
| 17×17 | M5 | 60 | 30AE14-2850-3003 ^c | 0.46 \pm 0.11 | 9,800 | 10.6 | 127.0 | 193 | 0.22 \pm 0.05 | 23.6 \pm 6.5 |
| 17×17 | M5 | 56 | 30AE14-3156-3309 ^c | 0.21 \pm 0.10 | 113,000 | 5.0 | 59.5 | 92 | 0.10 \pm 0.05 | 23.2 \pm 18.9 |
| 17×17 | Zirc-4 | 66 | F35P17-2027-2180 ^c | 0.15 \pm 0.10 | 1,340,000 | 4.0 | 47.8 | 66 | 0.07 \pm 0.04 | 26.8 \pm 34.8 |
| 17×17 | Zirc-4 | 62 | F35P17-3159-3312 ^{c,d} | 0.32 \pm 0.10 | 773 | 8.6 | 101.0 | 122 | 0.15 \pm 0.05 | 30.7 \pm 12.5 |
| 17×17 | LT Zirc-4 | 48 | 3A1F05-3214-3367 | 0.41 \pm 0.11 | 3,450 | 8.8 | 105.9 | 178 | 0.19 \pm 0.05 | 21.6 \pm 6.7 |
| 17×17 | LT Zirc-4 | 56 | 3A1F05-1853-2006 ^a | 0.82 \pm 0.16 | 1,300 | 15.9 | 191.5 | 357 | 0.39 \pm 0.07 | 19.3 \pm 3.9 |
| 17×17 | LT Zirc-4 | 56 | 3A1F05-2025-2178 | 0.38 \pm 0.11 | 48,200 | 8.8 | 105.9 | 165 | 0.18 \pm 0.05 | 23.2 \pm 7.5 |
| 17×17 | LT Zirc-4 | 44 | 3A1F05-3367-3520 | 0.14 \pm 0.09 | 214,000 | 4.0 | 48.6 | 59 | 0.06 \pm 0.04 | 29.7 \pm 42.2 |
| 17×17 | ZIRLO | 64 | 3D8E14-0719-0872 ^a | 0.58 ² \pm 0.12 | 9,589 | 15.3 | 181.0 | 362 | 0.39 ^b | 18.4 ^b |
| 17×17 | ZIRLO | 64 | 3D8E14-2412-2565 ^c | 0.18 \pm 0.10 | 191,000 | 5.0 | 60.1 | 70 | 0.08 \pm 0.04 | 31.3 \pm 31.0 |
| 17×17 | ZIRLO | 62 | 3D8E14-2963-3116 | 0.31 \pm 0.10 | 39,700 | 8.7 | 104.2 | 136 | 0.15 \pm 0.05 | 28.1 \pm 10.5 |
| 17×17 | ZIRLO | 63 | 3D8E14-1178-1331 | 0.16 \pm 0.10 | 212,000 | 4.9 | 58.4 | 69 | 0.08 \pm 0.04 | 30.9 \pm 32.4 |
| 17×17 | ZIRLO | 59 | 3F9N05-0719-0872 ^{a,c} | 0.86 \pm 0.16 | 3,540 | 15.5 | 186.3 | 374 | 0.41 \pm 0.08 | 18.0 \pm 3.6 |
| 17×17 | ZIRLO | 59 | 3F9N05-2329-2482 ^c | 0.21 \pm 0.10 | 189,000 | 4.8 | 57.3 | 92 | 0.10 \pm 0.05 | 22.6 \pm 19.3 |
| 17×17 | ZIRLO | 57 | 3F9N05-2710-2863 ^c | 0.40 \pm 0.11 | 33,000 | 8.7 | 104.7 | 173 | 0.19 \pm 0.05 | 21.8 \pm 6.9 |
| 17×17 | ZIRLO | 59 | 6U3K09-2310-2463 | 0.42 \pm 0.11 | 17,500 | 12.7 | 152.3 | 182 | 0.20 \pm 0.05 | 30.2 \pm 8.5 |
| 17×17 | ZIRLO | 59 | 6U3K09-2463-2616 | 0.27 \pm 0.10 | 39,200 | 8.9 | 106.5 | 119 | 0.13 \pm 0.05 | 32.4 \pm 13.3 |
| 17×17 | ZIRLO | 58 | 6U3K09-2635-2788 | 0.17 \pm 0.10 | 110,000 | 6.4 | 76.8 | 75 | 0.08 \pm 0.04 | 37.1 \pm 21.7 |
| 17×17 | ZIRLO | 50 | 6U3K09-3200-3353 | 0.31 \pm 0.10 | 34,900 | 8.8 | 105.3 | 127 | 0.15 \pm 0.05 | 30.0 \pm 11.8 |
| 17×17 | ZIRLO | 46 | 6U3K09-3353-3506 | 0.43 \pm 0.11 | 14,100 | 11.7 | 140.2 | 187 | 0.21 \pm 0.05 | 27.0 \pm 7.4 |

^a Dynamically tested following a static test.

^b Estimated based on average flexural rigidity of valid static/dynamic tests.

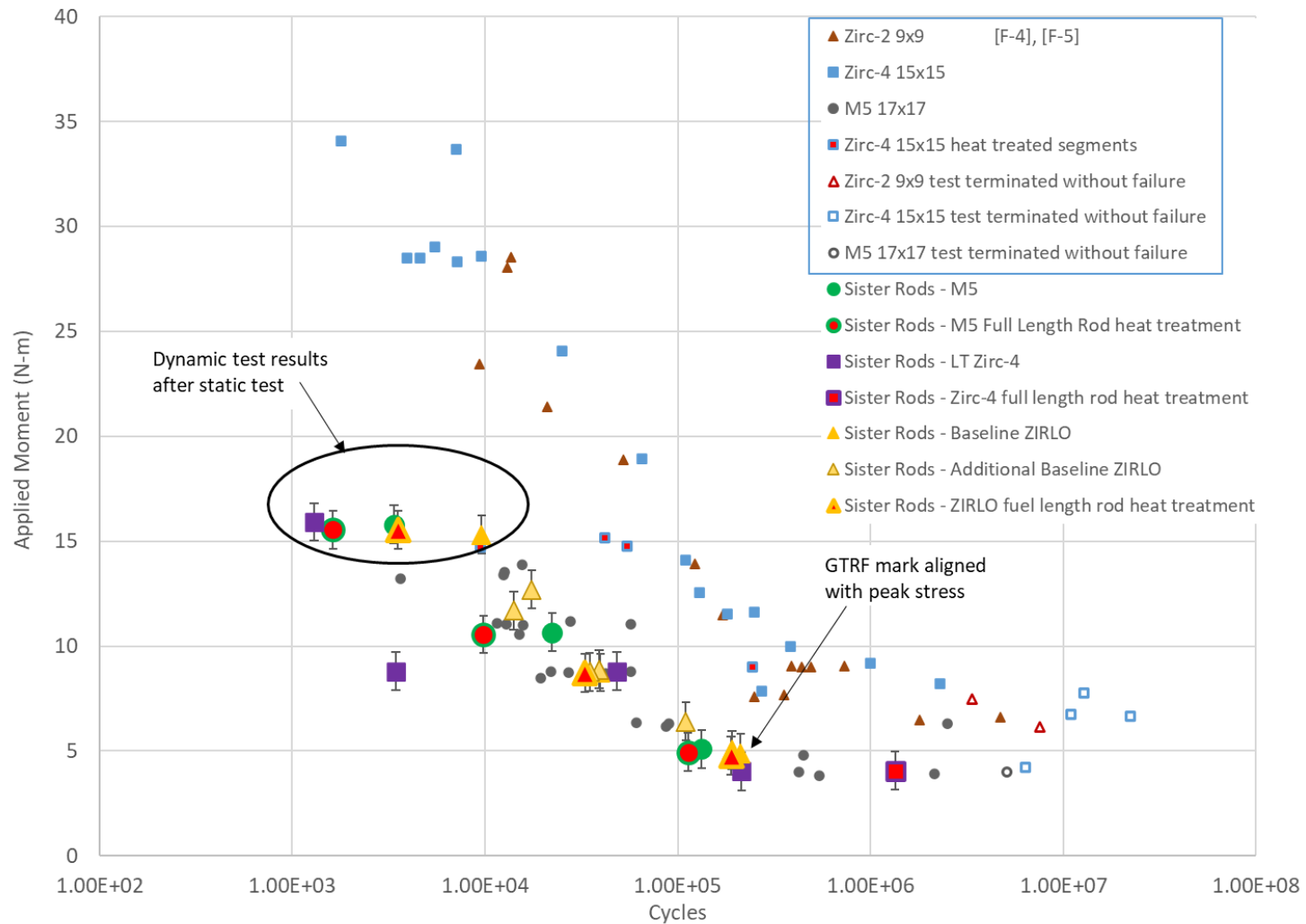
^c Specimen from heat-treated rod.

^d Erratic load cell data were recorded during the test. The applied moment might have been higher.

^e Specimen had a GTRF mark in the gauge section that was aligned (as was possible) with the expected maximum strain location.

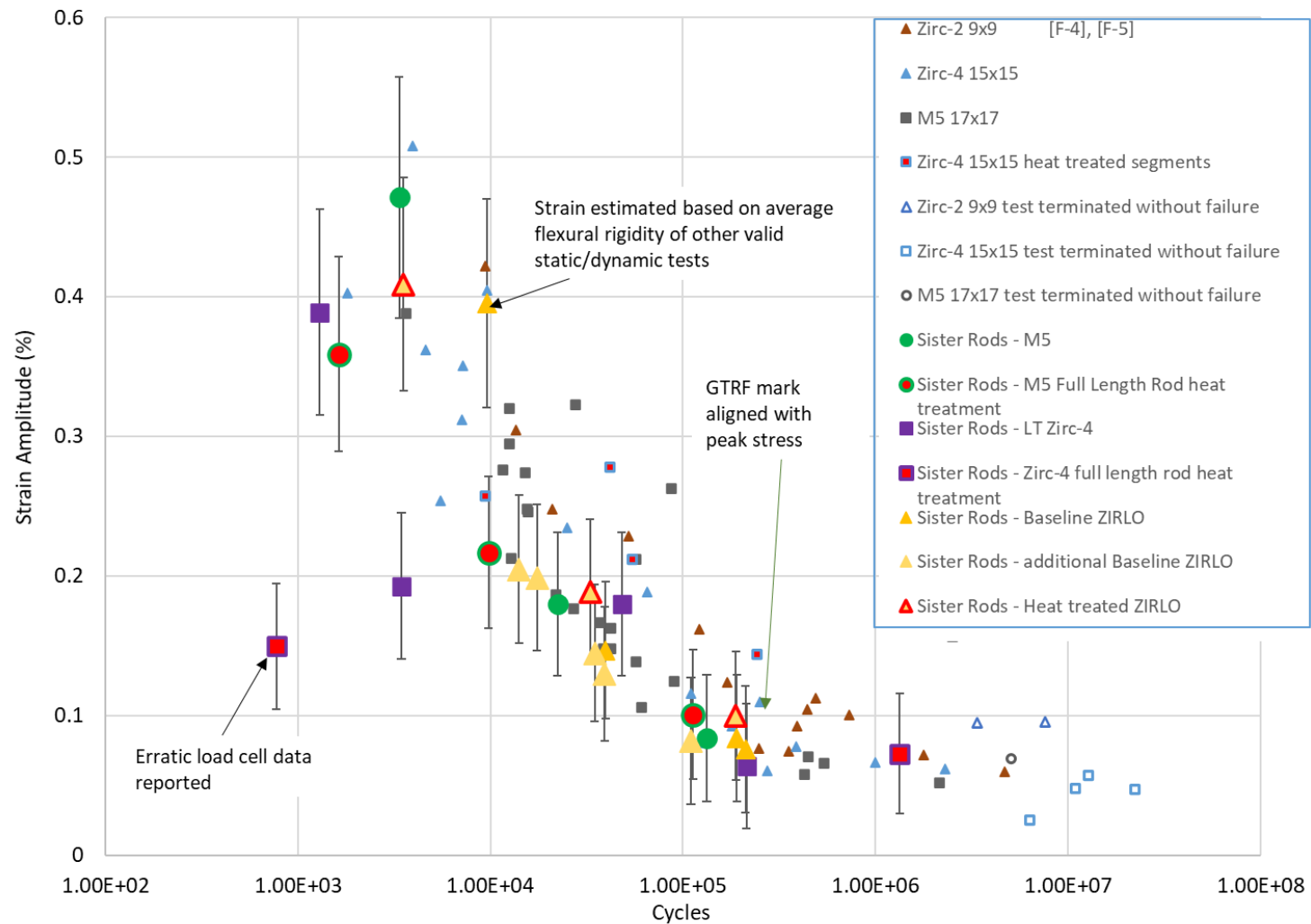
^f Stress calculated using the equivalent stress approach per Eq. (F-7). Measured ODs used in calculation were typically approximately 9.5 mm.

^g Stress calculated using the modified equivalent stress approach in Reference [F-4] to represent the cladding surface stress.



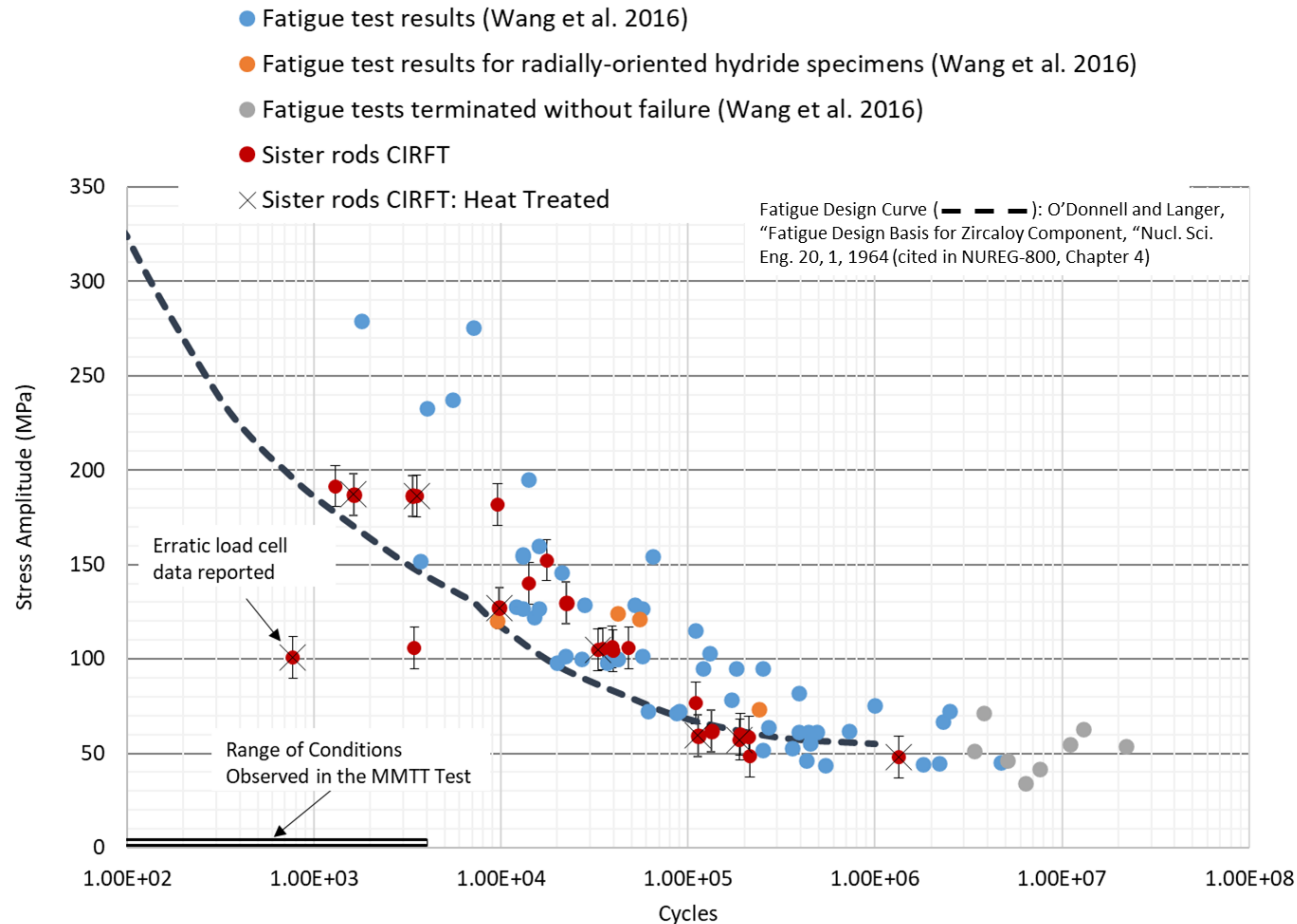
The error bars on the sister rod data represent the calculated uncertainty (0.8 N-m) in Section G-3.3, Appendix G (non-sister rod data from [F-4], [F-5])

Figure F-10. Results of CIRFT tests plotted with reference data, applied moment vs. cycles to failure.



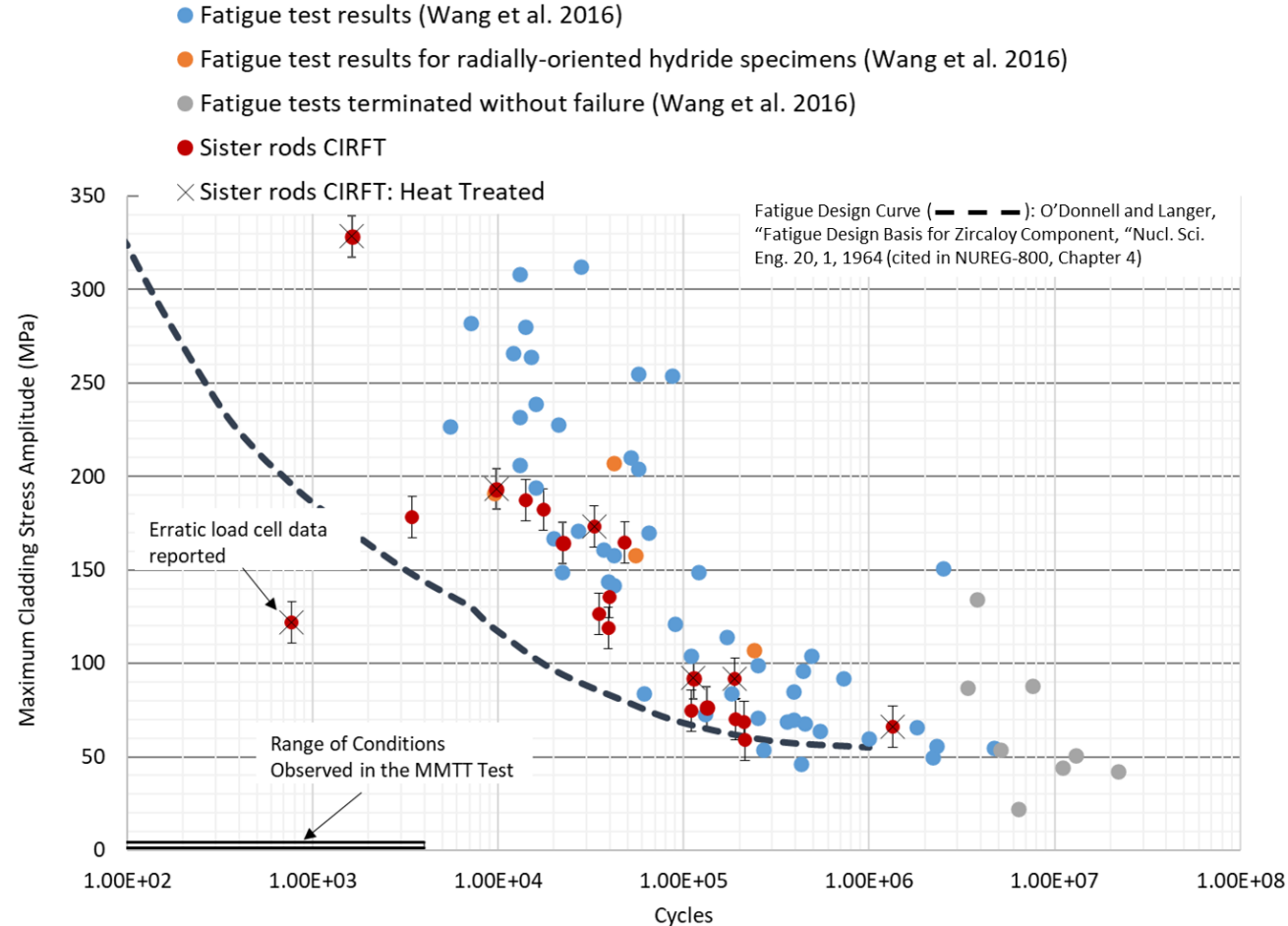
The error bars on the sister rod data represent the calculated uncertainty in Section G-3.4, Appendix G (non-sister rod data from [F-4], [F-5]).

Figure F-11. Results of CIRFT tests completed to date, strain amplitude vs. cycles to failure.



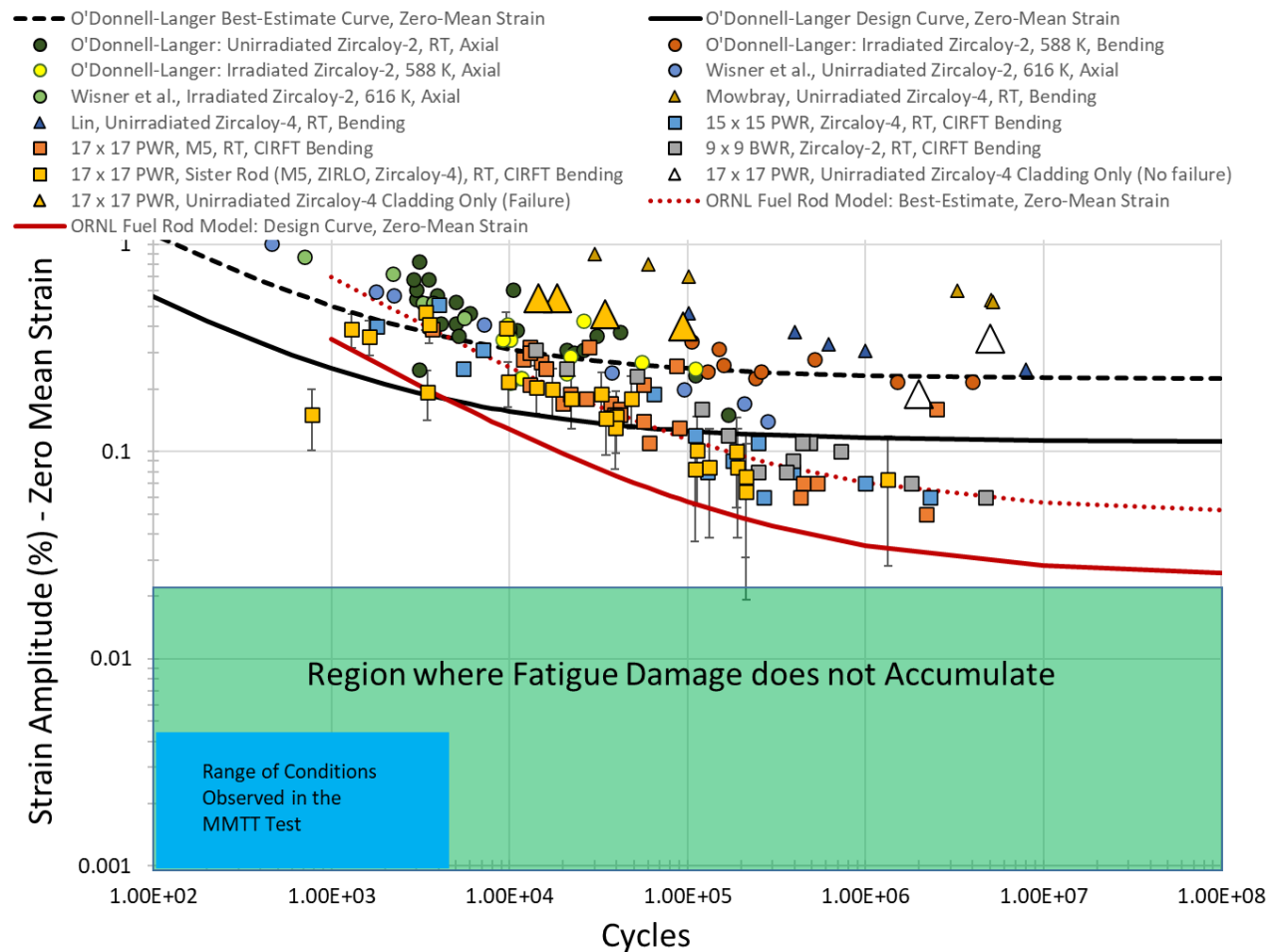
The error bars on the sister rod data represent the calculated uncertainty in Section G-3.5, Appendix G.

Figure F-12. Stress amplitude of the composite rod based on Eq. (F-7), as a function of cycles to failure for the sister rods. The stresses representing the conditions observed in the MMTT test are calculated based on measured strains: 1 MPa for the lower strain of 0.001% (or 10 μ strain) [F-25], which is the minimum strain of the highest 4000 cycles observed, and 4.2 MPa for the upper strain of 0.0042% (or 42 μ strain), which is the maximum strain observed during TTCI testing [F-16].



The error bars on the sister rod data represent the calculated uncertainty in Section G-3.5, Appendix G.

Figure F-13. Cladding stress amplitude as a function of cycles to failure for the sister rods. The stresses representing the conditions observed in the MMTT test are calculated based on measured strains: 1 MPa for the lower strain of 0.001% (or 10 μ strain) [F-25], which is the minimum strain of the highest 4000 cycles observed, and 4.2 MPa for the upper strain of 0.0042% (or 42 μ strain), which is the maximum strain observed during TTCI testing [F-16].



The error bars on the sister rod data represent the calculated uncertainty in Section G-3.5, Appendix G.

Figure F-14. Strain amplitude as a function of cycles to failure for the sister rods compared to the fatigue data on cladding alloys from Figure F-7 and the proposed ORNL fatigue limit for fuel rods. [F-24] The strains representing the conditions observed in the MMTT test are based on measured strains: the lower strain is 0.001% (or 10 μ strain) [F-25], which is the minimum strain of the highest 4000 cycles observed, and the upper strain is 0.0042% (or 42 μ strain), which is the maximum strain observed during TTCI testing [F-16].

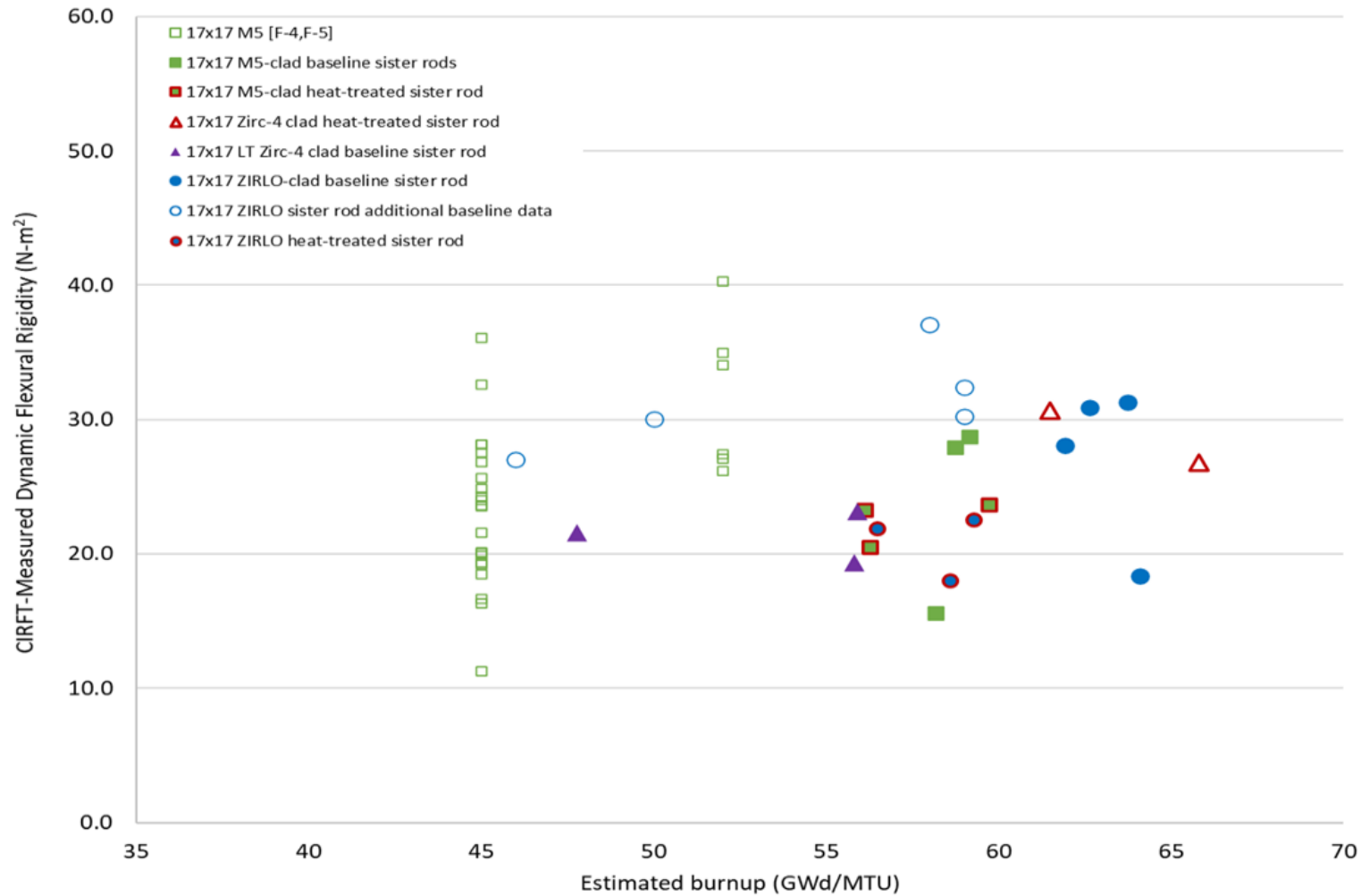
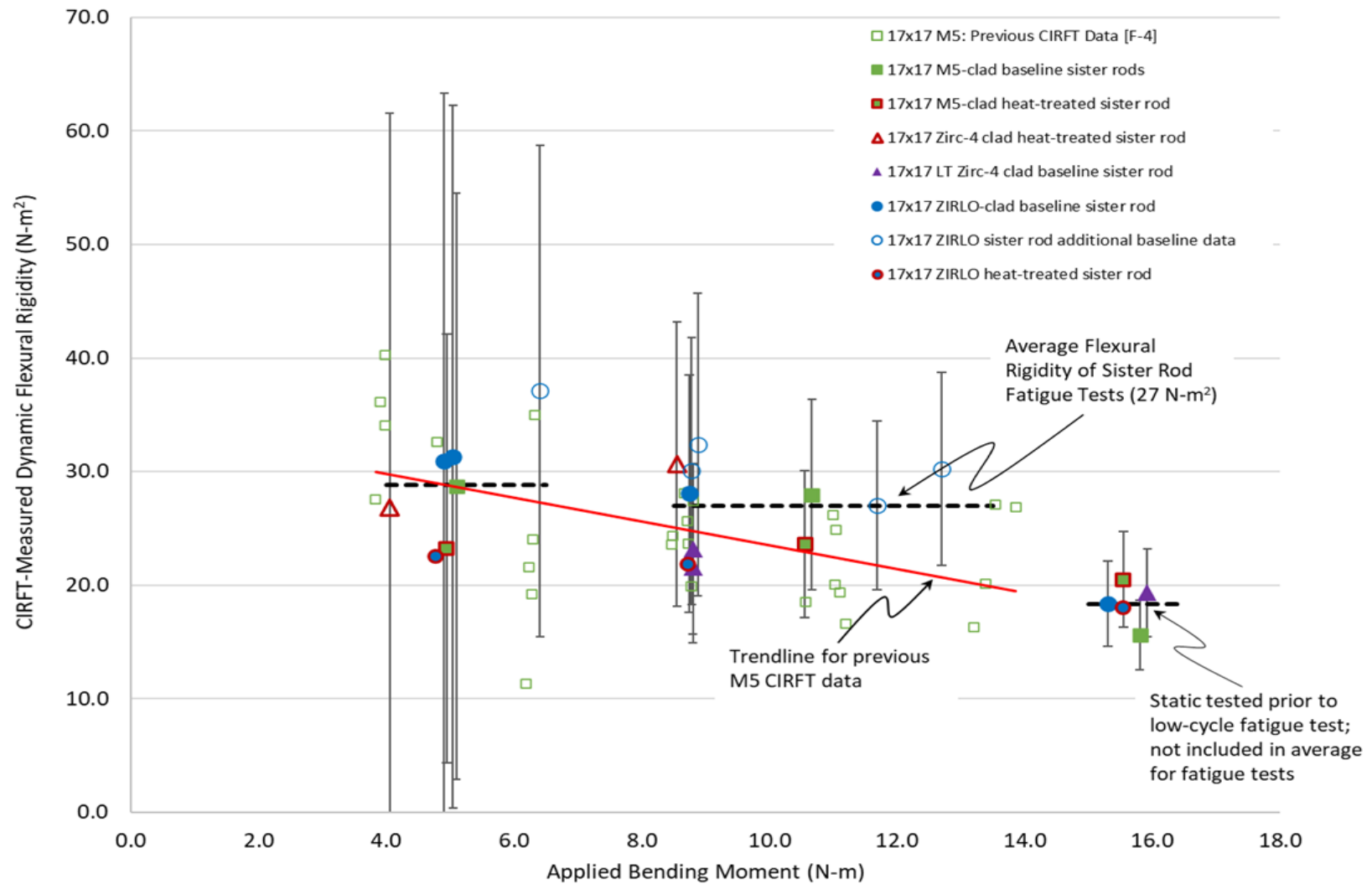


Figure F-15. CIRFT-measured flexural rigidity of the sister rod segments tested as a function of estimated segment burnup plotted with previous CIRFT data.



The error bars on the sister rod data represent the calculated uncertainty in Section G-3.6, Appendix G.

Figure F-16. Trend of CIRFT-measured dynamic flexural rigidity with applied bending moment.

F-8.3 Comparisons of Paired Specimens

The paired results are tabulated in Table F-11. Averages are provided for burnup, cycles to failure, strain, and flexural rigidity for comparison purposes. For the M5-clad and ZIRLO-clad segments, the heat-treated rods generally have a shorter fatigue lifetime and lower flexural rigidity. Revisiting Figure F-15, the small but consistent difference in flexural rigidity between the baseline and heat-treated rods is clear. The reverse seems to be true for the Zirc-4-clad and LT Zirc-4-clad pairs; the heat-treated Zirc-4-clad segments have a higher flexural rigidity and a longer fatigue lifetime than the baseline LT Zirc-4-clad segments. However, there are several differences in the parent rods, and these two rods are not good matches for comparing heat-treatment effects. One potential explanation for the difference in performance is the pellet length. As shown in Table 4 of the NDE report [F-6], the pellets in the Zirc-4-clad rod are ~13.6 mm long, whereas the pellets in all other sister rods are ~10 mm long. It is possible that the increased stiffness is related to the longer pellet length.

Figure F-10 further illustrates a reduced fatigue lifetime related to the heat treatments. This effect is seen for all M5-clad and ZIRLO-clad heat-treated specimens. However, when the cycles to failure are plotted with the calculated strain amplitude, the offset related to the heat-treatment is eliminated, as shown in Figure F-11. Because the rods have nearly the same geometry, the calculated strain would normally be expected to provide the same offset between baseline and heat-treated specimen results. However, for CIRFT, the strain is calculated based on the measured rod deflection and flexural rigidity. Because the heat-treated rods have a lower flexural rigidity, the stress and strain corresponding to the same bending moment are higher. Thus, plotting the fatigue lifetime by strain amplitude resolves the offset and the heat-treated specimen's fatigue lifetime is consistent with the baseline specimen's performance given the same amount of applied stress and strain.

On the basis of the CIRFT rigidity measurements alone, as shown in Figure F-15, the observed difference between the heat-treated and baseline could be considered within measurement uncertainty. However, given the good alignment of the strain-amplitude results and the results of mechanical tests (Appendix E), the heat treatments clearly resulted in a lower flexural rigidity that led to a shorter fatigue lifetime for the same applied load. There are at least three potential sources for a reduction in flexural rigidity with FHT: (1) a permanent increase in cladding OD and a pellet-cladding gap that resulted from the increased pressure at temperature during the heat-treatment, (2) the annealing of irradiation defects resulting from the FHT, and (3) the reorientation of precipitated hydrides in the cladding during the heat-treatment that make it more susceptible to cladding fracture. The latter source is unlikely because the amount of hydride reorientation resulting from the sister rod heat treatments (Appendices A and B) varied by cladding alloy; only very short, reoriented hydrides were observed on the Zirc-4/LT Zirc-4-clad rods, isolated hydrides were observed at the ID/OD on the ZIRLO-clad rods, and many reoriented hydrides were observed on the M5-clad rods. Because reorientation was not observed for all heat-treated rods, the difference in flexural rigidity and fatigue lifetime is not likely to be related to hydride reorientation. However, irradiation defect annealing could have occurred during FHT (particularly on the M5-clad rod as discussed in Appendix A), resulting in a lower overall rigidity of the FHT rod, leading to a shorter fatigue lifetime. The other two potential sources are being investigated.

One specimen with visible GTRF marks was tested with the marks aligned (as was possible) with the highest cladding strain location, and the GTRF marks did not reduce the fatigue lifetime. The GTRF marks on this specimen are not considered representative or bounding; the specimen was selected based on availability only and further tests should be completed to fully explore the effect.

Table F-11. Results Arranged by Paired Specimens (Baseline Rods vs. Heat-treated Rods) for Static/Dynamic and Dynamic CIRFT.

| Baseline rods | | | | | | | | Heat-treated rods | | | | | | |
|---------------|------------------------|---------------|---|-------------------|---|------------------------------|--|-------------------|----------------------------|---------------|---|-------------------|---|------------------------------|
| Specimen ID | | Cladding type | Estimated specimen average burnup (GWd/MTU) | Cycles to failure | Dynamic flexural rigidity (N-m ²) | Applied strain amplitude (%) | | Specimen ID | | Cladding type | Estimated specimen average burnup (GWd/MTU) | Cycles to failure | Dynamic flexural rigidity (N-m ²) | Applied strain amplitude (%) |
| 30AD05 | 0697 0850 ^a | M5 | 58 | 3,368 | 15.6 | 0.47 | | 30AE14 | 0672 0825 ^a | M5 | 56 | 1,630 | 20.5 | 0.36 |
| 30AD05 | 2050 2203 | | 59 | 133,000 | 28.7 | 0.08 | | 30AE14 | 3156 3309 | | 56 | 113,000 | 23.2 | 0.10 |
| 30AD05 | 2630 2783 | | 59 | 22,300 | 28.0 | 0.18 | | 30AE14 | 2850 3003 | | 60 | 9,800 | 23.6 | 0.22 |
| Average | | | 59 | 52,889 | 24.1 | 0.24 | | | | | 57 | 41,477 | 22.4 | 0.23 |
| 3A1F05 | 1853 2006 ^a | LT Zirc-4 | 56 | 1,300 | 19.3 | 0.39 | | F35P17 | 1855 2008 ^{a,c,e} | Zirc-4 | 53 | 525 | 28.7 ^b | 0.16 ^b |
| 3A1F05 | 3367 3520 | | 44 | 214,000 | 29.7 | 0.06 | | F35P17 | 2027 2180 | | 52 | 1,340,000 | 26.8 | 0.07 |
| 3A1F05 | 2025 2178 | | 56 | 48,200 | 23.2 | 0.18 | | | | | | | | |
| 3A1F05 | 3214 3367 | | 48 | 3,450 | 21.6 | 0.19 | | F35P17 | 3159 3312 ^c | | 47 | 773 | 30.7 | 0.15 |
| Average | | | 51 | 66,738 | 24.8 | 0.14 | | | | | 51 | 447,099 | 28.8 | 0.11 |
| 3D8E14 | 0719 0872 ^a | ZIRLO | 64 | 9,589 | 18.4 ^b | 0.39 ^b | | | | | | | | |
| 3D8E14 | 2412 2565 ^d | | 64 | 191,000 | 31.3 | 0.08 | | | | | | | | |
| 3D8E14 | 2963 3116 | | 62 | 39,700 | 28.1 | 0.15 | | | | | | | | |
| 3D8E14 | 1178 1331 | | 63 | 212,000 | 30.9 | 0.08 | | | | | | | | |
| 6U3K09 | 2310 2463 | | 59 | 17,500 | 30.2 | 0.20 | | 3F9N05 | 0719 0872 ^a | ZIRLO | 59 | 3,540 | 18.0 | 0.41 |
| 6U3K09 | 2463 2616 | | 59 | 39,200 | 32.4 | 0.13 | | 3F9N05 | 2329 2482 | | 59 | 189,000 | 22.6 | 0.10 |
| 6U3K09 | 2635 2788 | | 58 | 110,000 | 37.1 | 0.08 | | 3F9N05 | 2710 2863 | | 57 | 33,000 | 21.8 | 0.19 |
| 6U3K09 | 3200 3353 | | 50 | 34,900 | 30.0 | 0.15 | | | | | | | | |
| 6U3K09 | 3353 3506 | | 46 | 14,100 | 27.0 | 0.21 | | | | | | | | |
| Average | | | 60 | 50,400 | 31.4 | 0.15 | | | | | 58 | 75,180 | 21.8 | 0.19 |

^a Dynamically tested following a static test.

^b Estimated.

^c Erratic load cell data were recorded during the test. The applied moment and strain amplitude was likely higher.

^d Specimen had a GTRF mark in the gauge section that was aligned (as possible) with the expected maximum strain location.

^e Deeper examination indicates that this specimen broke during the static test and therefore the dynamic test results are invalid.

F-8.4 Optical Imaging of the Fractured Specimens

To provide additional information regarding how the specimens fractured, magnified images were obtained using the Irradiated Microsphere Gamma Analyzer facility at the Irradiated Fuels Examination Laboratory. The images provide information about the location where the fatigue crack propagated to fracture and about whether the fracture occurred at a pellet-pellet interface.

In many cases, the locations of the highest strains appear on the specimen surface as dull oval areas, as shown on Figure F-18. Rods with higher oxide thicknesses had some additional spalling during the test, which is particularly visible in LT Zirc-4 clad rods such as 3A1F05-1853-2006 (Figure F-31).

The M5-clad specimens tended to break cleanly around the circumference of the rod, but the break occurred in the body of the pellet, rather than at the pellet-pellet interface. Three of the six specimens broke in the center third of the specimen, whereas the other three broke near or inside a dogbone grip.

The ZIRLO-clad specimens broke differently, depending upon the parent rod. The baseline 3D8E14 specimens tended to break cleanly around the circumference of the rod but at approximately a 30-degree angle. Three of the four specimens broke at pellet-pellet interfaces, and the cladding fracture extended into the body of a pellet. Three of the four specimens broke in the center third, and one broke near the dogbone. All 6U3K09 specimens broke circumferentially: three of the five broke near or inside the dogbone grip, and three of the five broke at pellet-pellet interfaces. Two of the 6U3K09 specimens had double fractures—a partial circumference break in the center third, with the full fracture near the dogbone. All specimens from FHT rod 3F9N05 broke in the center third of the specimen: two had a flat circumferential break at the pellet-pellet interface, and one broke in the body of a pellet at approximately a 30-degree angle.

The Zirc-4-clad specimens all broke dramatically in the same way, with a flat circumferential crack around half the rod that was sheared around the half of the rod and at a pellet-pellet interface. One specimen fractured in the center third of the dogbone, and two fractured near the dogbone grip. The Zirc-4 clad fractures are jagged, and the sheared sections span a full pellet length or more, although the crack appears to have nucleated at a pellet-pellet interface. The baseline LT Zirc-4-clad specimens look similar to the LT Zirc-4 specimens at higher rod elevations, and at lower elevations they also look similar to the ZIRLO rods. Two baseline LT Zirc-4-clad specimens fractured in the center third of the specimen, and three fractured at pellet-pellet interfaces.

There does not appear to be a difference in the fracture mode of the baseline and heat-treated rods. The specimens with lower-than-expected fatigue lifetimes did not fracture in an anomalous manner.

Table F-12 summarizes the visual observations of CIRFT-fractured dogbones.

Table F-12. Summary of Visual Observations of CIRFT-fractured Dogbones.

| Rod type | Cladding material | Estimated specimen-average burnup (GWd/MTU) | Specimen ID | Fracture location | Cladding fracture orientation | Pellet fracture appearance |
|----------|-------------------|---|-------------------------------|---|---|--------------------------------|
| 17×17 | M5 | 58 | 30AD05-0697-0850 | Center third | Circumferential | Pellet body |
| 17×17 | M5 | 59 | 30AD05-2050-2203 | In grip | Circumferential | Pellet body |
| 17×17 | M5 | 59 | 30AD05-2630-2783 | Near grip | Circumferential with some flaring and uneven ends | Pellet body but very near end |
| 17×17 | M5 | 56 | 30AE14-0672-0825 | Center third | Circumferential with some flaring and uneven ends | Pellet body |
| 17×17 | M5 | 60 | 30AE14-2850-3003 | Near grip | Circumferential | Pellet body |
| 17×17 | M5 | 56 | 30AE14-3156-3309 | Center third | Circumferential with partial shearing | Pellet body |
| 17×17 | Zirc-4 | 66 | F35P17-1855-2008 | Center third | Partially sheared | At pellet end and through body |
| 17×17 | Zirc-4 | 66 | F35P17-2027-2180 | Near grip | Partially sheared | At pellet end |
| 17×17 | Zirc-4 | 62 | F35P17-3159-3312 | Near grip | Partially sheared | At pellet end |
| 17×17 | LT Zirc-4 | 48 | 3A1F05-3214-3367 | In grip | Partially sheared | Pellet end |
| 17×17 | LT Zirc-4 | 56 | 3A1F05-1853-2006 | Near grip | Circumferential at ~30-degree angle | Just off pellet end |
| 17×17 | LT Zirc-4 | 56 | 3A1F05-2025-2178 | Center third | circumferential | Pellet end |
| 17×17 | LT Zirc-4 | 44 | 3A1F05-3367-3520 | Center third | Partially sheared | Pellet body |
| 17×17 | ZIRLO | 64 | 3D8E14-0719-0872 | Near grip | Circumferential with partial shearing | Pellet end |
| 17×17 | ZIRLO | 64 | 3D8E14-2412-2565 | Center third | Circumferential at ~30-degree angle | Pellet body |
| 17×17 | ZIRLO | 62 | 3D8E14-2963-3116 | Center third | circumferential | Pellet end |
| 17×17 | ZIRLO | 63 | 3D8E14-1178-1331 | Center third | Circumferential. GTRF mark obliterated. | Pellet end |
| 17×17 | ZIRLO | 59 | 3F9N05-0719-0872 ³ | Center third | Circumferential at ~30-degree angle | Pellet body |
| 17×17 | ZIRLO | 59 | 3F9N05-2329-2482 | Center third | Circumferential | Pellet end |
| 17×17 | ZIRLO | 57 | 3F9N05-2710-2863 | Center third | Circumferential | Pellet end |
| 17×17 | ZIRLO | 59 | 6U3K09-2310-2463 | Center and near grip; double fracture | Circumferential | Pellet end |
| 17×17 | ZIRLO | 59 | 6U3K09-2463-2616 | Near grip | Circumferential | Pellet end |
| 17×17 | ZIRLO | 58 | 6U3K09-2635-2788 | At grip | Circumferential | Pellet end |
| 17×17 | ZIRLO | 50 | 6U3K09-3200-3353 | Center third and near grip, double fracture | Circumferential | Pellet body |
| 17×17 | ZIRLO | 46 | 6U3K09-3353-3506 | Near grip | Circumferential | Pellet body |

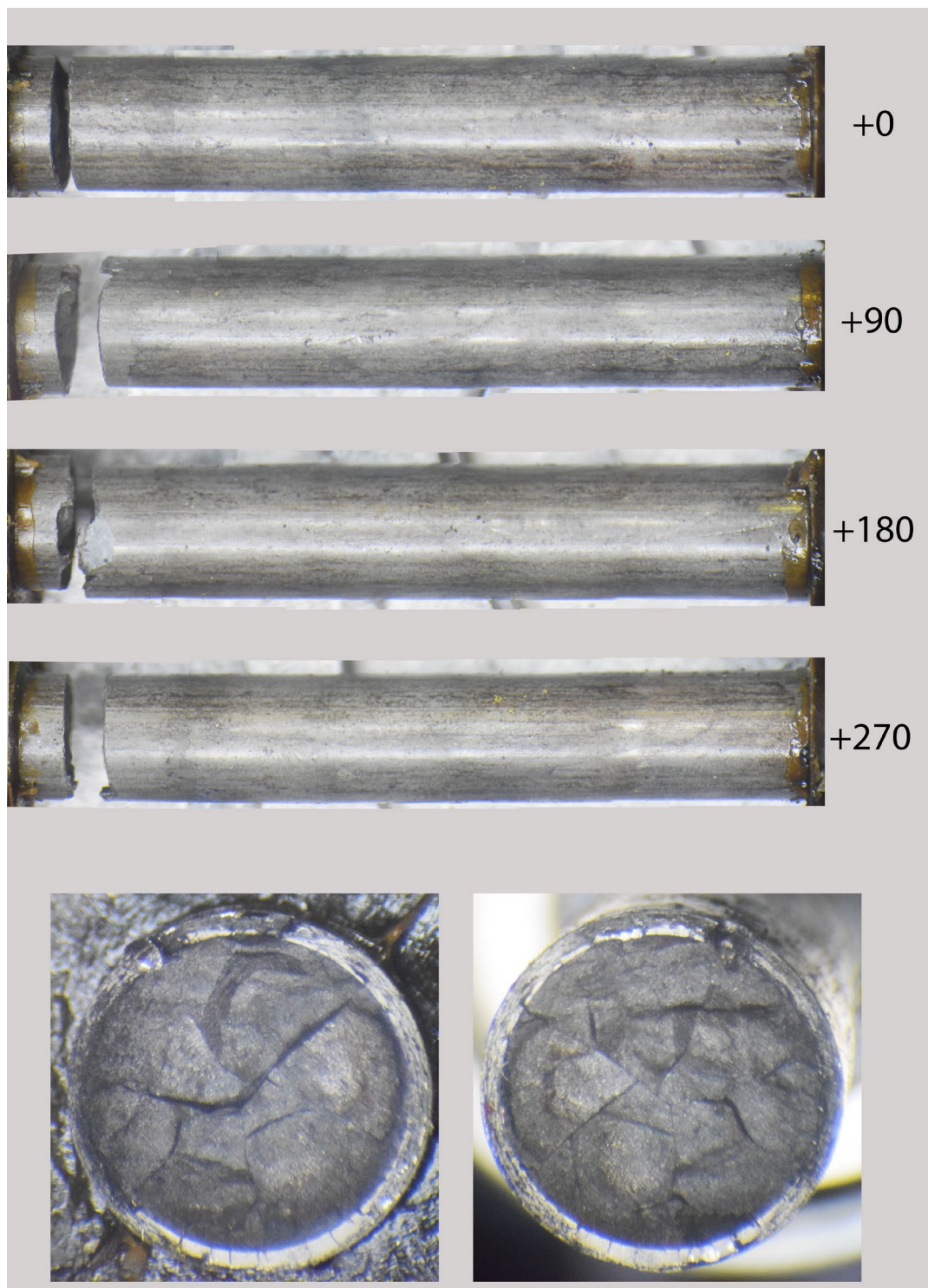


Figure F-17. 6U3K09-3353-3506 post-fatigue test condition.

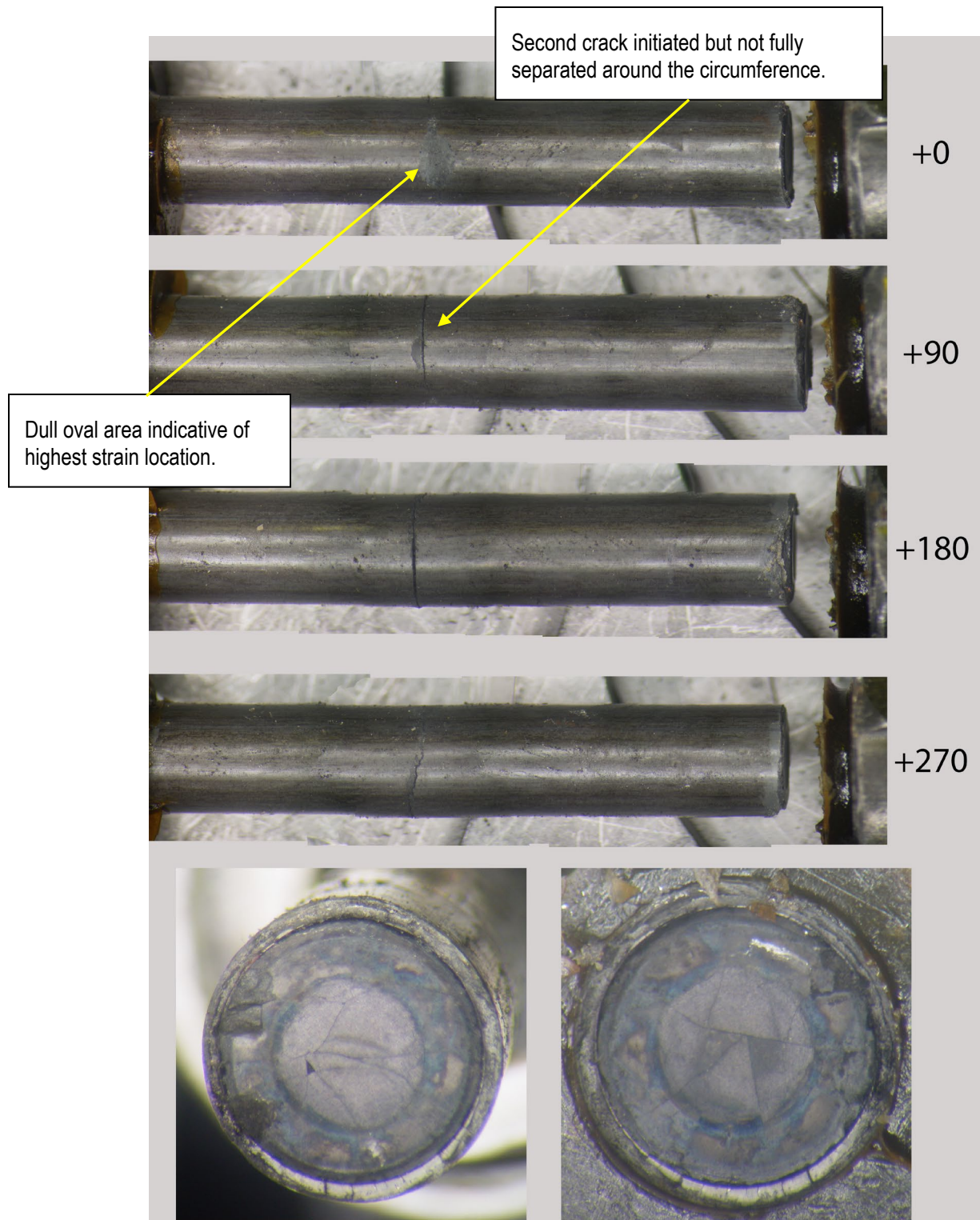


Figure F-18. 6U3K09-2310-2463 post-fatigue test condition.

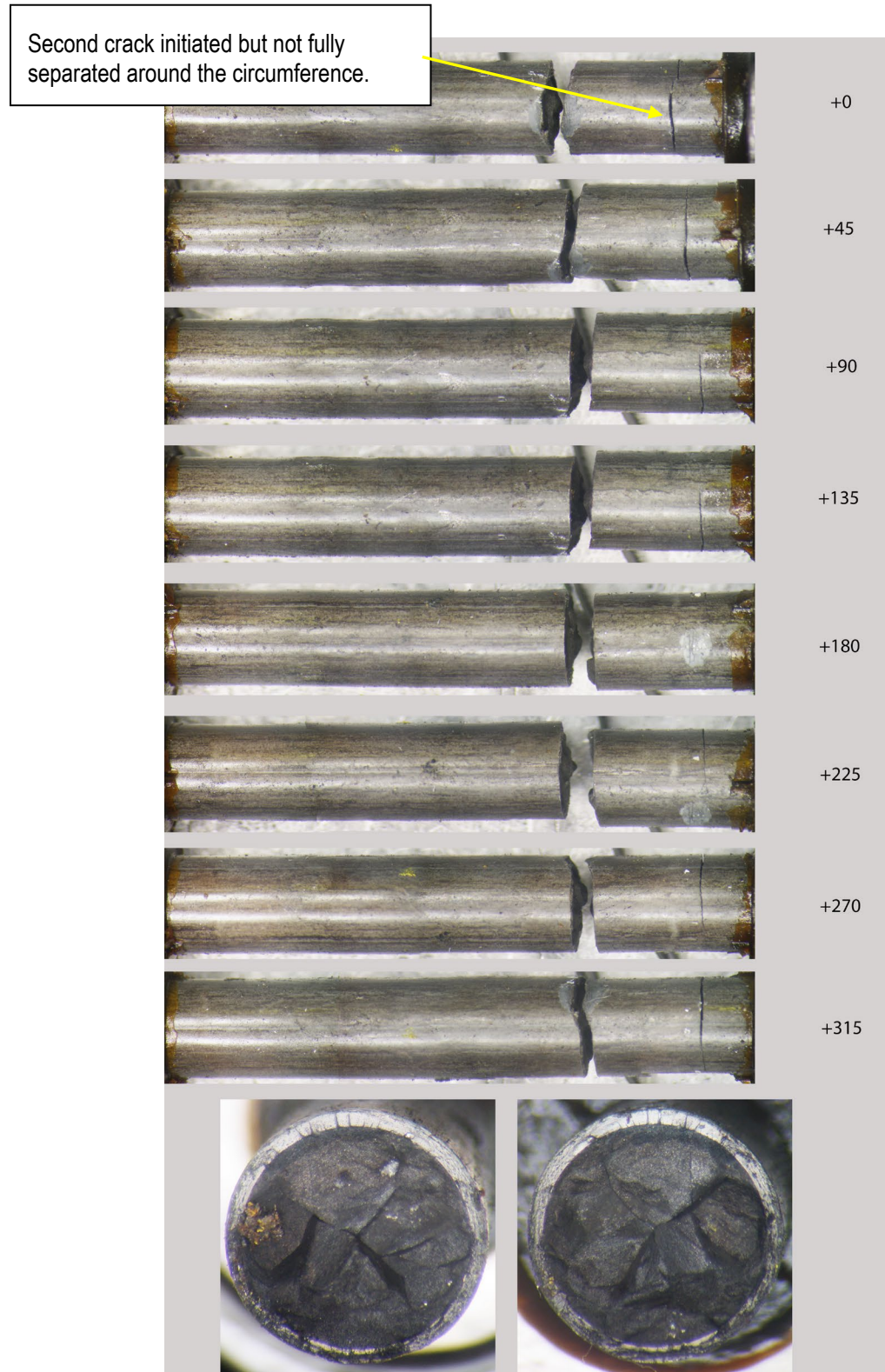


Figure F-19. 6U3K09-3200-3353 post-fatigue test condition.

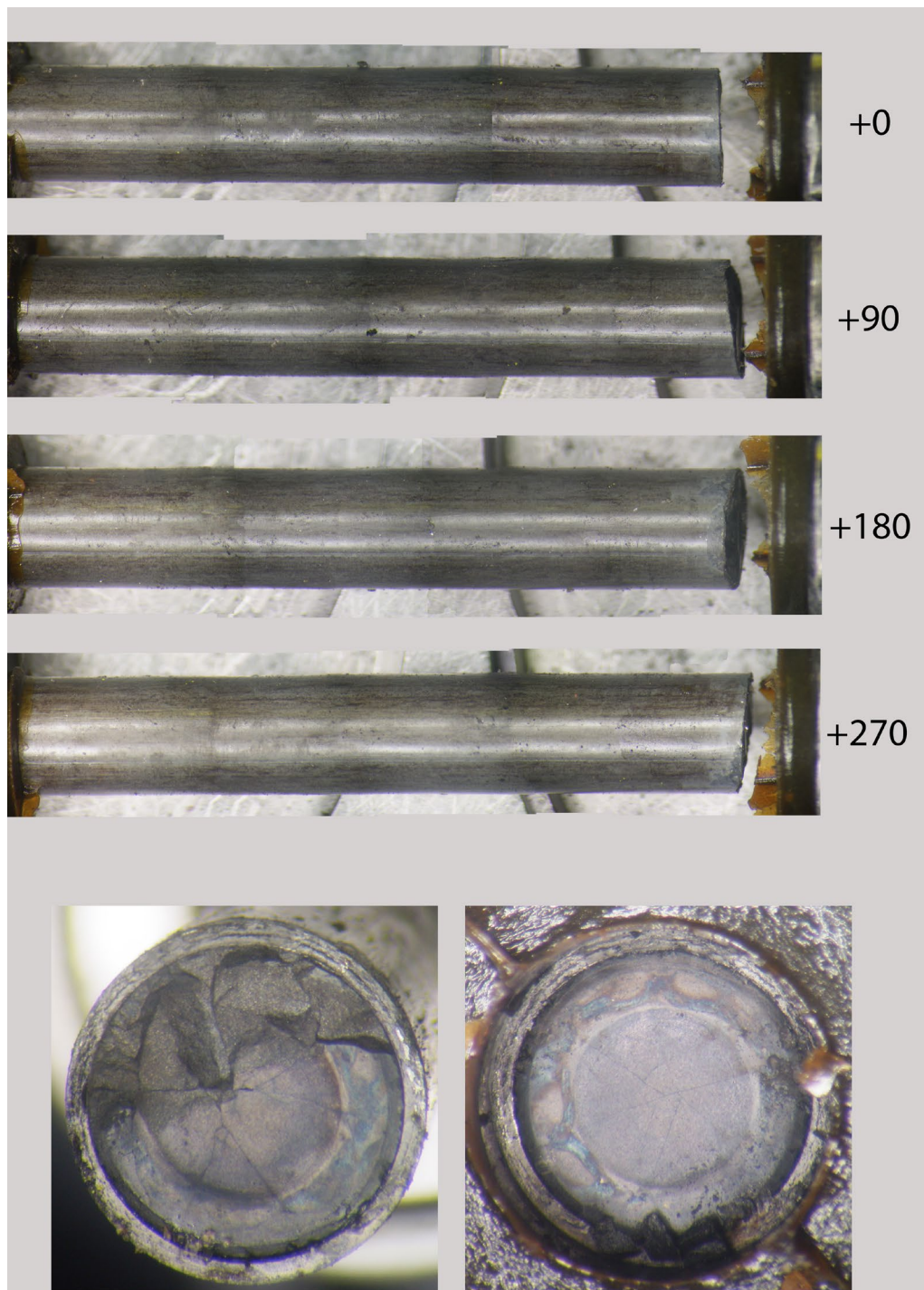


Figure F-20. 6U3K09-2635-2788 post-fatigue test condition.

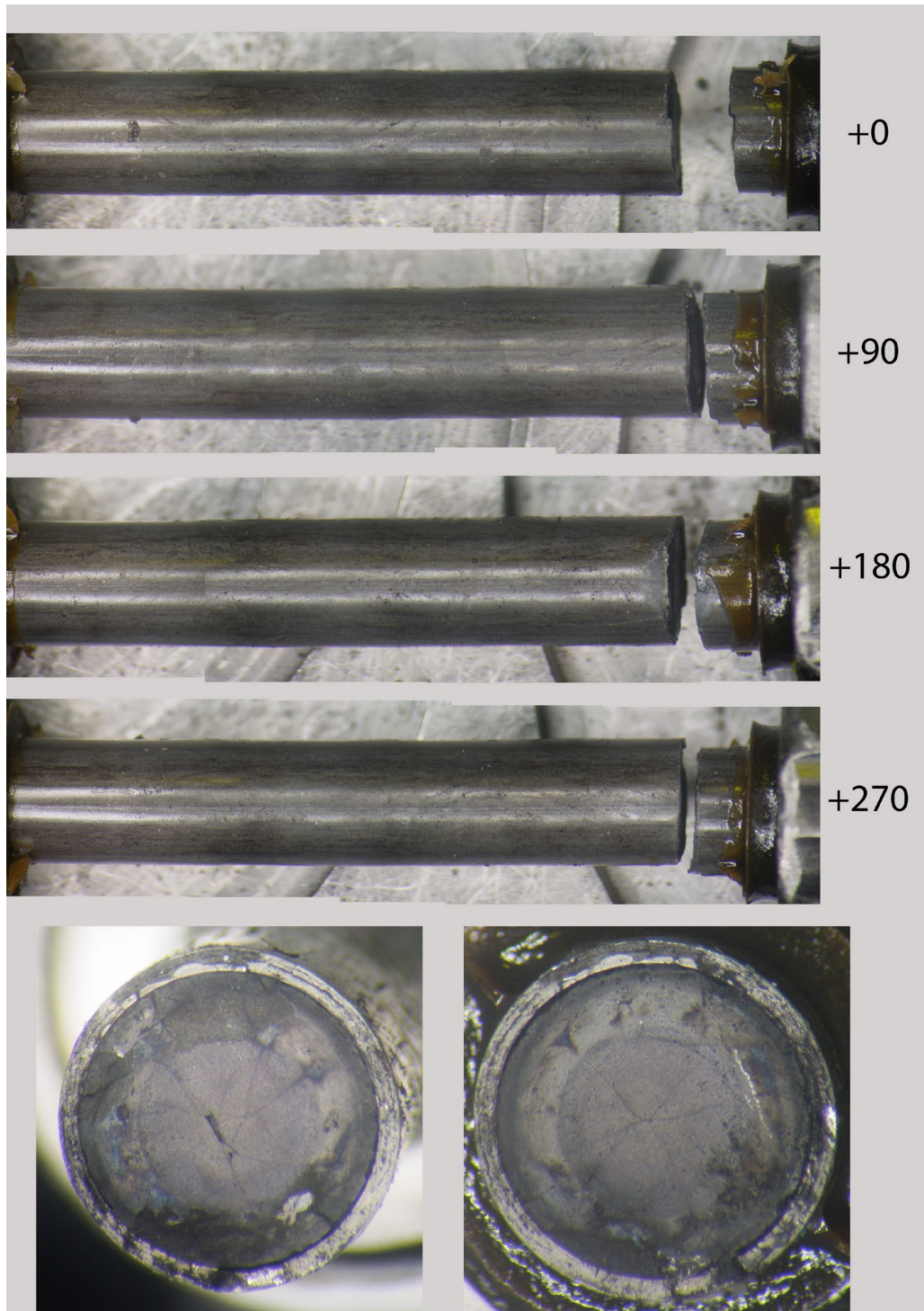


Figure F-21. 6U3K09-2463-2616 post-fatigue test condition.

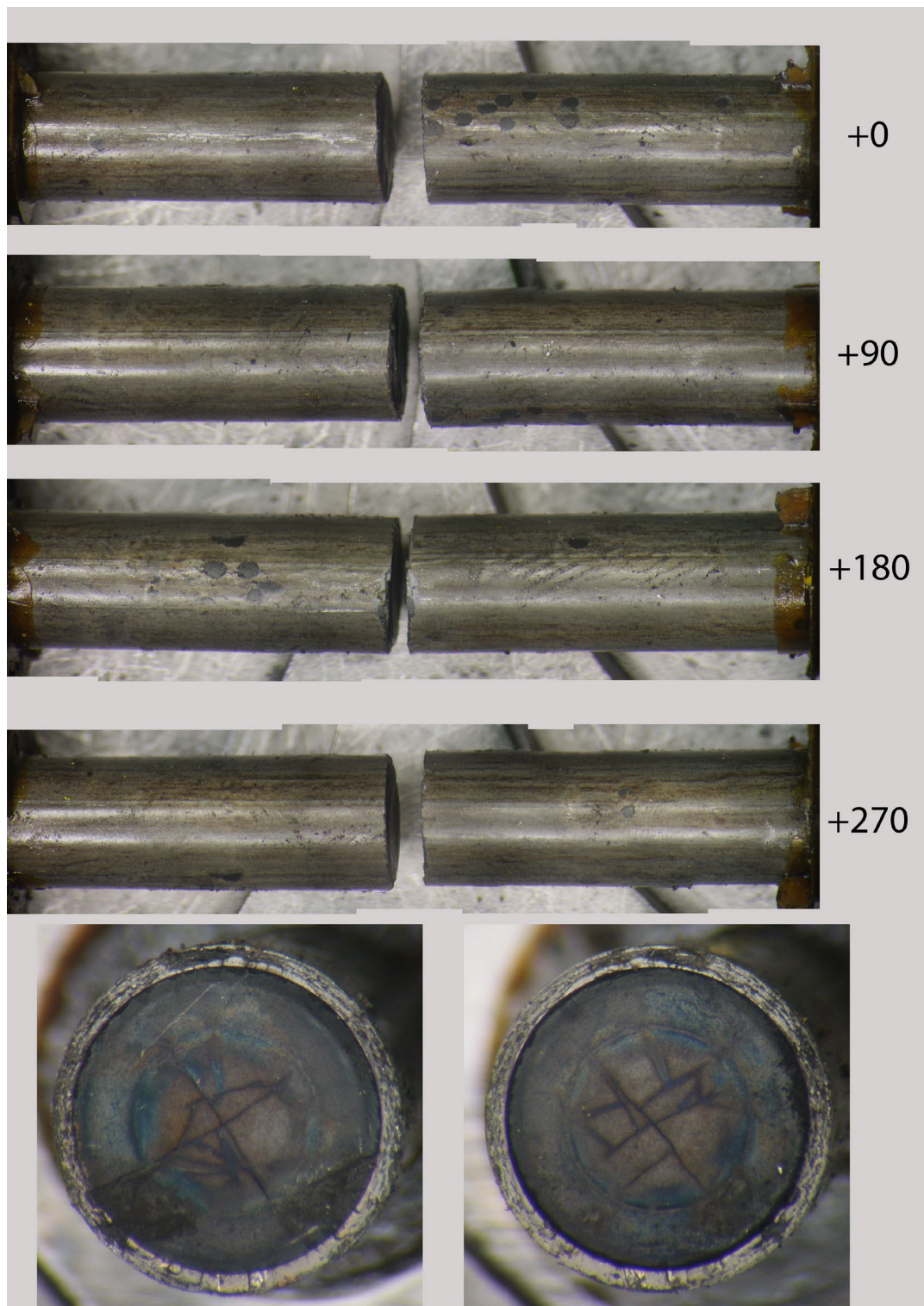


Figure F-22. 3F9N05-2710-2863 post-fatigue test condition.

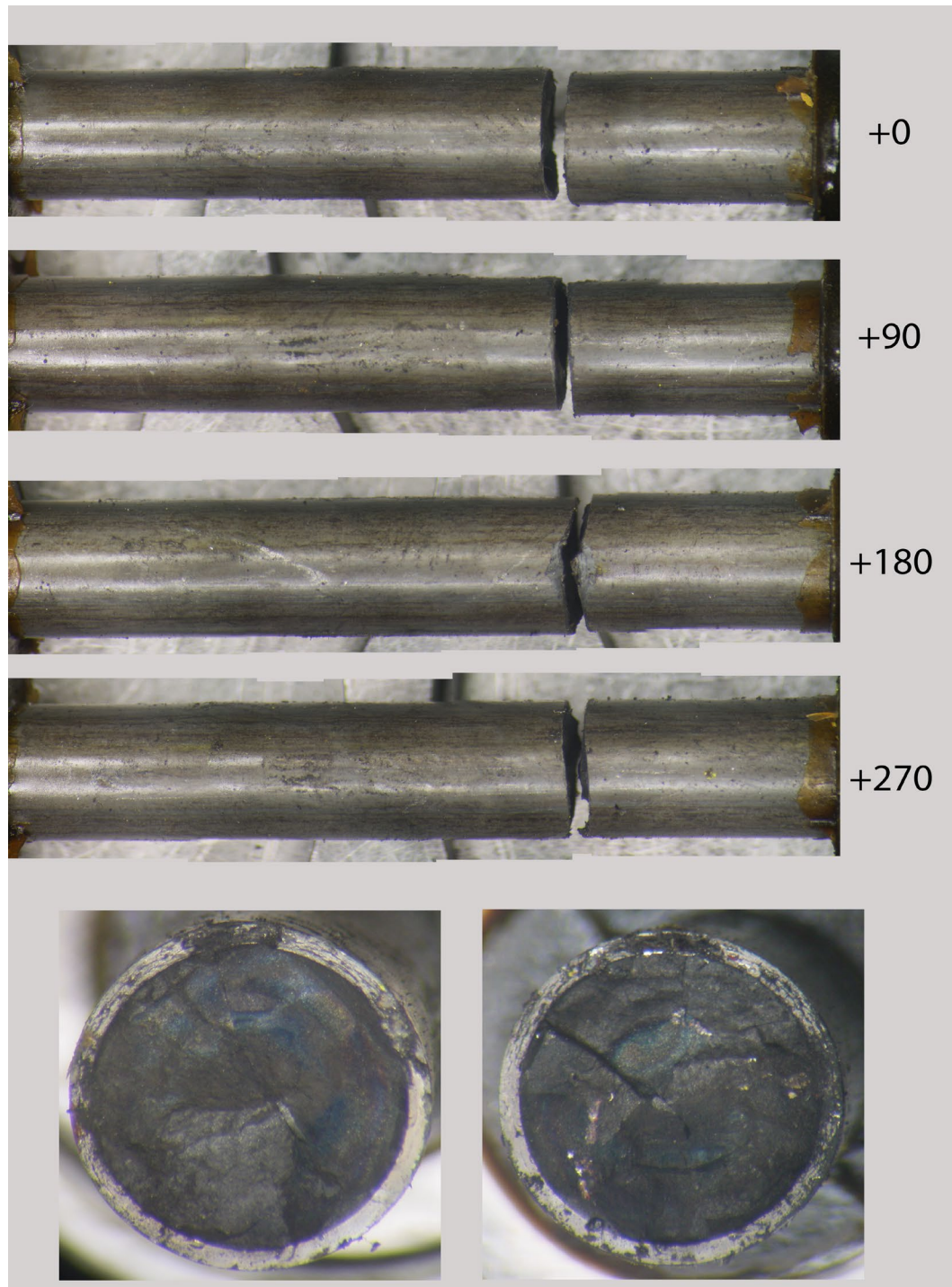


Figure F-23. 3F9N05-2329-2482 post-fatigue test condition.

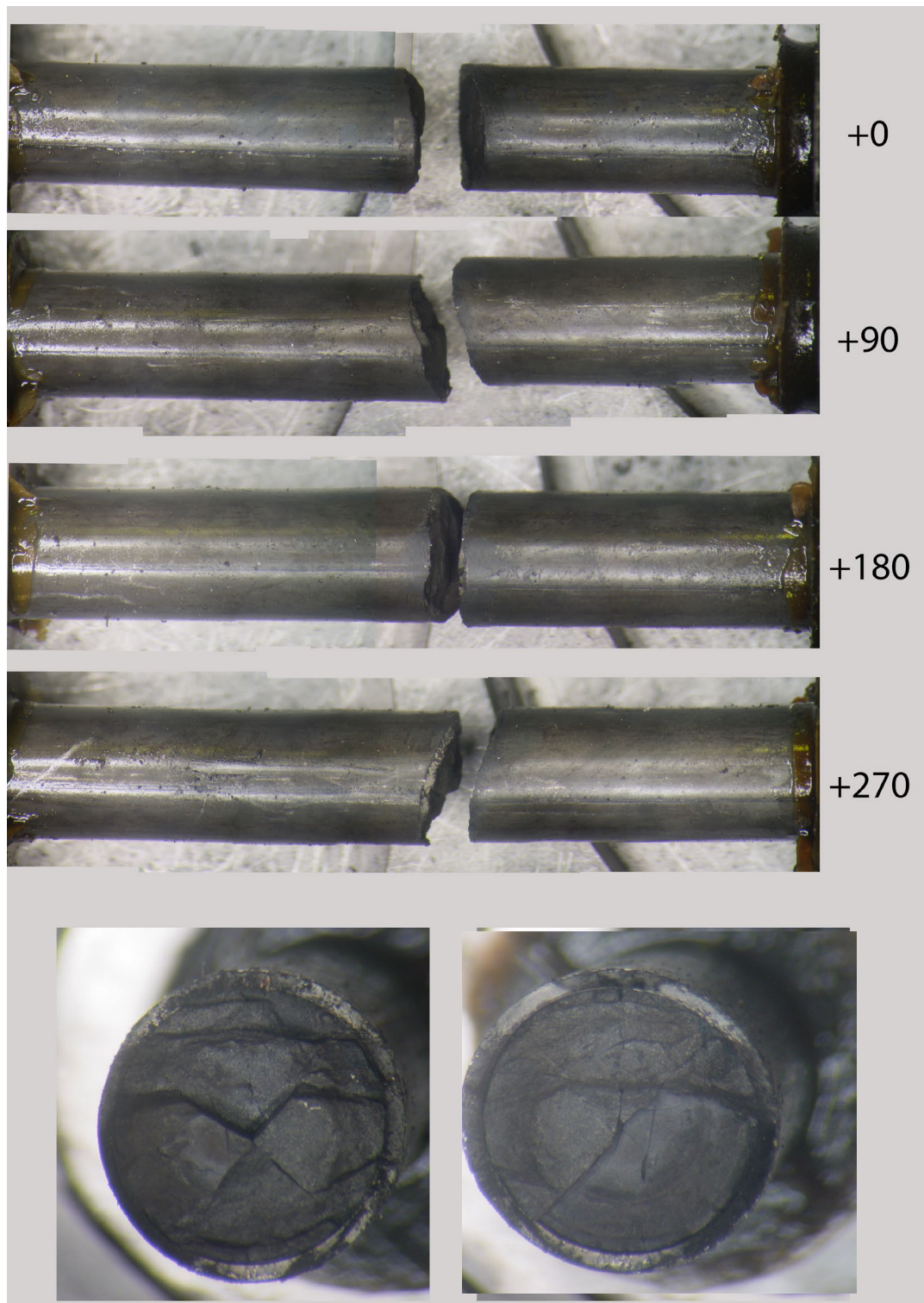


Figure F-24. 3F9N05-0719-0872 post-fatigue test condition.

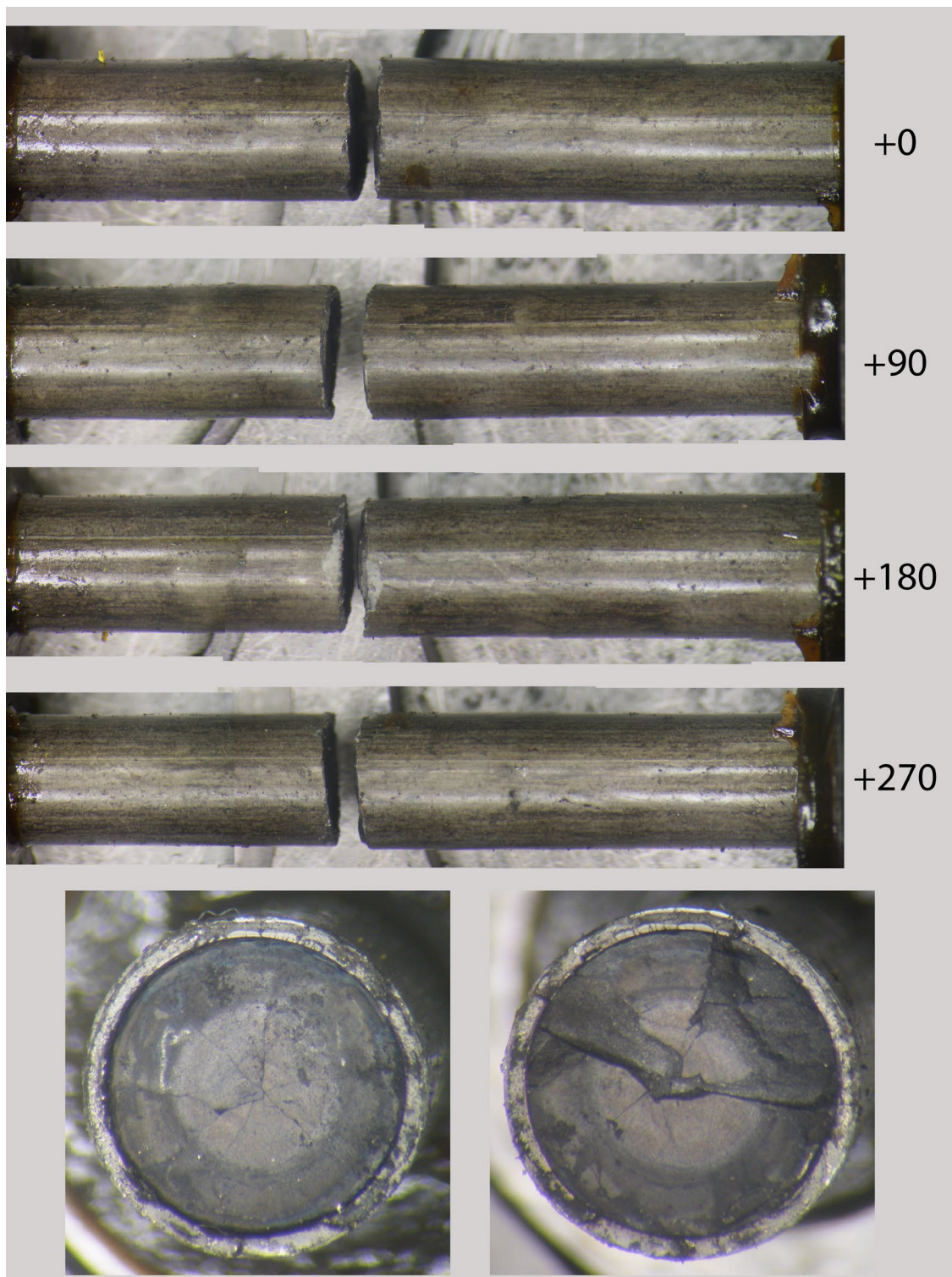


Figure F-25. 3D8E14-2963-3116 post-fatigue test condition.

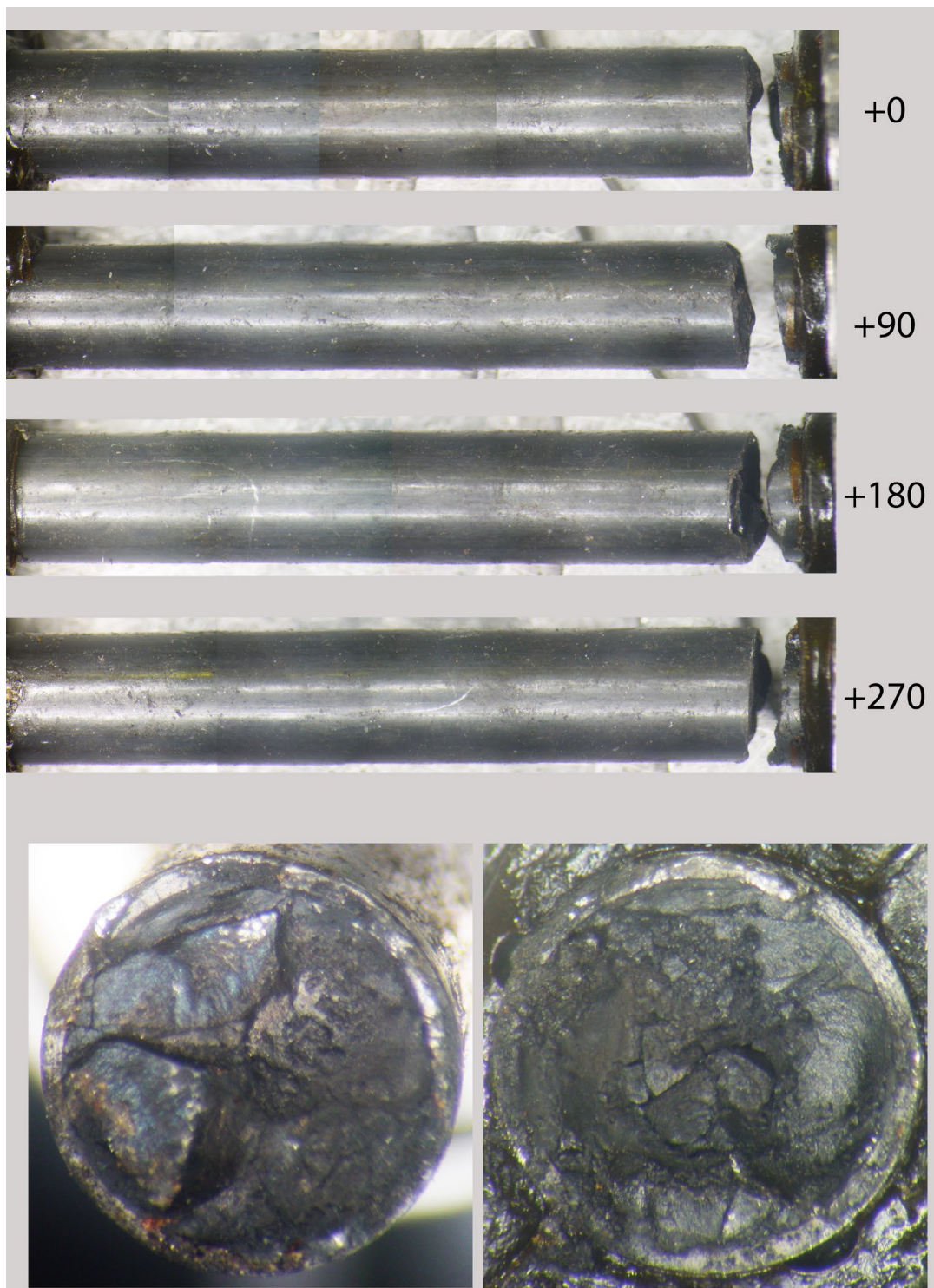


Figure F-26. 30AD05-2630-2783 post-fatigue test condition.

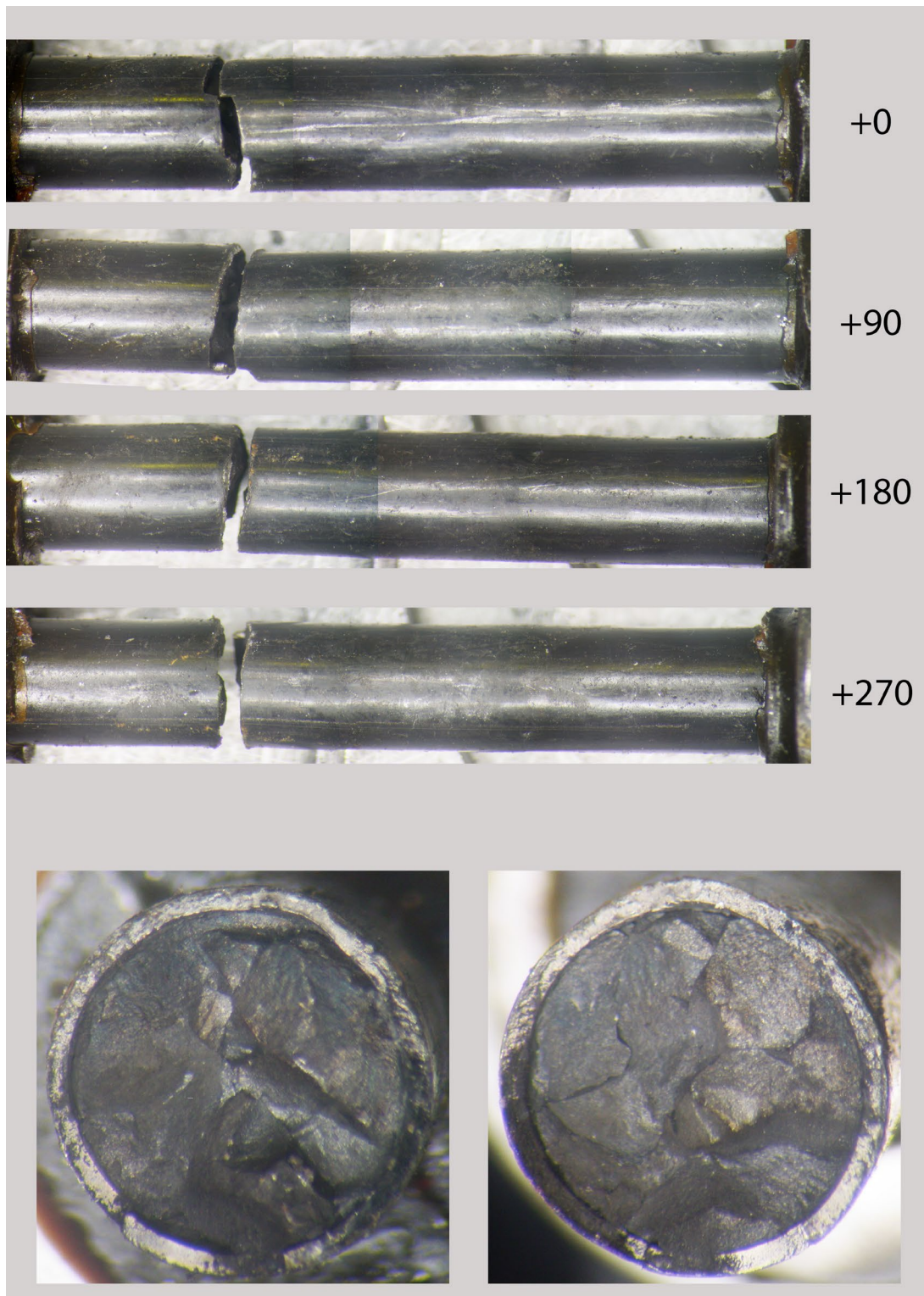


Figure F-27. 30AE14-0672-0825 post-fatigue test condition.

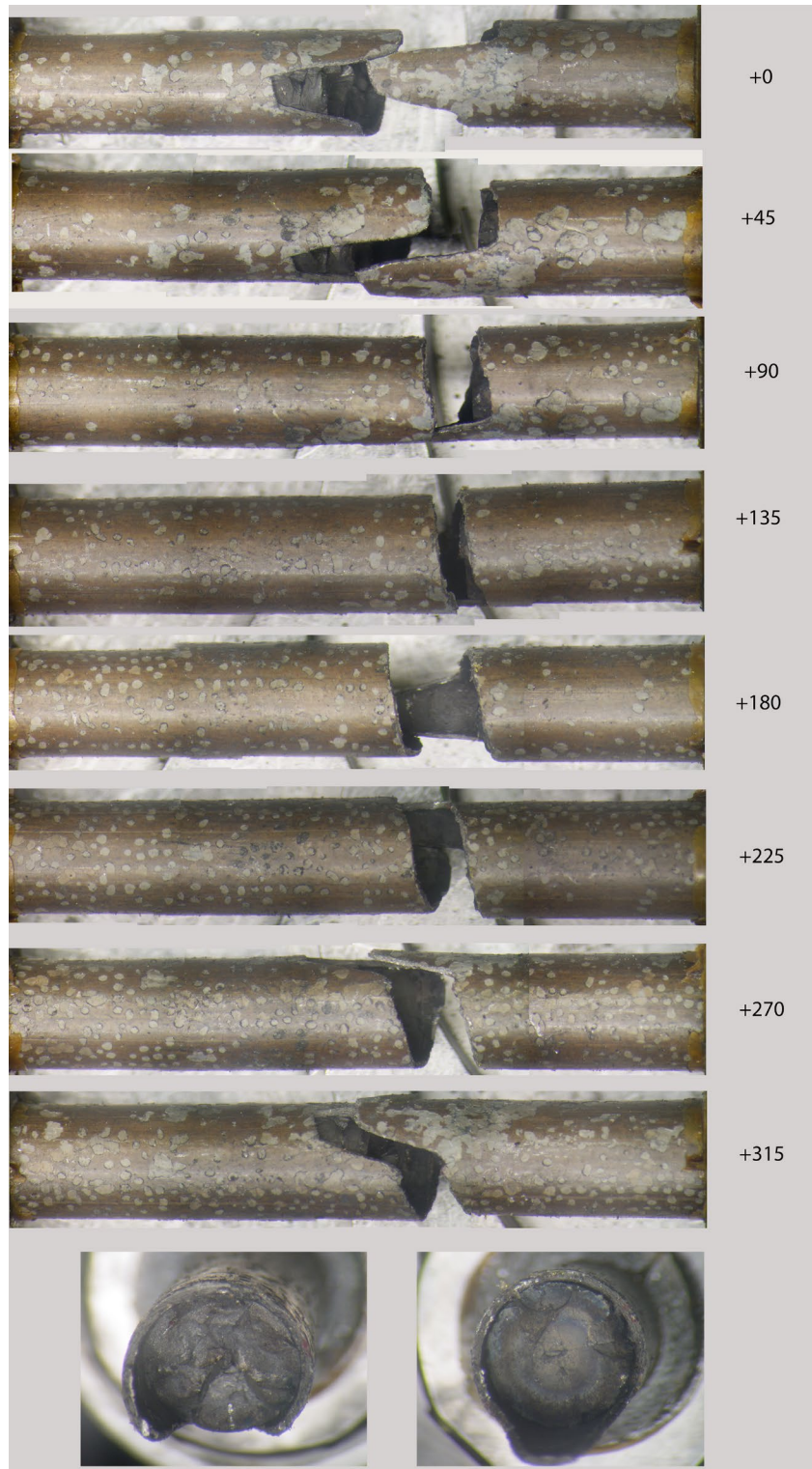


Figure F-28. F35P17-1855-2008 post-fatigue test condition.

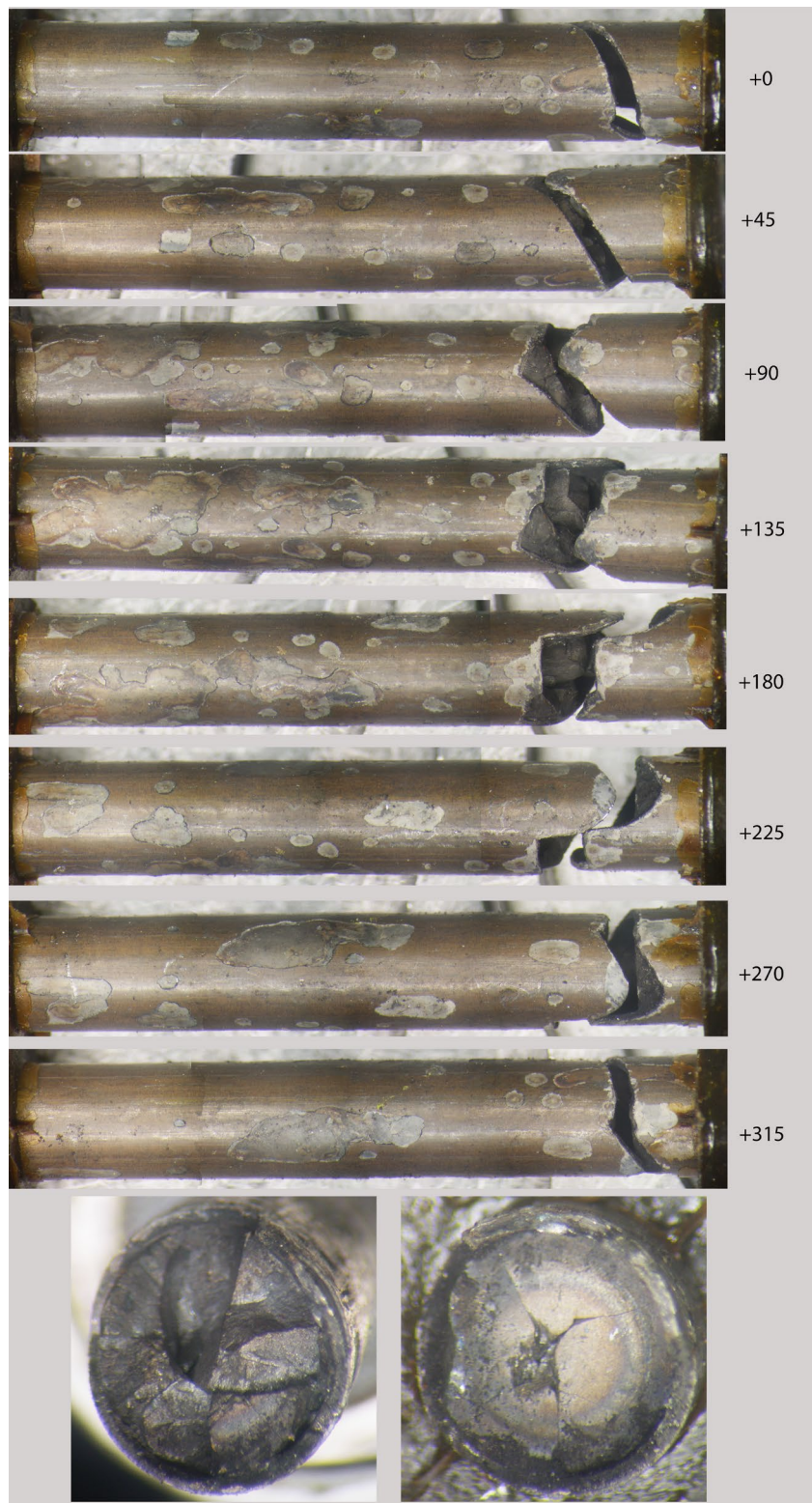


Figure F-29. F35P17-3159-3312 post-fatigue test condition.

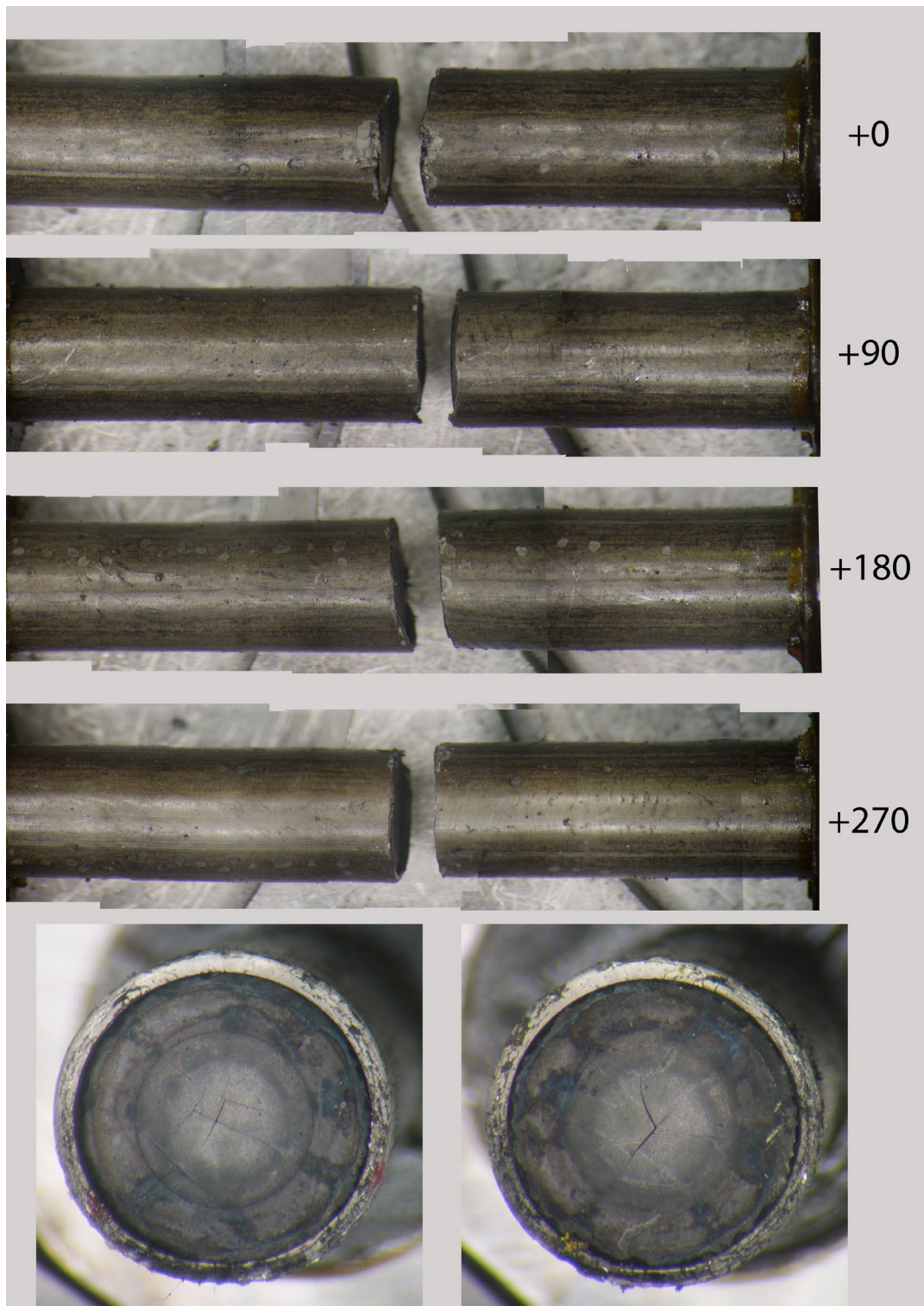


Figure F-30. 3A1F05-2025-2178 post-fatigue test condition.

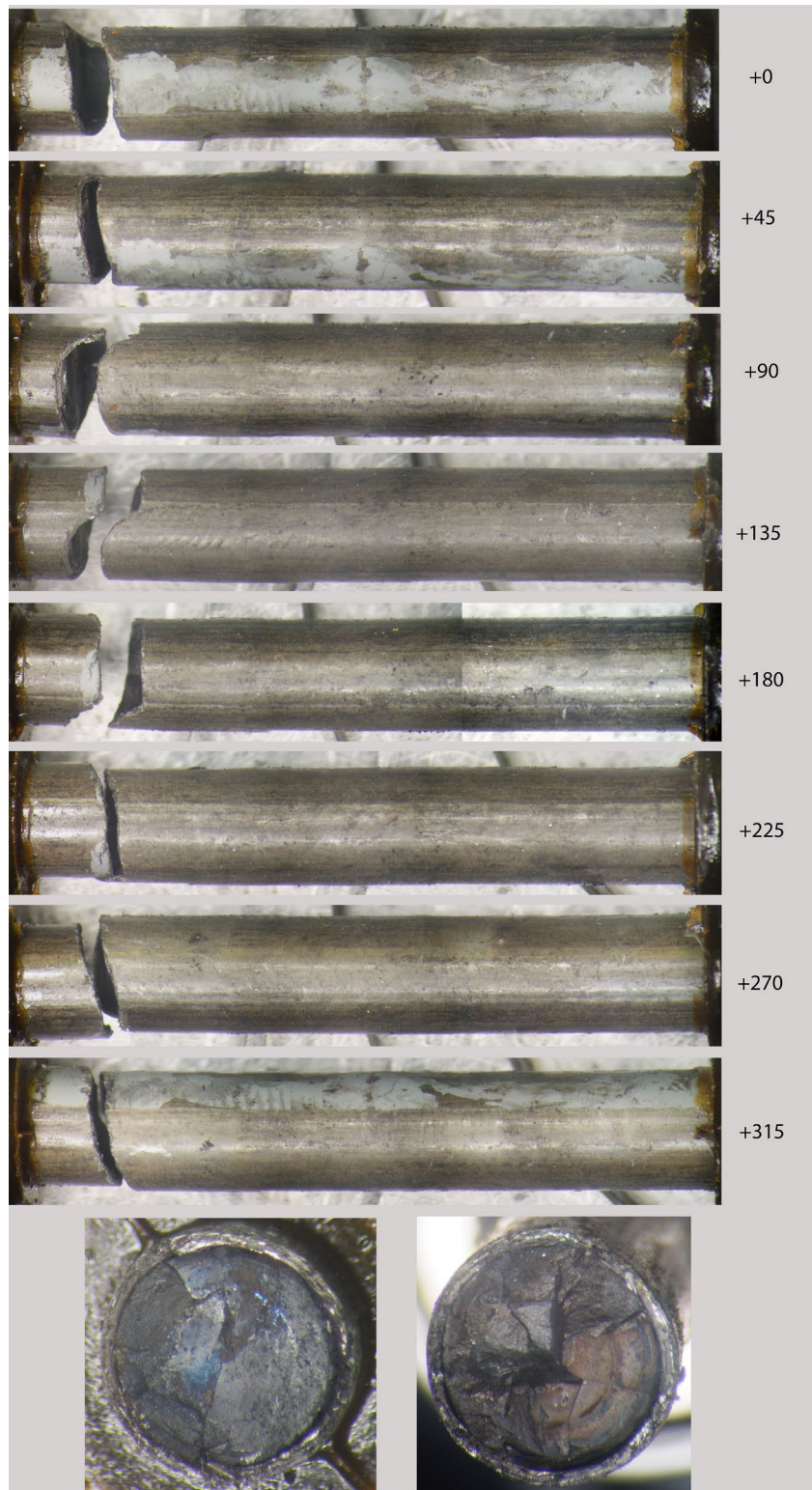


Figure F-31. 3A1F05-1853-2006 post-fatigue test condition.

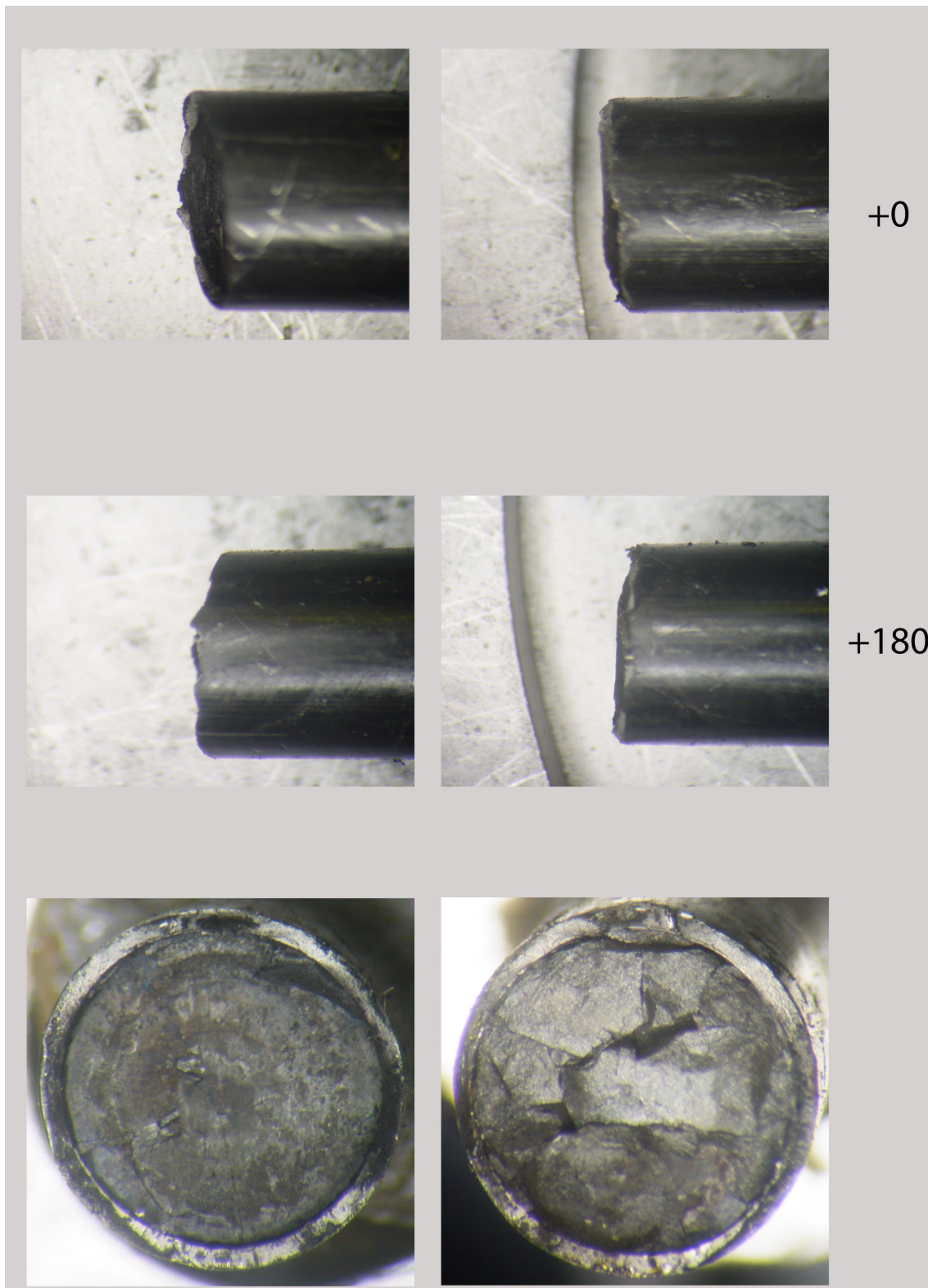


Figure F-32. 30AD05-0697-0850 post-fatigue test condition (broken ends only).

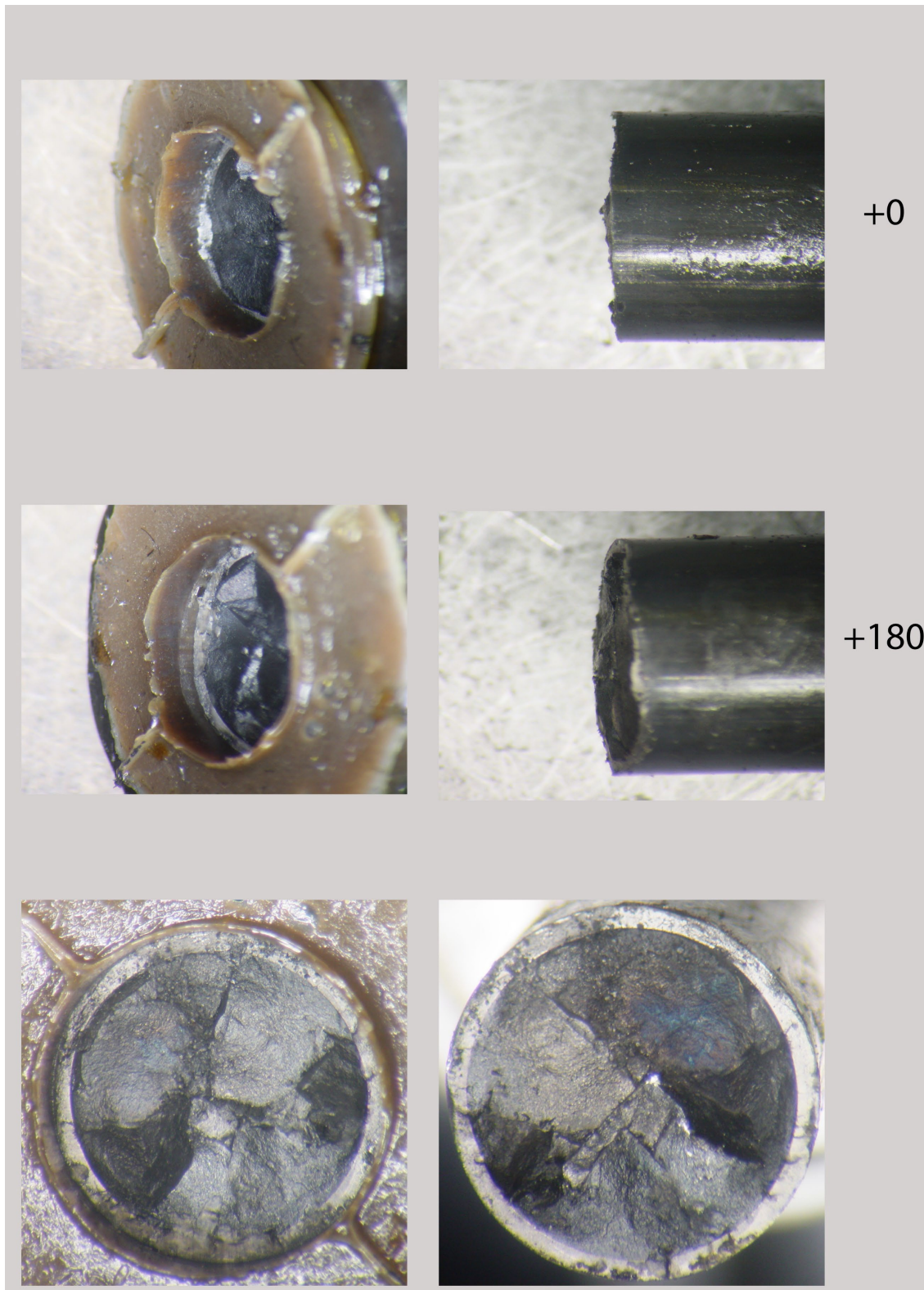


Figure F-33. 30AD05-2050-2203 post-fatigue test condition (broken ends only).

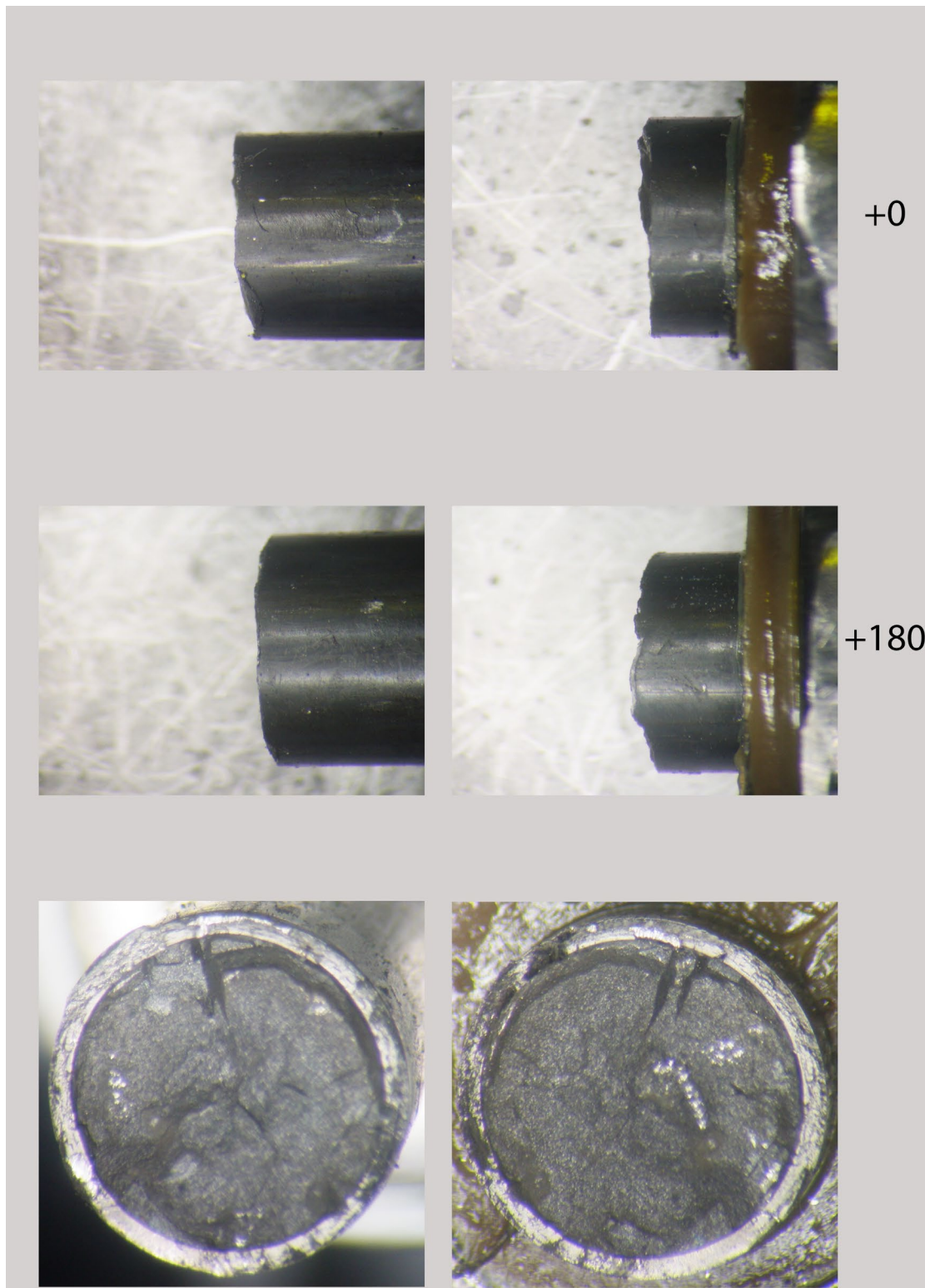


Figure F-34. 30AE14-2850-3003 post-fatigue test condition (broken ends only).

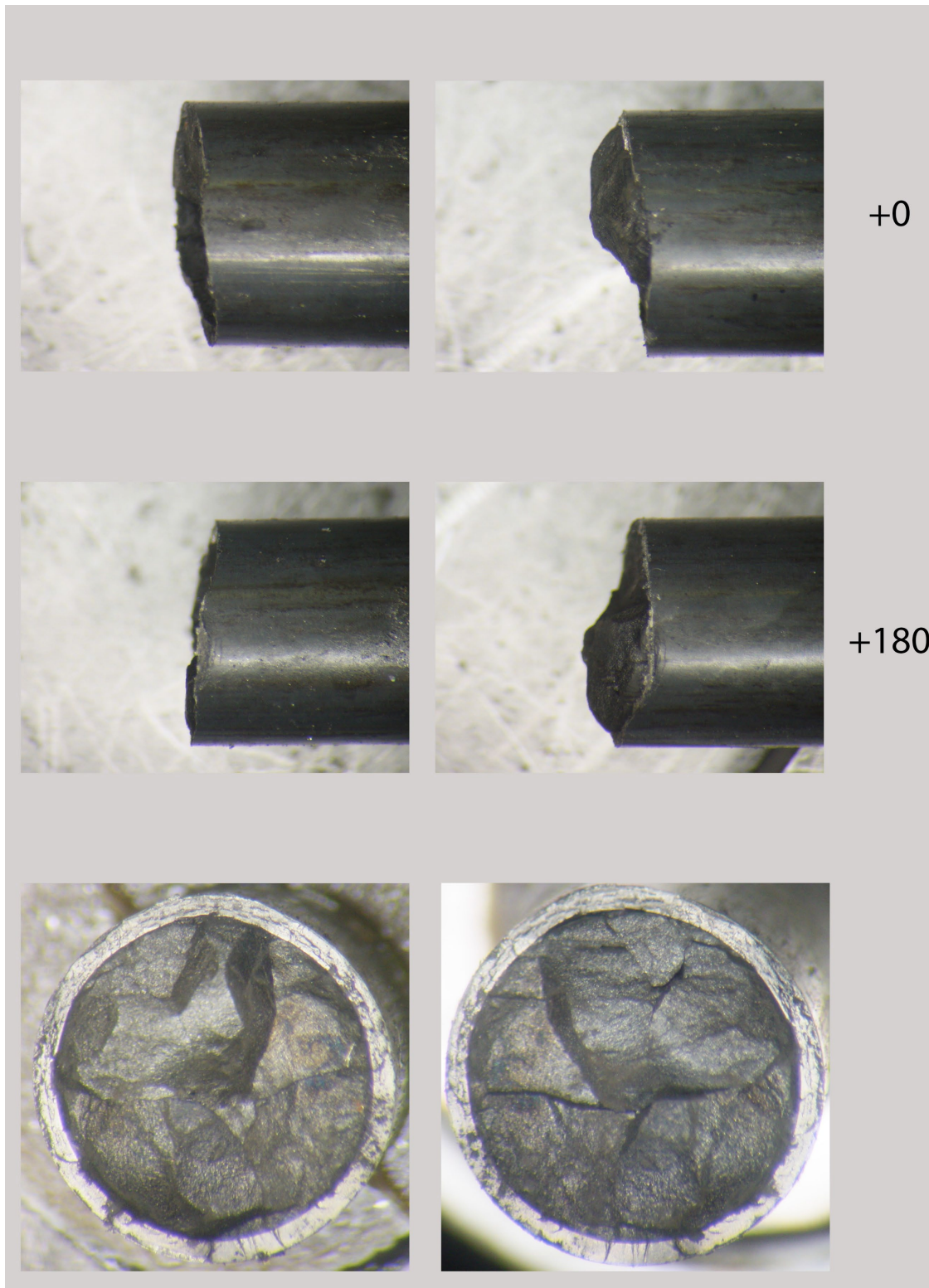


Figure F-35. 30AE14-3156-3309 post-fatigue test condition (broken ends only).

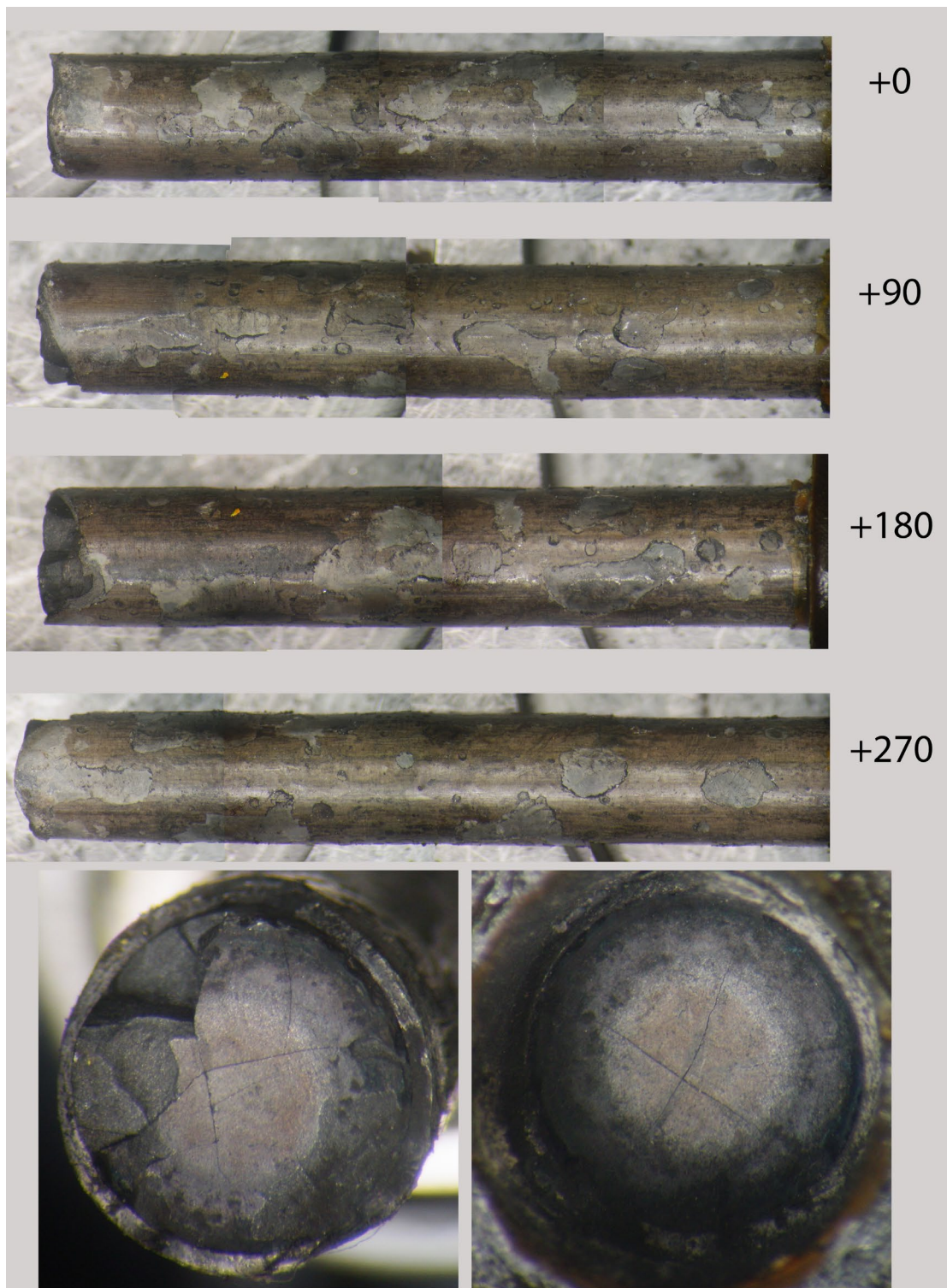


Figure F-36. 3A1F05-3214-3367 post-fatigue test condition.

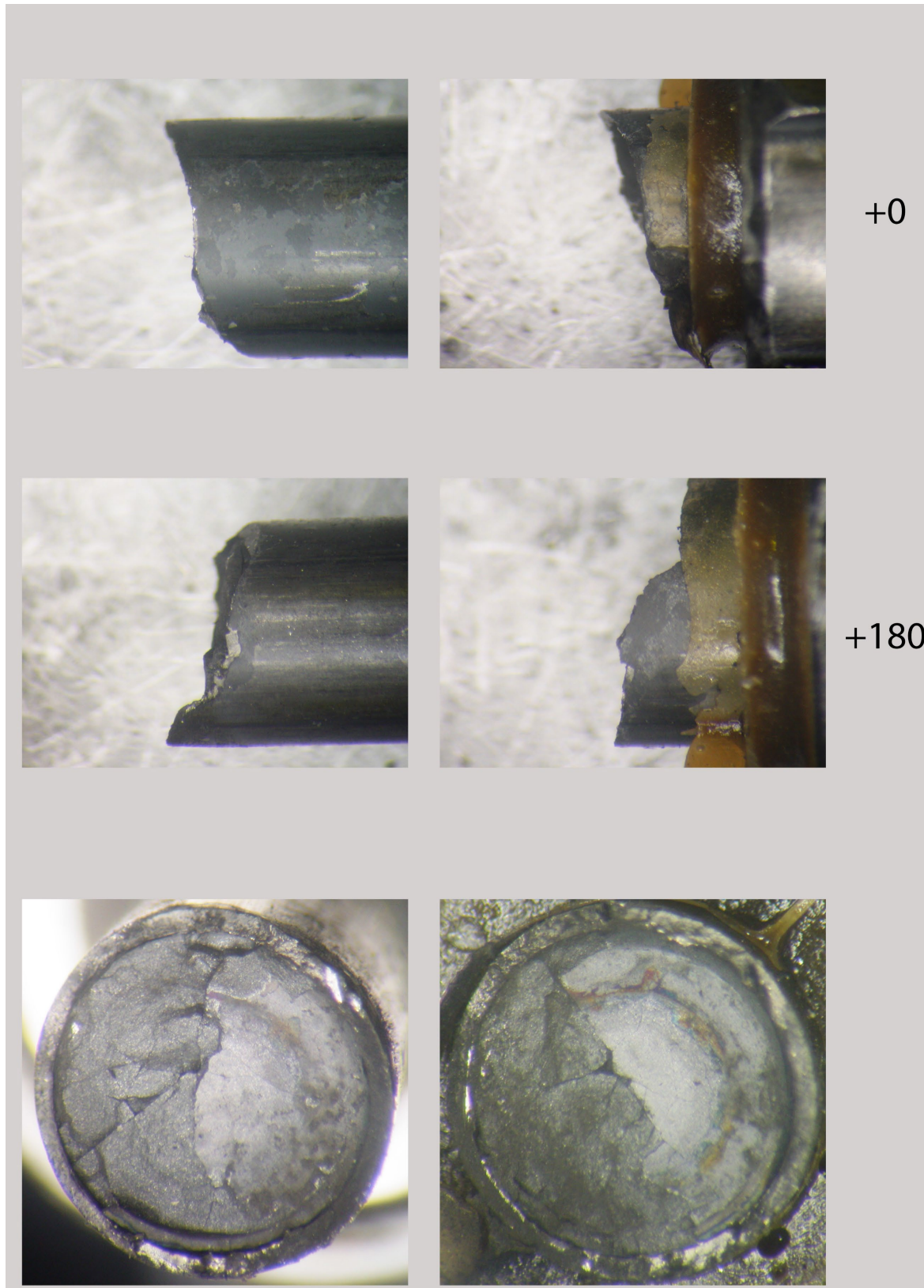


Figure F-37. 3D8E14-719-872 post-fatigue test condition.

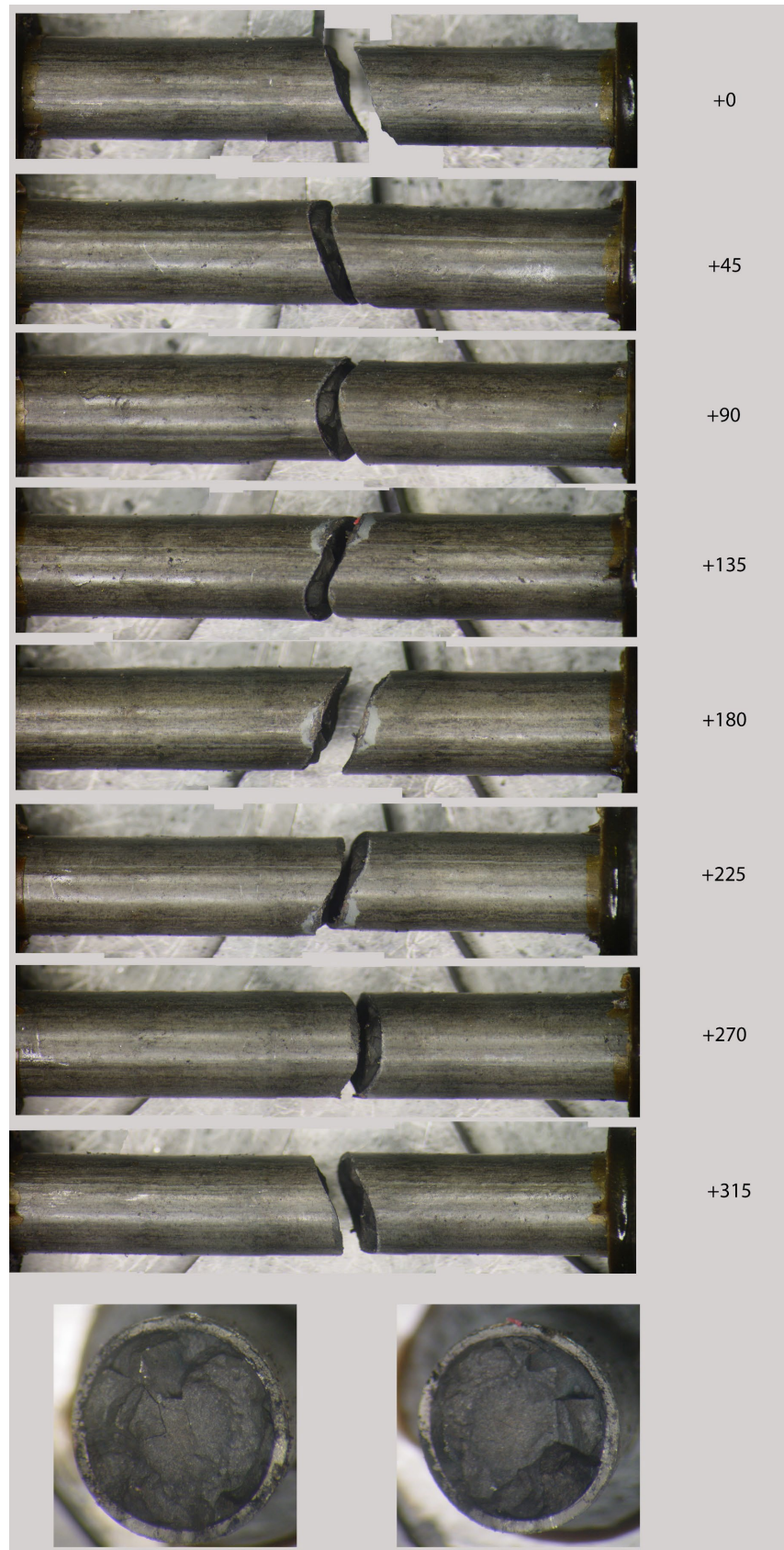


Figure F-38. 3D8E14-2412-2565 post-fatigue test condition.

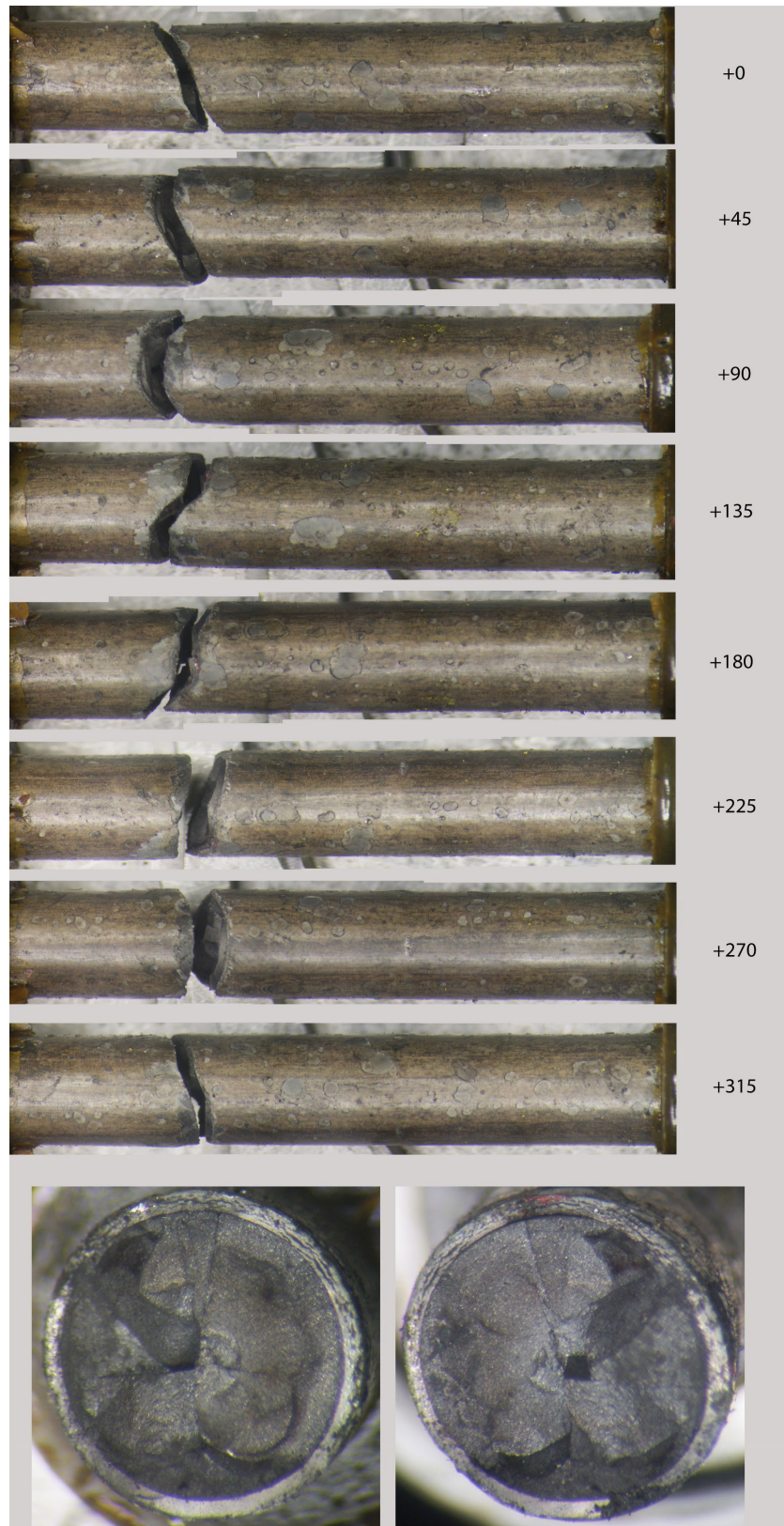


Figure F-39. 3A1F05-3367-3520 post-fatigue test condition.

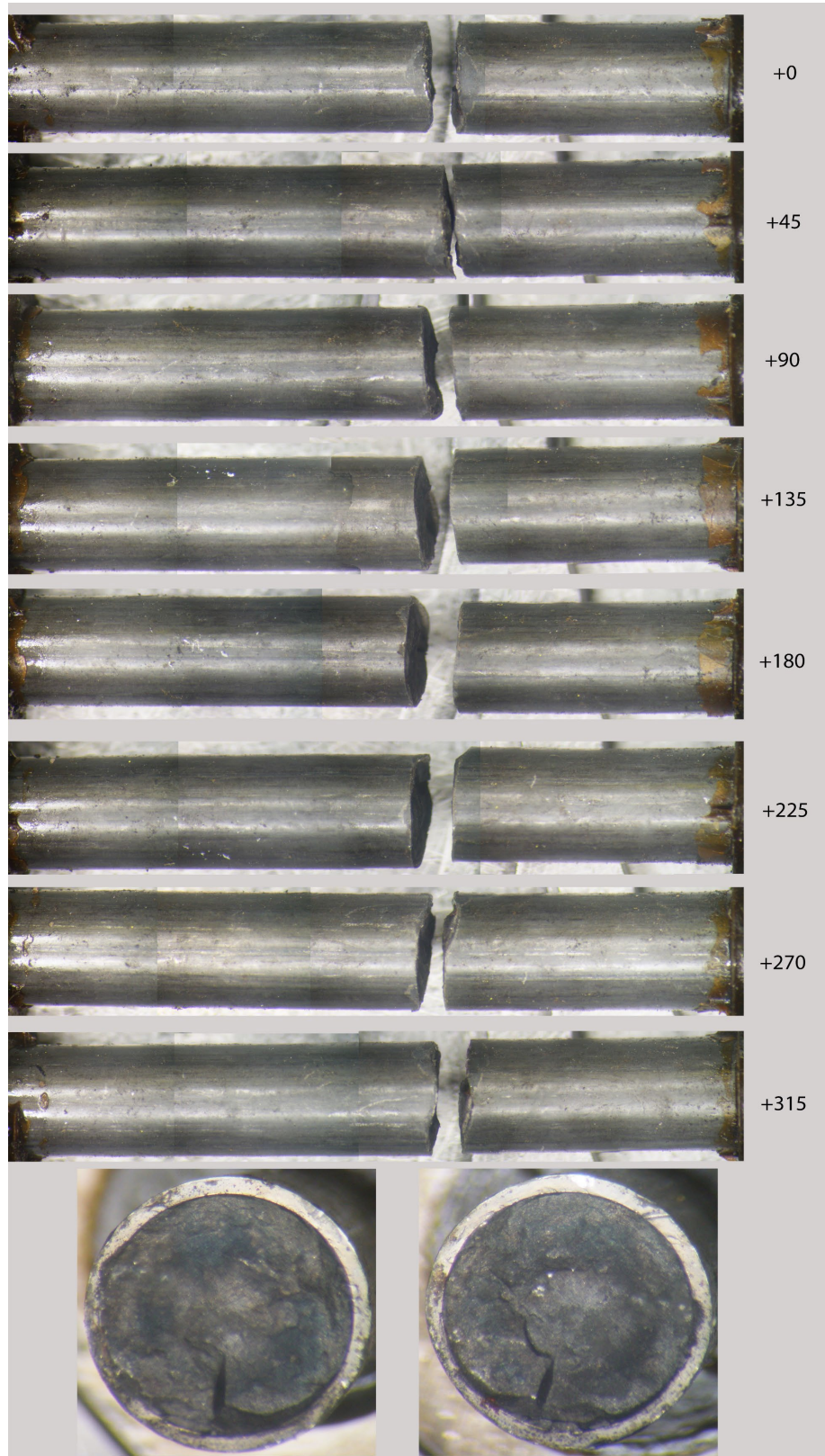


Figure F-40. 3D8E14-1178-1331 post-fatigue test condition.

F-8.5 Scanning Electron Microscope (SEM) Characterization of Selected CIRFT Fractures

To gain insight into the fatigue failure mechanism, the fracture surfaces of a subset of the samples are being evaluated using SEM. There are several goals for the SEM characterization: (1) to provide a more thorough investigation of the two specimens that failed at a lower-than-expected-number of cycles, (2) to determine whether surface features like oxide spalling are associated with fatigue initiation, (3) to further investigate the role of pellet discontinuities causing stress concentration and pellet-clad bonding, (4) to determine the direction of fracture (from waterside to pellet-side, or vice versa), (5) to further investigate the role of precipitated hydrides in the fracture, and (6) to characterize the mode of fracture (brittle or ductile) and identify accessible materials. A list of potential failed rods for characterization is provided in Table F-13. Fractography of two samples that failed between 40,000 and 50,000 cycles (applied strain amplitudes were 0.15% and 0.18%) are reported herein and are highlighted in Table F-13.

In addition, fractography of two unirradiated cladding-only CIRFT specimens are documented herein to better understand how failure occurs without the presence of the pellet, which will provide a reference for the fractography on the failed fuel rods. The two samples reported herein failed between 30,000 and 100,000, which is comparable to the fuel rods characterized, though the applied strain amplitudes were larger (0.40% and 0.46%).

Finally, future work for next year is described that will investigate the role of precipitated hydrides in the fracture.

Table F-13. CIRFT Specimens Identified for Potential SEM Characterization.

Samples highlighted with shading have been started and those in **bold** have been completed.

| Cladding material | CIRFT Specimen ID | Estimated specimen-average burnup (GWd/MTU) | Cycles to failure | Strain Amplitude (%) | Status |
|-------------------|-------------------------|---|-------------------|----------------------|-----------------|
| M5 | 30AD05-0697-0850 | 58 | 3,368 | 0.47 | Not started |
| M5 | 30AD05-2050-2203 | 59 | 133,000 | 0.08 | Not started |
| M5 | 30AD05-2630-2783 | 59 | 22,300 | 0.18 | Started |
| M5 | 30AE14-0672-0825 | 56 | 1,630 | 0.36 | Not started |
| Zirc-4 | F35P17-2027-2180 | 66 | 1,340,000 | 0.07 | Not started |
| Zirc-4 | F35P17-3159-3312 | 62 | 773 | 0.15 | Not started |
| LT Zirc-4 | 3A1F05-3214-3367 | 48 | 3,450 | 0.19 | Not started |
| LT Zirc-4 | 3A1F05-1853-2006 | 56 | 1,300 | 0.39 | Not started |
| LT Zirc-4 | 3A1F05-2025-2178 | 56 | 48,200 | 0.18 | Complete |
| ZIRLO | 3D8E14-2412-2565 | 64 | 191,000 | 0.08 | Started |
| ZIRLO | 3D8E14-2963-3116 | 62 | 39,700 | 0.15 | Complete |
| ZIRLO | 3F9N05-2329-2482 | 59 | 189,000 | 0.10 | Not started |
| ZIRLO | 6U3K09-2310-2463 | 59 | 1.75E+04 | 0.20 | Started |
| ZIRLO | 6U3K09-3200-3353 | 50 | 3.49E+04 | 0.15 | Not started |

F-8.5.1 Sample preparation

A CIRFT fueled specimen is prepared in the hot cell for SEM characterization by cutting the tip off of one side of the fractured specimen. The cut is made a few millimeters from the fractured end, and the sample is then defueled. The sample is then attached to a metallic mount using conductive adhesive, avoiding the fracture surfaces. After curing, the sample is transferred out of the hot cell to the SEM enclosure. Once in

the SEM, a montage of the entire circumference is created at a relatively low magnification ($\sim 25\times$). The circumference is divided into four quadrants to allow for imaging and identifying regions of interest.

The CIRFT unirradiated cladding specimens were similarly prepared out of cell but were able to be inserted directly in a mounting fixture rather than being attached to a metallic mount with conductive adhesive.

F-8.5.2 Characterization of Fracture in ZIRLO- 17×17

To provide a baseline characterization, a ZIRLO-clad sister rod that fractured as expected and with a fatigue lifetime consistent with other data (3D8E14-2963-3116) was sectioned, SEM-imaged, and characterized. Optical images of this sample are provided in Figure F-25 and Figure F-41. This sample failed near the center of the CIRFT test gauge section, and its fatigue life (39,700 cycles) was consistent with previous test data.

The most distinct feature of 3D8E14-2963-3116's fracture surface is in the upper part of quadrant 1 near the boundary with quadrant 4. At the end of each CIRFT test, the specimen must be removed from the CIRFT machine. Often, the specimen has not fractured completely, and the fracture must be manually completed in order to remove it from the CIRFT machine. An area in quadrant 1 was likely created after the fatigue test was stopped, during removal of these dogbone specimen from the test equipment. At higher magnification (Figure F-42), the features near the center of the cladding wall have a classic ductile dimple appearance, further suggesting that the fracture surface was created as the specimen was removed from the equipment rather than during the fatigue test. In contrast, the features in quadrant 1 near the cladding ID appear to be more brittle, with ratchet lines typical of fatigue, thus indicating that these features were created during the fatigue test.

In quadrant 3, shown in Figure F-43 ($\sim 180^\circ$ from the quadrant 1 region), the features are flat compared to those in quadrant 1. This is likely the quadrant where the fatigue crack first initiated, and then wear of the surfaces progressed as the test continued. High magnification of one area in quadrant 3 shows ratchet lines emanating from the cladding ID surface, suggesting that the fatigue crack initiated on the ID in this region.

The high magnification images from quadrants 2 and 4 both show remnants of fatigue crack propagation in the form of fatigue striations (see Figure F-44 and Figure F-45). These images also show indications of circumferential cracks in both quadrants, which may be associated with propagation of the crack along precipitated hydrides. The flat area on the cladding ID in quadrant 4 may be a fatigue crack initiation site.

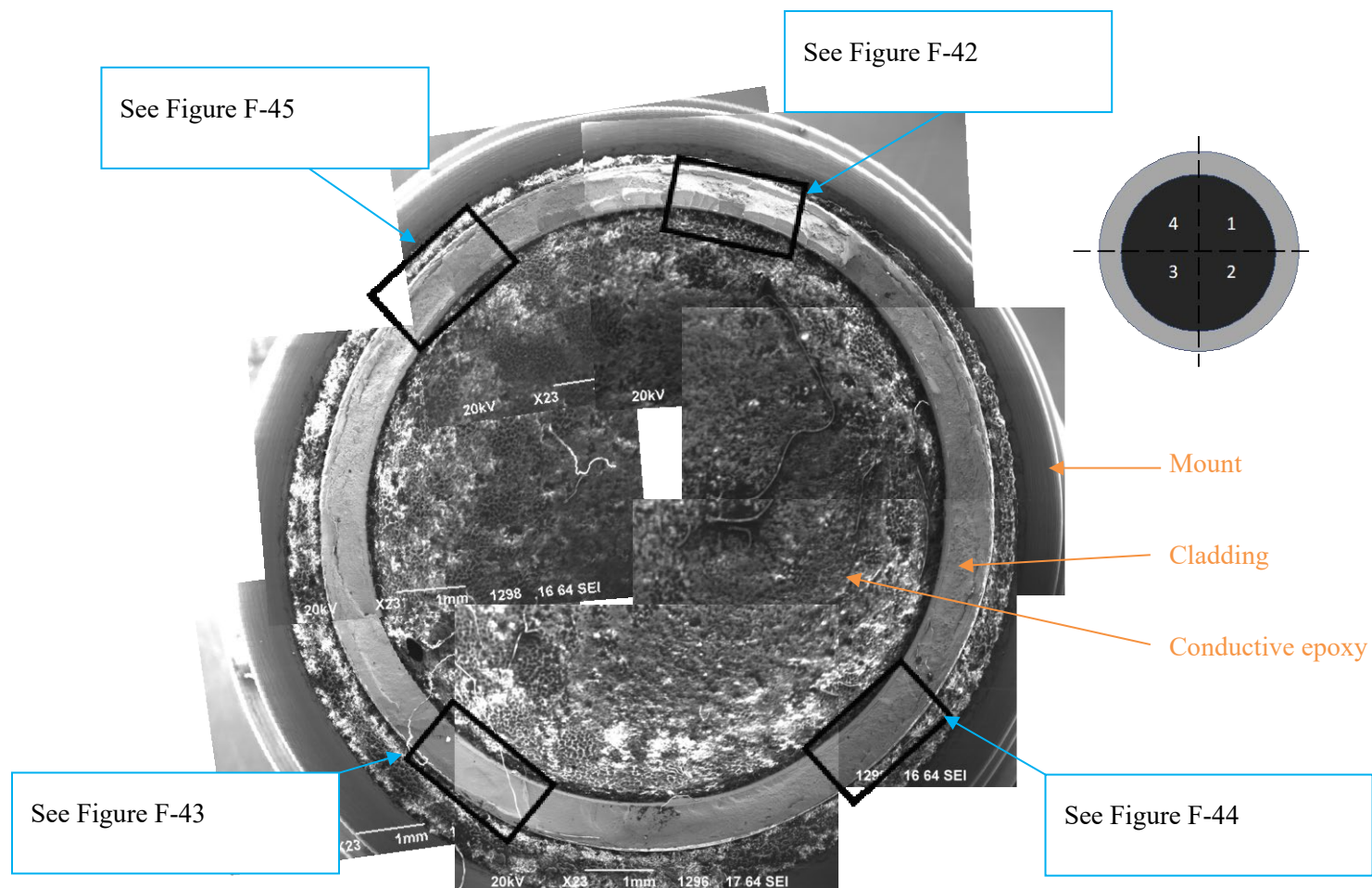


Figure F-41. 23× montage of the surface of the fatigue failure in sample 3D8E14-2963-3116. The areas identified in the various quadrants were investigated at higher magnification (see Figures F-42 to F-45).

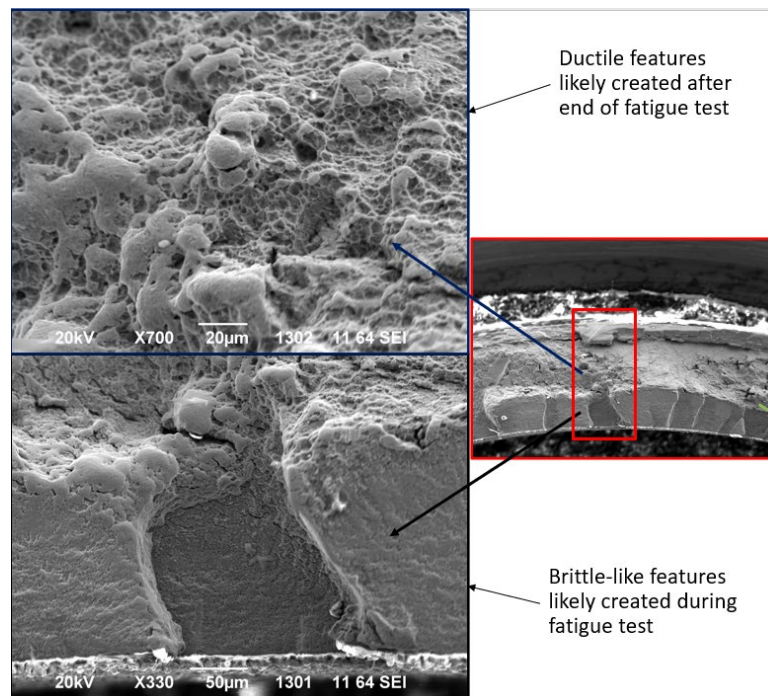


Figure F-42. 330× and 1,000× images of quadrant 1 in sample 3D8E14-2963-3116.

Quadrant – 3

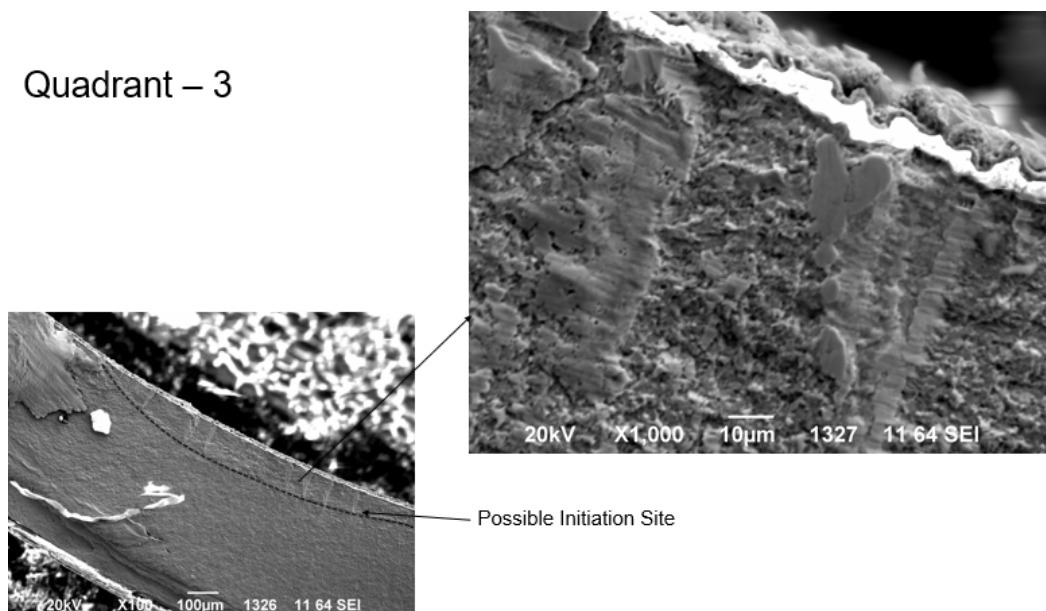


Figure F-43. 100× and 1,000× images of quadrant 3 in sample 3D8E14-2963-3116, approximately 180° from region in quadrant 1, that is suspected to have failed after fatigue test ended.

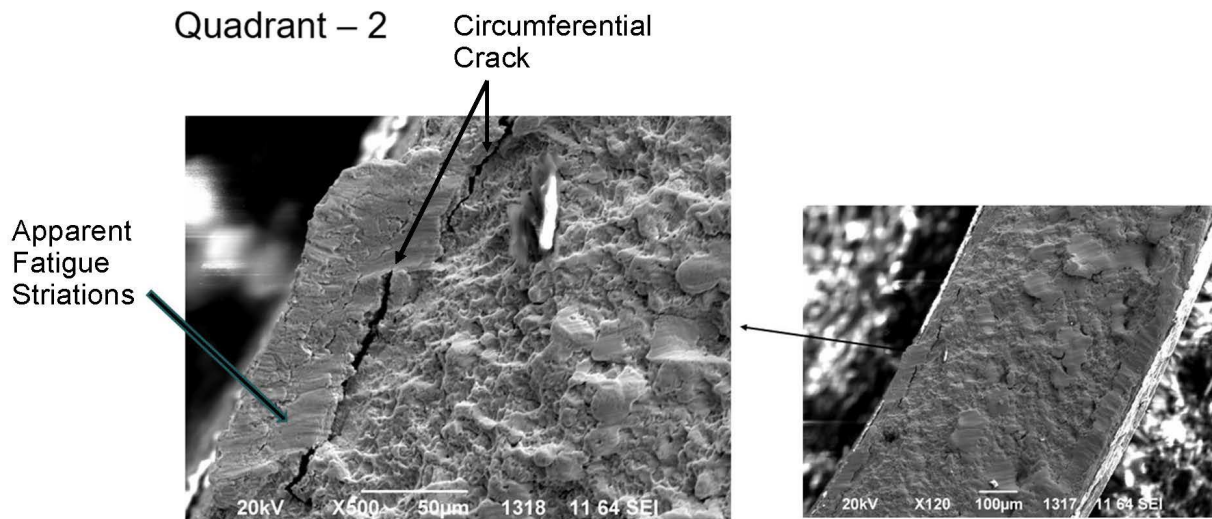


Figure F-44. 120× and 500× images of quadrant 2 in sample 3D8E14-2963-3116, showing signs of fatigue striations typical of fatigue crack propagation, indicating propagation in the circumferential direction.

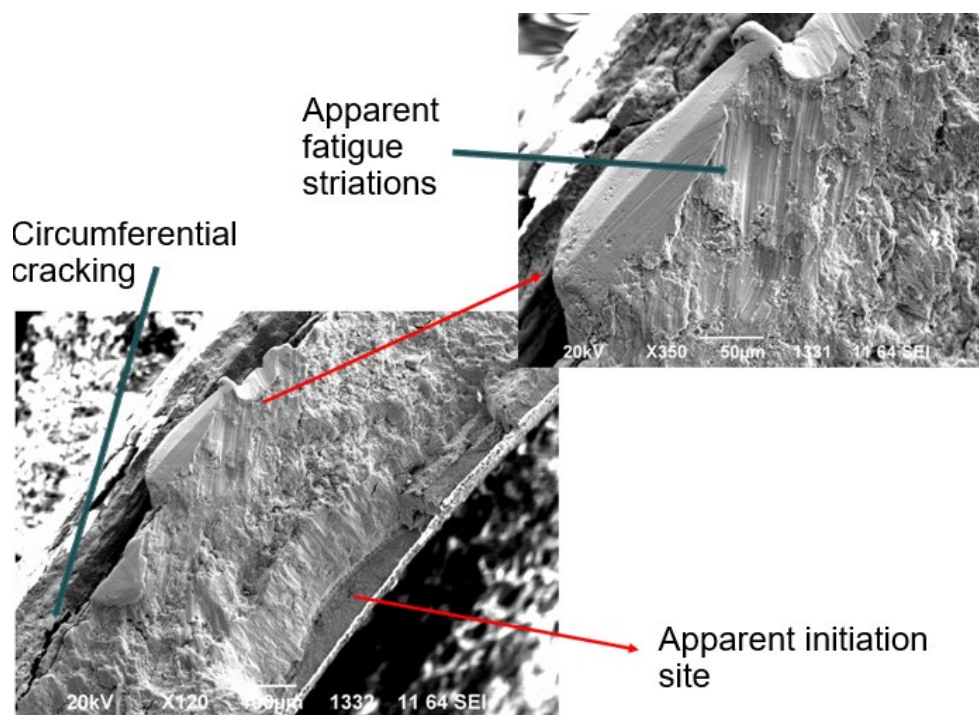


Figure F-45. 120× and 350× images of quadrant 4 in sample 3D8E14-2963-3116 showing signs of fatigue striations typical of fatigue crack propagation. The flatness of the feature on the cladding ID may be associated with fatigue initiation. There are also circumferential cracks near the cladding OD that may be associated with hydrides.

F-8.5.3 Characterization of Fracture in LT Zirc-4 Fuel Rods

Figure F-30 and Figure F-46 provide the optical images of sample 3A1F05-2025-2178 (DE50017) after failure. Figure F-46 is a montage of the failed surfaces of 3A1F05-2025-2178 taken at 100× magnification around the fracture surface. Various regions of interest were identified from the montage for further imaging at higher magnification. This sample was failed under medium load at a pellet-pellet interface, near the center of the CIRFT test gauge section, and its fatigue life (48,200) was consistent with previous test data. The fatigue initiation appears very close to fatigue failure, as can be observed from the moment vs. curvature data.

The montage is divided into 4 quadrants (Q1, Q2, Q3 and Q4). From a simple observation in the montage, Q2 appears relatively flat and has no visible circumferential cracks, which are most often seen due to precipitated hydrides. Q4, like Q2, has flat brittle or cleavage-like areas that appear to be crack initiation sites on the ID; these are similar to those seen in sample 3D8E14-2963-3116 as reported in the last FY.

Figure F-47 and Figure F-48 show two different regions in Q1. Whereas Q1 has areas of ductile fractures and circumferential cracks, there are cleavage like regions approaching Q2 that are indicative of brittle behavior. The features continue in Q2, as shown in Figure F-49, where many of these crack initiation features (termed “beach marks”), including cleavage like regions adjacent to fatigue striations, can be observed. There was an absence of ductile fracture regions in Q2. Figure F-49 also shows a different type of feature appear to be flat but with long running striations that did not quite match the fatigue striations seen elsewhere. This is thought to be formed by wear because the fractured rod continues a few cycles during and after propagation.

Figure F-50. shows the ductile fracture regions in Q3, along with long running circumferential cracks that were prominent between small brittle regions, and beach marks that are similar to the features seen in Q1 (Figure F-47).

Figure F-51 shows the flat brittle or cleavage like regions seen in Q4. The flat regions look similar to the brittle fracture regions seen in Q2 which are associated with fatigue failure. It is also important to note that the brittle regions, where the fatigue failure likely initiated can be seen on the fuel side of the sample. This points towards stress concentrations that were acting on this side of the cladding because of the fuel pellet. Thus, it can be stated that the pellet does play a role in the fatigue process and acts as a source for the initiation.

Although the fracture surfaces were marked as Q1, Q2, Q3 and Q4, the actual regions can be divided as brittle fracture regions where the fatigue crack initiated, ductile fracture regions corresponding to a low cycle fatigue propagation, or regions of failure caused at the end of the test when the sample was failed manually for removal from the CIRFT. The closeness in texture seen in the opposite quadrants also helps illustrate how the fatigue failure might have initiated, propagated, and failed. Thus, from Figure F-47, Figure F-49, Figure F-50. and Figure F-51, it can be inferred that crack initiation occurred on the ID in both Q2 and Q4 but that the crack propagation started in Q2, slowly at first, creating the large flat region in Q2, and then increasing in velocity through regions in Q1 and Q3 towards Q4, creating a rougher crack surface with some indications of ductile failure where final failure occurred.

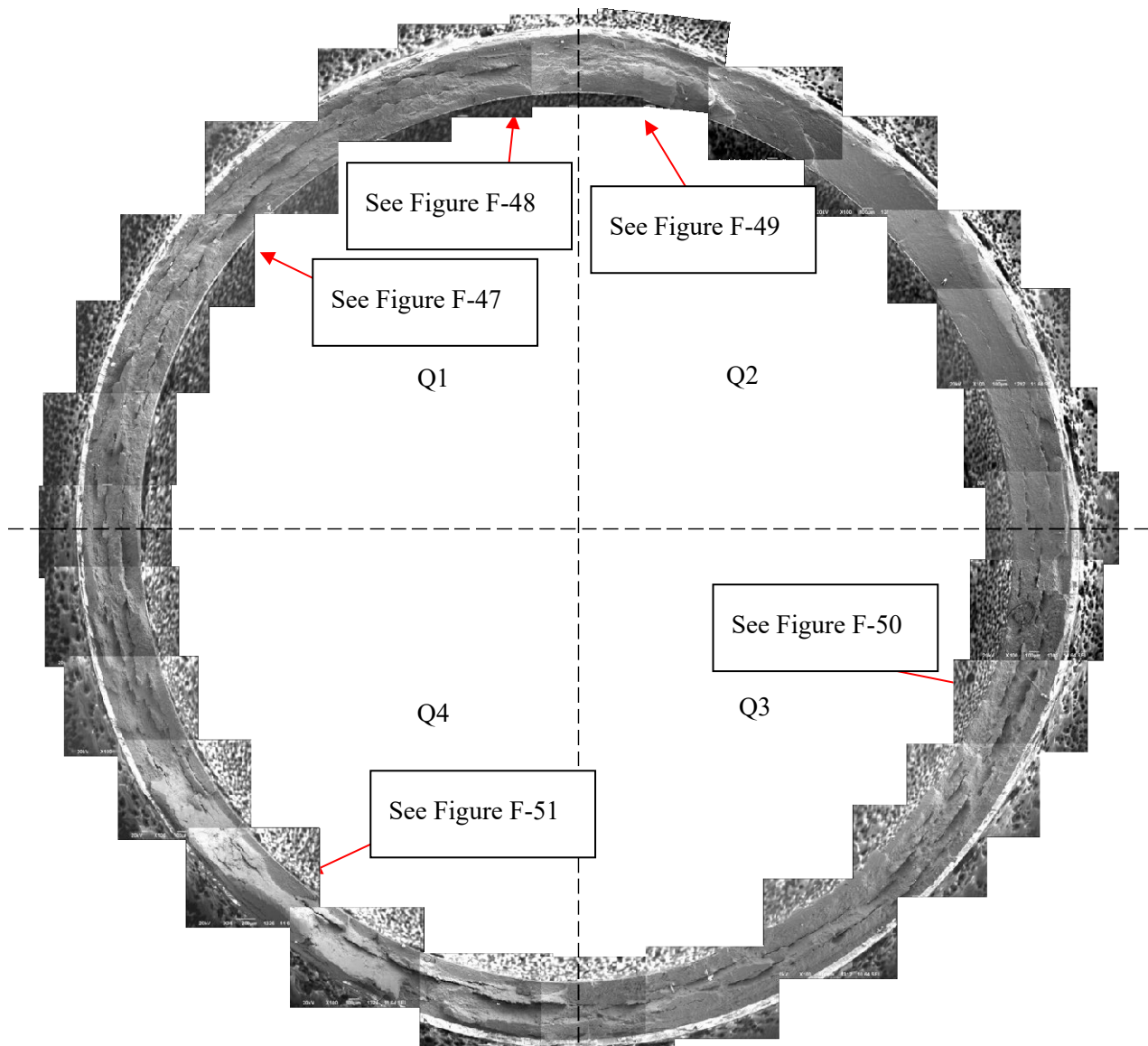


Figure F-46. 100X montage of the surface of the fatigue failure in dogbone sample DE50017. The areas identified in the various quadrants were investigated at higher magnification.

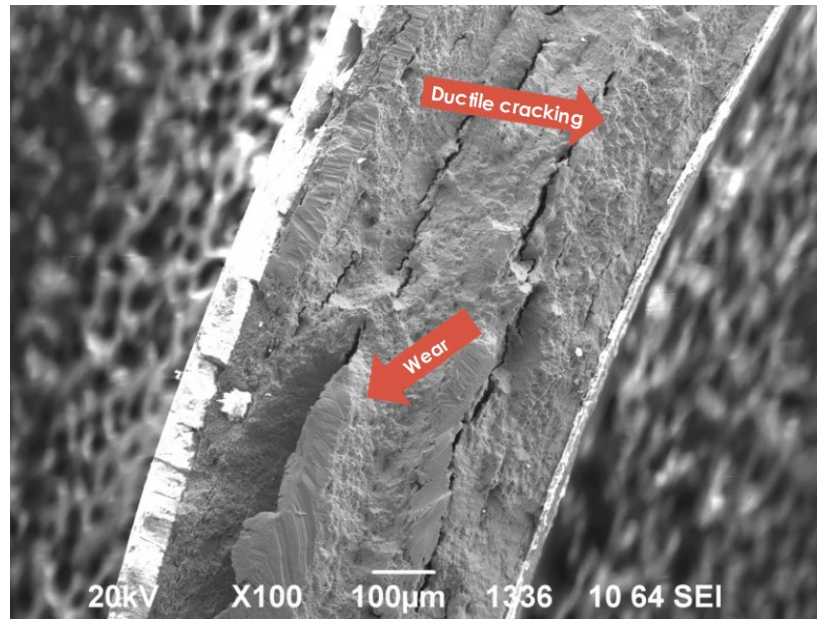


Figure F-47. Ductile regions and wear marks of Q1 in sample 3A1F05-2025-2178.

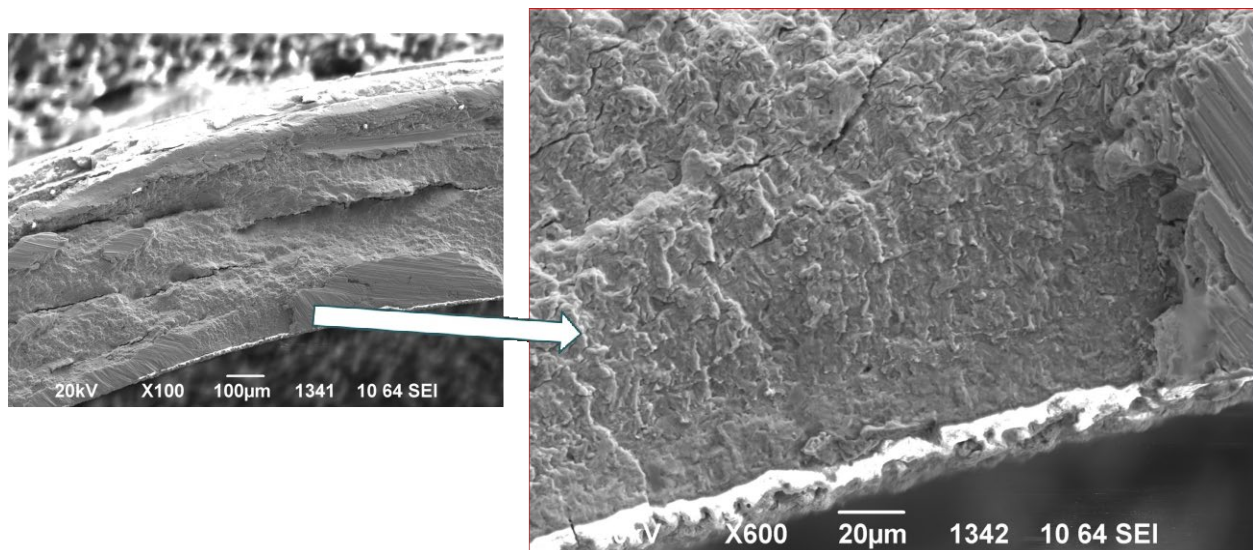


Figure F-48. Fuel-side brittle regions of Q1 (approaching Q2) in sample 3A1F05-2025-2178.

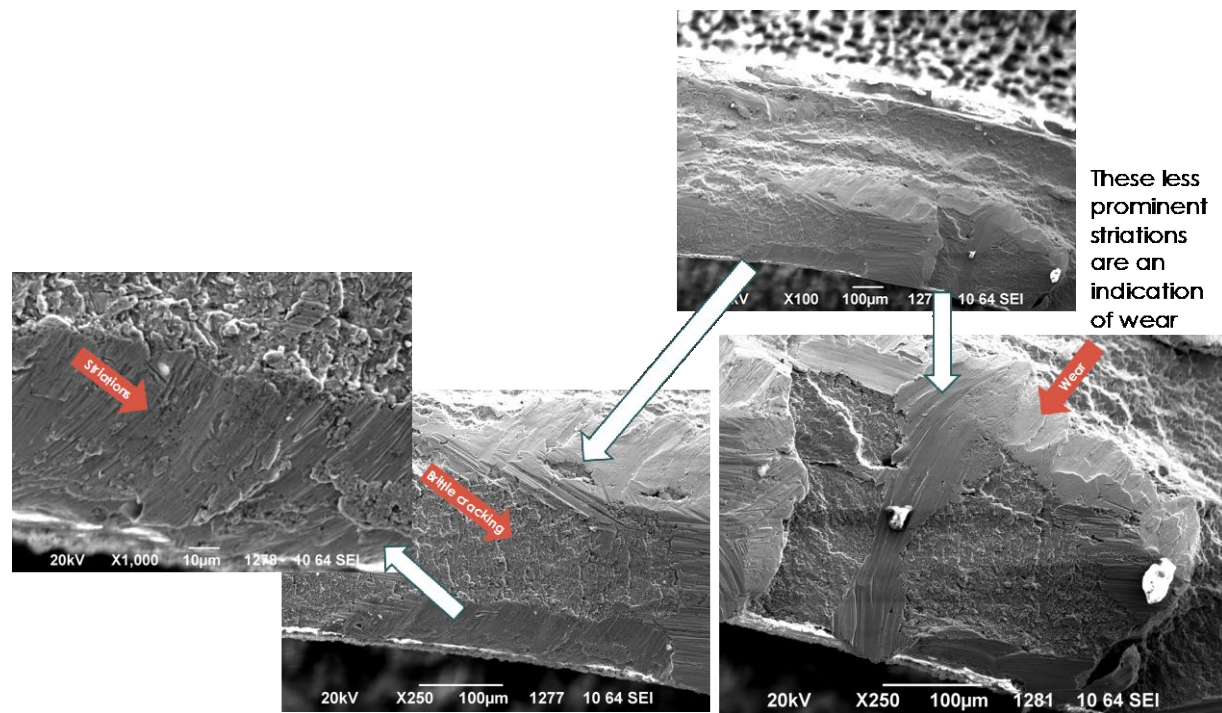


Figure F-49. Cleavage-like regions, apparent fatigue striations, and flat wear marks on the fuel side of Q2 in sample 3A1F05-2025-2178.

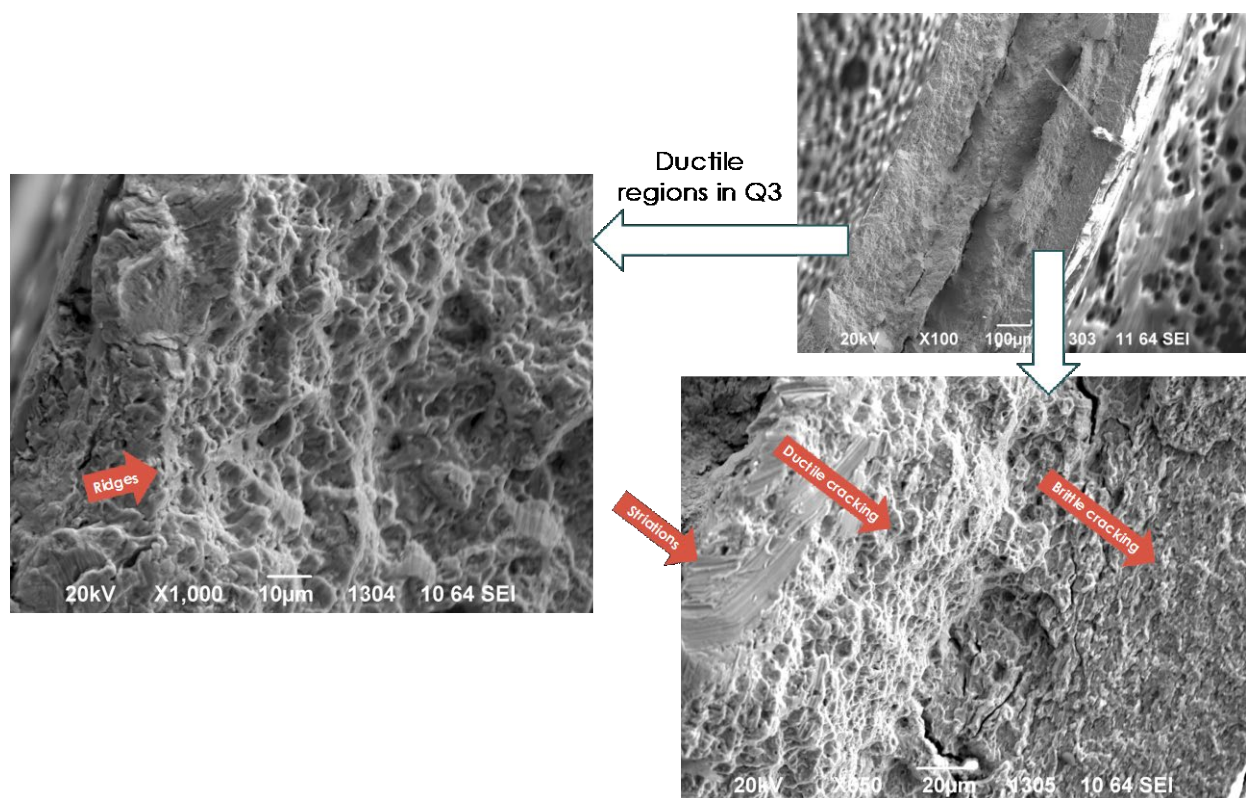


Figure F-50. Ductile fracture regions amidst striations and brittle cracks on Q3 in sample 3A1F05-2025-2178.

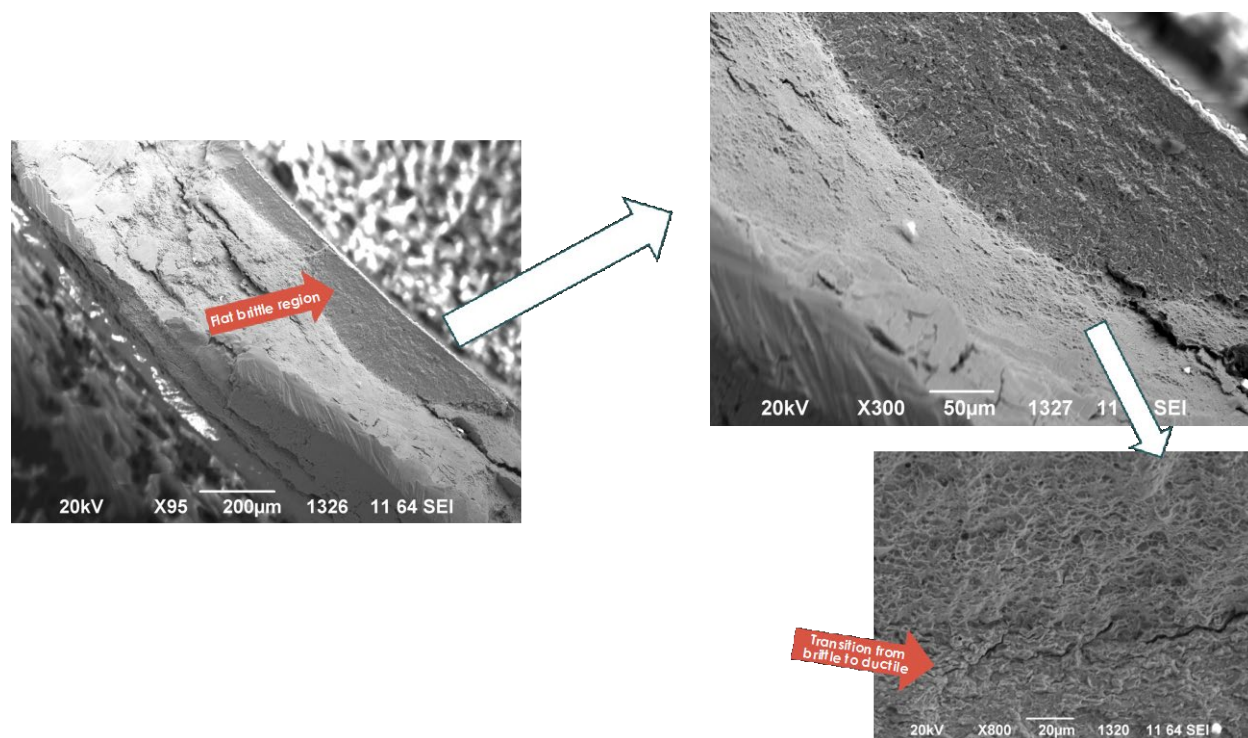


Figure F-51. Flat cleavage-like regions on the fuel side leading to cracks and ductile failure seen on Q4 in sample 3A1F05-2025-2178.

F-8.5.4 Fractography of unirradiated Zirc-4 CIRFT specimens

Two unirradiated fuel cladding samples were tested for fatigue until failure (see Section F-5.1) and were characterized using scanning electron microscopy (SEM). This section discusses major insights from the SEM data and draws certain conclusions from comparison with fueled sample fractography analysis.

The samples were unirradiated Zirc-4 cladding tested at 0.46 and 0.40% strain amplitude. One confounding issue is that sample Zr4-W-3 experienced ~6,300 cycles after fatigue initiation, and specimen Zr4-W-4 experienced ~4,500 cycles after fatigue initiation; thus, some indication of wear on the fracture surfaces are expected. After the specimen was removed from the CIRFT, a short segment of the tube with the fracture surfaces was cut from the dogbone using a tube cutter and then was mounted onto an SEM fixture for imaging in a manner similar to that used for the fueled CIRFT sample as described in Sections F-8.5.2 and F-8.5.3.

F-8.5.4.1 Zr4-W-4

Figure F-52 gives a montage of images taken at 100× magnification around the fracture surface of sample Zirc-4-W-4. It was divided into four quadrants to make it easier to identify different regions of interest. Certain firsthand observations can be made from Figure F-52:

- The highest strains occurred in the planer region in Q4, suggesting that the fatigue crack initiated in this area and then propagated through Q1 and Q3
- The long circumferential striations observed in Q2 and Q3 adjacent to the diagonal markings correspond to a change in the crack plane, as illustrated in Figure F-53, where the region is matched with the side view of the failed specimen in the CIRFT machine.

Figure F-54 shows the crack initiation region in Q4. It can be seen as a damaged region on the ID, with long branch-like radial beach marks extending into the cladding surface. The OD region of the fractured

surface seems to be flatter with straight striations, which may be associated with crack propagation in the circumferential direction. Figure F-55 is a tilted image showing the ID side of the crack initiation region. Surface damage can be observed on the ID below the crack surface, along with localized regions of surface damage extending well below the crack surface. This suggests a line of ID surface damage at the point on the cladding where the maximum strain occurred. In future exams, the ID surface in Q1 that is approximately 90° from the initiation and in Q2 that is 180° from the initiation site will be examined to compare these observations to a surface on the neutral axis and one where similar strain occurred. Figure F-55 shows the flat fracture regions in Q1. The flat fracture surface can be associated to a slow initial propagation rate of fatigue. This observation is supported by the increased fracture surface roughness seen in Q2 and Q3 prior to failure when the propagation rate is higher. Figure F-56 also shows flat, featureless marks in between the brittle regions. These may be caused by wear from the cycles that occurred after failure.

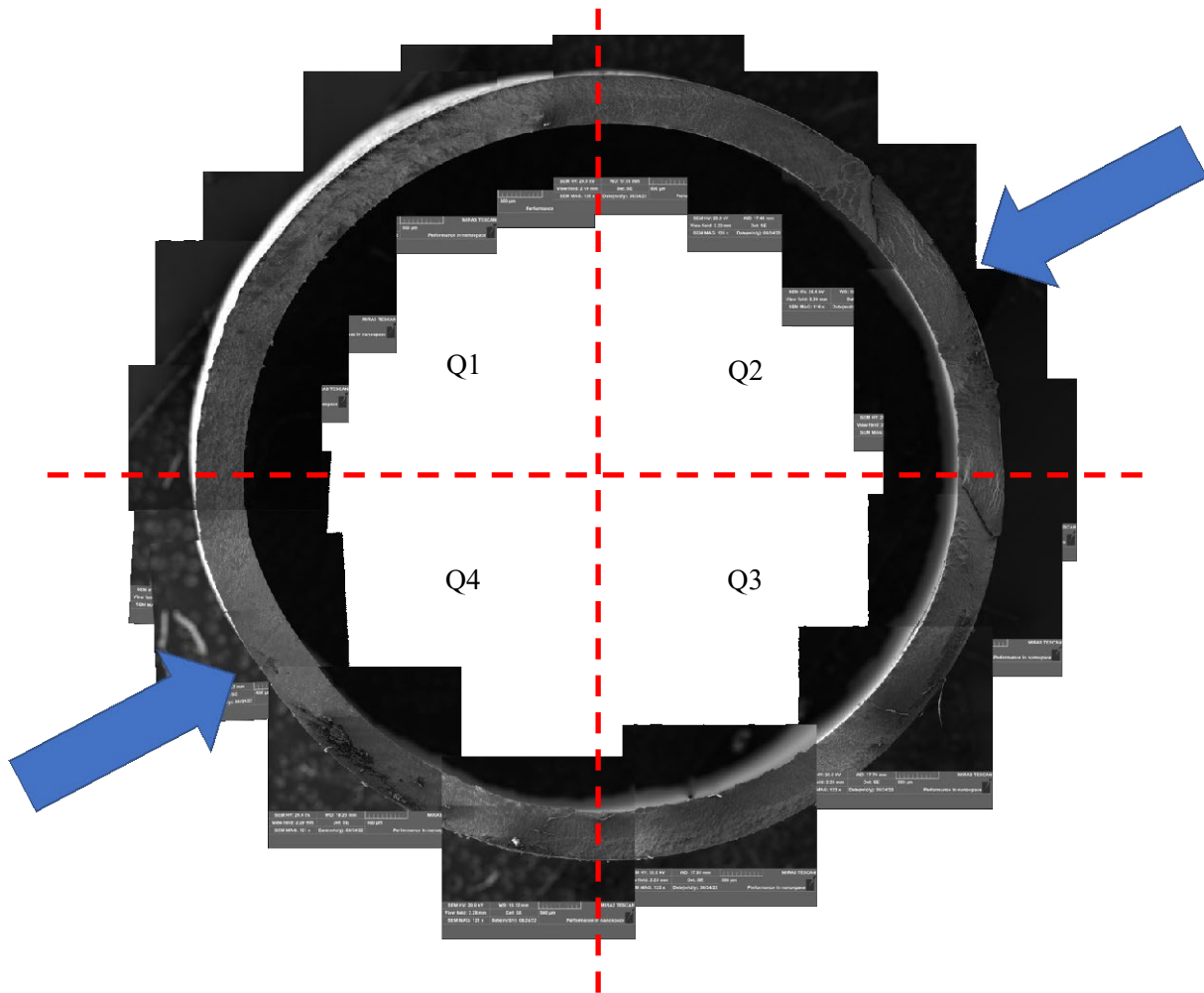


Figure F-52. 100× montage of the surface of the fatigue failure in dogbone sample Zirc-4-W-4. Arrow marks show regions of high bending strain in the sample.

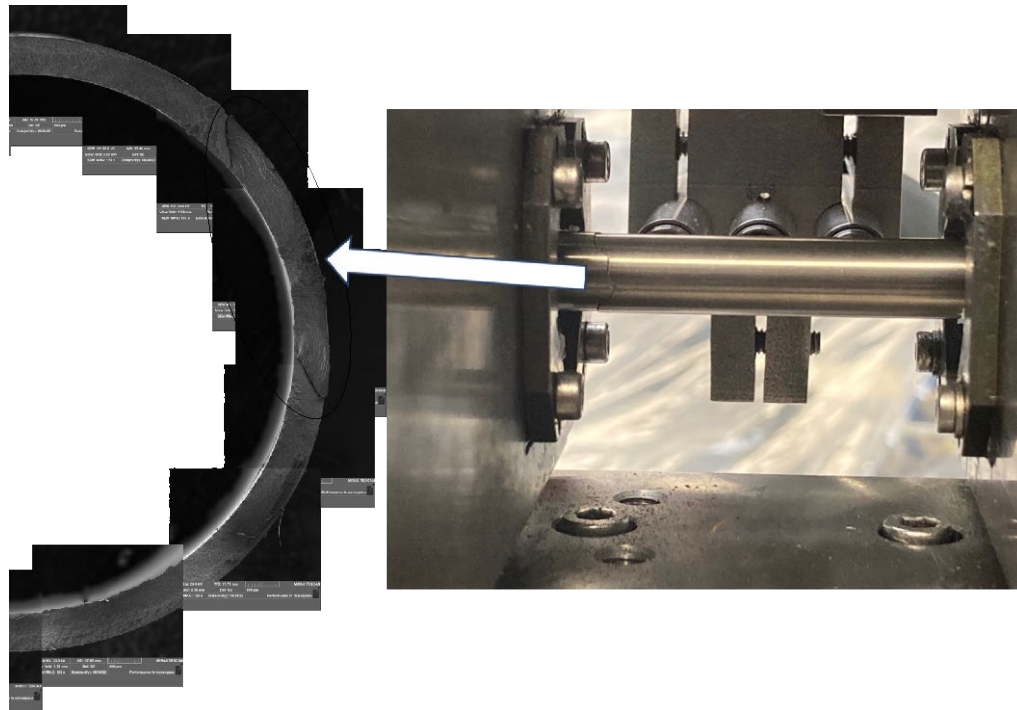


Figure F-53. Top (fracture) view and side view of the fatigue failure region in Q2 and Q3 of sample Zirc-4-W-4.

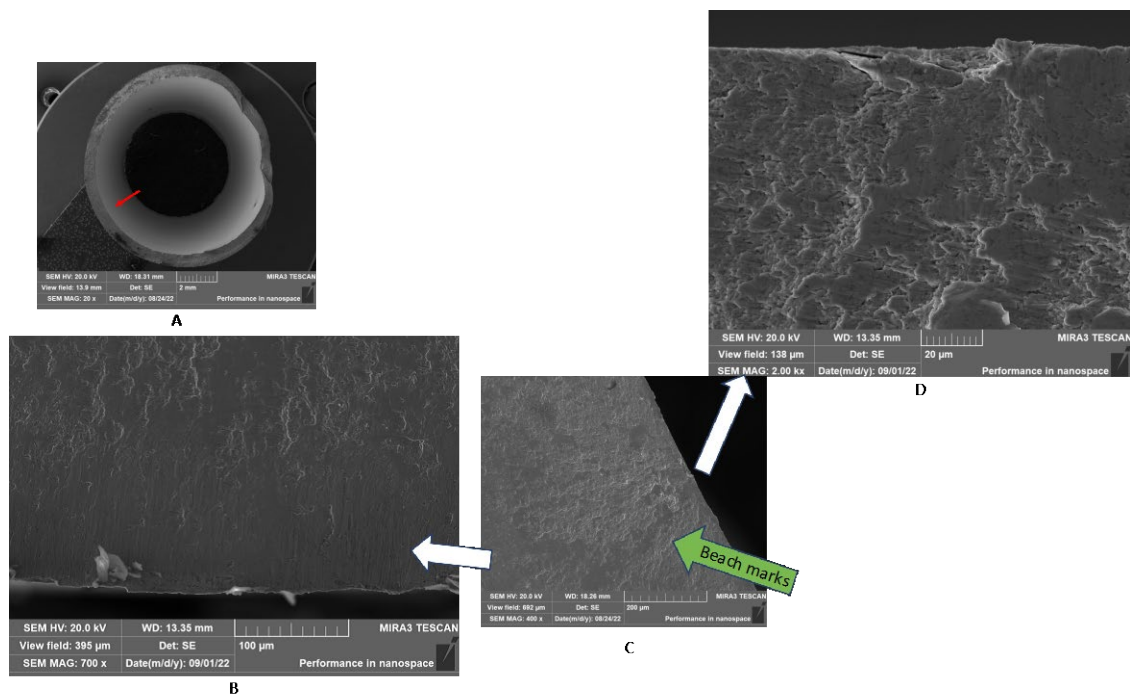


Figure F-54. Fatigue crack initiation region in Q4 of sample Zirc-4-W-4: (A) location of the region in a low-magnification image of the sample; (B) OD side of the fatigue failure initiation site; (C) ID side of the fatigue crack initiation site; and (D) detail view of C.

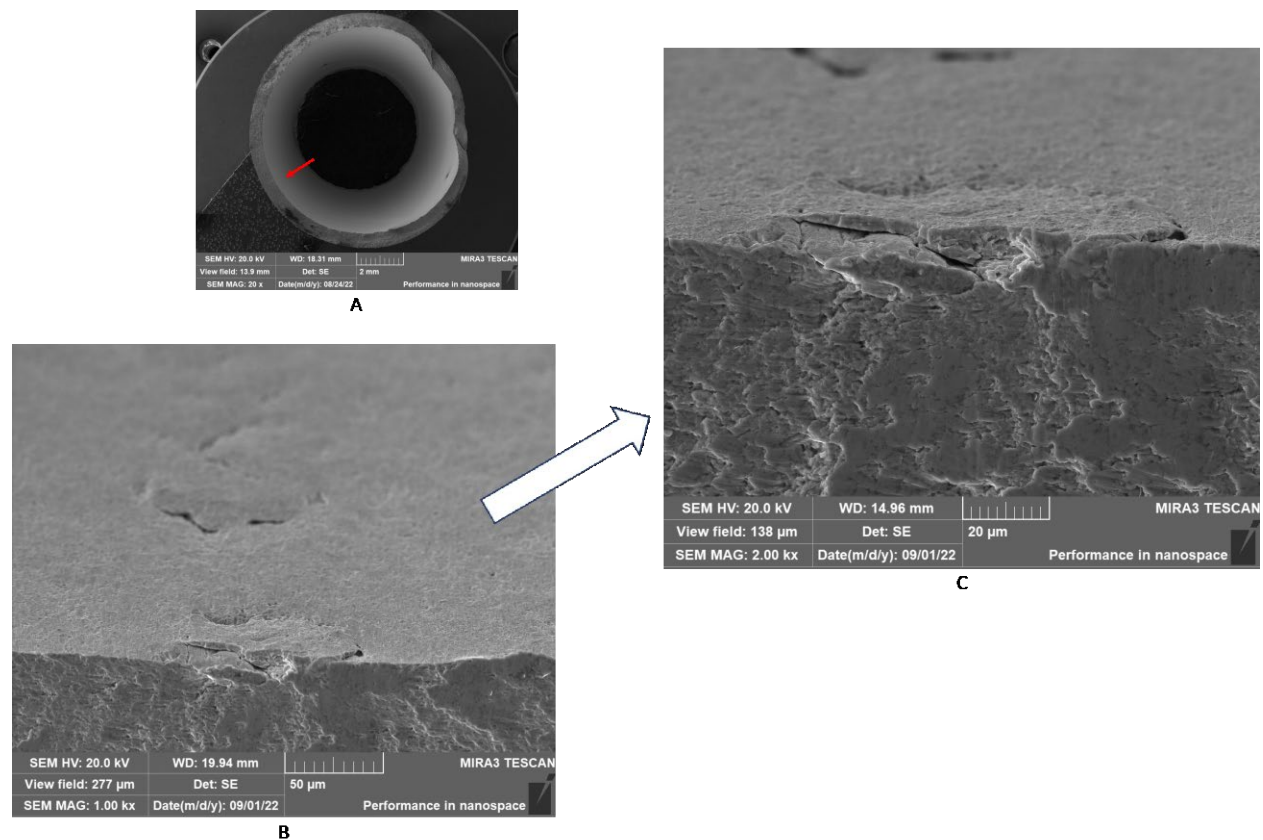


Figure F-55. Tilted image of Figure F-53 revealing the ID side of the fatigue failure initiation site on sample Zirc-4-W-4: (A) location of the region in a low magnification image of the sample; (B) ID side of the fatigue failure initiation site; and (C) detail view of the fatigue failure initiation fracture surface.

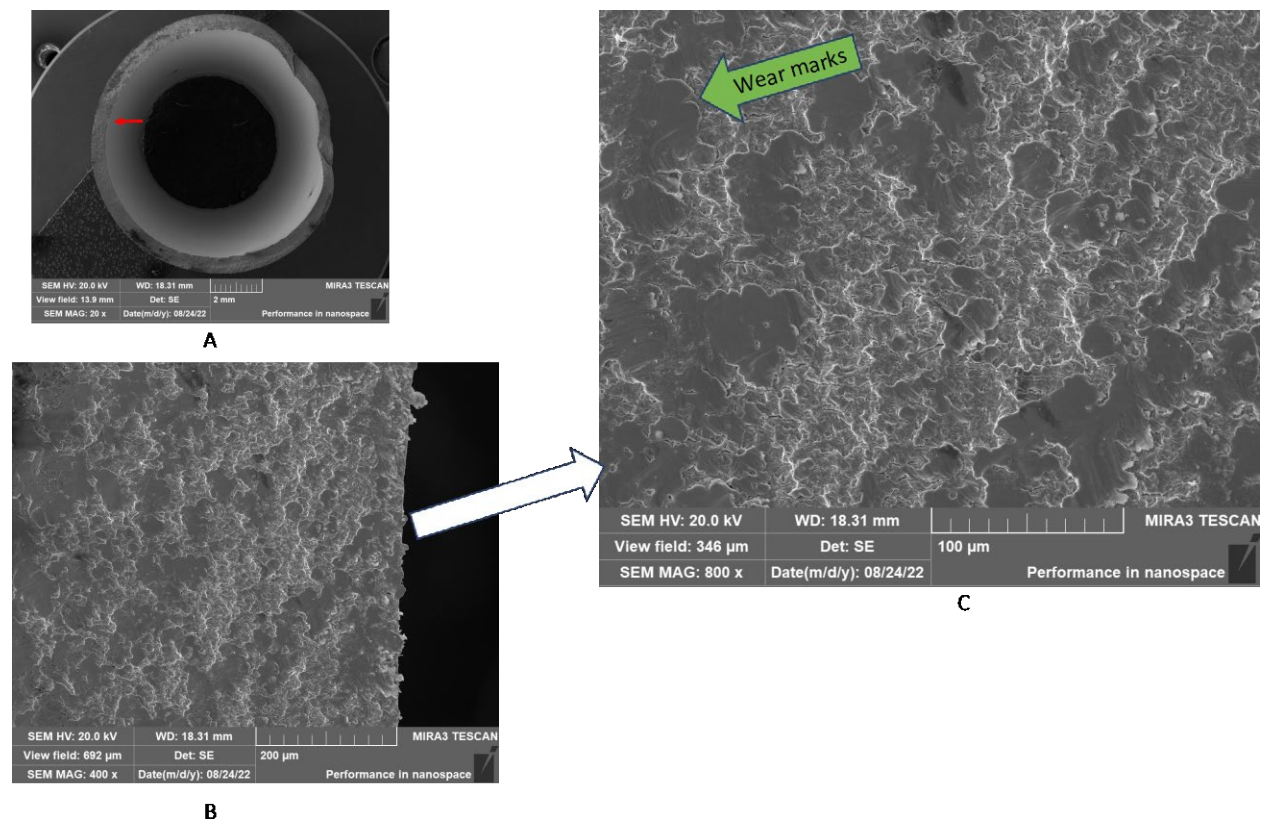


Figure F-56. Brittle fracture regions and potential wear marks of sample Zirc-4-W-4: (A) location of the region in a low magnification image of the sample; (B) Brittle or cleavage-like regions on Q1; and (C) potential wear marks observed between the brittle regions in Q1.

F-8.5.4.2 Zr4-W-3

Figure F-57 is a montage of images taken at 100× magnification around the fracture surface of sample Zirc-4-W-3. It is divided into four quadrants to make it easier to identify different regions of interest. As in sample Zirc-4-W-4, the planer region in Q4 in sample Zirc-4-W-3 is where the highest strains occurred, suggesting the fatigue crack initiation in this area. In fact, a similar initiation feature is observed on the ID of this sample in Q4. The fatigue crack is thought to have propagated through Q1 and Q3, leading to the final failure features observed in Q2 and Q3. In Figure F-58, the final failure region is matched with the side view of the failed specimen in the CIRFT machine.

Figure F-59 shows the fatigue initiation region in sample Zirc-4-W-3. The initiation can be seen as long brittle cracks originating from the ID and radial beach marks propagating towards the OD, similar to that observed in sample Zirc-4-W-4. Furthermore, the sample periphery was analyzed to discern the relation of fatigue initiation to the maximum bending strain direction. As expected, the LVDT marks that correspond to the sample loading position in the CIRFT rig can be seen exactly opposite to the failure initiation site (Figure F-60). Figure F-61B shows the OD side of the fracture surface near the fatigue initiation site of sample Zirc-4-W-3. This region has some radial striations similar to those observed in sample Zirc-4-W-4 at the same location; the orientation of the straight striations indicates that the fatigue crack propagated in the circumferential direction in this region. Figure F-61D is a tilted image showing the ID side of the crack initiation region where surface cracks can be seen along the length of the ID. Although this feature is similar to that observed in sample Zirc-4-W-4, sample Zirc-4-W-3 had a higher density of localized surface damage extending well below the crack surface. In addition, the initiation site in sample Zr4-W-3 looks different than Zr4-W-4. Clear void-like features can be observed very near the surface in Figure F-61D, indicating ductile failure. The transition from void-like features to planar cleavage-like features is striking. Future work is proposed to probe this ductile region further by employing focused ion beam (FIB) machining and characterizing the regions underneath and around the site to look for localized bulk effects contributing to the crack initiation process. Also, electron backscatter diffraction (EBSD) is proposed to obtain texture maps of the fracture surface to determine whether the propensity of crack propagation is inter- or intra-granular.

Figure F-62 shows the fatigue striations in Q1 amidst brittle or cleavage like regions. The striations can be associated to the fatigue propagation process around this quadrant. There is also evidence of flat wear marks in between the brittle regions. This is thought to be caused by wear during the cycles after failure.

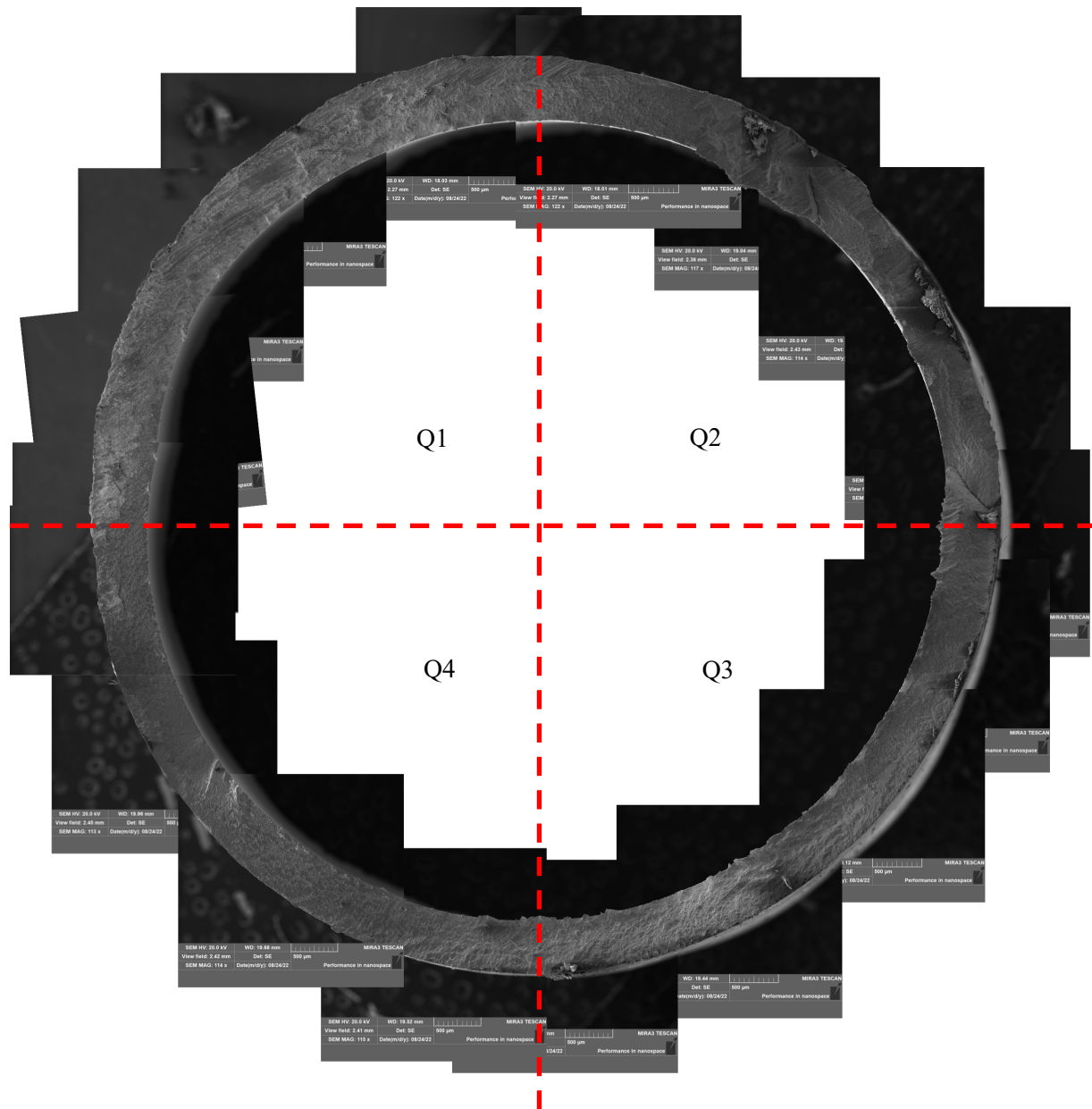


Figure F-57. 100X montage of the fatigue failure surface in dogbone sample Zirc-4-W-3.

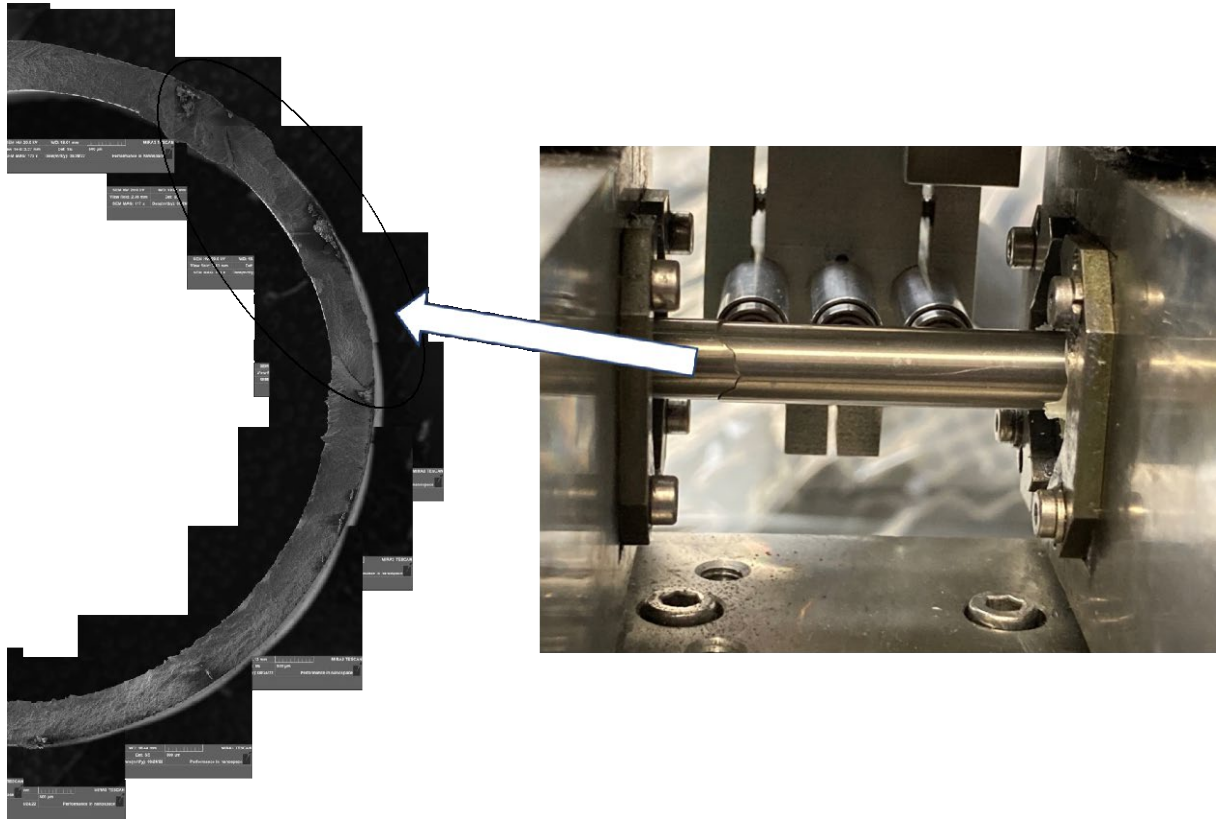


Figure F-58. The top (fracture) view and side view of the fatigue failure region in Q2 and Q3 of sample Zirc-4-W-3.

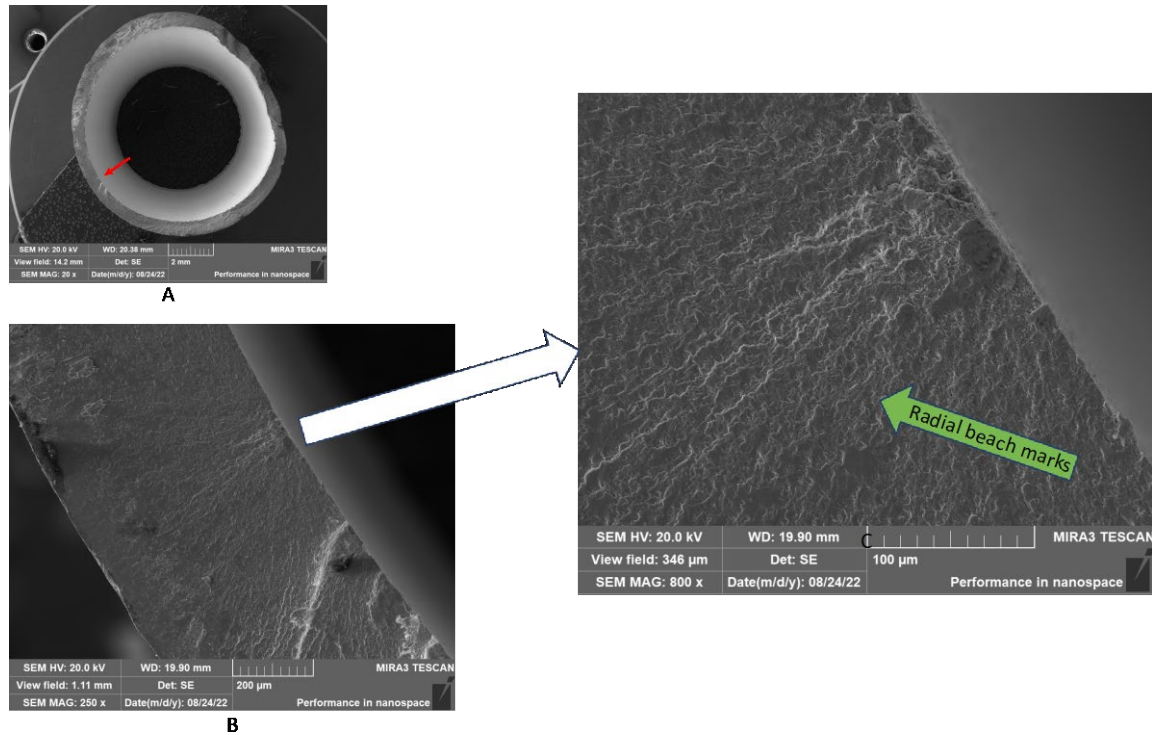


Figure F-59. Fatigue crack initiation region in Q4 of sample Zirc-4-W-3: (A) The location of the region in a low magnification image of the sample; (B) ID side of the fatigue crack initiation site; and (C) detail view of B

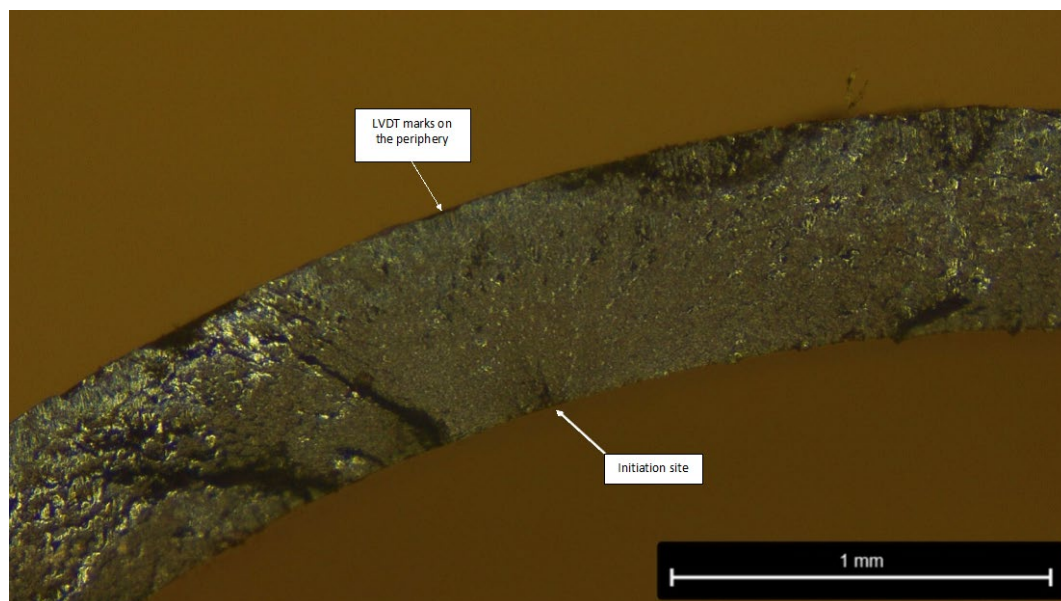


Figure F-60. Optical microscope image of sample Zirc-4-W-3 showing the fatigue failure initiation site; the peripheral region containing the LVDT marks is not visible.

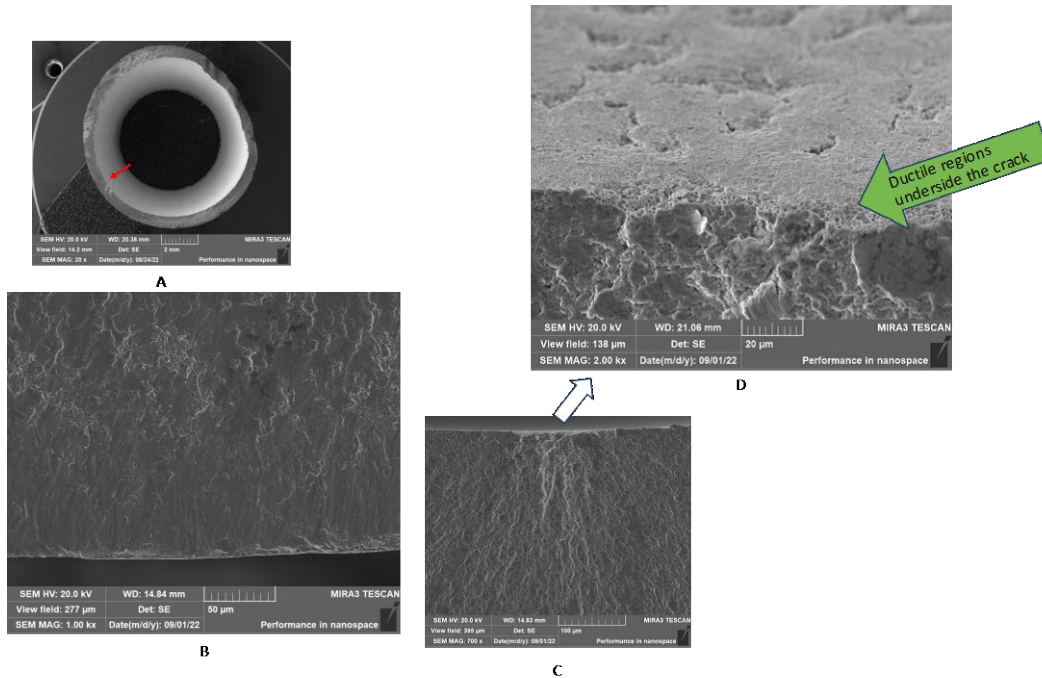


Figure F-61. Tilted SEM image of Figure F-59 revealing the ID side of the fatigue failure initiation site of sample Zirc-4-W-3: (A) location of the region in a low magnification image of the sample; (B) OD side of the fatigue failure initiation site; (C) ID side of the fatigue initiation site; and (D) inside of the ID side of sample Zirc-4-W-3 at the fatigue initiation site.

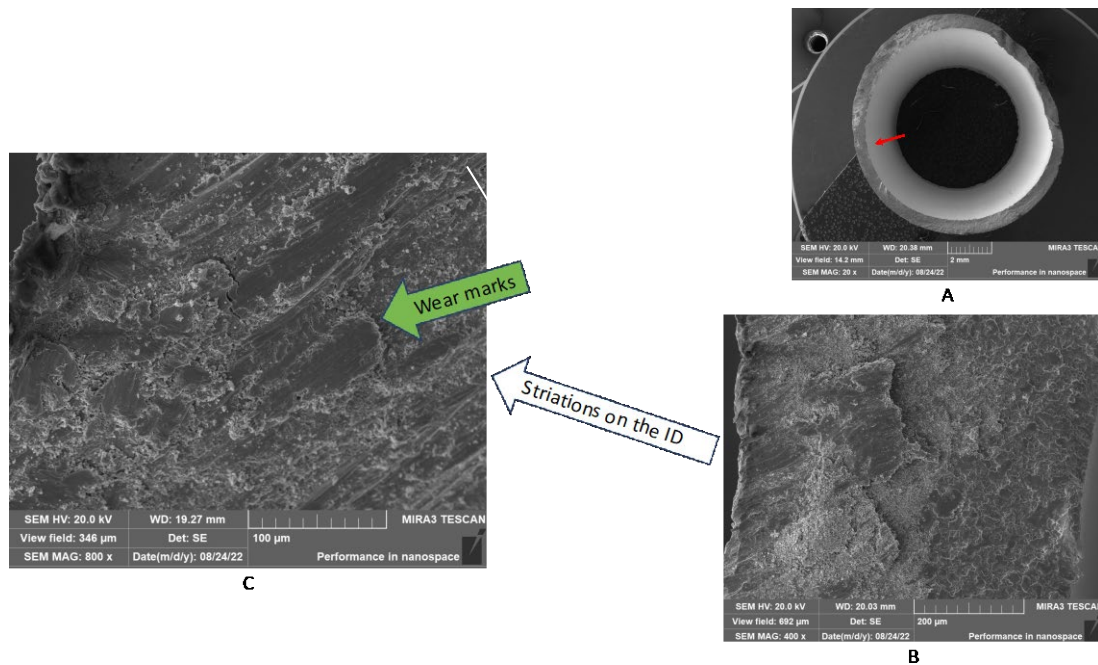


Figure F-62. Some striations visible amidst brittle or cleavage fracture like regions and wear marks of sample Zirc-4-W-3: (A) location of the region in a wide field view of the sample; (B) wear marks observed on the ID with striations on the OD and brittle fracture regions in the middle of Q1; and (C) detail view of the flat wear-like features between striations.

F-8.5.5 Future work

As part of understanding the fatigue failure mechanisms in SNF rods, ORNL plans to further characterize the brittle fracture regions (e.g., as described in Figure F-48 and Figure F-51).

Additionally, sample 6U3K09-2310-2463 presents a unique opportunity to probe the fatigue initiation and propagation sites from an underdeveloped failure, seen as a second crack on the sample (Figure F-63) and sectioned image (Figure F-64). This ZIRLO sample failed under a high load of 12.7 N-m at a pellet-pellet interface, near the grip of the CIRFT test gauge section, and its fatigue life (17,500 cycles) was consistent with previous test data. The fatigue initiation occurred in the last 1,000 cycles.

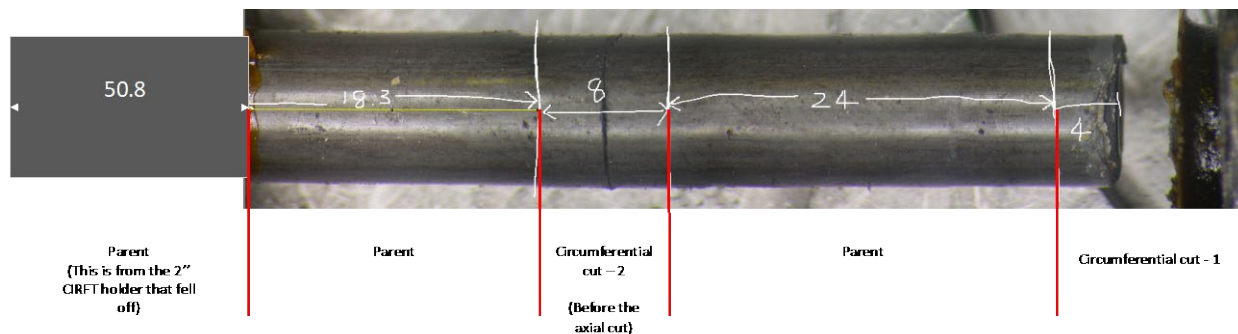


Figure F-63. Fatigue failure in sample 6U3K09-2310-2463 showing the second crack observed in the sample.

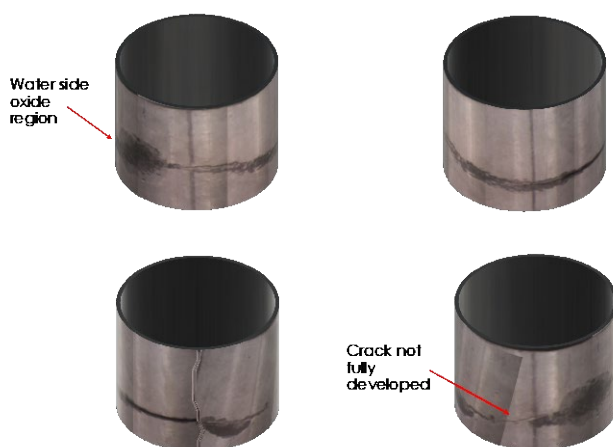


Figure F-64. Images of the circumferential cut-2 from sample 6U3K09-2310-2463 wrapped around a 3D cylinder to show a realistic image.

F-9. CIRFT Cumulative Effects Fixture Development

Equipment for performing the cumulative shock tests, as shown in Figure F-65, was developed and is currently being tested out-of-cell. The design incorporates an electromagnet and weight and uses gravity to deliver one or more impacts to the CIRFT specimen before fatigue testing. The parameters for the impact (e.g., impact load, number of impacts) have not yet been established. To help determine the necessary drop height, impactor weight, and impactor weight geometry for postulated normal condition impacts, a finite element model was developed for the impact system. The model and results are discussed in the following sections.

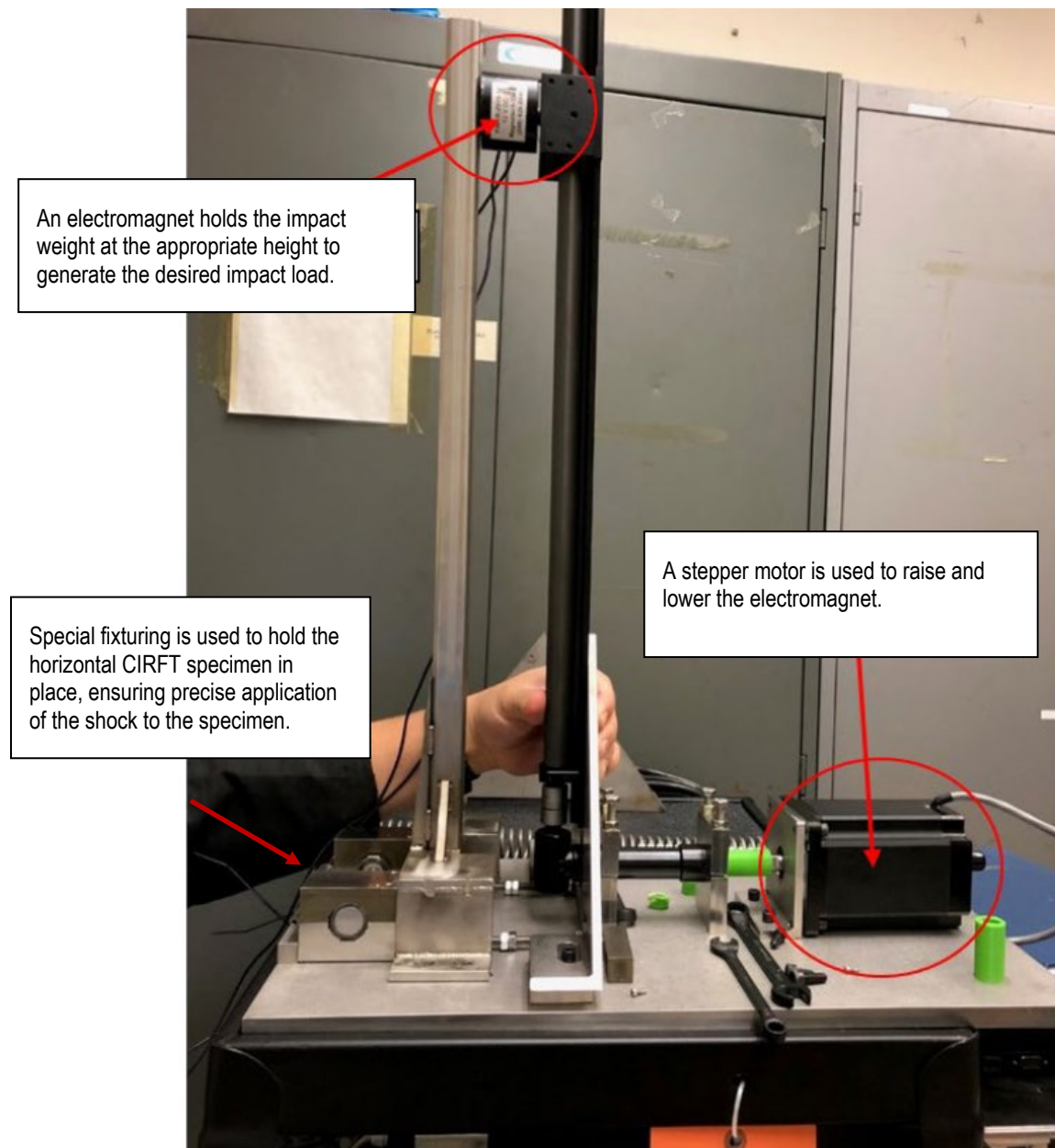


Figure F-65 Cumulative shock fixture developed to apply a normal transport condition shock before fatigue testing.

F-9.1 Finite Element Modeling of the Cumulative Impactor

An impact analysis of the cumulative impactor was performed using a nonlinear dynamic FEA. Solid eight-node elements and shell four-node elements are used for all the models in which structure failure modes can be simulated during the impact.

The cumulative impactor model includes the impactor weight, a fuel rod test segment, and supports/restraints representing the lower bed of the impactor, as shown in Figure F-66. The fuel rod is supported by guide blocks at both ends. The cumulative impactor weight was centered over the rod and at a variable height above the outer surface of the cladding. Several different impactor end geometries were evaluated, including:

- a. a grid strip wall with dimples (shown in Figure F-66)
- b. a grid strip wall without dimples
- c. a rectangular weight only (the brown feature shown in Figure F-66)
- d. a plate with dimples
- e. a plate without dimples

These studies are focused on determining the g-load on the rod segment for various cumulative impactor conditions to determine whether such conditions reflect expected normal conditions of transport. Per Kalina et al. [F14], the normal condition g-loads experienced during transport of the SNF are less than 15 g and more typically less than 3 g.

F-9.1.1 Finite Element Modeling Software

A nonlinear finite element model is developed using ANSYS Workbench. The dynamic analysis with time integration and contact configuration is used to solve the transient impact problem.

LS-DYNA, developed by Livermore Software Technology Corporation (LSTC), is a multipurpose explicit and implicit finite element program used to analyze the nonlinear response of structures. Its fully automated contact analysis and wide range of material models enable users worldwide to solve complex real-world problems. It is used by the automobile, aerospace, construction, military, manufacturing, bioengineering industries, and nuclear industries. LS-DYNA is optimized for shared and distributed memory on Unix-, Linux-, and Windows-based platforms, and it is fully qualified by LSTC. The code's origins lie in highly nonlinear, transient dynamic FEA using explicit time integration [F-15].

LS-DYNA has an extensive material library that includes metals, plastics, glass, foams, fabrics, elastomers, honeycombs, concrete and soils, viscous fluids, and user-defined materials.

LS-DYNA has been widely used in various applications, including automotive crashworthiness and occupant safety, metal forming, aerospace (e.g., blade containment, bird strike, failure analysis), drop testing, nuclear shipping container design, metal cutting, earthquake engineering, offshore platform design, and sports equipment design.

Because impact is a transient structural dynamics problem that involves large deformation of solid structures and nonlinear material behavior, LS-DYNA is chosen to perform the impact analysis of the cumulative impactor.

F-9.1.2 Finite Element Model

Structurally insignificant features such as small curves and lines such as fillets and chamfers were omitted from the finite element model. The omitted features are small and are not expected to significantly influence the structural response. The mesh element size near the impact zone was 0.5 mm; all other element sizes ranged from 0.5 to 2 mm. The cladding was modeled using linear shell elements.

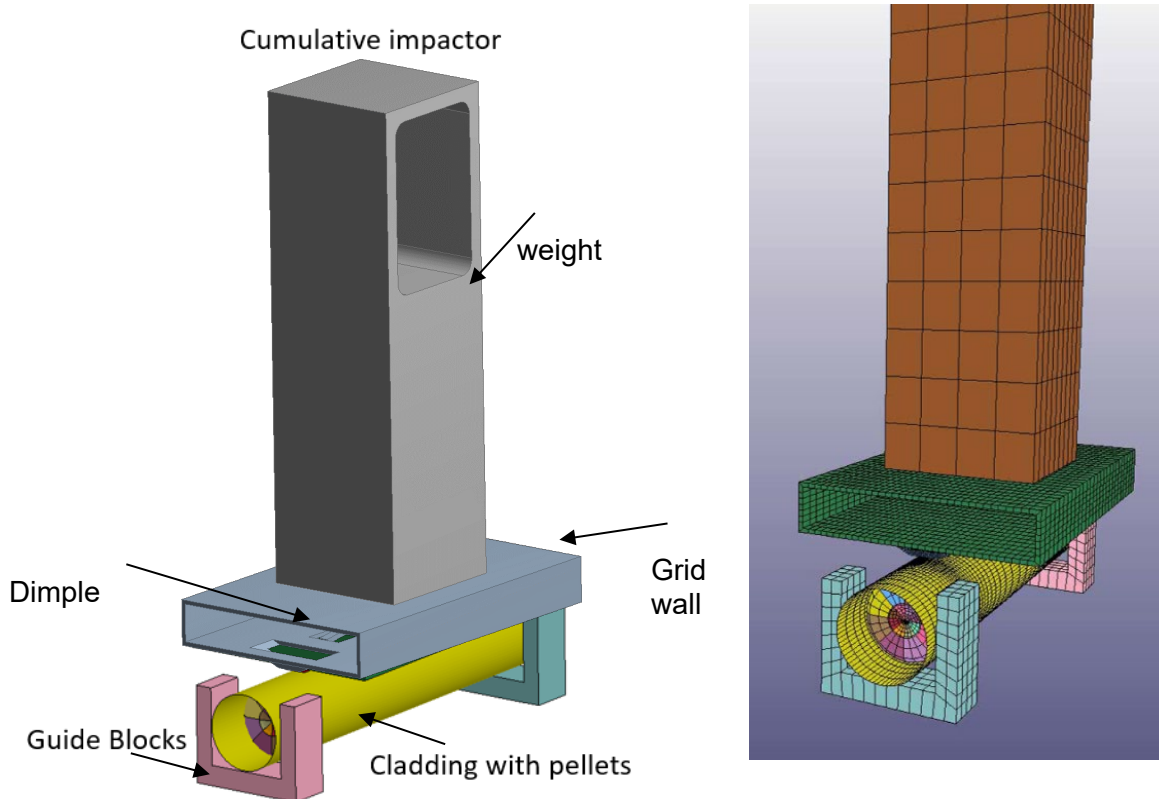


Figure F-66. The cumulative impactor CAD model (left) and finite element model (right) include a rod segment with discrete pellets, guide blocks, and a weight with impact geometry.

The units and values used for the simulations are:

- mass, kg
- length, m
- time, s
- force, N
- stress, Pa
- energy, Joule
- density, kg/m^3
- elastic modulus, Pa

The cumulative impactor was modeled as separate parts, with the surface-to-surface interfaces modeled using the bonded surface-to-surface connection. The surface-to-surface connections in the finite element model cannot deform, but they can break in accordance with the user-input stress criteria. The model uses various contacts to model the interaction between the elements. Automatic single-to-surface contact is an all-purpose contact used to model component interaction. Friction in LS-DYNA is modeled through the classic Coulomb friction model. In the cumulative impactor fuel rod segment model, contacts between the pellet-to-pellet and pellet-to-cladding contacts were assigned a static friction coefficient of 0.95 and a

dynamic friction coefficient of 0.85 to simulate a relatively rigid system. The friction values are being investigated with other models; these values might not be entirely representative of the actual frictional contact, but they are considered acceptable for the purposes of this work.

F-9.1.3 Material Models

The cladding, spring, and dimples are modeled as Zirc-4; the pellets are modeled using a response profile similar to concrete, which is load-bearing in compression and has a lower strength in tension; and the cumulative impactor is modeled as stainless-steel. The pellets are modeled with a concrete material property as a surrogate for UO₂. The compression strength of the pellets was 15 Mpa, with an aggregate grain size of 25.4 mm.

To model the plastic deformation of metal materials, the LS-DYNA code needs the true stress–strain curve of the material. Up to the maximum point on the engineering stress–strain curve, a uniform elongation and a uniform area reduction occur. The minimum true stress–strain curve used is based on the model provided in the American Society of Mechanical Engineers (ASME) Boiler and Pressure Vessel Code (BPVC) Sec. VIII, Div. 2, Annex 3-D [F-16], which uses the minimum yield stress, the minimum ultimate tensile stress, and elastic modulus of the material at the specified temperature. The true stress–strain curves obtained with this model are valid up to the value of the true ultimate tensile stress at true ultimate tensile strain.

The LS-DYNA material model used in the analysis is the *MAT_PIECEWISE_LINEAR_PLASTICITY, also known as *MAT_024. This material model prompts the user to specify the elastic modulus, Poisson’s ratio, yield stress, and failure strain of the material. When the calculated element’s plastic strain reaches the specified failure strain, the material has failed, and the element is deleted from the analysis. Additionally, the effective stress vs. plastic strain curve must be entered as a *DEFINE_CURVE entry.

Following the ASME model, a true stress–strain curve was developed for stainless steel and Zirc-4 using the minimum yield strength, minimum ultimate tensile strength, and elastic modulus of the material in Table F-14 [F-17]; the curve is shown in Figure F-67. Before the true stress–strain curve was entered into to LS-DYNA, the elastic portion of the strain was subtracted from the total strain to develop the effective plastic strain used by LS-DYNA.

Table F-14. Cumulative Impactor Model Minimum Material Properties.

| Material properties | | | | |
|---------------------|----------------------------|-------------------------------|-----------------------|--------------|
| Material | Minimum yield stress (MPa) | Minimum ultimate stress (MPa) | Elastic modulus (GPa) | Reference |
| 304 | 106 | 392 | 172 | [F-16, F17] |
| Zirc-4 | 241 | 413 | 99.3 | [F-16, F-17] |

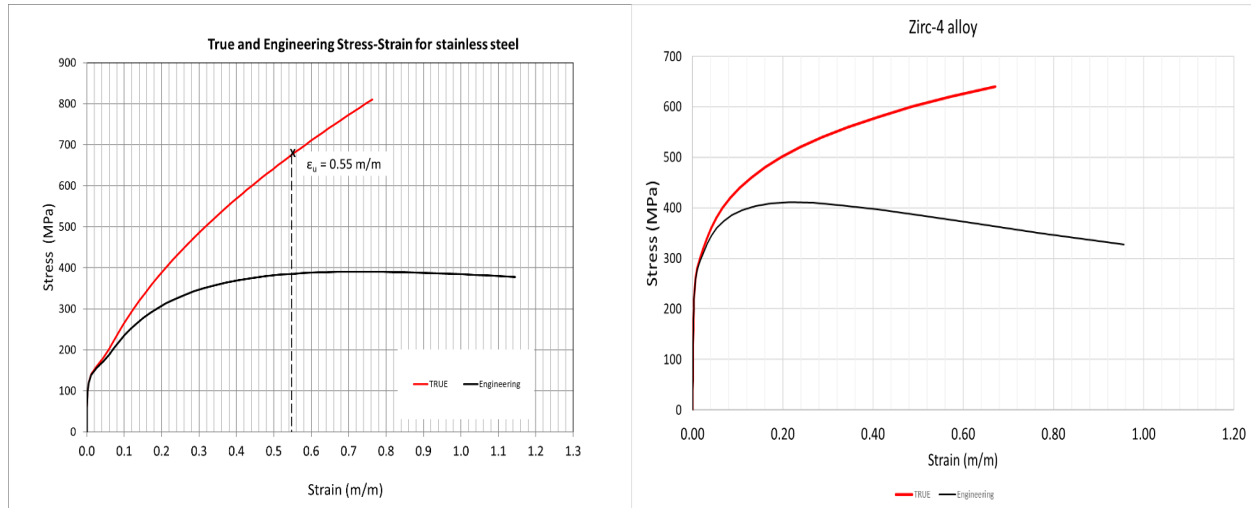


Figure F-67. 304 stainless steel (left) and Zirc-4 (right) true stress–strain curves used compared with corresponding engineering stress–strain curves.

F-9.1.4 Initial Conditions, Boundary Conditions and Load Cases

All simulations were completed using room temperature material properties. A gravity load of 9.81 m/s^2 was applied to all components in the finite element model. The guide rods were constrained in all three directions using the *BOUNDARY_SPC_SET keyword. The fuel rod segment was placed on the guide blocks with full frictional contact.

F-9.1.5 Load Cases

The impact of the weight was studied using nine load cases, as listed in Table F-15, for each of the impactor end geometries. Load cases 1–4 correspond to a maximum cumulative impactor weight of 0.11 kg, with height increasing from 0.15 to 0.61 m (0.5 to 2.0 ft). Load cases 5–7 correspond to a 25% reduction in the cumulative impactor weight with increasing drop height. The cumulative impactor mass for load case 8 was reduced by 50% when compared with load case 1, and the drop height was 0.15 m (0.5 ft). Finally, for load case 9, the mass for the cumulative impactor was reduced by 75% when compared with load case 1, and the drop height was 0.15 m (0.5 ft).

Table F-15. Cumulative Tester FEA Load Case Summary.

| Load case | Impactor mass (kg) | Impactor height (m) |
|-----------|--------------------|---------------------|
| 1 | 0.107 | 0.15 |
| 2 | 0.107 | 0.30 |
| 3 | 0.107 | 0.46 |
| 4 | 0.107 | 0.61 |
| 5 | 0.080 | 0.15 |
| 6 | 0.080 | 0.30 |
| 7 | 0.080 | 0.46 |
| 8 | 0.053 | 0.15 |
| 9 | 0.027 | 0.15 |

F-9.2 Results, Discussion, and Conclusions from the Cumulative Effects Fixture Modeling

The analysis focused on determining the g-load applied to the cladding when subjected to an impact from the cumulative impactor. The cladding g-load for each load case was extracted from the analysis and was plotted as a function of time. The system can dissipate the impact energy in three ways:

(1) rebound/deflection of the impactor, (2) bending deflection of the target rod segment, and (3) absorption into the rod cladding and pellets and supporting end blocks. End configurations (a) and (b), described in section F-8.1, resulted in a significant amount of rebound and the lowest g-load impacts. The concentrated load application in end configuration (c) resulted in rod segment bending, but the g-loads on the rod segment were extremely high. The plate type end configuration, (d) and (e), resulted in high shear loads on the rod segment near the guide blocks that are not considered representative of the target g-load of <15 g.

None of the combinations resulted in a g-load below 20 g. For example, the results from impactor end configuration (d), the plate with dimples, are provided. The impactor-applied g-load as a function of time is provided in Figure F-68 for load cases 1–4 and in Figure F-69 for load cases 5–9. For this impactor geometry, the initial impact takes less than 0.3 ms, after which the weight is rebounded. The g-load on the rod during the impact ranges from 781 to 3,298 g, as listed in Table F-16. Load case 4 has the highest drop height and heaviest weight, and it resulted in the maximum g-load because it had the largest potential energy when compared with the other load cases. Load cases 1, 8, and 9 resulted in a cladding g-load less than 800. All load cases resulted in g-loads greater than 500, with multiple shock waves on the cladding and localized plastic strain on the impactor weight dimples, as shown in Figure F-70.

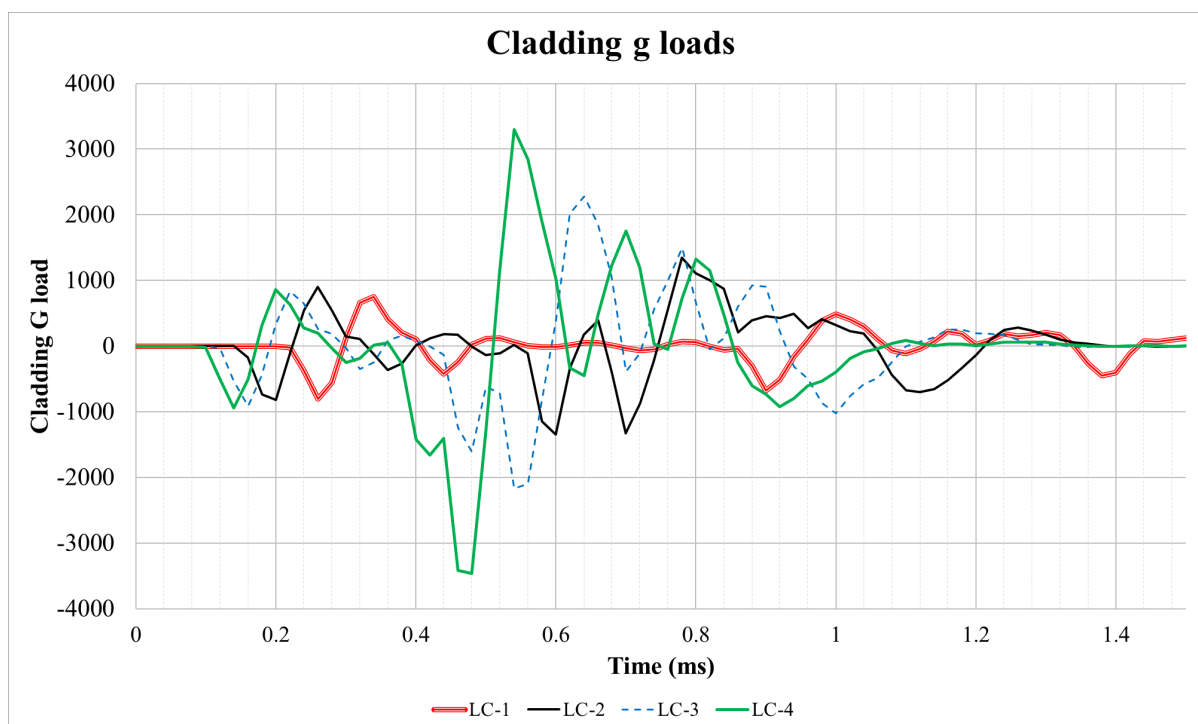


Figure F-68. Impactor end configuration (a) results for load cases 1–4.

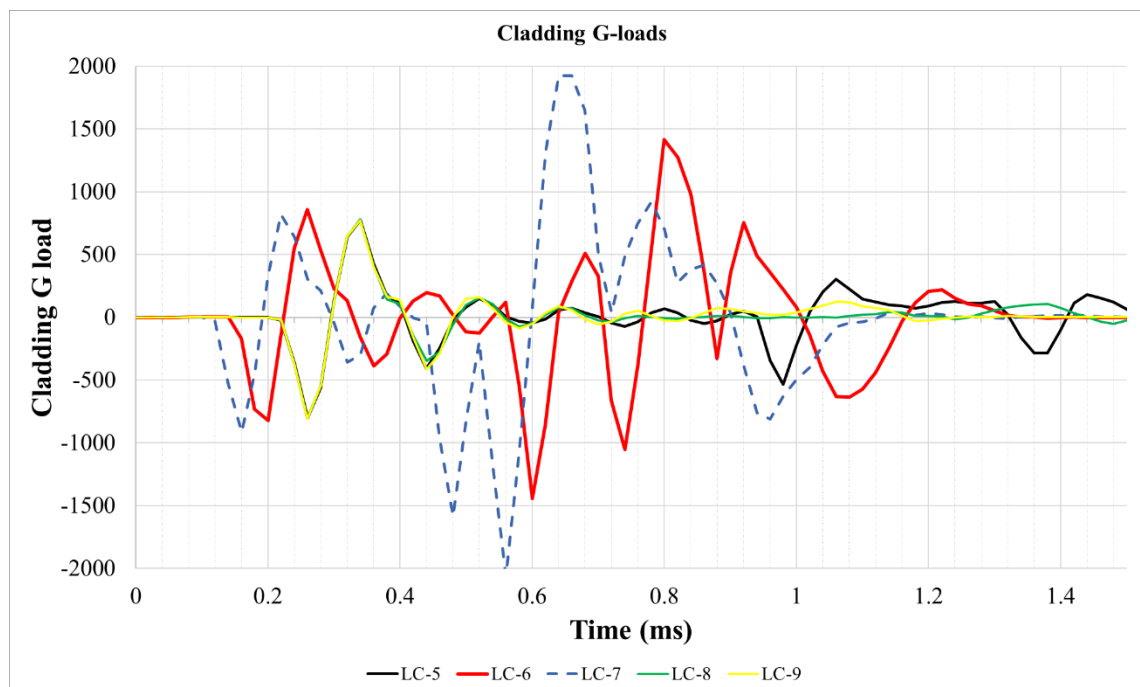


Figure F-69. Impactor end configuration (a) results for load cases 5–9.

Table F-16. Summary of Fuel Rod Maximum g-load during Impact with End Configuration (a).

| Load case | Cladding maximum g-load |
|-----------|-------------------------|
| LC-1 | 754 |
| LC-2 | 1,344 |
| LC-3 | 2,279 |
| LC-4 | 3,298 |
| LC-5 | 774 |
| LC-6 | 1,414 |
| LC-7 | 1,925 |
| LC-8 | 781 |
| LC-9 | 773 |

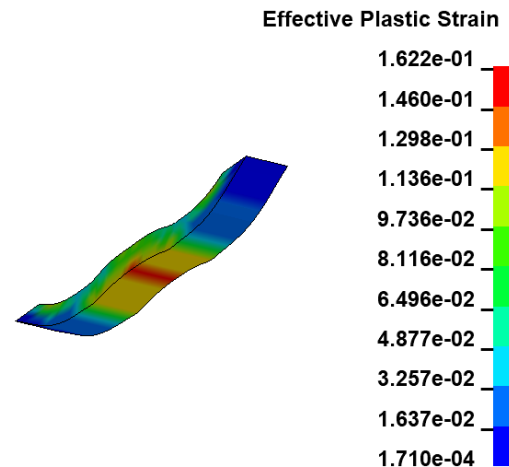


Figure F-70. Plastic strain occurred on the dimples for impactor end configuration (a).

In addition to the permanent deformation of the impactor end dimples, configuration (a) also resulted in large rebound and fluttering of the grid wall portion of the impactor. Because these effects would produce uncontrolled variation in the impacts, this configuration was not appropriate for future cumulative shock testing prior to fatigue testing in CIRFT.

Based on the FEA, the main reason that the target g-load range cannot be achieved has nothing to do with the impactor itself. Rather, the problem is that the target rod segment is very stiff. It is necessary to prepare the segment for CIRFT testing by installing the heavy dogbone grips on each end. Only 50 mm of segment length is exposed for impact, as shown in Figure F-71. The dogbone provides a very stiff target that does not deflect in bending, so any impact will result in a high g-load, even with very low drop height, low impactor weight, and a soft impactor end configuration such as the dimples with a grid wall. With the dogbone as the target, low g-load impacts are not possible with the current fixture.



Figure F-71. CIRFT dogbone.

F-9.3 Verification of FEA Results Using the Cumulative Effects Fixture

Physical tests using the cumulative effect fixture were completed as a verification of the FEA. A CIRFT dogbone surrogate with stainless-steel cladding and ceramic pellets was constrained in the specimen holder, as shown in Figure F-72. Various impactors with masses ranging from 355 to 47 g were used for the tests. These impactors had end geometries designed to mimic grid dimples, but they were solid, as shown in Figure F-73.

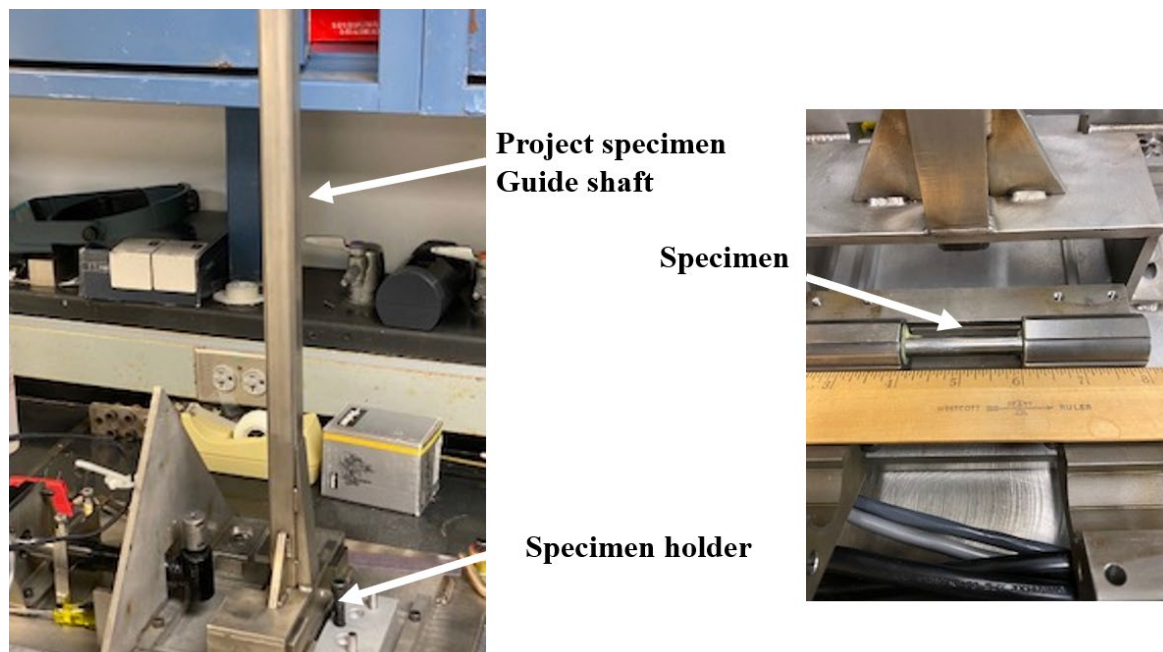


Figure F-72. Physical test configurations with the cumulative effects fixture.



Figure F-73. Impactors used in the physical tests.

To record the maximum g-load on the specimen, a single axis accelerometer was mounted on the specimen with epoxy adhesive. The maximum recordable load for the accelerometer used is 1,100 g. The 85 g projectile was dropped from two different heights: 127 and 25 mm. The mounted accelerometer on the specimen recorded its maximum acceleration of 1,100 g for all tests, indicating a load greater than 1,100 g for all tests. Some attempts were made to reduce the impact load by adding compliant layers to the impact surfaces, but this was unsuccessful.

F-9.4 Summary, Cumulative Effects Fixture Development

Both FEA and experimental evidence indicate that the current configuration of the drop test is not able to recreate the desired g loads on the dogbone specimens used in CIRFT fatigue testing. It was concluded that the stiffness of the dogbone specimen results in very high g-loads. No further investigations were completed, but alternatives will be considered in the coming year. For example, one potential change is to control the impact velocity rather than dropping a target.

REFERENCES

- [F-1]. *High Burnup Dry Storage Cask Research and Development Project: Final Test Plan*, contract no. DE-NE-0000593, Electric Power Research Institute, Palo Alto, California (2014).
- [F-2]. S. Saltzstein et al., *Visualization of the High Burnup Spent Fuel Rod Phase I Test Plan*, SAND2018-8042-O (2018).
- [F-3]. R. A. Montgomery et al., *Post-Irradiation Examination Plan for High Burnup Demonstration Project Sister Rods*, SFWD-SFWST-2017-000090 ORNL/SR-2016/708, Oak Ridge National Laboratory (2016).
- [F-4]. J.-A. Wang and H. Wang, *FY 2017 Status Report: CIRFT Data Update and Data Analyses for Spent Nuclear Fuel Vibration Reliability Study, Revision 1*, ORNL/SPR-2017/521, SFWD-SFWST-2017-000030/R1 (2017).
- [F-5]. J.-A. Wang and H. Wang, *Mechanical Fatigue Testing of High Burnup Fuel for Transportation Applications*, NUREG/CR-7198/R1 (2017).
- [F-6]. R. A. Montgomery et al., *Sister Rod Nondestructive Examination Final Report*, SFWD-SFWST-2017-000003 Rev. 1 (M2SF-17OR010201021) / ORNL/SPR-2017/484 Rev. 1 (ORNL/SPR-2018/801), Oak Ridge National Laboratory (2019).
- [F-7]. J.-A. Wang and H. Wang, *FY 2017 Status Report: CIRFT Data Update and Data Analyses for Spent Nuclear Fuel Vibration Reliability Study, Revision 1*, ORNL/SPR-2017/521, SFWD-SFWST-2017-000030/R1 (2017).
- [F-8]. J.-A. Wang and H. Wang, *Mechanical Fatigue Testing of High Burnup Fuel for Transportation Applications*, NUREG/CR-7198/R1 (2017).
- [F-9]. W. J. O'Donnell and B. F. Langer, "Fatigue Design Basis for Zircaloy Components," *Nuclear Science and Engineering* 20 (1964): 1–12.
- [F-10]. X. Lin and G. Haicheng, "Low Cycle Fatigue Properties and Microscopic Deformation Structure of Zirc-4 in Recrystallized and Stress-relieved Conditions," *J. Nucl. Mater.*, 265, 213-217 (1999).
- [F-11]. D. Mowbray, "Effects of 1.0% Superimposed Mean Strain on the Bending Fatigue Strength of Zirc-4," *Nuclear Applications*, 1:1, 39-48 (1965)
- [F-12]. P. McConnell et al. *Normal Conditions of Transport Truck Test of a Surrogate Fuel Assembly*, SAND2014-20495/FCRD-UFD-2014-000066, Revision 0.1, Sandia National Laboratory, December 2014.
- [F-13]. K. Geelhood et al. "Modeling Structural Loading of Used Nuclear Fuel under Conditions of Normal Transportation," *Ceramic Materials for Energy Application IV*, The American Ceramic Society, 2015.
- [F-14]. J.-A. Wang and H. Wang, *FY 2017 Status Report: CIRFT Data Update and Data Analyses for Spent Nuclear Fuel Vibration Reliability Study, Revision 1*, ORNL/SPR-2017/521, SFWD-SFWST-2017-000030/R1 (2017).
- [F-15]. J.-A. Wang and H. Wang, *Mechanical Fatigue Testing of High Burnup Fuel for Transportation Applications*, NUREG/CR-7198/R1 (2017).
- [F-16]. E. A. Kalinina et al., *Data Analysis of ENSA/DOE Rail Cask Tests*, SFWD-SFWST-2018-00049/ SAND2018-13258R (2018).
- [F-17]. LS-DYNA. "LS-DYNA." <http://www.lstc.com/products/ls-dyna>, (9/1/2020).

- [F-18]. ASME BPVC Sec VIII Div. 2 *Annex 3-D Rules for Construction of Nuclear Facility Components*, 2013
- [F-19]. ASME BPVC Sec II, Part D *Rules for Construction of Nuclear Facility Components*, 2013.
- [F-20]. P. Efsing and K. Pettersson, “Delayed Hydride Cracking in Irradiated Zircaloy Cladding,” *Zirconium in the Nuclear Industry: 12th International Symposium*, ASTM STP 1354, G. P. Sabol and G. D. Moan, Eds, ASTM, West Conshohocken, PA, 340-355, 2000.
- [F-21]. J.-A. Wang and H. Wang, *Data Processing Package for Cyclic Integrated Reversible Bending Fatigue Testing*, ORNL/TM-2021/2114 (2021).
- [F-22]. NUREG-2224, “Dry Storage and Transportation of High Burnup Spent Nuclear Fuel,” US NRC, November 2020.
- [F-23]. J-A. Wang, H. Wang, H. Jiang, B. Bevard, “High Burnup Spent Nuclear Fuel Transport Reliability Investigation,” *Nuclear Engineering and Design*, 330, 497-515 (2018).
- [F-24]. P. Cantonwine, R. Montgomery, and H. Wang, “Evaluation of Fuel Rod Fatigue During Spent Fuel Transportation Conditions,” ORNL/TM-2022/2736 (2022).

Sister Rod Destructive Examinations (FY22)

Appendix F2: Evaluation of Fuel Rod Fatigue During Spent Fuel Transportation

Spent Fuel and Waste Disposition

*Prepared for
US Department of Energy
Spent Fuel and Waste Science
and Technology*

Oak Ridge National Laboratory

*Paul Cantonwine, Rose Montgomery,
Hong Wang, Bruce Bevard,*

*January 13, 2023
M2SF-23OR010201024
ORNL/SPR-2022/2678*

This report was prepared as an account of work sponsored by an agency of the United States Government. Neither the United States Government nor any agency thereof, nor any of their employees, makes any warranty, express or implied, or assumes any legal liability or responsibility for the accuracy, completeness, or usefulness of any information, apparatus, product, or process disclosed, or represents that its use would not infringe privately owned rights. Reference herein to any specific commercial product, process, or service by trade name, trademark, manufacturer, or otherwise, does not necessarily constitute or imply its endorsement, recommendation, or favoring by the United States Government or any agency thereof. The views and opinions of authors expressed herein do not necessarily state or reflect those of the United States Government or any agency thereof.

SUMMARY

This report documents work performed under the Spent Fuel and Waste Disposition's Spent Fuel and Waste Science and Technology program for the US Department of Energy (DOE) Office of Nuclear Energy (NE). This work was performed to fulfill Level 2 Milestone M2SF-23OR010201024, "FY22 Report on ORNL Sibling Rod Testing Results," within work package SF-23OR01020102 and is an update to the work reported in M2SF-22OR010201047, M2SF-21OR010201032, M2SF-19OR010201026, and M2SF-19OR010201028.

As a part of DOE NE High Burnup Spent Fuel Data Project, Oak Ridge National Laboratory (ORNL) is performing destructive examinations (DEs) of high burnup (HBU) (>45 GWd/MTU) spent nuclear fuel (SNF) rods from the North Anna Nuclear Power Station operated by Dominion Energy. The SNF rods, called *sister rods* or *sibling rods*, are all HBU and include four different kinds of fuel rod cladding: standard Zircaloy-4 (Zirc-4), low-tin (LT) Zirc-4, ZIRLO, and M5. The DEs are being conducted to obtain a baseline of the HBU rods' condition before dry storage and are focused on understanding overall SNF rod strength and durability. Composite fuel and defueled cladding will be tested to derive material properties. Although the data generated can be used for multiple purposes, one primary goal for obtaining the post-irradiation examination data and the associated measured mechanical properties is to support SNF dry storage licensing and relicensing activities by (1) addressing identified knowledge gaps and (2) enhancing the technical basis for post-storage transportation, handling, and subsequent disposition.

This appendix documents an evaluation of the fatigue data to enhance the technical basis for post-storage transportation, handling, and subsequent disposition and to identify future testing needs for Phase 2 of the project.

The purpose of this report is to enhance the technical basis for post-storage transportation. Specifically, this report documents a fatigue evaluation of the ORNL fatigue data on high burnup fuel rods using the Cyclic Integrated Reversible-Bending Fatigue Tester (CIRFT). The following is a summary of the evaluation process, findings, and future plans.

The fatigue evaluation of spent nuclear fuel under transportation conditions is one where the magnitude of the cyclic history is expected to be less than the fatigue limit of the fuel rods. Thus, to conclude fatigue failures do not occur, it is sufficient to show that a strain amplitude representing an expected cyclic history is less than the fatigue or endurance limit of the spent nuclear fuel rods (also defined in terms of strain amplitude). The fatigue evaluation herein considers the current available fatigue test data on cladding materials and high burnup fuel rods, the potential non-conservatism in the HBU fuel rod test data, and the measured cyclic data reported in the MMTT for defining a conservative bounding strain amplitude to represent the expected cyclic history resulting from normal transportation vibration environments.

The HBU fuel rod fatigue data (tested under zero mean strain conditions) indicate the rod level fatigue limit is degraded compared to cladding alloy only test data. Using the form of the O'Donnell-Langer design curve for Zircaloy components, an ORNL design curve for HBU fuel rods was developed to account for this degradation, which is likely caused by stress concentrations at pellet discontinuities during bending. However, the potential detrimental effect of a nonzero tensile mean strain in spent nuclear fuel rods due to the rod-internal pressure and bending under gravity was also considered. Initial estimates predict a 7% degradation because of this expected nonzero mean strain. Additional fatigue testing of high burnup fuel rods is recommended to validate this estimate and quantify the potential magnitude of the degradation in performance. The effect of temperature on the fatigue limit of high burnup fuel rods is also discussed and is concluded to be minor. While data at elevated temperatures would be beneficial, there is currently no additional fatigue testing of high burnup fuel rod planned to determine the magnitude of the effect of temperature. Finally, there is a significant gap between the maximum strain amplitude measured in the MMTT (0.0042%) and the fatigue limit of the ORNL design

curve for HBU fuel rods ($\sim 0.03\%$), indicating that fatigue damage is not expected during normal transportation conditions. However as noted above, additional fatigue testing is recommended to confirm that that fatigue limit at nonzero-mean strain does not decrease significantly.

CONTENTS

| | |
|--|------|
| SUMMARY | iii |
| CONTENTS..... | v |
| LIST OF FIGURES | vi |
| LIST OF TABLES | vii |
| REVISION HISTORY..... | viii |
| ABBREVIATIONS | ix |
| ACKNOWLEDGMENTS | x |
| F2-1. Introduction..... | 1 |
| F2-2. Background..... | 3 |
| F2-2.1 Stress Amplitude vs. Strain Amplitude..... | 3 |
| F2-2.2 Zirconium Alloy Fatigue..... | 3 |
| F2-2.3 The O'Donnell-Langer Fatigue Curve | 5 |
| F2-2.4 Fatigue of High-Burnup Fuel Rods..... | 6 |
| F2-3. Fatigue Design Curves | 9 |
| F2-3.1 Limitation of Applicability | 10 |
| F2-4. Effect Of Nonzero-Mean Strain..... | 11 |
| F2-4.1 Method for Calculating the Effects of Bending under Gravity | 11 |
| F2-4.2 Method for Calculating the Axial Cladding Strain due to Gas Pressure..... | 13 |
| F2-4.2.1 Method for Calculating Average Axial Cladding Strain..... | 13 |
| F2-4.2.2 Method for Calculating Local Axial Cladding Strain | 14 |
| F2-4.3 Total Estimated Additional Strain Due to Static Bending and Rod Internal Pressure..... | 14 |
| F2-4.4 Cladding Strain Results and Discussion | 16 |
| F2-4.4.1 Estimated Effect of Mean Strain on Fatigue Performance..... | 19 |
| F2-5. Effect Of Temperature On Fatigue | 21 |
| F2-6. Measurement Uncertainty Discussion | 23 |
| F2-7. Expected Cyclic History For Transporting Spent Nuclear Fuel | 25 |
| F2-8. Summary And Conclusions | 27 |
| F2-9. REFERENCES | 29 |

LIST OF FIGURES

| | |
|--|----|
| Figure F2-1. Fatigue response of unirradiated and irradiated Zircaloy for various sample geometries and temperatures..... | 5 |
| Figure F2-2. Fatigue of HBU fuel rods compared with Zr alloy and cladding-only test data. Note the strain amplitude of the HBU fuel rod data is calculated from the measured curvature in the CIRFT tests [F2-13]..... | 7 |
| Figure F2-3. Axial cross section of a fuel rod highlighting the discontinuities in the pellet stack. | 8 |
| Figure F2-4. Fatigue of HBU fuel rods compared with Zr alloy and cladding-only test data, including fatigue design curves. | 10 |
| Figure F2-5. Schematic of a fuel rod under gravity between grid spacers..... | 11 |
| Figure F2-6. Schematic of a fuel rod under gravity near the top of the assembly where the top or bottom end plug is not constrained. | 11 |
| Figure F2-7. Schematic of a simple beam with a uniform load. | 12 |
| Figure F2-8. Schematic of how the pressure applied load in an internally pressurized tube. | 13 |
| Figure F2-9. Observations of microstructure at pellet-cladding interface | 15 |
| Figure F2-10. Schematic of how pressure interacts with the pellet ends when the pellets are bonded to the cladding, | 16 |
| Figure F2-11. Fatigue response of unirradiated and irradiated Zircaloy for various sample geometries and temperatures, highlighting the better fatigue performance at RT (circles) compared with elevated temperatures (squares). | 21 |
| Figure F2-12. Comparison of the most severe range of conditions in the MMTT with the fatigue design curve for fuel rods tested under zero-mean strain conditions..... | 26 |

LIST OF TABLES

| | |
|---|----|
| Table F2-1. Reported fatigue limits for Zircaloy-2 and Zircaloy-4 under various test conditions | 4 |
| Table F2-2. O'Donnell-Langer Best-estimate curve for irradiated Zircaloy (zero-mean strain). | 6 |
| Table F2-3. ORNL Fuel Rod best-estimate curve for 17×17 PWR fuel rods (zero-mean strain). | 7 |
| Table F2-4. Correlation parameters for the Zero-Mean Strain O'Donnell-Langer design curve for Zr alloys and the Zero-Mean Strain ORNL Fuel Rod design curve for 17×17 PWR fuel rods (zero-mean strain). | 9 |
| Table F2-5. Dimensions assumed for the various fuel rod types. | 12 |
| Table F2-6. Calculated maximum surface strain from bending in the fuel rod under gravity at RT. | 17 |
| Table F2-7. Calculated minimum and maximum axial strain in a 17×17 PWR fuel rod from internal gas pressure at RT for 150 and 250°C axial strain. | 17 |
| Table F2-8. Calculated maximum axial strain due to RIP in a 17×17 PWR fuel rod for three burnup conditions where the pressures at 150 and 250°C are based on the pressure at RT, assuming no change in volume of number of moles of gas. | 18 |
| Table F2-9. Calculated maximum axial surface strain due to both bending and RIP in a 17×17 PWR fuel rod for three burnup conditions where the pressures at 150°C and 250°C are based on the pressure at RT, assuming no change in volume of number of moles of gas. | 18 |

REVISION HISTORY

| Date | Changes |
|--------|-----------------|
| 3/3/23 | Initial release |

ABBREVIATIONS

| | |
|--------|---|
| BWR | boiling water reactor |
| CIRFT | Cyclic Integrated Reversible-Bending Fatigue Tester |
| DOE | US Department of Energy |
| ENSA | Equipos Nucleares S.A., S.M.E. |
| HBU | high burnup |
| MMTT | multimodal transportation test |
| NE | Office of Nuclear Energy |
| NRC | US Nuclear Regulatory Commission |
| OD | outer diameter |
| ORNL | Oak Ridge National Laboratory |
| PWR | pressurized water reactor |
| RIP | rod internal pressure |
| RT | room temperature |
| Sandia | Sandia National Laboratories |
| SNF | spent nuclear fuel |

ACKNOWLEDGMENTS

The authors thank their US Department of Energy Office of Nuclear Energy sponsor Ned Larson and the Spent Fuel and Waste Science and Technology storage and transportation program leadership for their continued support. The Sister Rod Project would not have been possible without the vision and support of the Electric Power Research Institute, Westinghouse, Framatome, and Dominion Energy.

F2-1. Introduction

The fatigue performance of high-burnup (HBU) light-water reactor (LWR) fuel rods under transportation conditions is a regulatory concern for the disposition of spent nuclear fuel (SNF) [F2-1]. During LWR fuel transportation, the internally pressurized fuel rods are oriented horizontally and experience the vibrations typical of transportation, which cause cyclic bending strains and stresses in the fuel rod. Additionally, the fuel rods may be at an elevated temperature (100–250°C). Thus, an evaluation of fuel rod bending fatigue must consider the following questions.

- What is the expected cyclic history during transportation?
- What is the effect of elevated temperature on fatigue performance?
- What is the effect of the rod internal pressure (RIP) and bending under gravity, which are preloads on the cladding?
- What is the effect of the fuel pellet, which is in contact with, and chemically bonded to, the cladding at HBU?

Using the standard approach to design for fatigue, failures are not expected to occur when the accumulated fatigue damage ratio (D_{fat}) [F2-18] is less than 1.0:

$$D_{fat} = \sum_i^n \frac{N_i}{N_{f(i)}}, \quad (F2-1)$$

where N_i is the expected number of cycles at condition i , $N_{f(i)}$ is the number of cycles that causes failure at condition i , and n is the number of different conditions needed to represent the cyclic history experienced by the component. This method of design for fatigue is only applied when the expected cyclic history contains conditions above the fatigue or endurance limit. When the expected cyclic history conditions are less than the fatigue limit, which is typical for transportation, fatigue damage and thus failure is shown to not occur when¹:

$$\varepsilon_{a,expected} < \varepsilon_{a,limit}, \quad (F2-2)$$

where $\varepsilon_{a,expected}$ or $\sigma_{a,expected}$ is a conservative representation of the expected cyclic history, and $\varepsilon_{a,limit}$ or $\sigma_{a,limit}$ is the fatigue or endurance limit defined as the strain or stress amplitude in which fatigue damage does not occur. This is often defined as the stress/strain amplitude that causes fatigue failure at 1×10^7 cycles.

The fatigue response of a material or component represented by $N_{f(i)}$ cycles and the fatigue limit, $\varepsilon_{a,limit}$, is determined through cyclic fatigue testing of components. Because most of the cycles to failure are needed for initiation rather than propagation, features inherent in the material or component (e.g., surface roughness, nonhomogeneous cross sections, heat-affected zones, welds, residual stress, stress concentrations) are important to consider when testing for fatigue. Additionally, to provide the necessary confidence in predicting that fatigue failures do not occur, conservatism is added to create a design fatigue curve (N_f^{design}) where the design fatigue limit ($\varepsilon_{a,limit}^{design}$) is the strain amplitude at $N_f^{design} = 1 \times 10^7$. Depending on the certainty in the expected cyclic history and consequence to failure, conservatism may also be added by making a design cyclic history more severe than the expected cyclic history. One source of conservatism when the actual number of cycles at $\varepsilon_{a,expected}$ is small is that it is assumed to occur over 1×10^7 cycles, consistent with the fatigue limit. As an example, the expected

¹ The calculation of fatigue damage is not meaningful when the expected cyclic history is below the fatigue limit because it requires extrapolation of the fatigue curve well beyond the range of the data.

number of cycles near an expected strain amplitude (i.e., above the noise) in the MMTT test were ~4000 cycles [F2-31].

This report provides a fatigue evaluation of SNF rods based on testing irradiated and unirradiated cladding alloys [F2-2]–[F2-12] and irradiated fuel rods [F2-14]–[F2-19] to create a design fatigue curve so that a design fatigue limit can be compared with an expected cyclic history based on shipping tests [F2-20]–[F2-21].

The evaluation begins with a review of the fatigue data for Zr alloys and the O'Donnell-Langer correlations. These data are compared with fatigue testing on HBU fuel rods², and the comparison shows a degradation in fatigue performance of fueled rod segments when compared with estimates based on Zr alloy fatigue test data. A modified version of the O'Donnell-Langer design curve referred to herein as the ORNL Fuel Rod design curve is then developed based on the irradiated fuel rod test data, but there are two potential non-conservatisms in the fuel rod data that require further evaluation: (1) the fatigue testing was performed under zero-mean strain conditions, whereas the fuel rod will be under nonzero mean tensile strain conditions, which tends to degrade fatigue performance (see Section 4), and (2) the testing is performed at RT, whereas the fuel rods are at elevated temperature during transportation. These potential non-conservatisms are discussed, and additional testing is identified where necessary to quantify the effect.

² O'Donnell-Langer data was collected on flat samples in reversible bending and rod samples in reversible axial fatigue tests where the strain amplitude was controlled [F2-2]. The HBU fuel rods were tested in reversible bending using the ORNL CIRFT system under load control where strain is calculated from the measured curvature in the test [F2-13].

F2-2. Background

F2-2.1 Stress Amplitude vs. Strain Amplitude

Fatigue testing is performed by applying an alternating stress or strain amplitude and counting the number of cycles to failure.

The fatigue response of a material may be different under stress-controlled fatigue than under strain-controlled fatigue because of the nonlinear behavior of ductile materials. When work hardening occurs during a stress-controlled fatigue test, the maximum strain decreases for a given stress amplitude because work hardening increases the yield strength. In contrast, if the test is performed under strain control, then the stress will increase for the applied strain amplitude. Because of the nonlinear behavior in ductile materials, there may be differences in the plastic energy associated with the hysteresis curve for the two different loading conditions in the low-cycle fatigue regime. However, in the high-cycle regime where the stress and strain are well within the elastic regime, the difference in the two loading conditions is minimal. This justifies measuring high-cycle fatigue data under strain-controlled conditions but reporting the data in terms of stress, which is the approach that O'Donnell-Langer used when developing the fatigue design curves for Zircaloy [F2-2].

Another factor of an SNF rod is that under bending, the stress distribution through the composite rod is nonlinear, which contrasts with the linear stress distribution in a homogeneous material. Thus, there is the potential for confusion regarding how stress is calculated. From a fatigue performance perspective, it is more logical to account for the nonlinear stress distribution, but it is easier to assume that the rod is a homogeneous material in a finite element evaluations of transportation conditions. Unlike stress, the strain distribution remains linear in the composite spent fuel rod under bending. Thus, the measured and predicted strains on the cladding surface will be consistent, regardless of how the spent fuel rod is modeled.

Finally, it is better to present the fatigue data in terms of strain amplitude because the strain-amplitude fatigue limit can be compared directly to measurements of strain amplitude (on the cladding surface) in surrogate fuel rods that have experienced transportation conditions [F2-20].

F2-2.2 Zirconium Alloy Fatigue

The starting point for creating a design fatigue curve for SNF is to understand the fatigue behavior of Zr alloy cladding materials [F2-2]–[F2-10]. O'Donnell and Langer [F2-2] remains the definitive work for fatigue behavior of Zircaloy when designing Zr components for nuclear power applications. O'Donnell-Langer developed design fatigue curves for both unirradiated and irradiated Zircaloy over a temperature range from room temperature (RT) to 315°C (600°F), although all the high-cycle fatigue data were exclusively at 315°C. The use of the high-temperature data to represent fatigue at RT was considered conservative because the data indicated better fatigue performance at RT [F2-2]. The best estimated fatigue limit of both unirradiated and irradiated Zircaloy-2 was reported in terms of zero-mean stress amplitude as 24,790 psi (171 MPa) and 25,730 psi (177 MPa), respectively. Thus, irradiation exposure ranging from 1.5×10^{21} n/cm² to 5.5×10^{21} n/cm² did not significantly affect the fatigue performance of Zircaloy-2. Considering these are essentially equivalent, the corresponding fatigue limit in terms of zero-mean strain amplitude is 0.2%³ (See Table F2-1). This result contrasts with later work by Nakatsuka et al. [F2-3] in which irradiation decreased the fatigue limit from 0.22% for unirradiated Zircaloy-2 to 0.18% for irradiated Zircaloy-2 at a test temperature of 350°C (660°F). Like O'Donnell and Langer, Snowden et al. [F2-4] found that any temperature effect on fatigue of cladding alloys is minor so that

³ This conversion (dividing the stress-based endurance limit by the Young's modulus) is valid because the testing was performed at constant strain amplitudes rather than at constant stress amplitudes, and the stresses are well within the elastic regime.

fatigue curves based on data between 300 and 350°C (570 and 660°F) are applicable to RT. However, the fatigue limit of unirradiated Zircaloy at RT was reported from 0.25% [F2-4] (calculated from stress amplitude of 235 MPa) to ~0.5% [F2-12], which is significantly different than data at higher temperatures [F2-2], [F2-3], [F2-5], [F2-6]. For example, fatigue testing from Wisner et al. [F2-5] on unirradiated Zircaloy-2 indicated that the fatigue limit at 343°C (650°F) was less than 0.14%. Because the transportation of SNF may occur at elevated temperatures, these observations suggests that the effect of temperature on the fatigue performance of irradiated fuel rods should be considered, as discussed in Section F2-5.

Table F2-1 Reported fatigue limits for Zircaloy-2 and Zircaloy-4 under various test conditions

| Material | Test Conditions | Reported Fatigue Limit | Reference |
|------------|--|------------------------|-----------|
| Zircaloy-2 | Zero-Mean Strain, Irradiated and Unirradiated, 315°C | 0.2% | [F2-2] |
| Zircaloy-2 | Zero-Mean Strain, Irradiated, 350°C | 0.18% | [F2-3] |
| Zircaloy-2 | Zero-Mean Strain, Unirradiated, 350°C | 0.22% | [F2-3] |
| Zircaloy-2 | Zero-Mean Strain, Unirradiated, R.T. | 0.25% | [F2-4] |
| Zircaloy-4 | Zero-Mean Strain, Unirradiated, R.T. | ~0.5% | [F2-12] |
| Zircaloy-2 | Zero-Mean Strain, Unirradiated, 343°C | <0.14% ^a | [F2-5] |

^a Wisner et al. measured a fatigue life of 283091 cycles at a strain amplitude of 0.14%.

The standard geometry test samples used in previous tests are flat plates tested in bending or rods tested in the axial direction [F2-2]. In each case, the entire surface area of the sample experiences the maximum strain at the peaks of the fatigue cycles. Pure bending of a rod or tube is different in the sense that the maximum strain in bending occurs only on a line over the surface rather than over the entire surface area. Thus, the volume of material that experiences the maximum strain during testing is significantly smaller than a standard geometry sample. To explore this potential sample geometry effect, Zircaloy-4 cladding tube samples were fatigue-tested in bending using the Cyclic Integrated Reversible-Bending Fatigue Tester (CIRFT) (Section F2-2.4) and compared with the fatigue data from standard sample geometries [F2-13]. These data are replotted in Figure F2-1, where the mean strain is the average of the maximum and minimum strain during testing, which is zero in this case. The Zircaloy-4 cladding-only data are consistent with other Zircaloy-4 data that used a standard sample geometry but are generally higher than the Zircaloy-2 data, as represented by the best-estimate correlation from O'Donnell-Langer for irradiated Zircaloy [F2-2]. This could be because there are differences in composition or because the O'Donnell-Langer correlation is based on fatigue testing at 315°C (600°F). The conclusion from testing the cladding-only sample geometry is that fatigue performance is not affected by sample geometry.

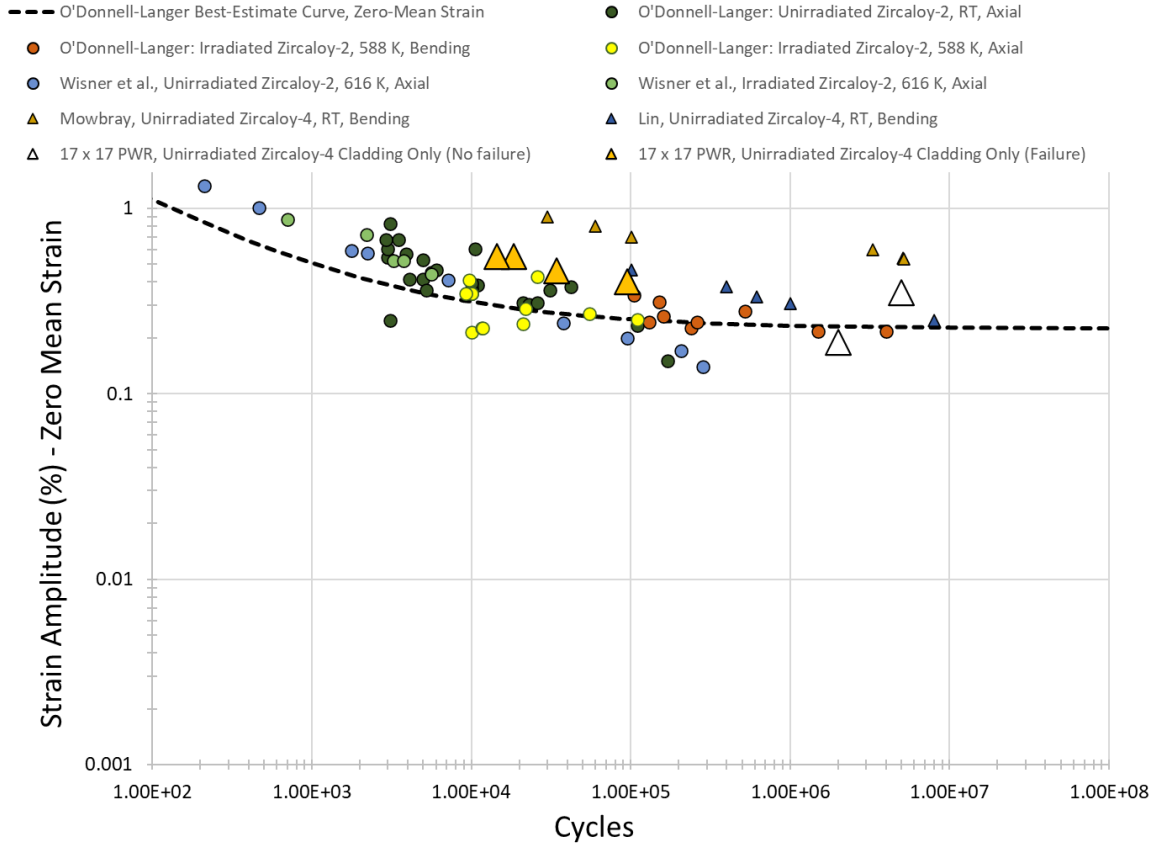


Figure F2-1. Fatigue response of unirradiated and irradiated Zircaloy for various sample geometries and temperatures.

F2-2.3 The O'Donnell-Langer Fatigue Curve

The original O'Donnell-Langer fatigue curve [F2-2] was in the form of stress vs. fatigue cycles, as shown in Eq. (F2-3):

$$S = \frac{E}{F_c \sqrt{N}} \ln \frac{100}{100 - RA} + S_e, \quad (F2-3)$$

where S is the stress amplitude that causes fatigue failure at N cycles; S is calculated from the applied range of strain as $\frac{1}{2} \varepsilon_{range} E$; E is the elastic modulus; F_c is a constant that is equal to 4; RA is the reduction in area of a tensile test but is effectively used as a fit parameter; and S_e is the endurance limit or fatigue limit below which fatigue failure is not expected for a practical number of fatigue cycles.

This model can be redefined in terms of the strain amplitude (ε_a) by dividing Eq. (F2-3) by the elastic modulus to give

$$\varepsilon_a = \frac{1}{F_c \sqrt{N}} \ln \frac{100}{100 - RA} + \varepsilon_e, \quad (F2-4)$$

where ε_e is the fatigue limit in terms of strain amplitude. The strain-based parameters of the O'Donnell-Langer model for irradiated Zircaloy shown in Figure F2-1 are provided in Table F2-2.

Table F2-2. O'Donnell-Langer Best-estimate curve for irradiated Zircaloy (zero-mean strain).

| Parameters for Eq. (F2-4)* | |
|----------------------------|--------|
| RA | 30 |
| ε_e | 0.0022 |
| F_c | 4 |

* These values are calculated from the stress-based O'Donnell-Langer model for irradiated Zircaloy. Because O'Donnell-Langer did not report RA for irradiated Zircaloy, the value of 30 was determined by matching the model predictions to that plotted in Figure 2 of O'Donnell and Langer [F2-2].

F2-2.4 Fatigue of High-Burnup Fuel Rods

The US Nuclear Regulatory Commission (NRC) sponsored the development of the CIRFT system to measure the fatigue performance of various fuel rod designs from both pressurized water reactors (PWRs) and boiling water reactors (BWRs) [F2-14]–[F2-16], and Oak Ridge National Laboratory (ORNL) developed the system. The system can perform reversible cyclic pure-bending testing at either a zero or nonzero mean strain, although in the past, it has only been applied to zero-mean strain conditions [F2-14]–[F2-16]. Three different spent fuel rod types were tested under both NRC and US Department of Energy sponsorship: (1) 15×15 PWR fuel rods with Zircaloy-4 cladding, (2) 17×17 PWR fuel rods with M5 cladding, and (3) 9×9 BWR fuel rods with Zircaloy-2 cladding [F2-16]. Additionally, CIRFT testing of 17×17 PWR fuel rods with Zircaloy-4, M5, and ZIRLO cladding was completed as part of the Sister Rod Project [F2-17]. The exposures in this database range from 45 to 67 GWd/MTU rod-average exposure. These data are replotted in Figure F2-2 and show a significant degradation in the high-cycle fatigue performance of the HBU fuel rods compared with the performance of Zr alloys.

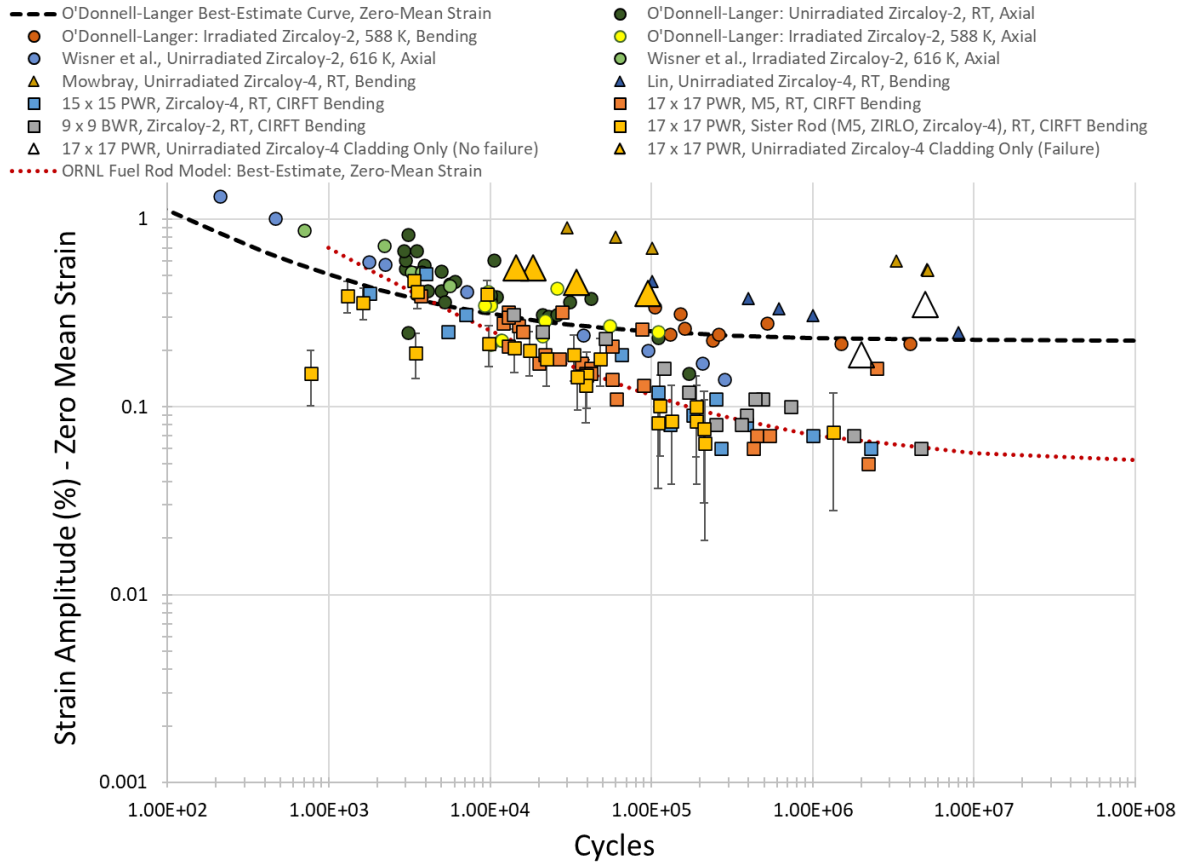


Figure F2-2. Fatigue of HBU fuel rods compared with Zr alloy and cladding-only test data. Note the strain amplitude of the HBU fuel rod data is calculated from the measured curvature in the CIRFT tests [F2-13]

The best estimate correlation through the 17×17 PWR fuel rod data is the ORNL Fuel Rod correlation. Table F2-3 provides the parameters of Eq. (F2-4).

Table F2-3. ORNL Fuel Rod best-estimate curve for 17×17 PWR fuel rods (zero-mean strain).

| Parameters for Eq. (F2-4) | |
|---------------------------|--------|
| RA | 56 |
| ε_e | 0.0005 |
| F_c | 4 |

One outcome of fatigue-testing fuel rods was the recognition that discontinuities in the pellet (e.g., pellet cracks, pellet-to-pellet interfaces) (Figure F2-3) cause stress concentration in HBU (45–70 GWd/MTU rod-average exposure) fuel rods under bending [F2-16]–[F2-19]. Because fatigue failures initiate at the high-stress/high-strain locations, the increase in local stress/strain in the cladding near the discontinuities in the pellet causes the observed decrease in fuel rod fatigue performance compared with the performance of the cladding alone. The magnitude of the stress/strain concentration can be estimated as the ratio of the fatigue limit for cladding alloys to that of the HBU fuel rods ($0.2\%/0.06\% = 3.3$).

Best estimate correlations are typically not used for system design or conservative decision-making. Design curves that provide a factor of safety are typically used and are developed in Section 3.

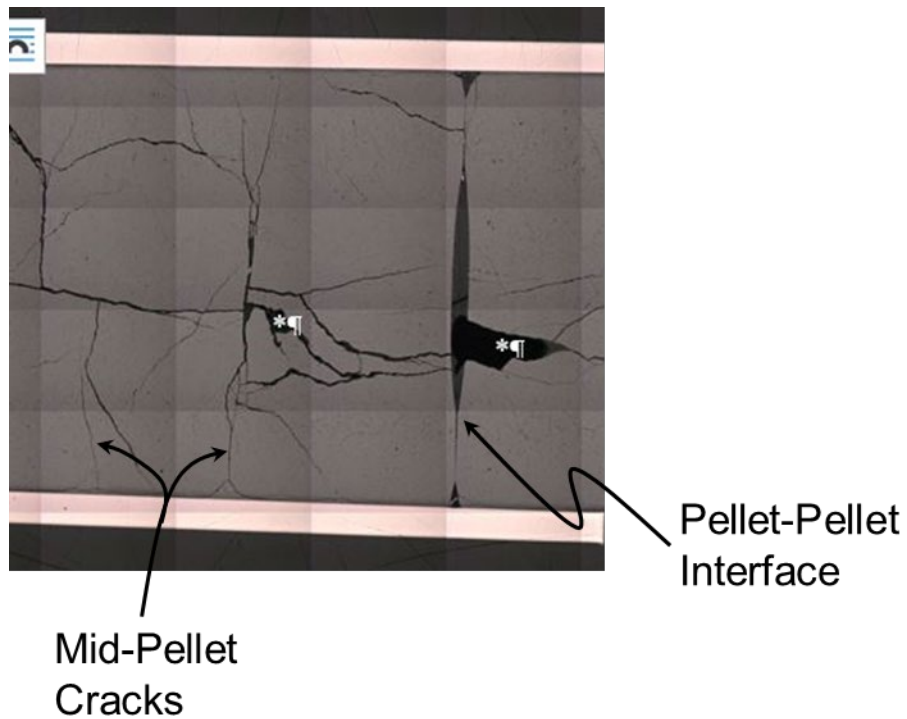


Figure F2-3. Axial cross section of a fuel rod highlighting the discontinuities in the pellet stack.

F2-3. Fatigue Design Curves

For design purposes, O'Donnell-Langer used the lowest of either decreasing the stress/strain amplitude by a factor of two or decreasing the number of cycles by a factor of 20. For high cycle fatigue performance considered herein, the more conservative change is decreasing the stress/strain amplitude by a factor of two, and only this version was considered herein. O'Donnell-Langer [F2-2] did not indicate that these design factors were based on a statistical data evaluation. Rather, they appear to be based on engineering judgement. However, the approach has been universally accepted by industry [F2-32] and thus is a reasonable approach to apply to the ORNL Fuel Rod correlation. The design curve parameters for both Zr alloys and HBU fuel rods are provided Table F2-4, and Figure F2-2 is replotted in Figure F2-4 with both correlations to show that the design curves bounds the data, except the ORNL Fuel Rod design curve does not bound the reported uncertainty in the sister rod data [F2-17]. This exception is discussed in Section F2-6, but the expectation is that fatigue damage does not occur at strain amplitudes below the fatigue limit.

Table F2-4. Correlation parameters for the Zero-Mean Strain O'Donnell-Langer design curve for Zr alloys and the Zero-Mean Strain ORNL Fuel Rod design curve for 17×17 PWR fuel rods (zero-mean strain).

| | O'Donnell-Langer design curve parameters for Eq. (F2-4) | ORNL Fuel Rod design curve parameters for Eq. (F2-4) |
|-----------------|--|---|
| RA | 30 | 56 |
| ε_e | 0.0011 | 0.00025 |
| F_c | 8 | 8 |

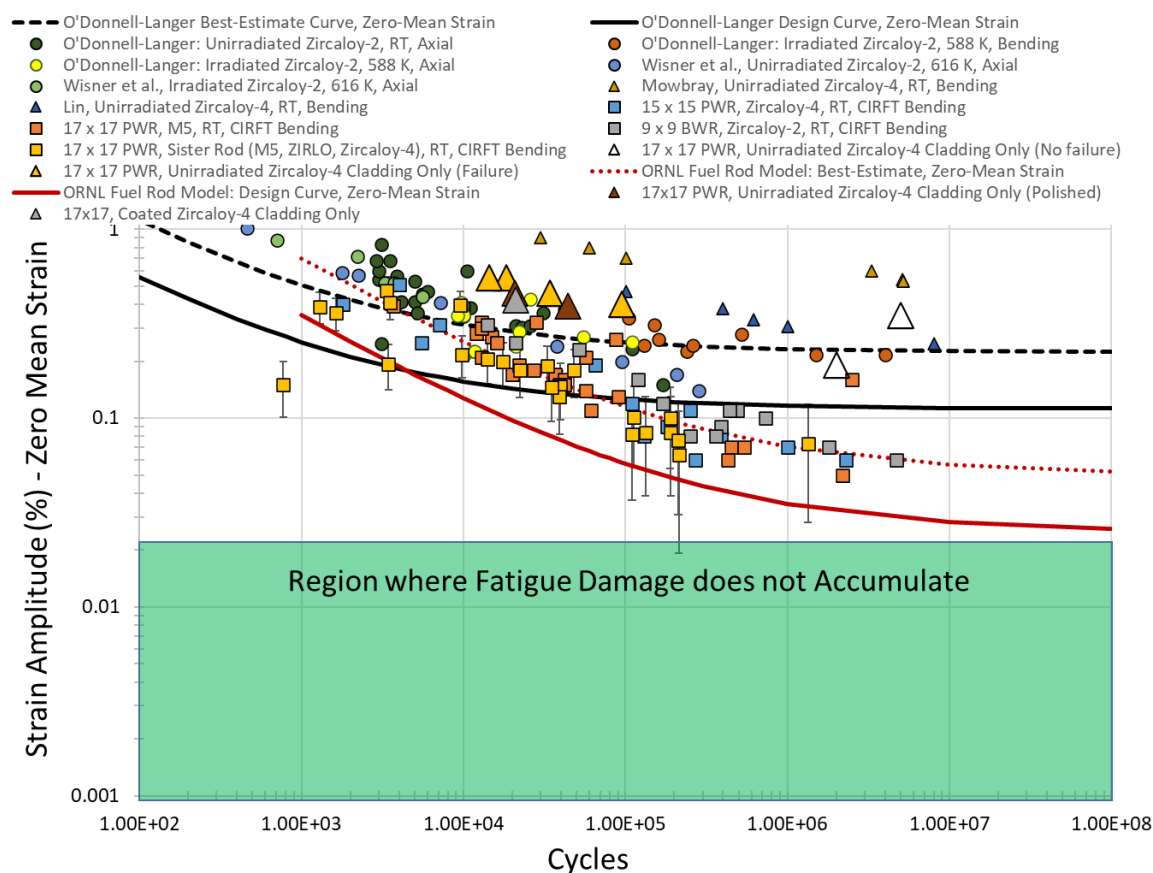


Figure F2-4. Fatigue of HBU fuel rods compared with Zr alloy and cladding-only test data, including fatigue design curves.

F2-3.1 Limitation of Applicability

Consistent with NUREG-2224 [F2-18], the applicability of the ORNL Fuel Rod design curve is limited to loading of HBU fuel rods (45-67 GWd/MTU, rod average exposure) in bending where the cyclic strain is in the axial direction. This design curve is not applicable to evaluating the fatigue performance when the cyclic strain is in the hoop direction.

F2-4. Effect Of Nonzero-Mean Strain

Traditionally, fatigue testing is performed at zero-mean strain, which means the testing is performed in a reversible manner so that the average strain ($\frac{\epsilon_{max} + \epsilon_{min}}{2}$) is zero. However, fatigue in real components is rarely under a zero-mean strain condition. In most cases, the components are under load when experiencing fatigue cycles, and when the load is tensile this causes a decrease in the fatigue performance. The best approach is to directly test the effect of a prototypical nonzero-mean tensile strain on the fatigue performance and then multiply the zero-mean strain design curve by the observed degradation factor. These observed degradation factors can then be fit to a correlation, such as the Goodman factor ($1 - \frac{\sigma_{mean}}{\sigma_{UTS}}$), which can then be applied more generically in design. O'Donnell and Langer [F2-2] considered the effect of mean tensile strain using a degradation factor that was validated by fatigue testing performed under conditions in which the mean tensile strain was 1% [F2-12]. The O'Donnell-Langer degradation factor for mean strain is:

$$\frac{\sigma_{UTS} - S_b}{\sigma_{UTS} - S}, \quad (F2-5)$$

where σ_{UTS} is the ultimate strength, S_b is the cyclic yield strength, and S is the stress amplitude defined in Eq. (F2-3). For irradiated Zircaloy, O'Donnell and Langer [F2-2] reported that ultimate strength was between 60 and 70 ksi (410–480 MPa), and the cycle yield strength was measured as 34 ksi (~230 MPa).

Because the testing performed on spent fuel rods was under zero-mean strain conditions, the design curve in Figure F2-4 may be nonconservative given that internal gas pressure and bending under gravity cause cladding strain that results in a nonzero-mean tensile strain. The following section evaluates those strains to determine whether they are significant.

F2-4.1 Method for Calculating the Effects of Bending under Gravity

To assess the magnitude of static bending stress and strain when the rod is transported in a horizontal orientation, simple beam correlations are used, assuming a uniform load as a function of the mass of the rod times gravity. For a PWR rod, the deflection and slope at the spacer grid locations is assumed to be zero (Figure F2-5), except at the ends of the rods where there is no neighboring grid (Figure F2-6).

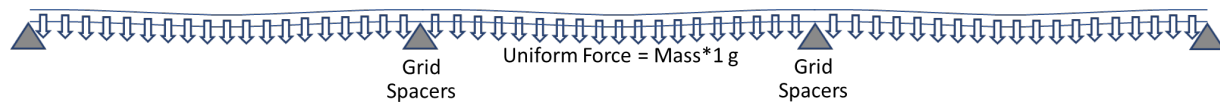


Figure F2-5. Schematic of a fuel rod under gravity between grid spacers.

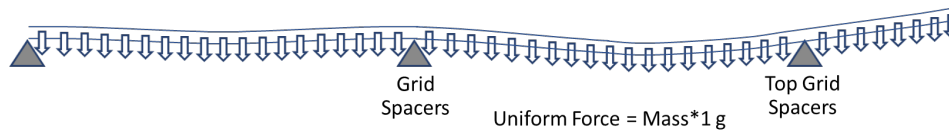


Figure F2-6. Schematic of a fuel rod under gravity near the top of the assembly where the top or bottom end plug is not constrained.

In BWRs, the top and bottom ends of the rods are constrained so that the PWR condition is conservative. Thus, by assuming that both ends are simply constrained, the maximum deflection and strain will be more conservative than the most limiting section at the top or bottom of the PWR assembly.

A schematic of a simply supported beam with a uniform load is shown in Figure F2-7, and the deflection is calculated by Eq. (F2-6) [F2-22]:

$$\Delta_x = \frac{wx}{24EI} (l^3 - 2lx^2 + x^3). \quad (\text{F2-6})$$

where Δ_x is the displacement (mm) from horizontal as a function of x , x is the distance from the left most simple support (mm), l is the length of the span between the spacer grids (mm), w is the uniform load (N/mm), and EI is the flexural rigidity of the fuel rod (N-mm²).

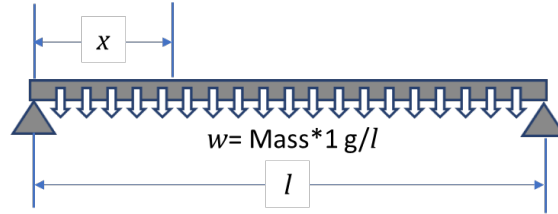


Figure F2-7. Schematic of a simple beam with a uniform load.

The maximum moment at the midpoint of the span is [F2-22]:

$$M_{max} = \frac{wl^2}{8}. \quad (\text{F2-7})$$

The dimensions used in this evaluation for the various fuel rod types are provided in Table F2-5. The burnup of the fuel rods is assumed to be high enough to close the gap between the pellet and cladding. Thus, the cladding thickness is the rod outer diameter [OD] minus the pellet OD, then divided by two. This information is used to calculate the mass between the spacer grids.

Table F2-5. Dimensions assumed for the various fuel rod types.

| | 17 × 17 PWR | 15 × 15 PWR | 9 × 9 BWR |
|---|--------------|--------------|--------------|
| Fuel rod (or Cladding) OD (mm) | 9.45 [F2-23] | 10.7 [F2-24] | 11.4 [F2-27] |
| Pellet OD (mm) | 8.3 [F2-23] | 9.25 [F2-24] | 10.1** |
| Flexural rigidity at RT (N-m ²) | 26 [F2-26] | 41* | 50*** |

* Calculated as average of flexural rigidity data reported in Table 2 of Wang et al. [F2-27].

** Estimated as fuel rod OD minus 2 × 0.66 mm (cladding thickness reported in NUREG-1754 [F2-25]).

*** Calculated as average of LMK data reported in Table 6b of Wang et al. [F2-24]. (LMK01 was excluded because it was static tested before dynamic testing.)

For calculating the mass, the pellet density was 10.8 g/cm³ (98.5% of theoretical density, 10.97 g/cm³), and the cladding density was 6.5 g/cm³.

The radius of curvature at the midpoint is calculated from the maximum moment and flexural rigidity as

$$\rho = \frac{EI}{M_{max}}, \quad (\text{F2-8})$$

The maximum cladding surface strain in the axial direction over the region in pure bending can then be calculated using the standard beam theory relationship:

$$\varepsilon_b = \frac{OD/2}{\rho}. \quad (F2-9)$$

F2-4.2 Method for Calculating the Axial Cladding Strain due to Gas Pressure

The purpose of this calculation is only to determine if the mean strain is potentially significant compared to the fatigue performance, which will help determine whether testing of pressurized segments (capturing the nonzero mean strain effects) is valuable. Two methods are defined to calculate a minimum and maximum axial strain, thus defining the potential range. The first method assumes that the gas pressure is only applied at the ends of the fuel rod and the resulting axial strain are uniform over the entire length of the cladding. This method defines the minimum of the range. The second method assumes the pellets are largely bonded to the cladding, which effectively localizes the axial strain at pellet-pellet interfaces. This method defines the maximum of the range.

F2-4.2.1 Method for Calculating Average Axial Cladding Strain

The average axial cladding strain is calculated assuming the fission gas pressure at end-of-life is modelled as an internally pressurized closed tube (see Figure F2-8), which induces biaxial tension with an approximate 2:1 ratio for the hoop-to-axial directions.

The cladding hoop stress can be estimated by:

$$\sigma_h = P \frac{OD_{pellet}}{(OD_{cladding} - OD_{pellet})} \quad (F2-10)$$

where P is the internal pressure; OD_{pellet} is the outer diameter of the pellet or inner diameter of the cladding; and $OD_{cladding}$ is the outer diameter of the cladding.

The average axial stress in the fuel rod due to gas pressure is then:

$$\sigma_{z-average} = P \frac{(OD_{pellet}/2)^2}{\left(\frac{OD_{cladding}}{2}\right)^2 - \left(\frac{OD_{pellet}}{2}\right)^2} \quad (F2-11)$$

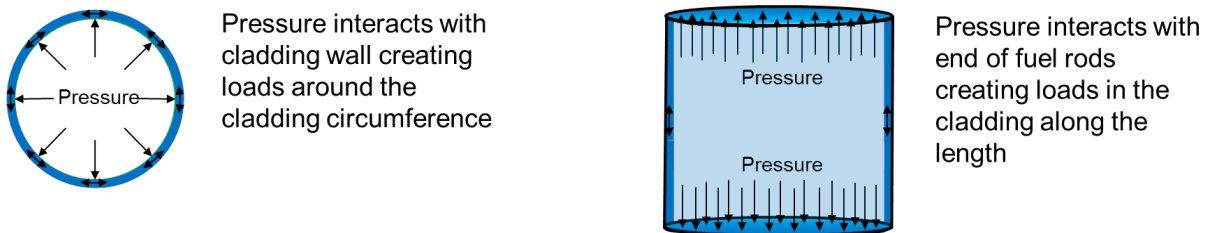


Figure F2-8. Schematic of how the pressure applied load in an internally pressurized tube.

The average axial cladding strain for an internally pressurized tube is then

$$\varepsilon_{z-average} = \frac{\sigma_{z-average}}{E_{clad}} - \nu \frac{\sigma_h}{E_{clad}}, \quad (F2-12)$$

which accounts for the negative strain from the hoop stress due to the Poisson effect.

F2-4.2.2 Method for Calculating Local Axial Cladding Strain

In a high-burnup fuel rod, the stress state in the cladding of an SNF rod due to the fission gas pressure at end-of-life is complicated by the observation of chemical bonding between the pellet and cladding and the crack structure within the pellet where the fission gas resides. While there are often circumferential cracks in the pellet near the pellet-cladding interface, which might be considered a gap, there are also many areas where no such gap is obvious (see Figure F2-9). Under these circumstances, the internal pressure will not apply uniformly to the cladding like an internally pressurized tube. Rather, the fission gas will apply force to the cladding through pellet pieces. Another consideration in dry storage is that there will likely be some temperature distribution in the pellet, which could create pressure distributions. Given the low thermal conductivity of the fuel pellet, it is reasonable to conclude the maximum temperature would be at the center of the pellet, meaning the fission gas pressure of the internal cracks would dominate over the pressure in the circumferential cracks near the cladding, which pushes the pellet pieces against the cladding. The forces from internal gas pressure are then applied to the cladding through the solid pellet.

Another important implication of the forces being transferred through a solid-solid interface is that there will be frictional forces at the interface, as opposed to the case when gas is in direct contact with the tube and the frictional forces at the interface are zero. In high-burnup fuel rod, the axial stress in the cladding will be non-uniform. A schematic of a pellet stack in a high burnup fuel rod is provided in Figure F2-10. Assuming the pellets are bonded to the cladding, the axial cladding stress in the region in contact with the pellet will be a combination of the compressive stress due to the pressure compressing the pellet in the axial direction and the tensile stress caused by the pellet constraining the Poisson contraction in the axial direction due to the cladding hoop stress (i.e., the plane strain assumption, see Figure F2-10b).

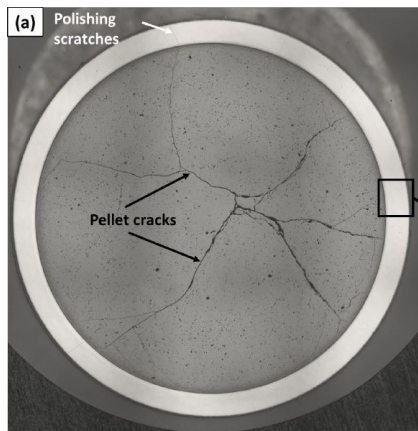
In contrast, the local axial tensile stresses at the pellet ends can be estimated based on the schematic in Figure F2-10c. In this region the pressure acts on the pellet ends, which induces an axial tensile stress (and strain) that is equivalent to the average axial stress and strain prediction. However, it is further assumed that there is sufficient contact between the pellet ends to constrain the Poisson contraction from the hoop stress, which means that the second term in Eq. 12 is now zero. Thus, the local axial cladding strain in the cladding near a pellet-pellet interface is then defined as

$$\varepsilon_{z-local} = \frac{\sigma_{z-average}}{E_{clad}}, \quad (F2-13)$$

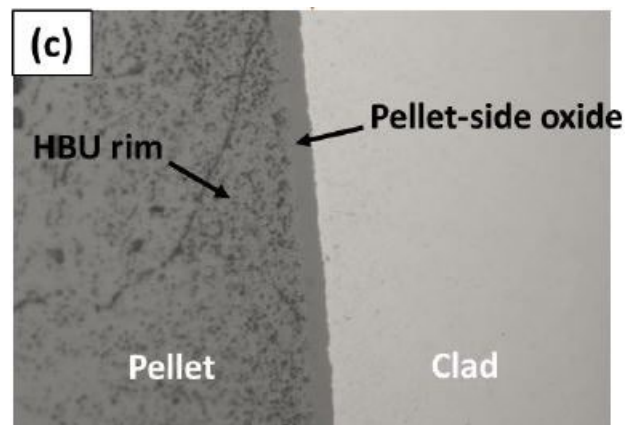
F2-4.3 Total Estimated Additional Strain Due to Static Bending and Rod Internal Pressure

The total axial cladding strain on the cladding surface is then Eq. (F2-9) plus Eq. (F2-12) or Eq. (F2-13):

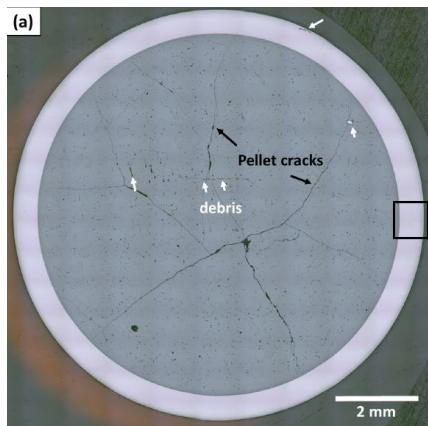
$$\varepsilon_T = \varepsilon_b + \varepsilon_z. \quad (F2-14)$$



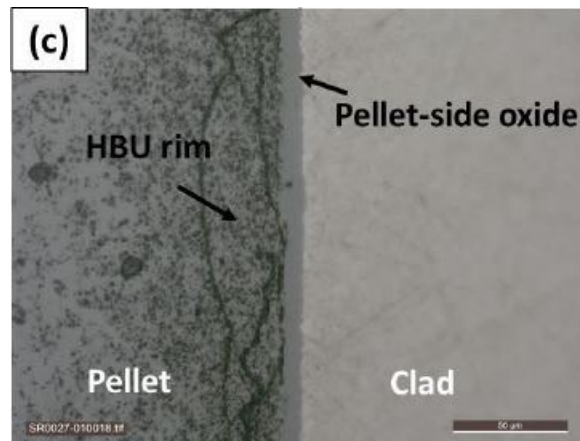
a) Pellet cracks in an M5 fuel rod 30AE14 (elevation = ~1685 mm, Figure B-9a from [F2-23])



b) Pellet-cladding interface in a region where there is not clear circumferential cracking that could be considered a gap (Figure B-9c from [F2-23])

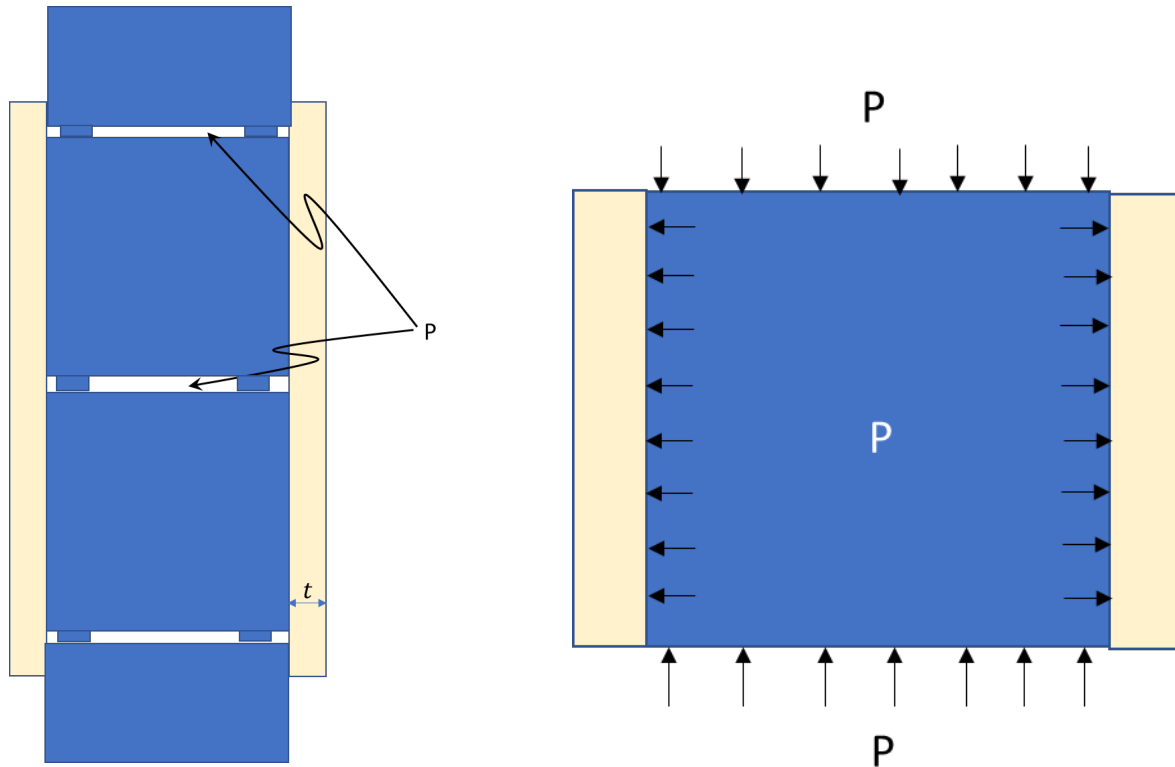


c) Pellet cracks in an M5 fuel rod 30AE14 (elevation = ~2210 mm, Figure B-10a from [F2-23])



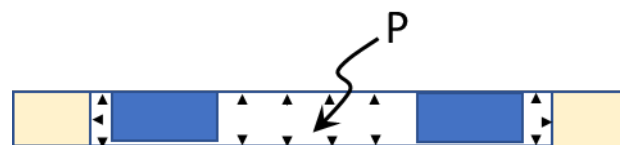
d) Pellet-cladding interface in a region where there is clear circumferential cracking that could be considered a gap (Figure B-10c from [F2-23])

Figure F2-9. Observations of microstructure at pellet-cladding interface



a) An idealized representation of a pellet stack in a high burnup fuel rod where the pellet and cladding are bonded and the pellet ends are in contact but not bonded

b) schematic of how pressure within the pellet interacts with bonded cladding.



c) schematic of how the pressure at the pellet ends interacts with the cladding. The pellet features shown will resist the Poisson contraction in the axial direction due to the local hoop stress.

Figure F2-10. Schematic of how pressure interacts with the pellet ends when the pellets are bonded to the cladding,

F2-4.4 Cladding Strain Results and Discussion

The calculated maximum strains for horizontally oriented fuel rods under gravity are provided in Table F2-6 for different spans between the grid spacers. Although the 17×17 PWR fuel rod is predicted to have the highest strains under gravity, there is very little difference between the designs. This indicates that as mass increases (causing more strain) and flexural rigidity increases (causing less strain) with rod diameter, the effects nearly cancel each other out. Currently, it is assumed that the calculated strains from

bending at RT apply to higher temperatures. However, flexural rigidity is expected to decrease at elevated temperature because of the decrease in Young's modulus of both the cladding and the pellet, which would tend to increase the bending strains. This effect likely can be accounted for by added conservatism when defining the expected cyclic strain history. The typical span in PWR and BWR fuel is between 500 and 550 mm.

Table F2-6. Calculated maximum surface strain from bending in the fuel rod under gravity at RT.

| Span length (mm) | Maximum bending strain (%) | | |
|------------------|----------------------------|-------------|-----------|
| | 17 × 17 PWR | 15 × 15 PWR | 9 × 9 BWR |
| 400 | 0.0025 | 0.0022 | 0.0023 |
| 450 | 0.0031 | 0.0028 | 0.0029 |
| 500 | 0.0038 | 0.0035 | 0.0035 |
| 550 | 0.0046 | 0.0042 | 0.0043 |
| 600 | 0.0055 | 0.0050 | 0.0051 |
| 650 | 0.0065 | 0.0059 | 0.0060 |
| 700 | 0.0075 | 0.0068 | 0.0069 |
| 750 | 0.0086 | 0.0079 | 0.0080 |

When considering the effect of internal pressure on axial strain, the 17 × 17 PWR fuel rod exhibited the highest axial strain at a given pressure. Thus, the 17 × 17 PWR fuel rod represents the conservative condition when compared with the 15 × 15 PWR and 9 × 9 BWR fuel rods. The effect of the internal pressure on the local (max) and average (min) axial strain in a 17 × 17 PWR fuel rod is provided in Table F2-7. There is almost an order of magnitude difference in the min and max predicted strains.

Based on the data in Figure C-10 of Morris and Montgomery [F2-29], an approximate RIP at RT can be estimated for different rod-average burnups. For 50 GWd/MTU, the estimated RIP is 4 MPa; for 70 GWd/MTU, the estimated RIP is 6 MPa; for 80 GWd/MTU, the estimated RIP is 7 MPa. Given this input, the predicted maximum axial strain caused by RIP at the potential transportation temperatures for each burnup level is provided in Table F2-8. The effect of adding the bending strains to the strains due to RIP are provided in Table F2-9. Thus, the total maximum axial strain is estimated to vary from ~0.02 to ~0.06%, depending on burnup and temperature during transportation. The corresponding minimum range in axial strain is ~0.007 to ~0.012%

Table F2-7. Calculated minimum and maximum axial strain in a 17 × 17 PWR fuel rod from internal gas pressure at RT for 150 and 250°C axial strain.

| Pressure | Hoop stress | Axial stress | RT Average axial strain (min) | RT Local axial strain (max) | 150°C Average axial strain (min) | 150°C Local axial strain (max) | 250°C Average axial strain (min) | 250°C Local axial strain (max) |
|----------|-------------|--------------|-------------------------------|-----------------------------|----------------------------------|--------------------------------|----------------------------------|--------------------------------|
| (MPa) | (MPa) | (MPa) | (%) | (%) | (%) | (%) | (%) | (%) |
| 2 | 14.4 | 6.7 | 0.001 | 0.007 | 0.001 | 0.008 | 0.001 | 0.008 |
| 3 | 21.7 | 10.1 | 0.002 | 0.011 | 0.002 | 0.012 | 0.002 | 0.013 |
| 4 | 28.9 | 13.5 | 0.002 | 0.015 | 0.002 | 0.016 | 0.002 | 0.017 |
| 5 | 36.1 | 16.9 | 0.003 | 0.018 | 0.003 | 0.020 | 0.003 | 0.021 |

Table F2-7. Calculated minimum and maximum axial strain in a 17×17 PWR fuel rod from internal gas pressure at RT for 150 and 250°C axial strain, continued.

| Pressure | Hoop stress | Axial stress | RT Average axial strain (min) | RT Local axial strain (max) | 150°C Average axial strain (min) | 150°C Local axial strain (max) | 250°C Average axial strain (min) | 250°C Local axial strain (max) |
|----------|-------------|--------------|-------------------------------|-----------------------------|----------------------------------|--------------------------------|----------------------------------|--------------------------------|
| 6 | 43.3 | 20.2 | 0.003 | 0.022 | 0.003 | 0.024 | 0.004 | 0.025 |
| 7 | 50.5 | 23.6 | 0.004 | 0.026 | 0.004 | 0.028 | 0.004 | 0.029 |
| 8 | 57.7 | 27.0 | 0.004 | 0.029 | 0.005 | 0.032 | 0.005 | 0.034 |
| 9 | 65.0 | 30.4 | 0.005 | 0.033 | 0.005 | 0.035 | 0.005 | 0.038 |
| 10 | 72.2 | 33.7 | 0.005 | 0.036 | 0.006 | 0.039 | 0.006 | 0.042 |
| 11 | 79.4 | 37.1 | 0.006 | 0.040 | 0.006 | 0.043 | 0.007 | 0.046 |
| 12 | 86.6 | 40.5 | 0.006 | 0.044 | 0.007 | 0.047 | 0.007 | 0.051 |
| 13 | 93.8 | 43.9 | 0.007 | 0.047 | 0.007 | 0.051 | 0.008 | 0.055 |

Table F2-8. Calculated maximum axial strain due to RIP in a 17×17 PWR fuel rod for three burnup conditions where the pressures at 150 and 250°C are based on the pressure at RT, assuming no change in volume of number of moles of gas.

| Temp. (°C) | Temp. (K) | Beginning of Life pressure (MPa) | Axial strain (%) | ~50 GWd/MTU | | ~70 GWd/MTU | | ~80 GWd/MTU | |
|------------|-----------|----------------------------------|------------------|----------------|------------------|----------------|------------------|----------------|------------------|
| | | | | Pressure (MPa) | Axial strain (%) | Pressure (MPa) | Axial strain (%) | Pressure (MPa) | Axial strain (%) |
| 25 | 298 | 2.0 | 0.007 | 4.0 | 0.015 | 6.0 | 0.022 | 7.0 | 0.029 |
| 150 | 423 | 2.8 | 0.011 | 5.7 | 0.022 | 8.5 | 0.034 | 9.9 | 0.039 |
| 250 | 523 | 3.5 | 0.015 | 7.0 | 0.029 | 10.5 | 0.044 | 12.3 | 0.052 |

Table F2-9. Calculated maximum axial surface strain due to both bending and RIP in a 17×17 PWR fuel rod for three burnup conditions where the pressures at 150°C and 250°C are based on the pressure at RT, assuming no change in volume of number of moles of gas.

| Temp. (°C) | Temp. (K) | Beginning of Life pressure (Mpa) | Total strain (%) | ~50 GWd/MTU | | ~70 GWd/MTU | | ~80 GWd/MTU | |
|------------|-----------|----------------------------------|------------------|----------------|------------------|----------------|------------------|--------------|------------------|
| | | | | Pressure (Mpa) | Total strain (%) | Pressure (Mpa) | Total Strain (%) | Pressure Mpa | Total Strain (%) |
| 25 | 298 | 2.0 | 0.012 | 4.0 | 0.019 | 6.0 | 0.026 | 7.0 | 0.034 |
| 150 | 423 | 2.8 | 0.016 | 5.7 | 0.027 | 8.5 | 0.038 | 9.9 | 0.044 |
| 250 | 523 | 3.5 | 0.019 | 7.0 | 0.034 | 10.5 | 0.049 | 12.3 | 0.056 |

F2-4.4.1 Estimated Effect of Mean Strain on Fatigue Performance

The potential effect of a nonzero mean strain on the fatigue limit can be estimated by various degradation models [F2-2],[F2-33]. The Soderberg relation is one model that is amenable to a strain-based representation and is considered more conservative than other models [F2-33]. The strain-based version of the Soderberg relation is as follows:

$$\varepsilon_a(\varepsilon_{mean} \neq 0) = \varepsilon_a(\varepsilon_{mean} = 0) \left(1 - \frac{\varepsilon_{mean}}{\varepsilon_{yield}} \right) \quad (15)$$

Based on axial tensile testing of tube material [F2-34], the strain at yield (ε_{yield}) is estimated to be between 0.6% and 0.8%. If the mean strain is assumed to be 0.05% (see Table F2-9) and the strain at yield is 0.7%, the model predicts an ~7% degradation. Like any model, validation testing is needed to determine if the predicted degradation is a reasonable estimate of how fatigue of HPU fuel rods degrades because of a pressure-induced nonzero-mean strain effect.

This page is intentionally blank

F2-5. Effect Of Temperature On Fatigue

O'Donnell and Langer [F2-2] considered the effect of temperature when developing a design curve for Zircaloy-2. O'Donnell and Langer [F2-2] argued that it was applicable to temperatures from 25 to 315°C (77 to 600°F) [F2-2]. The O'Donnell-Langer justification for this conclusion was to base the design limit on elevated test data, recognizing that this was conservative relative to RT data, which typically has better fatigue performance. This trend is observed in Figure F2-11, which indicates better high-cycle fatigue performance at RT compared with elevated temperature.

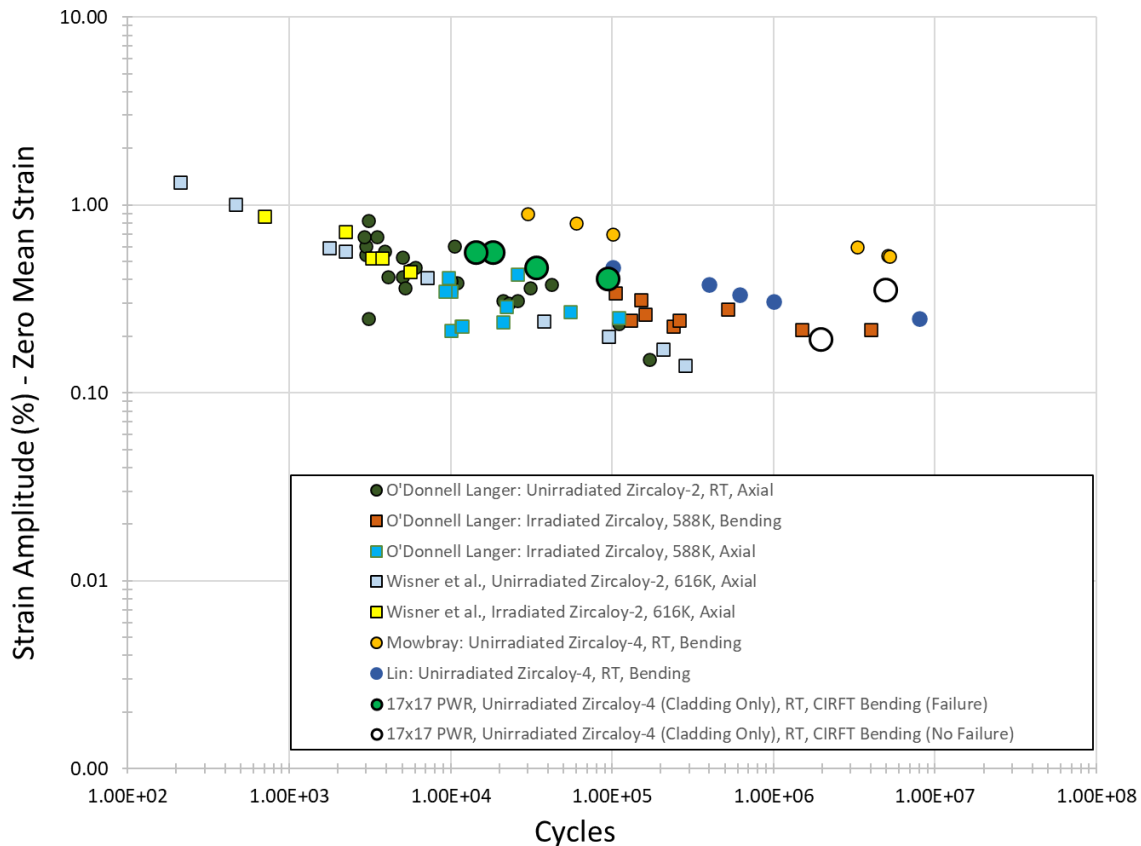


Figure F2-11. Fatigue response of unirradiated and irradiated Zircaloy for various sample geometries and temperatures, highlighting the better fatigue performance at RT (circles) compared with elevated temperatures (squares).

Several additional studies have evaluated the temperature effect on fatigue in Zircaloy, and the general conclusion is that the effect of temperature on fatigue performance from RT to ~400°C is small [F2-4], [F2-8], [F2-10].

The small effect of temperature on the Zircaloy cladding fatigue performance suggests a similar response to temperature should be seen in the fatigue data for the fuel rods. Although fatigue testing at elevated temperature would be beneficial, it is expected that the main effect of temperature on the fuel rod will be increasing the RIP and thus the mean strain. It is expected that once the effect of mean strain is better understood, the design limit based on the RT measurement would be applicable to the higher temperatures during transportation.

This page is intentionally blank

F2-6. Measurement Uncertainty Discussion

The measurement uncertainty of the sister rod CIRFT data was evaluated in Montgomery [F2-30] and is shown in Figure F2-4 with error bars on the datapoints. The analysis found that the relative uncertainty in the data increased as the strain amplitude in testing decreased. For example, the uncertainty at 0.2% strain amplitude was 0.05%, a relative uncertainty of 25%, whereas the uncertainty at 0.06% strain amplitude was approximately 0.04%, a relative uncertainty of 66%. One effect of this large uncertainty at strain amplitudes near the fatigue limit is that the uncertainty is outside the ORNL Fuel Rod design curve (Figure F2-4). To validate these estimated uncertainties, the strain amplitudes calculated based on the CIRFT linear variable differential transformer (LVDT) will be compared with direct measurement of strain amplitude on a cladding-only sample with a strain gage attached to the side that is experiencing the maximum strain. The data from this sample are reported in Wang et al. [F2-26], but the evaluation of the uncertainty has not yet been performed. This is planned as an FY23 activity.

This page is intentionally blank

F2-7. Expected Cyclic History For Transporting Spent Nuclear Fuel

The expected cyclic history for transporting SNF has been considered in shipping tests [F2-20], referred to as the *multimodal transportation test (MMTT)*, and in dynamic modeling of those shipping tests ([F2-21], [F2-31]). The MMTT was an instrumented shipping test of an ENSA ENUN 32P cask that contained three surrogate PWR assemblies in three locations within the basket and 29 dummy assemblies to mimic the expected weight distribution. The three surrogate PWR assemblies had slightly different designs and are designated (1) the Sandia National Laboratories (Sandia) fuel assembly, (2) the ENSA fuel assembly, and (3) the Korean fuel assembly. Each bundle had a few instrumented surrogate fuel rods that comprised of unpressurized unirradiated cladding tubes with either Pb or Mo pellets to represent the mass of UO₂ pellets. Because there is a gap between the pellets and cladding, the flexural rigidity of the surrogate rods should be equivalent to the cladding tube, which is considered conservative compared with HBU fuel. In HBU fuel, the UO₂ is in contact with the cladding, which increases the flexural rigidity and decreases the strains in bending compared with the cladding tube only. The differences in these three assemblies are described in Kalinina et al. [F2-20].

This report focuses on the strain gage and accelerometer data from the center of the surrogate fuel rods, which should represent the location of maximum strain. Based on the nomenclature in Kalinina [F2-20], the accelerometers of interest are A2Z on the Sandia assembly, A7Z on the ENSA assembly, and A11Z on the Korean assembly. The letter “Z” indicates that the accelerometer is measuring accelerations in the vertical direction. The strain gages at the Sandia, ENSA, and Korean fuel assembly locations are SG04-0, SG17, and SG28, respectively. These strain gages were put on top of the surrogate rods after orienting the bundles horizontally and thus do not include the bending strain due to gravity (estimated in Section F2-4).

Considering the strain under gravity, the expected cyclic history can be represented by modifying Eq. (F2-13) to include a time-dependent bending strain:

$$\varepsilon_T(t) = \varepsilon_b(t) + \varepsilon_z, \quad (14)$$

where the bending strain is the bending strain under gravity plus any bending strains associated with accelerations during transportation:

$$\varepsilon_b(t) = \varepsilon_b(1g \text{ gravity}) + \varepsilon_b(\text{transportation accelerations}(t)). \quad (15)$$

Thus, the MMTT data is a representation of the bending strains associated with accelerations during transportation, and while the MMTT only included standard PWR fuel designs, it has been suggested to be conservative relative to other potential future transportation configuration [F2-21]. Because the observed strain amplitudes in the MMTT are significantly lower than the fatigue limit of the fuel rods, the suggested approach herein is to define a single conservative strain amplitude to bound all expected fuel assembly design and all future transportation configurations. As an example, the maximum observed strain on the fuel assemblies in the MMTT (0.0042%, (Figure 11-10 of [F2-20])) could be used to bound the expected strain amplitudes for the PWR designs tested. This is considered conservative because most cycles are significantly less than this maximum value, and it was observed that only ~4000 cycles occurred above a strain amplitude of 0.001% in the MMTT [F2-31]. To develop a generic strain amplitude that bounds all current and future fuel designs, conservatism, uncertainties and limitations in the MMTT should be considered. The range of conditions observed in MMTT test are shown in Figure F2-12 and are well within the range where fatigue damage is not expected to accumulate. However, as noted in Section F2-4, this design limit does not include the mean strain expected in HBU fuel rods. Further CIRFT testing is recommended to measure the potential effect of a prototypical mean strain, which is expected to be small compared to the gap between the observed strain amplitudes and the fatigue limit.

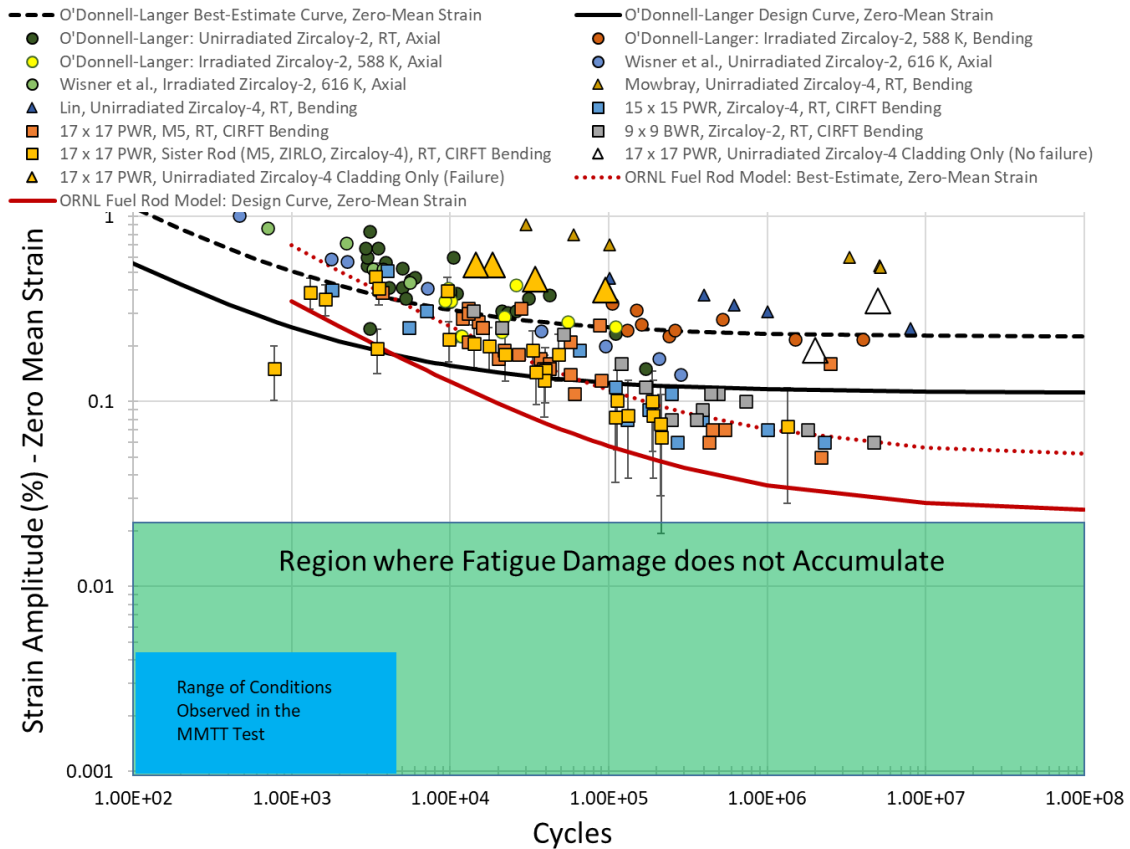


Figure F2-12. Comparison of the most severe range of conditions in the MMTT with the fatigue design curve for fuel rods tested under zero-mean strain conditions.

F2-8. Summary And Conclusions

In the fatigue evaluation of SNF under transportation conditions, the magnitude of the cyclic history is expected to be less than the fatigue limit of the fuel rods. Thus, to conclude that fatigue failures do not occur, it is sufficient to show that a strain amplitude representing an expected cyclic history is less than the fatigue limit of the SNF rods, which is also defined in terms of strain amplitude. The fatigue evaluation described in this paper considered the current available fatigue test data on cladding materials and HBU fuel rods, the potential non-conservatism in the HBU fuel rod test data, and the measured cyclic data reported in the MMTT.

The fatigue limit of HBU fuel rods was degraded compared with the fatigue of cladding alloys. As discussed in other studies [F2-13]–[F2-18], cracks within the pellets and pellet-pellet interfaces are sources of stress/strain concentration, and these discontinuities in the pellet were concluded to be the cause of the observed degradation in fatigue performance. The magnitude of the stress/strain concentration can be estimated as the ratio of the fatigue limit for cladding alloys to that of the HBU fuel rods ($0.2\%/0.06\% = 3.3$).

Additionally, because there will be a nonzero-mean strain in SNF rods due to the RIP and bending under gravity, the fatigue limit based on testing performed at zero-mean strain is potentially non-conservative. The maximum axial cladding strain in SNF was predicted to range from ~ 0.02 to $\sim 0.06\%$, depending on assumed burnup and temperature conditions. This range is comparable to the fatigue limit of HBU fuel rods, which is $\sim 0.06\%$ on a best-estimate basis and 0.03% on a design basis. Thus, strain due to mainly internal gas pressure may further degrade the fatigue performance of SNF tested at zero-mean strain conditions, and it was estimated that a nonzero mean strain could degrade the fatigue limit further by $\sim 7\%$. Additional fatigue testing of HBU fuel rods is recommended to determine the potential magnitude of the degradation in performance because of this nonzero-mean strain effect.

The effect of temperature on the fatigue limit of HBU fuel rods was also discussed. Although elevated temperature has been observed to decrease the fatigue limit of Zr alloys, the effect appears to be small. The authors concluded that fatigue testing of fuel rods at elevated temperature would be beneficial for determining whether there is a significant effect but that the conservatism in the fatigue design limit based on the RT test data alone likely covers any small degradation due to temperature. The main effect of temperature on the fuel rod is to increase RIP and thus the mean strain.

Finally, there is a significant gap between the maximum strain amplitude measured in the MMTT ($0.0042\%^4$) and the fatigue limit of the ORNL design curve for HBU fuel rods ($\sim 0.03\%$), indicating that fatigue damage is not expected during normal transportation conditions. However as noted above, additional fatigue testing is recommended to confirm that that fatigue limit at nonzero-mean strain does not decrease significantly.

⁴ Note that only ~ 4000 cycles were observed in the range of 0.001% to 0.0042% [31]

This page is intentionally blank

F2-9. REFERENCES

- [F2-1] US NRC. 2020. *Standard Review Plan for Transportation Packages for Spent Fuel and Radioactive Materials*. NUREG-2216. Washington, DC: US Nuclear Regulatory Commission
- [F2-2] W. J. O'Donnell and B. F. Langer. 1964. "Fatigue Design Basis for Zircaloy Components." *Nuclear Science and Engineering* 20, no. 1: 1–12.
- [F2-3] M. Nakatsuka, T. Kubo, and Y. Hayashi. 1994. "Fatigue Behavior of Neutron Irradiated Zircaloy-2 Fuel Cladding Tubes." *Zirconium in the Nuclear Industry: Ninth International Symposium*, ASTM STP 1132, American Society for Testing and Materials, 230–245.
- [F2-4] K. Snowden and P. Stathers. 1977. "The Fatigue Behavior of α -Zirconium and Zircaloy-2 in the Temperature Range of 20 to 700°C." *J. Nucl. Mater.* 67: 215–228.
- [F2-5] S. Wisner, M. Reynolds, and R. Adamson. 1994. "Fatigue Behavior of Irradiated and Unirradiated Zircaloy and Zirconium." *Zirconium in the Nuclear Industry: Tenth International Symposium*. ASTM STP 1245, American Society for Testing and Materials, 499–520.
- [F2-6] A. Soniak, S. Lansiaart, J. Royer, J.-P. Mardon, and N. Waeckel. 1994. "Irradiation Effect on Fatigue Behavior of Zircaloy-4 Cladding Tubes." *Zirconium in the Nuclear Industry: Tenth International Symposium*, ASTM STP 1245, American Society for Testing and Materials, 549–558.
- [F2-7] G. Brun, J. Pelchat, J. Floze, and M. Galimberti. 1987. "Cumulative Fatigue and Creep-Fatigue Damage at 350 °C on Recrystallized Zircaloy-4." *Zirconium in the Nuclear Industry: Seventh International Symposium*, ASTM STP 939, American Society for Testing and Materials, 597–616.
- [F2-8] K. Pettersson. 1975. "Low-Cycle Fatigue Properties of Zircaloy-2 Cladding." *J. Nucl. Mater.* 56: 91–102.
- [F2-9] D. Lee and P. Hill. 1976. "Effect of Oxygen on the Fatigue Behavior of Zircaloy." *J. Nucl. Mater.* 60: 227–230.
- [F2-10] P. Pandarinathan and P. Vasudevan. 1980. "Low-Cycle Fatigue Studies on Nuclear Reactor Zircaloy-2 Fuel Tubes at Room Temperature, 300 and 350°C." *J. Nucl. Mater.* 91: 47–58.
- [F2-11] X. Lin and G. Haicheng. 1999. "Low Cycle Fatigue Properties and Microscopic Deformation Structure of Zircaloy-4 in Recrystallized and Stress-Relieved Conditions." *J. Nucl. Mater.* 265: 213–217.
- [F2-12] D. Mowbray. 1965. "Effects of 1.0% Superimposed Mean Strain on the Bending Fatigue Strength of Zircaloy-4." *Nuclear Applications* 1, no. 1: 39–48.
- [F2-13] P. Cantonwine, R. Montgomery, J.-A. Wang, H. Wang, B. Bevard, D. Skitt, Y. Sasikumar and O. Martinez. 2022. *Sister Rod Destructive Examinations (FY22) Appendix F: Cyclic Integrated Reversible Bending Fatigue Tests*. ORNL/TM-2022/2733. Oak Ridge: Oak Ridge National Laboratory.
- [F2-14] H. Wang, J.-A. J. Wang, T. Tan, H. Jiang, T. S. Cox, R. L. Howard, B. B. Bevard, and M. E. Flanagan. 2013. "Development of U-Frame Bending System for Studying the Vibration Integrity of Spent Nuclear Fuel." *J. of Nuclear Materials* 440: 201–213.
- [F2-15] J.-A. Wang and H. Wang. 2017. *Mechanical Fatigue Testing of High-Burnup Fuel for Transportation Applications*. NUREG/CR-7198, Rev. 1. Washington, DC: US Nuclear Regulatory Commission.

- [F2-16] J.-A. Wang, H. Wang, H. Jiang, and B. Bevard. 2018. “High Burn-up Spent Nuclear Fuel Transport Reliability Investigation.” *Nuclear Engr. and Design* 330: 497–515.
- [F2-17] R. Montgomery, J.-A. Wang, P. Cantonwine, Y. Sasikumar, H. Wang, B. Bevard, D. Skitt, and O. Martinez. 2021. *Sister Rod Destructive Examinations (FY21) Appendix F: Cyclic Integrated Reversible Bending Fatigue Tests*. ORNL/TM-2021/2291. Oak Ridge: Oak Ridge National Laboratory.
- [F2-18] US NRC. 2020. *Dry Storage and Transportation of High Burnup Spent Nuclear Fuel*. NUREG-2224. Washington, DC: US Nuclear Regulatory Commission.
- [F2-19] H. Jian, J.-A. Wang, and H. Wang. 2016. “The Impact of Interface Bonding Efficiency on High-Burnup Spent Nuclear Fuel Dynamic Performance.” *Nuclear Engineering and Design* 309: 40–52.
- [F2-20] E.A. Kalinina, C. Wright, L. Lujan, N. Gordon, S.J. Saltzstein, and K.M. Norman. 2018. *Data Analysis of ENSA/DOE Rail Cask Tests*. SAND2018-13258R. Sandia National Laboratory.
- [F2-21] N. Klymyshyn, P. Ivanusa, K. Kadooka, C. Spitz, I. Ed, and P. R. Jensen. 2019. *Structural Dynamic Analysis of Spent Nuclear Fuel*. PNNL-29150, SFWD-SFWST-M2SF-19PN010202014. Richland: Pacific Northwest National Laboratory.
- [F2-22] American Institute of Steel Construction. *Steel Construction Manual*. 14th edition. Table 3-23, Shears, Moments and Deflections.
- [F2-23] R. Montgomery, R. N. Morris, R. Ilgner, B. Roach, J.-A. Wang, Z. Burns, J. T. Dixon, and S. M. Curlin. 2020. *Sister Rod Destructive Examination (FY20): Appendix B: Segmentation, Defueling, Metallographic Data and Total Cladding Hydrogen*. ORNL/SPR-2019/1251. Oak Ridge: Oak Ridge National Laboratory.
- [F2-24] J.-A. Wang, H. Wang, B. B. Bevard, and J. M. Scaglione. 2017. *FY2017 Status Report: CIRFT Data Update and Data Analysis for Spent Fuel Vibration Reliability Study, Revision 1*. ORNL/SPR-2017/521. Oak Ridge: Oak Ridge National Laboratory.
- [F2-25] G. M. O'Donnell and H. H. Scott. 2001. *A New Comparative Analysis of LWR Fuel Design*. NUREG-1754. US Nuclear Regulatory Commission.
- [F2-26] J.-A. Wang, P. Cantonwine, Y. Sasikumar, H. Wang, B. Bevard, D. Skitt, and O. Martinez. 2022. *Sister Rod Destructive Examination (FY20): Appendix F: Cyclic Integrated Reversible-Bending Fatigue Tests*. ORNL/SPR-2021/2291. Oak Ridge: Oak Ridge National Laboratory.
- [F2-27] J.-Y. Wang et al. 2018. “High Burnup Spent Nuclear Fuel Transport Reliability Investigation.” *Nuclear Engineering and Design* 330: 497–515.
- [F2-28] E. Schwenk et al. 1978. “Poisson’s Ratio in Zircaloy-4 between 24° and 316°C.” *J. Nucl. Mater.* 73: 129–131.
- [F2-29] R. N. Morris and R. Montgomery. 2022. *Sister Rod Destructive Examination (FY20): Appendix C: Rod Internal Pressure, Void Volume, and Gas Transmission Tests*. ORNL/SPR-2020/1769. Oak Ridge: Oak Ridge National Laboratory.
- [F2-30] R. Montgomery. 2021. *Sister Rod Destructive Examinations (FY21), Appendix G: CIRFT Uncertainty Calculations*. ORNL/SPR-2021/1840. Oak Ridge: Oak Ridge National Laboratory.
- [F2-31] N. A. Klymyshyn, P. Ivanusa, K. Kadooka, C. Spitz, P. Jensen, S. Ross, B. Hanson, D. Garcia, J. Smith, and S. Lewis. 2018. *Modeling and Analysis of the ENSA/DOE Multimodal Transportation Campaign*. PNNL-28088. Richland: Pacific Northwest National Laboratory.

- [F2-32] US NRC. 2007. *Standard Review Plan, Section 4.2 Fuel System Design, Revision 3*. NUREG-800. Washington, DC: US Nuclear Regulatory Commission.
- [F2-33] R.W. Hertzberg. 1989. *Deformation and Fracture Mechanics of Engineering Materials*. Section 12.2.1. 3rd Edition John Wiley and Sons.
- [F2-34] R.W. Shimskey et al. 2022. PNNL FY 2022 Sibling Pin Testing Results. M3SF-23PN010201043, PNNL-33781, Richland: Pacific Northwest National Laboratory.